

# Nanosized zeolites directed by easily accessible non-surfactant diquats: synthesis, crystallization mechanism and catalytic applications

**Citation for published version (APA):**

Li, S. (2022). *Nanosized zeolites directed by easily accessible non-surfactant diquats: synthesis, crystallization mechanism and catalytic applications*. [Phd Thesis 1 (Research TU/e / Graduation TU/e), Chemical Engineering and Chemistry]. Eindhoven University of Technology.

**Document status and date:**

Published: 08/09/2022

**Document Version:**

Publisher's PDF, also known as Version of Record (includes final page, issue and volume numbers)

**Please check the document version of this publication:**

- A submitted manuscript is the version of the article upon submission and before peer-review. There can be important differences between the submitted version and the official published version of record. People interested in the research are advised to contact the author for the final version of the publication, or visit the DOI to the publisher's website.
- The final author version and the galley proof are versions of the publication after peer review.
- The final published version features the final layout of the paper including the volume, issue and page numbers.

[Link to publication](#)

**General rights**

Copyright and moral rights for the publications made accessible in the public portal are retained by the authors and/or other copyright owners and it is a condition of accessing publications that users recognise and abide by the legal requirements associated with these rights.

- Users may download and print one copy of any publication from the public portal for the purpose of private study or research.
- You may not further distribute the material or use it for any profit-making activity or commercial gain
- You may freely distribute the URL identifying the publication in the public portal.

If the publication is distributed under the terms of Article 25fa of the Dutch Copyright Act, indicated by the "Taverne" license above, please follow below link for the End User Agreement:

[www.tue.nl/taverne](http://www.tue.nl/taverne)

**Take down policy**

If you believe that this document breaches copyright please contact us at:

[openaccess@tue.nl](mailto:openaccess@tue.nl)

providing details and we will investigate your claim.

# Nanosized zeolites directed by easily accessible non-surfactant diquats: synthesis, crystallization mechanism and catalytic applications

## PROEFSCHRIFT

ter verkrijging van de graad van doctor aan de Technische Universiteit Eindhoven, op gezag van de rector magnificus prof.dr.ir. F.P.T. Baaijens, voor een commissie aangewezen door het College voor Promoties, in het openbaar te verdedigen op donderdag 8 september 2022 om 13:30 uur

door

Shaojie Li

geboren te Hebei, China

Dit proefschrift is goedgekeurd door de promotoren en de samenstelling van de promotiecommissie is als volgt:

voorzitter:	prof.dr. A.P.H.J Schenning
1 <sup>e</sup> promotor:	prof.dr.ir. E.J.M. Hensen
copromotor:	dr. N.A. Kosinov
leden:	prof.dr.ir. J. van der Schaaf prof.dr. J. Yu (Jilin University) prof.dr. P.P. Pescarmona (Rijksuniversiteit Groningen) prof.dr.ir. J.A.M. Kuipers
adviseur:	dr.ir. M. Dusselier (KU Leuven)

*Het onderzoek of ontwerp dat in dit proefschrift wordt beschreven is uitgevoerd in overeenstemming met de TU/e Gedragscode Wetenschapsbeoefening.*

*to my family*

Shaojie Li

*Nanosized zeolites directed by easily accessible non-surfactant diquats: synthesis, crystallization mechanism and catalytic applications*

A catalogue record is available from the Eindhoven University of Technology Library

ISBN: 978-90-386-5559-8

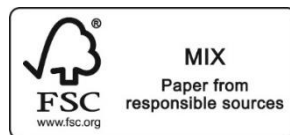
The work described in this thesis has been carried out at the Inorganic Material & Catalysis group, Eindhoven University of Technology, The Netherlands. We acknowledge China Scholarship Council (CSC) for financial support.



Printed by: Gildeprint - The Netherlands

Cover design: Shaojie Li and Peerapol Pornsetmetakul

Copyright © 2022 by Shaojie Li



# Contents

<b>Chapter 1</b>	Introduction and scope	1
<b>Chapter 2</b>	Synthesis of nanocrystalline mordenite zeolite with improved performance in benzene alkylation and n-paraffins hydroconversion	17
<b>Chapter 3</b>	Facile synthesis of nanosized mordenite and Beta zeolites with improved catalytic performance: non-surfactant diquateryary ammonium compounds as structure-directing agents	51
<b>Chapter 4</b>	Direct synthesis of Al-rich ZSM-5 nanocrystals with improved performance in aromatics formation from methane and methanol	101
<b>Chapter 5</b>	Rigid diquats structure-directing agents for synthesis of ZSM-12 nanocrystals with improved performance in n-paraffins hydroconversion and methanol-to-hydrocarbons reactions	137
<b>Chapter 6</b>	<i>P</i> -phenylenedimethylene-bis(trimethylammonium) as a versatile diaquat template for synthesizing nanosized mordenite, EU-1 and ZSM-12 zeolites	179
<b>Chapter 7</b>	Summary and outlook	209
<b>Acknowledgement</b>		213
<b>List of publications</b>		216
<b>Curriculum Vitae</b>		217



# Chapter 1

## Introduction and scope

### 1.1 Zeolites

Zeolites are crystalline inorganic materials whose oxide-based framework is built up with corner-sharing  $\text{TO}_4$  tetrahedrons, where T refers to a tetrahedral atom, most commonly Si and Al. Different ways of tetrahedra connection result in different zeolite framework types.<sup>1</sup>

<sup>2</sup> The name zeolite was first used by Swedish chemist Axel Cronstedt in 1756. He noted that the mineral stilbite appears to boil producing a large amount of steam when heated. Therefore, he named these materials zeolites, or boiling stones from Greek ζέω – to boil and λίθος – stone.<sup>3</sup> The first laboratory preparation of a zeolite can be traced back to the claim by Saint Clair Deville in 1862. Zeolite synthesis became an important research area since the pioneering works of artificial zeolite synthesis by Barrer and Milton in the late 1940s. Following the foundations laid in the 1950s, many significant developments were achieved in the next decade due to the addition of quaternary ammoniums to the initial gel, different from the utilization of only inorganic components in earlier synthesis of zeolites.<sup>4</sup> In general, zeolite synthesis is performed under hydrothermal and solvothermal conditions. The synthesis gel medium contains the zeolite framework precursors, solvents, template or structure-directing agents (SDAs), and mineralizers. The reaction mixture is subjected to hydrothermal treatment at an elevated temperature in the typical range of 30-200 °C for a period from minutes to days. To date, more than 250 zeolite frameworks have been recognized by the Structure Commission of the International Zeolite Association (IZA-SC).<sup>5</sup> Notably, computer modeling has predicted that millions of zeolite structures can be built from the primary building units, indicating the great potential of this research area for developing new functional microporous materials.<sup>6</sup>

Today, zeolites are widely used in industrial processes, especially in ion-exchange, adsorption/separation, and catalysis areas, and they are one of the most widely used classes of materials among the heterogeneous catalysts.<sup>7</sup> Their successful application in hydrocarbon conversion chemistry in petroleum refineries and petrochemical operations and the production of fine chemicals are due to their environmentally-benign nature, well-defined microporous structure, flexible chemical composition and excellent (hydro)thermal stability.<sup>8</sup> The catalytic performance of zeolites is closely associated with their physicochemical



properties, especially well-defined micropores ( $< 2$  nm), crystal morphologies and chemical composition.<sup>9, 10</sup> The well-defined microporous channels endow zeolites with unique shape selectivity. The shape selectivity involving reactants and products is related to a true molecular sieve effect.<sup>11</sup> Transition-state selectivity occurs when the geometry of the pore around the active sites can stabilize one specific transition state among several possible ones, while it can also impose steric constraints on the transition state of reaction intermediates (Figure 1.1).<sup>8</sup> However, despite the extraordinary shape selectivity conferred on zeolites, the intrinsic micropores can also impose severe transport limitations on reactants and products to and away from the acid sites, respectively, especially when bulky molecules with dimensions close to the diameter of the micropores are involved.<sup>12</sup> This leads to inefficient use of the internal active sites of zeolites, which can substantially reduce the catalytic activity.<sup>13</sup> Even for small molecules, long residence times favor consecutive decomposition (cracking) reactions or oligomerization/polymerization of reaction intermediates, resulting in undesired products that cannot leave the pores and induce rapid catalyst deactivation.<sup>14, 15</sup> An effective strategy to overcome such mass transfer limitation and improve the accessibility of active sites is to decrease the diffusion path length in the micropores. This can be achieved by introduction of intracrystalline mesopores (2-50 nm) or by preparation of zeolite nanocrystals, with a size below 100 nm.<sup>16, 17</sup> Moreover, given that most industrial applications of zeolitic catalysts are based on their acidic properties,<sup>18</sup> large efforts have been devoted to characterizing and tuning the acidic properties, *e.g.* concentration,<sup>19</sup> nature,<sup>20</sup> location<sup>21</sup> and distance,<sup>22</sup> to optimize the catalytic performance. Therefore, the rational synthesis of zeolitic materials with optimum properties based on practical catalytic requirements is an important research topic in both academia and industry.

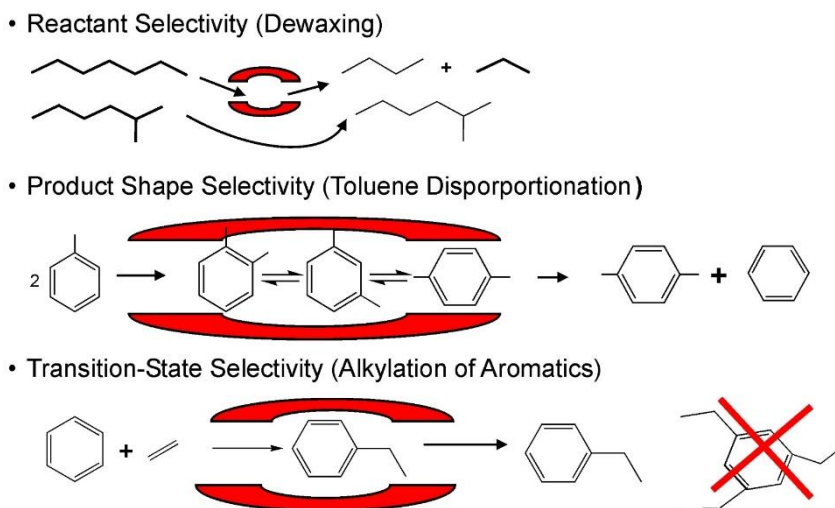


**Figure 1.1.** Examples of classical shape selectivity.<sup>8</sup>

## 1.2 Synthesis of nanosized zeolites

Nanosized zeolites refer to zeolites in which at least one dimension is reduced below 100 nm with the morphology of nanosheets, nanoneedles, nanorods or nanocrystals, which are attractive due to reduced diffusion lengths. Although there are difficulties in the separation of zeolite nanocrystals from the mother liquor after hydrothermal synthesis, nanosized zeolites are promising candidates for fundamental studies, *e.g.* to study the impact of diffusion length on the catalytic performance in a systematic manner.<sup>16</sup> In the last two decades, many efforts have been devoted to the synthesis of nanosized zeolites. Generally, the strategies can be divided into top-down and bottom-up approaches, based on whether nanocrystals are obtained after or during zeolite crystallization, respectively.<sup>7, 9</sup>

In the first approach, post-synthesis treatment of conventional bulk zeolites using ball-milling is effective for reducing the size of zeolite crystals to those of nanoparticles, although subsequent recrystallization is needed to restore the usually impeded crystallinity.<sup>23</sup> Delamination as an effective approach to obtain zeolite nanosheets as first reported by Corma's group. The success of this method is due to the relatively weak interactions between not full condensed, layered zeolite precursors, rendering the method only effective for particular zeolite topologies like FER and MWW.<sup>24, 25</sup>

Compared to top-down approaches, bottom-up approaches provide more flexibility when aiming at nanosized zeolites. Although zeolite synthesis is a complex process, the general assumption is that the process includes two steps, *i.e.* nucleation and crystal growth.<sup>26</sup> It has

been demonstrated that the number of nuclei in the system determines the ultimate crystal size. Therefore, formation of small zeolite crystals requires conditions that favor nucleation over crystal growth. These conditions may include prolonging the aging time,<sup>27</sup> utilization of easily dissolved aluminum and silica sources,<sup>28</sup> addition of seeds,<sup>29</sup> use of ultra-dense gels crystallized by steaming,<sup>30</sup> replacing traditional heating by microwave irradiation<sup>31</sup> and decoupling nucleation from crystal growth via a staged temperature approach.<sup>32</sup> The difficulties in controlling zeolite nucleation also resulted in the development of alternative methods, *e.g.* confined space synthesis. A confined space for zeolite synthesis can be provided by porous carbon materials and polymer hydrogels.<sup>33</sup> In such cases, zeolite growth is limited by a physical barrier and the available free space determines the ultimate crystal size.

As a more facile bottom-up approach, soft-templating methods have been used to prepare nanocrystalline zeolites. The most commonly used one is the dual-templating method, which involves the combined usage of a SDA for the formation of zeolite and a soft template for limiting both crystal grain growth and Ostwald ripening by adsorption on the growing crystal surfaces, thereby resulting in the formation of nanosized zeolites.<sup>34</sup> The soft templates can be organosilanes,<sup>35</sup> polymers<sup>36</sup> and surfactants,<sup>37</sup> *etc.* However, when all the components are introduced into the system at the beginning via a one-step synthesis, particularly for surfactants as soft template, amorphous materials may form instead of the crystalline zeolites due to the typical incompatibility between the self-assembly of surfactants and the growth of zeolite frameworks.<sup>38</sup> Alternatively, a two-step procedure was proposed, involving initial formation of protozeolitic units followed by addition of the soft template.<sup>39</sup> Compared to the dual-templating strategy, one can make the synthesis of nanocrystalline zeolites easier by using a dual-functional template. These “two-in-one” templates usually consist of a hydrophilic quaternary ammonium head group and a long hydrophobic tail. The hydrophilic group directs the zeolite micropores, while the hydrophobic tail limits the crystal growth. There have been many showcases of these bifunctional surfactants for the synthesis of nanosized zeolites.<sup>40-44</sup> However, a main drawback is that these complex quaternary ammonium surfactants are synthesized involving multiple chemical steps, which makes them too costly for industrial application. Notably, applying the commercially available and inexpensive soft templates, *i.e.* cetyltrimethylammonium (CTA) and polydiallyldimethylammonium (PDADMA), as dual-functional templates for synthesis of nanocrystalline zeolites is still limited to ZSM-5 and beta.<sup>45, 46</sup>

From the practical and economic perspective, it would be attractive to directly synthesize nanosized zeolites by use of relative simple and inexpensive organic molecules as dual-functional templates. The interest in this approach follows from the larger number of

publications concerning simple non-surfactant molecules for obtaining nanocrystalline zeolites during the last five years.<sup>5</sup> A common feature is that these simple molecules can be obtained by one-step synthesis procedure.<sup>47-52</sup> Among them, non-surfactant diquatery ammonium compounds have been used for the synthesis of various zeolites in nanocrystalline form. These compounds consist of two end groups and a linkage, which render them highly flexible. Their end groups and linkage can be tailored in terms of size, rigidity and charge density to control the crystal topology and morphology of the zeolites they template.<sup>53</sup> It should be noted that another important utilization of non-surfactant diquatery ammonium compounds is in the discovery of new zeolite structures during the last three decades.<sup>1, 54-58</sup> Despite the difficulty and complexity in understanding the exact host-guests interaction between the OSDAs and zeolites, it has been demonstrated that a flexible OSDA can open the possibility for synthesizing different framework structures due to their adaptable conformations towards a wide range of zeolite frameworks. In contrast, a rigid OSDA would be more selective towards a specific zeolite structure.<sup>1, 59</sup> While the OSDA is not strong enough itself to determine the phase selectivity, other factors, *e.g.* framework substituents, gel concentrations and crystallization temperature, are also important for the phase selectivity.<sup>26</sup>

## **1.3 Catalytic applications of nanosized zeolites**

There are two main differences between nanosized and conventional micron-sized zeolite crystals when they are employed as acid catalysts. First, nanosized zeolites exhibit a substantially higher external surface area, which is an advantage when bulky reactants that cannot penetrate through zeolite domains have to be processed. Second, nanocrystals can provide shorter diffusion pathways than their micron-sized counterparts. The faster desorption of reaction intermediates and products from the zeolite domains reduces the residence time in the crystals and therefore effectively suppresses undesired side reactions, *e.g.* overcracking and coke condensation, thus resulting in an improved product distribution and often longer catalyst life.<sup>5</sup>

### **1.3.1 Methanol-to-hydrocarbons**

The methanol-to-hydrocarbons (MTH) process constitutes promising reaction chemistry for the production of olefins, aromatics and gasoline from methanol which can be obtained from alternative carbon sources, *e.g.* coal, biomass, natural gas and carbon dioxide, to alleviate the global warming and maintain a sustainable economy in a post-oil society.<sup>60, 61</sup> Currently, it is widely accepted that product formation during steady-state operation of the MTH reaction follows an autocatalytic route via a dual-cycle mechanism (Figure 1.2).<sup>62</sup> Both the relative

propagation of each cycle and the exact intermediates depend on the reaction conditions and the properties of the employed catalyst.<sup>63</sup> This in turn can explain how the products of the MTH process can be tuned towards olefin-rich (methanol to olefins; MTO), propene-rich (methanol to propene; MTP) or gasoline-rich (methanol to gasoline; MTG) mixtures.<sup>60</sup> For instance, an Al-rich ZSM-5 catalyst has high acidity and suitable pore structure, which can promote aromatics formation.<sup>64</sup> Notably, the autocatalytic feature of the MTH reaction leads to confined hydrocarbons in micropores as the active species, on one hand, and deactivating precursors, on the other hand.<sup>65, 66</sup> Besides optimizing the physicochemical properties of zeolites to achieve targeted hydrocarbons production, decreasing coke formation rate and improving micropore utilization to solve the rapid catalytic deactivation is an important task. This can be achieved by the introduction of a hierarchically porous network in zeolite crystals or by reducing the crystal size to nanosized dimensions.<sup>67, 68</sup> Compared to zeolites in which pores run in more than one dimension, *e.g.* ZSM-5 (MFI) and SAPO-34 (CHA), tuning crystal size has a more significant impact on the catalytic lifetime of one-dimensional zeolites, *e.g.* ZSM-22 (TON) and ZSM-23 (MTT), because acid sites in each micropore are only accessible by the two ends of the crystals.<sup>69, 70</sup> For instance, Olsbye and co-workers showed that decreasing the average length of ZSM-23 channels from 160 nm to 50 nm led to an increased methanol conversion capacity by one order of magnitude.<sup>71</sup> Notably, these one-dimensional zeolites with medium-size channels are suitable catalysts for the production of aromatics-free gasoline, because the formation of aromatics is strongly suppressed due to the absence of channel intersections and large-size cavities.<sup>23, 72</sup>

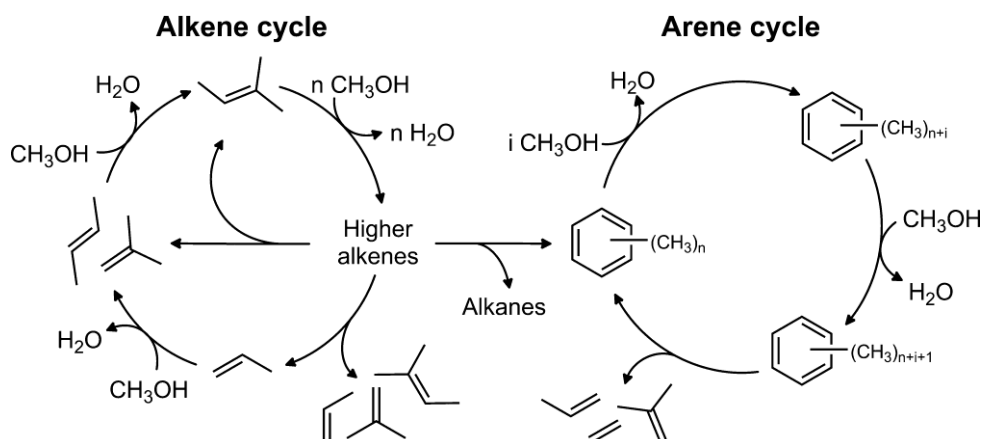


**Figure 1. 2.** Dual-cycle mechanism of MTH reaction.<sup>62</sup>

### 1.3.2 Hydroconversion of n-paraffins

Hydroconversion processes constitute one of the most important reaction units in petroleum refineries for the production of high-quality fuels.<sup>73</sup> Hydroconversion comprises two main reactions, *i.e.* hydrocracking and hydroisomerization. Hydrocracking involves the conversion of heavy hydrocarbon fractions into high-value hydrocarbons for use as transportation fuels.<sup>74</sup> Due to its versatility and flexibility, jet fuel, diesel and in some cases also gasoline can be obtained.<sup>75</sup> Hydroisomerization involves isomerization of paraffins to their branched isomers with limited cracking. It is used to increase the octane number of gasoline and improve the cold-flow properties of diesel, jet fuel and lubricants.<sup>76</sup> Besides processing conventional feedstocks derived from crude oil, *e.g.* vacuum gas oil, hydroconversion is also employed to upgrade non-petroleum hydrocarbons produced from Fischer-Tropsch synthesis and fast pyrolysis of biomass, both of which are effective routes to realize the utilization of renewable sources.<sup>77, 78</sup> Hydroconversion is performed using bifunctional catalysts containing a metal component supported on an acidic support. The metal sites, typically noble metal Pt or Pd or mixed sulfides of non-noble transition metal Ni or Co with Mo, catalyze hydrogenation/dehydrogenation reactions, while the acid sites, often zeolites or amorphous aluminosilicas, catalyze isomerization and cracking reactions.<sup>73</sup> The general mechanism of hydroconversion reactions over bifunctional catalysts involves several consecutive steps: (i) dehydrogenation of alkanes on the metal sites with the formation of olefins; (ii) diffusion of these olefins to the acid sites; (iii) protonation of the olefins on the acid sites with the formation of alkylcarbenium ions; (iv) skeletal isomerization or  $\beta$ -scission cracking; (v) desorption from the acid sites and diffusion of olefins to the metal sites; (vi) hydrogenation of the olefins to alkanes and (vii) desorption of alkanes from the bifunctional catalysts (Figure 1.3).<sup>79</sup> The catalytic performance, in terms of activity and selectivity, over bifunctional catalysts depends on various properties of the catalysts, such as metal dispersion,<sup>80</sup> metal-to-acid site ratio,<sup>81</sup> proximity of metal and acid sites,<sup>82</sup> and the porosity and acidity of the support.<sup>83-85</sup> For instance, nanosized SAPO-11 exhibited both a higher catalytic activity and isomer yield than its micron-sized counterpart in the hydroconversion of long n-paraffins due to the improved accessibility of acid sites and decreased residence time of reaction intermediates within zeolite domains.<sup>86</sup>

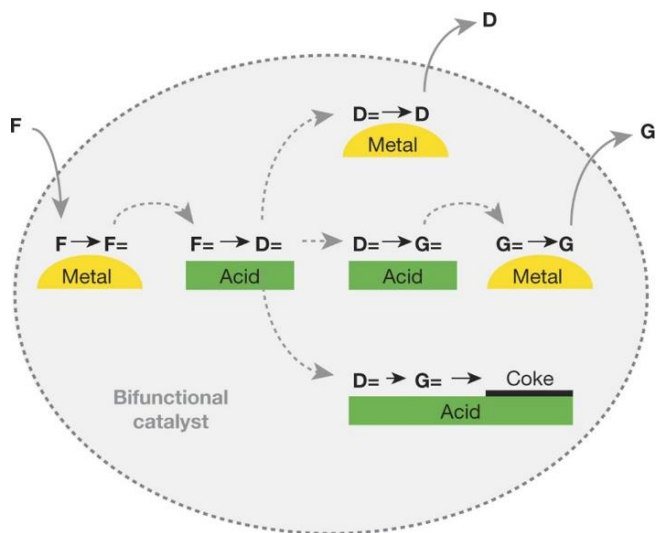


**Figure 1.3.** The general mechanism of hydroconversion reactions over bifunctional catalysts.<sup>82</sup>

### 1.3.3 Methane dehydroaromatization

Non-oxidative dehydroaromatization of methane (MDA) over Mo-containing zeolite catalysts is a promising process for the direct conversion of methane to high-valuable aromatics (mainly benzene) and hydrogen.<sup>87</sup> Since Xu *et al.* first reported the utility of a Mo/HZSM-5 catalyst for this reaction in 1993,<sup>88</sup> much work has been aimed at understanding the reaction mechanism and improving the catalytic performance.<sup>89</sup> Despite the fact that the reaction mechanism of MDA is still not fully understood, the general assumption is that the reaction proceeds via a bifunctional pathway. Most widely accepted, methane is activated and then coupled to ethylene over Mo-carbide species, followed by aromatization of ethylene over Brønsted acid sites in the shape-selective micropores. Among investigated catalysts, Mo/ZSM-5 is the most promising one for MDA reaction.<sup>90-92</sup> Although significant progress has been achieved in the past three decades, rapid catalyst deactivation due to coke deposition is still unsolved, which is a major obstacle to the industrial application of MDA process.<sup>93</sup> The important role of coke in MDA has been revealed in previous studies, in which at least three kinds of carbon deposits were recognized, *i.e.* carbidic carbon in molybdenum carbide, molybdenum-associated coke and aromatic-type coke on acid sites.<sup>94-96</sup> The study of coke evolution with time on stream suggests that the polyaromatic-type coke is the main reason for the catalyst deactivation.<sup>97</sup> Previous studies reported that hierarchical, nanosized and hollow zeolites displayed higher methane conversion and benzene yield than micro-sized counterparts due to a more rapid diffusion of aromatics out of zeolites to suppress the coke

formation.<sup>98-100</sup> Besides the textural properties, the acidity of zeolite is another important factor that can impact the catalytic performance.<sup>101</sup> It is generally accepted that the Brønsted acid sites have two functions, *i.e.* providing anchoring sites for the metal species and catalyzing the formation of aromatics, as well as coke.<sup>89</sup> Khatib *et al.* showed that a higher micropore occupation of highly dispersed Mo species, resulting from a higher Mo loading over ZSM-5 with a lower Si/Al ratio, was directly correlated with higher benzene selectivity and yield, as well as a higher methane conversion.<sup>102</sup> Overall, using a highly acidic ZSM-5 in the nanosized form or with hierarchically porous network can be an effective strategy to improve the catalytic performance of MDA reaction.

### 1.3.4 Friedel-Crafts reactions

The liquid-phase Friedel-Crafts alkylation/acylation is one of the important acid-catalyzed reactions for the production of various compounds used as pharmaceutical intermediates and fine chemicals.<sup>103</sup> These reactions are generally carried out in liquid phase by use of homogeneous acid catalysts, *e.g.* FeCl<sub>3</sub>, BF<sub>3</sub> and H<sub>2</sub>SO<sub>4</sub>. However, these homogeneous catalysts have several problems, such as the challenge in separation and recovery, corrosion and toxicity.<sup>104</sup> These inevitable drawbacks make it desirable to develop alternative solid acid catalysts, which should be more environmental and easy to reuse. Among the candidates, zeolites, as solid acid catalysts, have been widely studied in Friedel-Crafts reactions, due to their excellent (hydro)thermal stability, strong acidity and shape selectivity.<sup>105</sup> However, conventional zeolites show poor reactivity and rapid deactivation due to strong diffusion limitation of bulky aromatic substrates and corresponding products in micropores.<sup>106, 107</sup> Therefore, many efforts have been made to improve the mass transfer and accessibility of acid sites by decreasing the crystal size or introducing hierarchically porous network. Consequently, these nanosized and hierarchical zeolites exhibited remarkably enhanced activity and better product selectivity as compared to their conventional counterparts, which paves the way for their potential application in Friedel-Crafts reactions.<sup>108</sup>

Although it is clear that nanocrystalline zeolites outperform their micron-sized counterparts, revealing the different reaction behaviors in space and time based on a specific acidity for many zeolitic catalysts are still unsolved due to the difficulty in synthesis of well-defined materials.<sup>109</sup> Indeed, this remains one of the most challenging incentives for chemists, *i.e.* to obtain zeolite materials with well-defined properties, which is essential to pave the way for the understanding for designing and the designing for achieving the desired reaction route in heterogeneous catalysis.<sup>110</sup>



## 1.4 Scope of thesis

The goal of this PhD thesis is to synthesize nanosized zeolites with targeted physicochemical properties for improved or tailored catalytic performance in zeolite-catalyzed hydrocarbon conversion reactions. The focus is on the direct synthesis of zeolite nanocrystals by use of simple and inexpensive organic molecules, particularly non-surfactant diquaternary ammonium compounds, as the sole organic template. We speculate that such kind of bulky organic molecules not only have strong pore-filling ability to stabilize zeolite frameworks but can also be effective capping agents that allow obtaining zeolites in nanocrystalline form due to their divalent feature. Besides, the inorganic component of the synthesis gel is also optimized to ensure the success of such molecule as OSDA.

**Chapter 2** investigates the use of cetyltrimethylammonium (CTA) hydroxide as growth modifier for the direct synthesis of nanosized MOR zeolites, with different aluminum sources. CTA is a commercially available surfactant, which has been used as a growth modifier for obtaining various zeolites in nanocrystalline form. Nanosized MOR zeolites perform better than their bulk counterparts prepared without CTA in benzene alkylation and *n*-hexadecane (*n*-C<sub>16</sub>) hydroconversion.

**Chapter 3** explores the direct synthesis of nanosized MOR and BEA zeolites by use of non-surfactant diquaternary ammonium compounds as the sole organic template. One important consideration was that the employed organic molecule should fit in the micropore channels of MOR and BEA. These compounds are hexane- and *p*-xylene- bridged bis-methylpyrrolidinium, -methylpiperidinium and -DABCO diquats, which were synthesized in a single step from common chemicals. For selected samples, the crystallization mechanism was investigated by investigating the solid intermediates. The benefits of these nanosized zeolites over bulk reference samples were evaluated for Friedel-Crafts and *n*-C<sub>16</sub> hydroconversion reactions.

**Chapter 4** presents the direct synthesis of nanosized ZSM-5 with high acidity (Si/Al = 11) and excellent solid yield (99%), denoted as ZSM-5-11, using *p*-phenylenedimethylenebis(triethylammonium) dichloride as the OSDA. The crystallization process of ZSM-5-11 was investigated in detail. ZSM-5-11 shows significantly improved aromatics productivity in MTH and MDA reactions as compared to a commercial ZSM-5 (Si/Al = 12.9).

**Chapter 5** explores the direct synthesis of nanosized ZSM-12 zeolites with a wide range of Si/Al ratios, especially at the Al-rich compositions, by use of rigid organic molecules as the OSDA. Three rationally designed diquaternary ammonium compounds (*p*-xylene- bridged bis-methylpyrrolidinium, -methylpiperidinium and -1,2-dimethylimidazolium) are employed

in the zeolite synthesis. Nanosized ZSM-12 with different acidity (Si/Al = 18.3, 40.1 and 68.8) were evaluated in n-C<sub>16</sub> hydroconversion and MTH reactions.

**Chapter 6** presents how to employ versatility of a simple OSDA, *i.e.* (*p*-phenylenedimethylene-bis(trimethylammonium) dichloride (Me<sub>3</sub>N-benzyl-NMe<sub>3</sub>), in the synthesis of nanosized zeolites. By modifying the synthesis, including gel composition (Si/Al and NaOH/Si ratios) and crystallization time, direct synthesis of nanosized zeolites (MOR, EU-1 and ZSM-12) were achieved by use of Me<sub>3</sub>N-benzyl-NMe<sub>3</sub> as the sole organic template.

The results of this thesis are summarized in **Chapter 7** including an outlook on further challenges in the thriving field of zeolite synthesis.

## 1.5 References

1. M. Moliner, F. Rey and A. Corma, *Angew. Chem. Int. Ed.*, 2013, **52**, 13880-13889.
2. M. Dusselier and M. E. Davis, *Chem. Rev.*, 2018, **118**, 5265-5329.
3. B. M. Weckhuysen and J. Yu, *Chem. Soc. Rev.*, 2015, **44**, 7022-7024.
4. C. S. Cundy and P. A. Cox, *Microporous Mesoporous Mater.*, 2005, **82**, 1-78.
5. X. Wang, Y. Ma, Q. Wu, Y. Wen and F.-S. Xiao, *Chem. Soc. Rev.*, 2022, **51**, 2431-2443.
6. Y. Li and J. Yu, *Chem. Rev.*, 2014, **114**, 7268-7316.
7. H. Zheng, F. Gao and V. Valtchev, *J. Mater. Chem. A*, 2016, **4**, 16756-16770.
8. T. F. Degnan, *J. Catal.*, 2003, **216**, 32-46.
9. J. Čejka, R. Millini, M. Opanasenko, D. P. Serrano and W. J. Roth, *Catal. Today*, 2020, **345**, 2-13.
10. S. Li, J. Li, M. Dong, S. Fan, T. Zhao, J. Wang and W. Fan, *Chem. Soc. Rev.*, 2019, **48**, 885-907.
11. C. Martínez and A. Corma, *Coord. Chem. Rev.*, 2011, **255**, 1558-1580.
12. A. Bolshakov, R. van de Poll, T. van Bergen-Brenkman, S. C. C. Wiedemann, N. Kosinov and E. J. M. Hensen, *Appl. Catal., B*, 2020, **263**, 118356.
13. K. Na, M. Choi and R. Ryoo, *Microporous Mesoporous Mater.*, 2013, **166**, 3-19.
14. Z. Xu, J. Li, Y. Huang, H. Ma, W. Qian, H. Zhang and W. Ying, *Catal. Sci. Technol.*, 2019, **9**, 2888-2897.
15. W. Dai, V. Ruaux, X. Deng, W. Tai, G. Wu, N. Guan, L. Li and V. Valtchev, *J. Mater. Chem. A*, 2021.
16. S. Mintova, J.-P. Gilson and V. Valtchev, *Nanoscale*, 2013, **5**, 6693-6703.
17. D. Kerstens, B. Smeyers, J. Van Waeyenberg, Q. Zhang, J. Yu and B. F. Sels, *Adv. Mater.*, 2020, **32**, 2004690.

18. J. Shi, Y. Wang, W. Yang, Y. Tang and Z. Xie, *Chem. Soc. Rev.*, 2015, **44**, 8877-8903.
19. Y. Gao, B. Zheng, G. Wu, F. Ma and C. Liu, *RSC Adv.*, 2016, **6**, 83581-83588.
20. N. Rahimi and R. Karimzadeh, *Appl. Catal., A*, 2011, **398**, 1-17.
21. J. Chen, T. Liang, J. Li, S. Wang, Z. Qin, P. Wang, L. Huang, W. Fan and J. Wang, *ACS Catal.*, 2016, **6**, 2299-2313.
22. M. Bernauer, E. Tabor, V. Pashkova, D. Kaucký, Z. Sobalík, B. Wichterlová and J. Dedecek, *J. Catal.*, 2016, **344**, 157-172.
23. J. Wang, S. Xu, J. Li, Y. Zhi, M. Zhang, Y. He, Y. Wei, X. Guo and Z. Liu, *RSC Adv.*, 2015, **5**, 88928-88935.
24. A. Corma, V. Fornes, S. Pergher, T. L. Maesen and J. Buglass, *Nature*, 1998, **396**, 353-356.
25. A. Corma, U. Diaz, M. E. Domine and V. Fornés, *Angew. Chem. Int. Ed.*, 2000, **39**, 1499-1501.
26. J. Grand, H. Awala and S. Mintova, *CrystEngComm*, 2016, **18**, 650-664.
27. H. Mochizuki, T. Yokoi, H. Imai, R. Watanabe, S. Namba, J. N. Kondo and T. Tatsumi, *Microporous Mesoporous Mater.*, 2011, **145**, 165-171.
28. B. O. Hincapie, L. J. Garces, Q. Zhang, A. Sacco and S. L. Suib, *Microporous Mesoporous Mater.*, 2004, **67**, 19-26.
29. H. Zhang, H. Zhang, P. Wang, Y. Zhao, Z. Shi, Y. Zhang and Y. Tang, *RSC Adv.*, 2016, **6**, 47623-47631.
30. X. Cheng, J. Mao, X. Lv, T. Hua, X. Cheng, Y. Long and Y. Tang, *J. Mater. Chem. A*, 2014, **2**, 1247-1251.
31. M. Ansari, A. Aroujalian, A. Raisi, B. Dabir and M. Fathizadeh, *Adv. Powder Technol.*, 2014, **25**, 722-727.
32. C. J. Van Oers, K. Góra-Marek, K. Sadowska, M. Mertens, V. Meynen, J. Datka and P. Cool, *Chem. Eng. J.*, 2014, **237**, 372-379.
33. M. H. Sun, L. H. Chen, S. Yu, Y. Li, X. G. Zhou, Z. Y. Hu, Y. H. Sun, Y. Xu and B. L. Su, *Angew. Chem. Int. Ed.*, 2020, **59**, 19582-19591.
34. L.-H. Chen, M.-H. Sun, Z. Wang, W. Yang, Z. Xie and B.-L. Su, *Chem. Rev.*, 2020, **120**, 11194-11294.
35. H. Chen, M. Wang, M. Yang, W. Shang, C. Yang, B. Liu, Q. Hao, J. Zhang and X. Ma, *J. Mater. Sci.*, 2019, **54**, 8202-8215.
36. X. Feng, N. Sheng, Y. Liu, X. Chen, D. Chen, C. Yang and X. Zhou, *ACS Catal.*, 2017, **7**, 2668-2675.
37. T. Xue, S. Li and H. Wu, *Microporous Mesoporous Mater.*, 2021, **312**, 110748.

38. A. Karlsson, M. Stöcker and R. Schmidt, *Microporous Mesoporous Mater.*, 1999, **27**, 181-192.
39. Z. Li, M. T. Navarro, J. Martínez-Triguero, J. Yu and A. Corma, *Catal. Sci. Technol.*, 2016, **6**, 5856-5863.
40. M. Choi, K. Na, J. Kim, Y. Sakamoto, O. Terasaki and R. Ryoo, *Nature*, 2009, **461**, 246-249.
41. W. Kim, J.-C. Kim, J. Kim, Y. Seo and R. Ryoo, *ACS Catal.*, 2013, **3**, 192-195.
42. H. Y. Luo, V. K. Michaelis, S. Hodges, R. G. Griffin and Y. Román-Leshkov, *Chem. Sci.*, 2015, **6**, 6320-6324.
43. R. Kore, R. Srivastava and B. Satpati, *Chem. Eur. J.*, 2014, **20**, 11511-11521.
44. D. Xu, Y. Ma, Z. Jing, L. Han, B. Singh, J. Feng, X. Shen, F. Cao, P. Oleynikov, H. Sun, O. Terasaki and S. Che, *Nat. Commun.*, 2014, **5**, 4262.
45. L. Meng, B. Mezari, M. G. Goesten and E. J. M. Hensen, *Chem. Mater.*, 2017, **29**, 4091-4096.
46. J. Zhu, Y. Zhu, L. Zhu, M. Rigutto, A. van der Made, C. Yang, S. Pan, L. Wang, L. Zhu, Y. Jin, Q. Sun, Q. Wu, X. Meng, D. Zhang, Y. Han, J. Li, Y. Chu, A. Zheng, S. Qiu, X. Zheng and F.-S. Xiao, *J. Am. Chem. Soc.*, 2014, **136**, 2503-2510.
47. Y. Ma, X. Tang, J. Hu, Y. Ma, W. Chen, Z. Liu, S. Han, C. Xu, Q. Wu, A. Zheng, L. Zhu, X. Meng and F.-S. Xiao, *J. Am. Chem. Soc.*, 2022, DOI: 10.1021/jacs.1c12338.
48. H. Xu, W. Chen, G. Zhang, P. Wei, Q. Wu, L. Zhu, X. Meng, X. Li, J. Fei, S. Han, Q. Zhu, A. Zheng, Y. Ma and F.-S. Xiao, *J. Mater. Chem. A*, 2019, **7**, 16671-16676.
49. R. Martínez-Franco, C. Paris, M. E. Martínez-Armero, C. Martínez, M. Moliner and A. Corma, *Chem. Sci.*, 2016, **7**, 102-108.
50. K. Zhang, S. Luo, Z. Liu, C. Li, Z. Ke, X. Yan, Y. Wu and H. Xi, *Chem. Eur. J.*, 2018, **24**, 8133-8140.
51. P. Lu, S. Ghosh, M. Dorneles de Mello, H. S. Kamaluddin, X. Li, G. Kumar, X. Duan, M. Abeykoon, J. A. Boscoboinik and L. Qi, *Angew. Chem. Int. Ed.*, 2021, **133**, 19214-19221.
52. S. H. Keoh, W. Chaikittisilp, K. Muraoka, R. R. Mukti, A. Shimojima, P. Kumar, M. Tsapatsis and T. Okubo, *Chem. Mater.*, 2016, **28**, 8997-9007.
53. P. Wang, Y. Zhao, H. Zhang, T. Yu, Y. Zhang and Y. Tang, *RSC Adv.*, 2017, **7**, 23272-23278.
54. B. W. Boal, M. W. Deem, D. Xie, J. H. Kang, M. E. Davis and S. I. Zones, *Chem. Mater.*, 2016, **28**, 2158-2164.
55. P. Lu, A. Mayoral, L. Gómez-Hortigüela, Y. Zhang and M. A. Camblor, *Chem. Mater.*, 2019, **31**, 5484-5493.

56. S. B. Hong, E. G. Lear, P. A. Wright, W. Zhou, P. A. Cox, C.-H. Shin, J.-H. Park and I.-S. Nam, *J. Am. Chem. Soc.*, 2004, **126**, 5817-5826.
57. J. Li, A. Corma and J. Yu, *Chem. Soc. Rev.*, 2015, **44**, 7112-7127.
58. G. Bellussi, A. Carati, C. Rizzo and R. Millini, *Catal. Sci. Technol.*, 2013, **3**, 833-857.
59. Y. Kubota, M. M. Helmkamp, S. I. Zones and M. E. Davis, *Microporous Mater.*, 1996, **6**, 213-229.
60. U. Olsbye, S. Svelle, M. Bjorgen, P. Beato, T. V. Janssens, F. Joensen, S. Bordiga and K. P. Lillerud, *Angew. Chem. Int. Ed.*, 2012, **51**, 5810-5831.
61. E. Kianfar, S. Hajimirzaee, S. mousavian and A. S. Mehr, *Microchem. J.*, 2020, **156**, 104822.
62. M. Westgård Erichsen, S. Svelle and U. Olsbye, *Catal. Today*, 2013, **215**, 216-223.
63. I. Yarulina, A. D. Chowdhury, F. Meirer, B. M. Weckhuysen and J. Gascon, *Nat. Catal.*, 2018, **1**, 398-411.
64. Z. Wan, W. Wu, G. Li, C. Wang, H. Yang and D. Zhang, *Appl. Catal., A*, 2016, **523**, 312-320.
65. D. Chen, K. Moljord and A. Holmen, *Microporous Mesoporous Mater.*, 2012, **164**, 239-250.
66. X. Zhao, J. Li, P. Tian, L. Wang, X. Li, S. Lin, X. Guo and Z. Liu, *ACS Catal.*, 2019, **9**, 3017-3025.
67. Q. Sun, N. Wang, G. Guo, X. Chen and J. Yu, *J. Mater. Chem. A*, 2015, **3**, 19783-19789.
68. E. M. Gallego, C. Li, C. Paris, N. Martín, J. Martínez-Triguero, M. Boronat, M. Moliner and A. Corma, *Chem. Eur. J.*, 2018, **24**, 14631-14635.
69. M. Dyballa, U. Obenaus, M. Rosenberger, A. Fischer, H. Jakob, E. Klemm and M. Hunger, *Microporous Mesoporous Mater.*, 2016, **233**, 26-30.
70. S. Teketel, W. Skistad, S. Benard, U. Olsbye, K. P. Lillerud, P. Beato and S. Svelle, *ACS Catal.*, 2012, **2**, 26-37.
71. A. Molino, K. A. Łukaszuk, D. Rojo-Gama, K. P. Lillerud, U. Olsbye, S. Bordiga, S. Svelle and P. Beato, *Chem. Commun.*, 2017, **53**, 6816-6819.
72. A. Molino, J. Holzinger, K. A. Łukaszuk, D. Rojo-Gama, A. E. Gunnæs, J. Skibsted, L. F. Lundegaard, S. Svelle, P. Beato, S. Bordiga and K. P. Lillerud, *Catal. Sci. Technol.*, 2019, **9**, 6782-6792.
73. J. Weitkamp, *ChemCatChem*, 2012, **4**, 292-306.
74. M. O. Kazakov, K. A. Nadeina, I. G. Danilova, P. P. Dik, O. V. Klimov, V. Y. Pereyma, E. Y. Gerasimov, I. V. Dobryakova, E. E. Knyazeva, I. I. Ivanova and A. S. Noskov, *Catal. Today*, 2018, **305**, 117-125.

75. M. A. Cambor, A. Corma, A. Martínez, V. Martínez-Soria and S. Valencia, *J. Catal.*, 1998, **179**, 537-547.
76. W. Wang, C.-J. Liu and W. Wu, *Catal. Sci. Technol.*, 2019, **9**, 4162-4187.
77. V. Calemma, C. Gambaro, W. O. Parker, R. Carbone, R. Giardino and P. Scorletti, *Catal. Today*, 2010, **149**, 40-46.
78. J. L. Hodala, J.-S. Jung, E.-H. Yang, G. H. Hong, Y. S. Noh and D. J. Moon, *Fuel*, 2016, **185**, 339-347.
79. H. Deldari, *Appl. Catal., A*, 2005, **293**, 1-10.
80. K. Fang, J. Ren and Y. Sun, *J. Mol. Catal. A: Chem.*, 2005, **229**, 51-58.
81. X. Song, X. Bai, W. Wu, O. V. Kikhtyanin, A. Zhao, L. Xiao, X. Su, J. Zhang and X. Wei, *Mol. Catal.*, 2017, **433**, 84-90.
82. J. Zecevic, G. Vanbutsele, K. P. de Jong and J. A. Martens, *Nature*, 2015, **528**, 245-248.
83. S. Tao, X. Li, G. Lv, C. Wang, R. Xu, H. Ma, Z. J. C. S. Tian and Technology, *Catal. Sci. Technol.*, 2017, **7**, 5775-5784.
84. S. Mehla, K. Krishnamurthy, B. Viswanathan, M. John, Y. Niwate, K. Kumar, S. M. Pai and B. Newalkar, *J. Porous Mater.*, 2013, **20**, 1023-1029.
85. D. Romero, R. Rohling, L. Meng, M. Rigutto and E. J. M. Hensen, *J. Catal.*, 2021, **394**, 284-298.
86. S. Zhang, S.-L. Chen, P. Dong, Z. Ji, Z. Junying and X. Keqi, *Chin. J. Catal.*, 2007, **28**, 857-864.
87. N. Kosinov and E. J. M. Hensen, *Adv. Mater.*, 2020, **32**, 2002565.
88. L. Wang, L. Tao, M. Xie, G. Xu, J. Huang and Y. Xu, *Catal. Lett.*, 1993, **21**, 35-41.
89. P. Schwach, X. Pan and X. Bao, *Chem. Rev.*, 2017, **117**, 8497-8520.
90. K. Sun, D. M. Ginosar, T. He, Y. Zhang, M. Fan and R. Chen, *Ind. Eng. Chem. Res.*, 2018, **57**, 1768-1789.
91. T. Zhang, *Chem. Sci.*, 2021, **12**, 12529-12545.
92. I. Vollmer, S. Ould-Chikh, A. Aguilar-Tapia, G. Li, E. Pidko, J.-L. Hazemann, F. Kapteijn and J. Gascon, *J. Am. Chem. Soc.*, 2019, **141**, 18814-18824.
93. N. Kosinov, F. J. A. G. Coumans, E. Uslamin, F. Kapteijn and E. J. M. Hensen, *Angew. Chem. Int. Ed.*, 2016, **55**, 15086-15090.
94. H. Liu, W. Shen, X. Bao and Y. Xu, *Appl. Catal., A*, 2005, **295**, 79-88.
95. D. Ma, D. Wang, L. Su, Y. Shu, Y. Xu and X. Bao, *J. Catal.*, 2002, **208**, 260-269.
96. C. H. L. Tempelman and E. J. M. Hensen, *Appl. Catal., B*, 2015, **176-177**, 731-739.
97. B. S. Liu, L. Jiang, H. Sun and C. T. Au, *Appl. Surf. Sci.*, 2007, **253**, 5092-5100.
98. Y. Cui, Y. Xu, J. Lu, Y. Suzuki and Z.-G. Zhang, *Appl. Catal., A*, 2011, **393**, 348-358.

99. P. Zhu, G. Yang, J. Sun, R. Fan, P. Zhang, Y. Yoneyama and N. Tsubaki, *J. Mater. Chem. A*, 2017, **5**, 8599-8607.
100. N. Chu, J. Yang, C. Li, J. Cui, Q. Zhao, X. Yin, J. Lu and J. Wang, *Microporous Mesoporous Mater.*, 2009, **118**, 169-175.
101. K. Zhao, L. Jia, J. Wang, B. Hou and D. Li, *New J. Chem.*, 2019, **43**, 4130-4136.
102. M. Rahman, A. Infantes-Molina, A. S. Hoffman, S. R. Bare, K. L. Emerson and S. J. Khatib, *Fuel*, 2020, **278**, 118290.
103. I. Iovel, K. Mertins, J. Kischel, A. Zapf and M. Beller, *Angew. Chem. Int. Ed.*, 2005, **44**, 3913-3917.
104. C. Perego and P. Ingallina, *Catal. Today*, 2002, **73**, 3-22.
105. G. Sartori and R. Maggi, *Chem. Rev.*, 2006, **106**, 1077-1104.
106. K. Leng, Y. Wang, C. Hou, C. Lancelot, C. Lamonnier, A. Rives and Y. J. J. o. c. Sun, *J. Catal.*, 2013, **306**, 100-108.
107. H. Jin, M. B. Ansari, E.-Y. Jeong and S.-E. Park, *J. Catal.*, 2012, **291**, 55-62.
108. M.-N. Liu, Z.-X. Xie, Q.-X. Luo, J. Zhang, H. Chen, L. Xu, M. Sun, X. Ma and Q.-Q. Hao, *Ind. Eng. Chem. Res.*, 2022, **61**, 1078-1088.
109. A. Corma, *Angew. Chem. Int. Ed.*, 2016, **55**, 6112-6113.
110. B. M. Weckhuysen, *Angew. Chem. Int. Ed.*, 2009, **48**, 4910-4943.

# Chapter 2

## Synthesis of nanocrystalline mordenite zeolite with improved performance in benzene alkylation and n-paraffins hydroconversion

### Abstract

Nanocrystalline mordenite (MOR) zeolites were hydrothermally synthesized in a single step with commercial cetyltrimethylammonium (CTA) hydroxide as the sole organic template, while the aluminum source was varied in a typical synthesis gel. CTA can effectively reduce the crystal growth of MOR zeolites, in some cases selectively in the *a*- and *b*-directions of the unit cell. These nanocrystalline MOR zeolites do not only have a larger external surface area than their bulk counterparts prepared without CTA, but the Brønsted acid sites in the side-pockets are also more accessible. The combination of the use of CTA and  $\text{AlCl}_3 \cdot 6\text{H}_2\text{O}$  afforded the best-performing catalyst with much improved activity in benzene alkylation and hydroconversion of n-hexadecane (n-C<sub>16</sub>). Modifying MOR synthesis with CTA hydroxide is a cheap and effective method to open up the one-dimensional micropore system of mordenite, increasing the catalytic performance in hydrocarbon reactions.

This chapter has been published as: S. Li, H. Wu, R.C.J. van de Poll, R.R.M. Joosten, N. Kosinov and E.J.M. Hensen, *ChemCatChem*, 2022, 14, e202101852.



## 2.1 Introduction

Zeolites are microporous crystalline materials possessing well-defined channels and cavities in the molecular range, which can be synthesized with various chemical compositions, pore topologies and crystal sizes.<sup>1, 2</sup> This versatility allows zeolites to be used in numerous applications spanning from adsorption and gas separation to catalysis.<sup>3</sup> Even though more than 200 types of zeolite framework structures have been synthesized and identified, only a limited number of them have found practical applications.<sup>4</sup> Among them, mordenite (MOR) is one of the most important industrial catalysts, because of its high thermal stability, appropriate acidity and unique pore system. MOR is used in commercial processes such as the isomerization and dewaxing of alkanes, the alkylation of aromatics and the production of dimethylamines.<sup>5</sup>

MOR zeolite consists of 12-membered ring (12MR) channels ( $0.67 \times 0.70$  nm) and 8-membered ring (8MR) channels ( $0.26 \times 0.57$  nm), both of which run along the *c*-axis and are interconnected with 8MR side pocket ( $0.34 \times 0.48$  nm) parallel to the *b*-axis.<sup>6</sup> Effectively, MOR exhibits a two-dimensional topology. As the 8MR channels along the *c*-axis are too narrow for most molecules, MOR typically behaves as a one-dimensional zeolite in catalytic reactions.<sup>7</sup> Like most zeolites, MOR can suffer from transport limitations of reactants and products to and from the acid sites, thereby limiting the overall performance.<sup>8</sup> A specific issue with zeolites with a one-dimensional pore channel system is the propensity to fast deactivation due to pore blocking.<sup>9</sup>

The most common approach to enhance the catalytic performance of zeolites is to decrease the diffusion length in the zeolite micropores. Many efforts have been devoted to decreasing the crystal size or introducing secondary porosity in MOR crystals via top-down or bottom-up methods.<sup>4</sup> Top-down methods include dealumination in steam or by treatment with acid solutions, desilication in alkaline or sequential dealumination-desilication. However, it is hard to control the mesoporosity by this methods and typically the zeolite framework is damaged, often decreasing the acidity.<sup>10</sup> As the Si/Al of directly prepared MOR zeolite is normally lower than 15, desilication is difficult to achieve.<sup>11</sup> To deal with this, MOR can be first dealuminated.<sup>12</sup> Bottom-up methods modify the zeolite in the synthesis stage by involving a template that gives rise to additional porosity. One can distinguish hard-templating and soft-templating approaches.<sup>11</sup> It is worth noting that soft templating is beneficial for obtaining mesoporosity of controlled size inside zeolite crystals.<sup>13</sup> Among soft templates, the cationic surfactant cetyltrimethylammonium (CTA) is popular because it is commercially available and inexpensive. CTABr and the slightly more expensive CTAOH have been widely used for preparing hierarchical zeolites.<sup>14-20</sup> Even though CTA has also

been used as an effective growth modifier to obtain hierarchical MOR zeolites, all the strategies reported so far involve the addition of a seed gel containing amorphous aluminosilicate intermediates, time-consuming synthesis protocols (7 days or longer) or complicated steam-assisted synthesis approaches.<sup>21-26</sup> Therefore, for practical application, it is still challenging to develop approaches to prepare hierarchical MOR zeolites in a more facile and economical strategy.

Moreover, studies have shown that physicochemical properties of the MOR zeolite, such as morphology, composition, acidity and crystal purity, are closely related to the synthesis conditions.<sup>27-34</sup> Hamid *et al.* found that the size of MOR crystals can be modified by a factor of 10 by appropriate aging of the silica source.<sup>35</sup> Zhang *et al.* reported that MOR zeolites with various morphologies were synthesized via a facile inorganic hydrothermal route, mainly including adding seeds, adjusting gel composition and silicon source.<sup>29</sup> Li *et al.* discovered that the distribution of Brønsted acid sites (BAS) in MOR zeolite can be adjusted by using different cyclic amine structure-directing templates.<sup>9</sup> Given that the aluminum source is an indispensable part of the MOR zeolite synthesis, its influence has also been extensively investigated. Lu *et al.* successfully synthesized highly crystalline MOR zeolite with a Si/Al ratio of approximately 30 when  $\text{Al}(\text{NO}_3)_3$  was employed as an aluminum source instead of  $\text{AlCl}_3$  or  $\text{Al}_2(\text{SO}_4)_3$ .<sup>33</sup> Previous studies have discovered that the proportion of framework Al atoms in the main channels of MOR zeolite decreased with decreasing the relative amount of aluminum in the synthesis.<sup>34, 36</sup> It has been reported that the crystal size of MOR zeolite prepared with alumina as aluminum source increased with crystallization time, due to the slow release of aluminate ions from undissolved aluminum into the synthesis solution, which is opposite to the trend of crystallization process with sodium aluminate as aluminum source.<sup>31</sup> Hence, it could be anticipated that the choice of aluminum sources can strongly impact the properties of the obtained samples during the synthesis of MOR zeolite with CTA.

In the present study, nanocrystalline MOR zeolites were prepared in a single step via hydrothermal synthesis method with CTAOH as the sole organic structure directing agent.  $\text{Al}(\text{NO}_3)_3$ ,  $\text{AlCl}_3$  and  $\text{Al}(\text{OH})_3$  were chosen as three different aluminum sources in this work. The physicochemical properties of obtained MOR zeolites were extensively characterized. The catalytic performance of these nanocrystalline MOR zeolites in comparison to their bulk counterparts in the benzylation of benzene with benzyl alcohol and in the bifunctional hydroconversion of n-hexadecane ( $n\text{-C}_{16}$ ) was evaluated.

## 2.2 Experimental Section

### 2.2.1 Chemicals

The following commercial chemicals were used in this work without further purification: sodium silicate solution (Merck, SiO<sub>2</sub> 27.0 wt%, Na<sub>2</sub>O 8.0 wt%), Al(NO<sub>3</sub>)<sub>3</sub>·9H<sub>2</sub>O (Sigma Aldrich, reagent grade), AlCl<sub>3</sub>·6H<sub>2</sub>O (Sigma Aldrich, 99%), Al(OH)<sub>3</sub> (Sigma Aldrich, reagent grade), NH<sub>4</sub>NO<sub>3</sub> (Sigma Aldrich, ≥99.5%), hexadecyltrimethylammonium hydroxide (CTAOH, TCI, 10 wt%), Pt(NH<sub>3</sub>)<sub>4</sub>(NO<sub>3</sub>)<sub>2</sub> (Alfa Aesar, 99.99% purity).

### 2.2.2 Synthesis MOR zeolite

A typical synthesis procedure to obtain nanocrystalline MOR zeolite was as follows. 1.885 g CTAOH solution and 0.781 g Al(NO<sub>3</sub>)<sub>3</sub>·9H<sub>2</sub>O were added to 13.26 g demi-water at room temperature. Afterwards, 5.55 g water glass was added to the mixture under vigorous stirring. The molar composition of the resulting synthesis gel was 1 SiO<sub>2</sub> : 0.042 Al<sub>2</sub>O<sub>3</sub> : 0.025 CTAOH : 0.287 Na<sub>2</sub>O : 42 H<sub>2</sub>O. After vigorous stirring for 3 h at room temperature, the gel was transferred into a 45 mL Teflon-lined stainless-steel autoclave and heated at 150 °C for 5 days under rotation at 50 rpm. Then, the autoclave was quenched and cooled to room temperature. The solid product was filtered, washed with demi-water until pH < 8 followed by drying overnight at 110 °C. The zeolites were calcined at 550 °C (heating rate of 1 °C/min) for 10 h in flowing air to remove the organic species. The calcined samples were ion-exchanged three times with 1.0 M NH<sub>4</sub>NO<sub>3</sub> solution followed by calcination at 550 °C (1 °C/min) for 4 h in an O<sub>2</sub> flow (20 vol% in N<sub>2</sub>) to obtain the final proton form. Depending on the aluminum source in the recipe, as-synthesized nanocrystalline MOR zeolites are denoted as MOR-NO<sub>3</sub>+CTA, MOR-Cl+CTA and MOR-OH+CTA. Reference bulk MOR zeolites were also prepared under the same conditions without CTAOH. These samples are denoted as MOR-NO<sub>3</sub>, MOR-Cl and MOR-OH.

### 2.2.3 Preparation of Pt-containing zeolites

The proton form of the zeolites was loaded with 0.5 wt% Pt by wet impregnation with an aqueous Pt(NH<sub>3</sub>)<sub>4</sub>(NO<sub>3</sub>)<sub>2</sub> solution. The resulting samples were calcined at 450 °C (heating rate of 0.5 °C/min) under an O<sub>2</sub> flow (20 vol% in N<sub>2</sub>) for 2 h.

### 2.2.4 Characterization

X-ray diffraction (XRD) patterns were collected on a Bruker D2 Endeavor diffraction system using Cu K $\alpha$  radiation with a step size of 0.01° and duration of 0.25 s in the 2 $\theta$  range of 5-40°.

The elemental composition of the zeolite samples was determined by inductively couple plasma optical emission spectrometry (ICP-OES). Prior to analysis, the samples were

dissolved in a 1:1:1 (by weight) mixture of HF (40 wt% in H<sub>2</sub>O), HNO<sub>3</sub> (60 wt% in H<sub>2</sub>O) and H<sub>2</sub>O.

Surface area and porosity of zeolites were determined by Ar physisorption in static mode at -186 °C on a Micromeritics ASAP 2020 instrument. The samples were outgassed at 400 °C for 6 h prior to the sorption measurements. The BET surface area of MOR zeolite was determined in the relative pressure ( $p/p_0$ ) range between 0.05-0.25. The total pore volume was calculated at  $p/p_0=0.97$ . The micropore volume was determined by the  $t$ -plot method using a thickness range of 0.35-0.70 nm. The mesopore volume and mesopore size distribution were calculated from the adsorption branch of the isotherm using the Barrett-Joyner-Halenda (BJH) method.

Thermogravimetric analysis (TGA) was performed using a TGA/DSC 1 instrument (Mettler Toledo). The temperature was increased from 40 °C to 800 °C at a rate of 5 °C/min in 20 ml/min O<sub>2</sub> and 40 ml/min He flow.

X-ray photoelectron spectroscopy (XPS) was carried out using a Thermo Scientific K-alpha spectrometer, equipped with a monochromatic Al K $\alpha$  X-ray source (1486.6 eV) and a 180° double-focusing hemispherical analyzer with a 128-channel detector.

Scanning electron microscope (SEM) images were taken on a FEI Quanta 200F scanning electron microscope at an accelerating voltage of 3 or 5 kV. Transmission electron microscopy (TEM) pictures were recorded on a FEI Tecnai 20 at 200 kV. Annular dark field scanning transmission electron microscopy (ADF-STEM) was performed on the TU/e CryoTitan (FEI, now Thermo Fischer Scientific) at 300 kV and room temperature. The samples were suspended in ethanol and dispersed over a holey Cu grid coated with a carbon film.

IR spectra of samples were recorded on a Bruker Vertex 70v instrument in the range of 4000-1000 cm<sup>-1</sup>. The spectra were acquired at a 2 cm<sup>-1</sup> resolution and an average of 64 scans. Typically, the samples were pressed as thin wafers of ~10 mg and placed inside a controlled-environment transmission cell. The samples were activated at 550 °C in artificial air before cooling the cell to 150 °C and measuring the background spectra under vacuum. To determine the density of acid sites in zeolites, pyridine was introduced into the cell from an ampoule kept at room temperature. The exposure time was 10 min followed by desorption for 1 h under evacuation at temperature of 150 °C, 300 °C and 500 °C. After each step, a spectrum was recorded at 150 °C. The spectra were normalized by the weight of the wafer. For the quantification of Brønsted and Lewis acid sites, molar extinction coefficient values of 0.73 cm<sup>2</sup>/μmol and 1.11 cm<sup>2</sup>/μmol were used, respectively.<sup>37</sup>

Nuclear magnetic resonance (NMR) spectra were recorded on a 11.7 Tesla Bruker DMX500 NMR spectrometer, operating at 132 MHz for  $^{27}\text{Al}$ , 99 MHz for  $^{29}\text{Si}$ , 500 MHz for  $^1\text{H}$  and 125 MHz for  $^{13}\text{C}$ . For the  $^{27}\text{Al}$  Magic Angle Spinning (MAS) NMR measurements, a Bruker 2.5 mm MAS probe head was used with a zirconia rotor having a diameter of 2.5 mm, operated at a spinning rate of 25 kHz. All other measurements were performed using a Bruker Triple Channel 4 mm MAS probe head and a 4 mm zirconia rotor, under a sample rotation rate of 10 kHz.  $^{27}\text{Al}$  NMR spectra were recorded using a single excitation pulse of 1  $\mu\text{s}$  and an interscan delay of 1 s. The saturated solution of  $\text{Al}(\text{NO}_3)_3$  was used for  $^{27}\text{Al}$  chemical shift calibration. Quantitative  $^{29}\text{Si}$  MAS NMR spectra were obtained by use of a high-power proton decoupling direct excitation (DE) pulse sequence with a  $54^\circ$  pulse duration of 3  $\mu\text{s}$  and an interscan delay of 120 s. The  $^{29}\text{Si}$  chemical shift was calibrated using tetramethylsilane (TMS). For  $^1\text{H}$  NMR measurements, the sample was first dehydrated at  $350^\circ\text{C}$  for 6 h under vacuum and then placed into the 4 mm zirconia rotor in a glovebox.  $^1\text{H}$  NMR spectra were recorded by a Hahn-echo pulse sequence of  $p_1-\tau_1-p_2-\tau_2-aq$  with a  $90^\circ$  pulse  $p_1 = 5 \mu\text{s}$ , a  $180^\circ$   $p_2 = 10 \mu\text{s}$  and  $\tau_1 = \tau_2 = 0.5 \mu\text{s}$ . The interscan delay was chosen to be 120 s to obtain quantitative spectra. The  $^1\text{H}$  chemical shift was referred to TMS.  $^1\text{H}$ - $^{13}\text{C}$  cross-polarization (CP) MAS NMR spectra were recorded using a ramped contact pulse of 3 ms and an interscan delay of 3 s. Solid adamantane was used for  $^{13}\text{C}$  chemical shift calibration.

## 2.2.5 Catalytic activity measurements

### 2.2.5.1 Alkylation of benzene with benzyl alcohol

The liquid-phase alkylation of benzene (B) with benzyl alcohol (BA) was carried out in a round-bottom flask equipped with a PTFE septum. The flask was heated in a temperature-controlled oil bath under atmospheric pressure. In a typical experiment, 0.1 g of catalyst (activated at  $500^\circ\text{C}$  in artificial air for 1 h) was mixed with 26.7 ml (0.301 mol) of benzene in a glovebox. After maintaining the reaction mixture at  $75^\circ\text{C}$  for 30 min under stirring, the reactor was depressurized through a side vessel. Then, 0.33 ml (0.003 mol) of BA was added and this moment was regarded as the initial reaction time. During the reaction, liquid samples were withdrawn at regular time intervals and analyzed by a gas chromatograph (Shimadzu GC-17A) after separation of the catalyst by filtration. The gas chromatograph was equipped with a flame ionization detector (FID) and a Rxi-5 ms capillary column (Restek; length 30 m; i.d. 0.25 mm; thickness 0.5  $\mu\text{m}$ ).

### 2.2.5.2 Hydroconversion of n-hexadecane

To evaluate the catalytic performance of the Pt-loaded MOR zeolite catalysts in n-hexadecane (n-C<sub>16</sub>) hydroconversion, a downstream fixed-bed continuous flow reactor was

employed. The catalyst was pressed, crushed and sieved to obtain a fraction in the range of 125-250  $\mu\text{m}$ . Prior to the reaction, the catalyst was dried in the reactor at 200  $^{\circ}\text{C}$  for 1 h under flowing He at atmospheric pressure followed by reduction in flowing hydrogen at the same pressure. During reduction, the temperature was increased from 50  $^{\circ}\text{C}$  to 400  $^{\circ}\text{C}$  with a rate of 3  $^{\circ}\text{C}/\text{min}$  followed by an isothermal period of 1 h. Then, the temperature of the catalyst bed was lowered to 150  $^{\circ}\text{C}$ , pressurized to 60 bar with  $\text{H}_2$  and wetted by maintaining a liquid flow of 1 ml/min for 10 min. The reaction was operated at a  $\text{H}_2/n\text{-C}_{16}$  molar ratio of 20 and a weight hourly space velocity (WHSV) of 10  $\text{g}_{n\text{-C}_{16}} \text{g}_{\text{cat}}^{-1} \text{h}^{-1}$ . At each reaction temperature, the reaction was stabilized for 5 h before product sampling. The reactor effluent was analyzed by an online gas chromatography (Thermo Scientific Focus GC) equipped with an Rtx-1 column (Restek; length 30 m; i.d. 0.25 mm; thickness 0.25  $\mu\text{m}$ ) and an FID detector.

## 2.3 Results and Discussion

### 2.3.1 Structural characterization

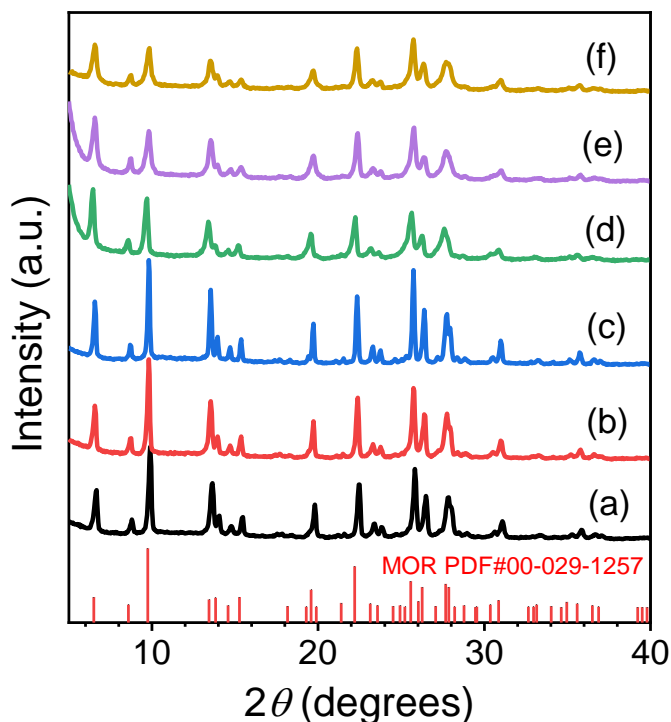


**Figure 2.1.** XRD patterns of as-synthesized MOR zeolites: (a) MOR- $\text{NO}_3$ , (b) MOR-Cl, (c) MOR-OH, (d) MOR- $\text{NO}_3$ +CTA, (e) MOR-Cl+CTA and (f) MOR-OH+CTA.

Figure 2.1 shows the XRD patterns of the as-synthesized MOR zeolites. In all cases, well-resolved diffraction peaks corresponding to the MOR topology can be observed without indications of impurity phases.<sup>38</sup> The XRD patterns of all CTA-templated MOR zeolites show lower intensities and broader peaks than those prepared in the absence of CTA, pointing to a reduction of the crystallinity and the crystal size.<sup>29</sup>

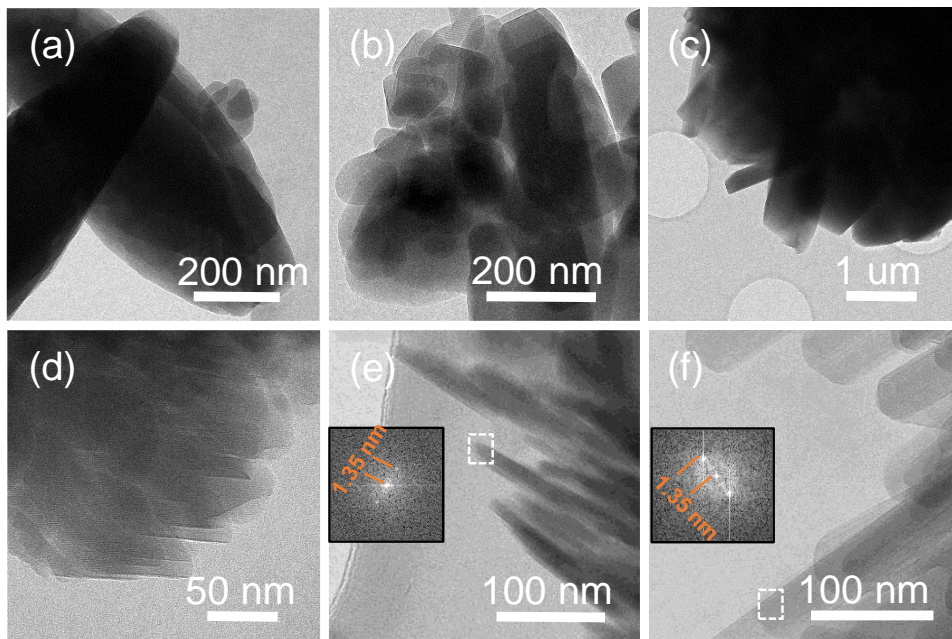


**Figure 2.2.** TEM images of calcined MOR zeolites: (a) MOR-NO<sub>3</sub>, (b) MOR-Cl, (c) MOR-OH, (d) MOR-NO<sub>3</sub>+CTA, (e) MOR-Cl+CTA and (f) MOR-OH+CTA.

SEM and TEM were used to understand differences in the morphology of the MOR zeolites (Figures A1 and 2.2). MOR-NO<sub>3</sub> and MOR-Cl consist of plate-shaped crystals, which are aggregated into particles with a size of ca. 0.5-1  $\mu\text{m}$ . MOR-OH contains irregular prism-shaped crystals. The 12MR channels in the *c*-direction are parallel to the longest side of such prism-shaped crystals (Figure A1c) as widely reported before.<sup>7, 38, 39</sup> It is clear that the addition of CTA to the synthesis mixture significantly changes the crystal morphology. MOR-NO<sub>3</sub>+CTA exhibits closely packed irregularly shaped nanocrystals without a specific orientation. MOR-Cl+CTA and MOR-OH+CTA show aggregated morphologies, composed of aggregated nanosheet-like particles. The insets in Figures 2.2e and 2.2f show fast Fourier transform (FFT) patterns taken along [110], indicating that nanolayers of MOR-Cl+CTA and MOR-OH+CTA are parallel to the *c*-axis.<sup>40</sup> According to previous studies, CTA can cover specific surface planes of the zeolite crystals via the electrostatic interaction, thus preventing

crystal growth.<sup>22, 26</sup> During MOR zeolite synthesis, this capping effect can favour preferential crystal growth resulting in the nanostrip morphology.<sup>8, 41</sup> This effect is more pronounced for MOR-Cl-CTA and MOR-OH-CTA synthesis than for MOR-NO<sub>3</sub>-CTA synthesis.

It is well known that the precursors in the synthesis gel can strongly impact the crystallization kinetics of hydrothermal zeolite synthesis, which will affect the morphology of the final crystals.<sup>42, 43</sup> The aluminum source can influence this in two manners. First, differences in the anion of the aluminum precursor can alter the ionic strength of the synthesis gel.<sup>42, 44, 45</sup> Second, as the formation of aluminate ions will depend on the solubility of aluminum source, aluminosilicate intermediates with varying Si/Al ratio can be formed, especially in the initial aging step.<sup>31, 46</sup> Comparing the three pairs of samples in our study, it is clear that only the MOR-OH sample show the typical prism-like morphology of MOR zeolite. Even though both Al(NO<sub>3</sub>)<sub>3</sub>·9H<sub>2</sub>O and AlCl<sub>3</sub>·6H<sub>2</sub>O can be easily dissolved, the morphologies of the obtained samples are different, which can be mostly attributed to the presence of CTA during synthesis.

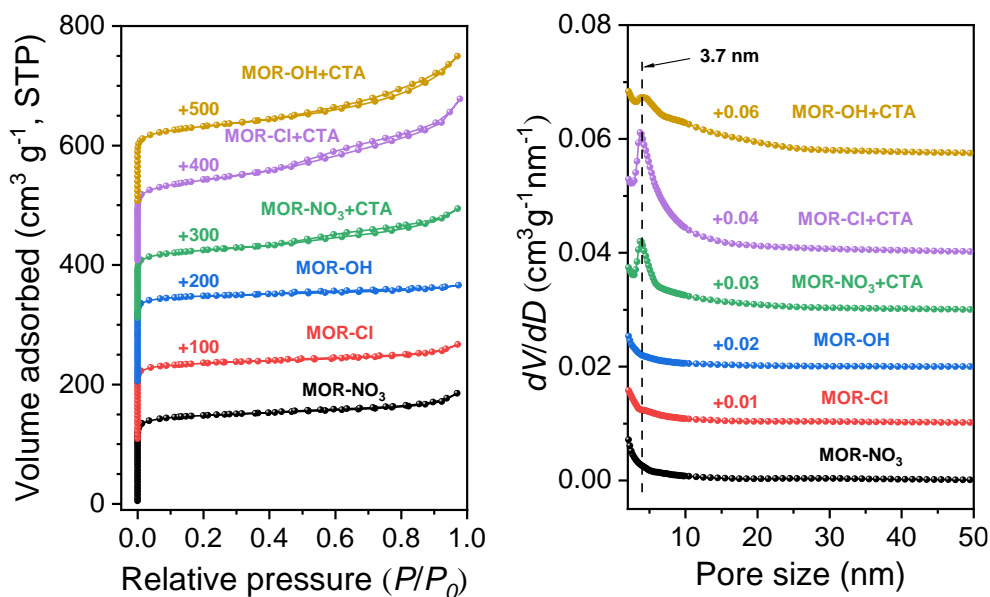


**Figure 2.3.** Ar physisorption isotherms (left) and pore size distributions (right) of calcined MOR zeolites. The pore size distributions were calculated using the *BJH* method using the adsorption branch.

The Ar physisorption isotherms and pore size distributions of all samples are shown in Figure 2.3. All isotherms show a steep Ar uptake at the relatively low relative pressure ( $p/p_0 < 0.1$ )



due to the filling of micropores.<sup>47</sup> The isotherms of the three reference samples have the usual type I shape of microporous materials.<sup>48</sup> In line with this, the pore size distributions of these samples do not indicate mesopores. The samples prepared with CTA, on the other hand, have the typical type IV isotherm with a clear H4 hysteresis loop, characteristic for slit-like mesopores.<sup>48</sup> The pore size distributions show relatively uniform mesopores of 3.7 nm for all nanocrystalline zeolites. Such mesopores are mostly due to the voids between thinner or smaller particles. Such morphological changes are in line with the SEM and TEM analysis in Figures A1 and 2.2. The textural properties derived from the isotherms are listed in Table 2.1. All the nanocrystalline MOR zeolites prepared with CTA have larger mesopore volumes and larger external surface areas than the corresponding reference samples. The mesopore volume and external surface area of MOR-Cl+CTA are 0.20 cm<sup>3</sup> g<sup>-1</sup> and 167 m<sup>2</sup> g<sup>-1</sup>, respectively. The micropore volumes of the nanocrystalline zeolites are 0.11 cm<sup>3</sup> g<sup>-1</sup>, lower than those of reference samples (0.15-0.16 cm<sup>3</sup> g<sup>-1</sup>). Such differences are commonly observed between microporous zeolites and their counterparts that contain additional intra-zeolitic mesopores.<sup>49</sup> The results discussed above suggest that CTA as a growth modifier has sufficient interaction with the growing zeolite, resulting in substantial mesoporosity in the final MOR samples.

**Table 2.1.** Textural properties of the calcined MOR zeolites determined by Ar physisorption.

Zeolite	S <sub>BET</sub> (m <sup>2</sup> g <sup>-1</sup> )	V <sub>tot</sub> (cm <sup>3</sup> g <sup>-1</sup> )	V <sub>meso</sub> (cm <sup>3</sup> g <sup>-1</sup> ) ( <i>BJH</i> )	V <sub>micro</sub> (cm <sup>3</sup> g <sup>-1</sup> ) ( <i>t-plot</i> )	S <sub>ext</sub> (m <sup>2</sup> g <sup>-1</sup> )
MOR-NO <sub>3</sub>	451	0.24	0.05	0.16	48
MOR-Cl	403	0.21	0.04	0.15	42
MOR-OH	449	0.21	0.03	0.16	35
MOR-NO <sub>3</sub> +CTA	400	0.24	0.10	0.11	91
MOR-Cl+CTA	428	0.35	0.20	0.11	167
MOR-OH+CTA	407	0.32	0.17	0.11	124

TGA was carried out to investigate the inclusion of CTA in the nanocrystalline zeolites (Figure A2). For the as-prepared reference samples prepared without CTA, a single weight-loss feature of ca. 10 wt% below 250 °C is observed, mostly due to the desorption of

physisorbed water.<sup>50</sup> The weight loss curves of the nanocrystalline MOR zeolites contain multiple features. The first weight-loss feature due to water removal was much less, which can point to the inclusion of CTA in the micropores. Similar to removal of CTA from mesoporous MCM-41, further weight-loss features can be related to decomposition due to the Hoffman elimination of CTA on the external surface (150-280 °C), combustion of remaining carbonaceous species such as residual adsorbed trimethylamine (280-340 °C)<sup>51</sup> and due to removal of CTA occluded in micropores (340-600 °C).<sup>52</sup> However, it would be difficult to correlate the CTA amount with zeolite porosity, since the CTA molecule can be fully or partially occluded in zeolite micropores or mesopores.

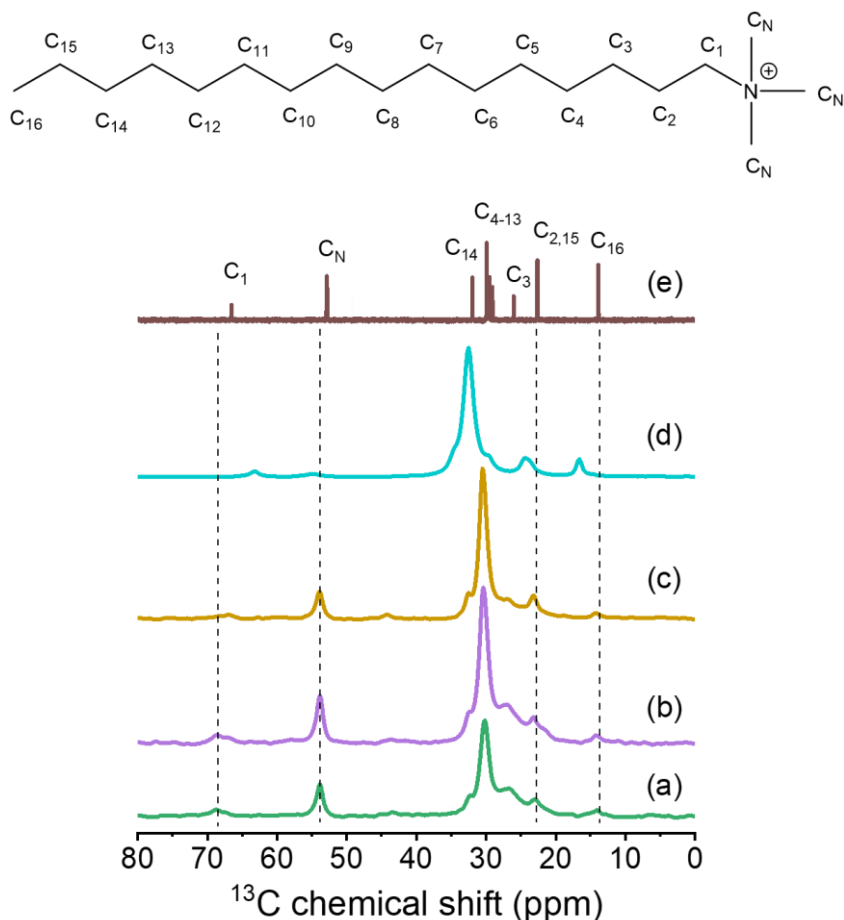


**Figure 2.4.**  $^{13}\text{C}$  NMR spectra of (a) MOR- $\text{NO}_3$ +CTA, (b) MOR-Cl+CTA, (c) MOR-OH+CTA, (d) Solid CTABr and (e) solution of CTA in  $\text{D}_2\text{O}$  (2 wt%).

The  $^{13}\text{C}$  NMR spectra of as-prepared MOR zeolites, crystalline CTA and CTA dissolved in  $\text{D}_2\text{O}$  are shown in Figure 2.4. We use the spectrum of CTA dissolved in  $\text{D}_2\text{O}$  (*cf.* Figure 2.4e and structural formula in Figure 2.4) to assign the resonances in the other spectra. As expected, the NMR spectra of solid CTA and CTA in the zeolites show broader and shifted peaks compared to that of the highly mobile CTA ions in water.<sup>52, 53</sup> The resonances for the zeolites are slightly sharper than in solid CTA. The chemical shifts of CTA in the as-synthesized zeolites are similar to those of CTA in water. From these observations, we can conclude that CTA is occluded in the zeolite pores.<sup>20, 52</sup> Together with TGA analysis, these findings demonstrate that, in the nanocrystalline zeolites, CTA is predominantly present in the zeolite micropores but also caps the external surface of the crystalline zeolite domains.

### 2.3.2 Bulk and surface characterization

**Table 2.2.** Physicochemical properties of the proton form of the calcined MOR zeolites.

Sample	Si/Al (ICP)	Si/Al (XPS)	Al distribution (%) <sup>a</sup>	
			$\text{Al}^{\text{IV}}$	$\text{Al}^{\text{VI}}$
MOR- $\text{NO}_3$	9.4	9.2	82	18
MOR-Cl	9.2	9.4	80	20
MOR-OH	6.8	6.6	80	20
MOR- $\text{NO}_3$ +CTA	9.5	9.2	80	20
MOR-Cl+CTA	9.2	9.4	81	19
MOR-OH+CTA	6.9	7.0	82	18

<sup>a</sup>  $^{27}\text{Al}$  NMR spectroscopy:  $\text{Al}^{\text{IV}}$  determined by integration of NMR signal between 20 and 100 ppm;  $\text{Al}^{\text{VI}}$  determined by integration of NMR signal between 20 and -50 ppm.

The bulk and surface composition of the MOR zeolites determined by ICP elemental analysis and XPS, respectively, are given in Table 2.2. The bulk Si/Al ratios of all samples, which are in the range of 6.8-9.5, are lower than the Si/Al ratio of the initial gel of 12. This means that not all Si in the synthesis gel was included in the zeolite product<sup>34</sup>. The bulk and surface Si/Al ratios are very similar, indicating that there are no strong Al gradients in these samples. Solid-state  $^{27}\text{Al}$  MAS NMR spectroscopy were carried out to investigate the local coordination environments of Al in the proton form of the calcined zeolites. As shown in Figure 2.5 left, the  $^{27}\text{Al}$  NMR spectra present an intense signal at 54 ppm for all samples, corresponding to tetrahedrally coordinated Al species ( $\text{Al}^{\text{IV}}$ ). The small feature at 0 ppm can be attributed to

extraframework Al species in octahedral coordination ( $\text{Al}^{\text{VI}}$ ).<sup>12</sup> Deconvolution of these spectra into these two contributions shows that ~80% of Al atoms are incorporated in the zeolite framework of the samples (Table 2.2). As shown in Figure 2.5 right, two major resonances at -112 and -106 ppm with a weak shoulder around -101 ppm appear in all  $^{29}\text{Si}$  MAS NMR spectra, which are assigned to  $\text{Q}^4(0\text{Al})$ ,  $\text{Q}^4(1\text{Al})$  and  $\text{Q}^3(0\text{Al})/\text{Q}^4(2\text{Al})$  species, respectively.<sup>54</sup> It can be clearly observed that the relative intensity of the signal corresponding to  $\text{Q}^4(1\text{Al})$  species in the spectrum of MOR-OH is higher than that of the other zeolites, indicating a higher framework Al content for MOR-OH. This is qualitatively in agreement with the elemental analysis showing the highest Al content for this sample ( $\text{Si}/\text{Al} = 6.8$ ).

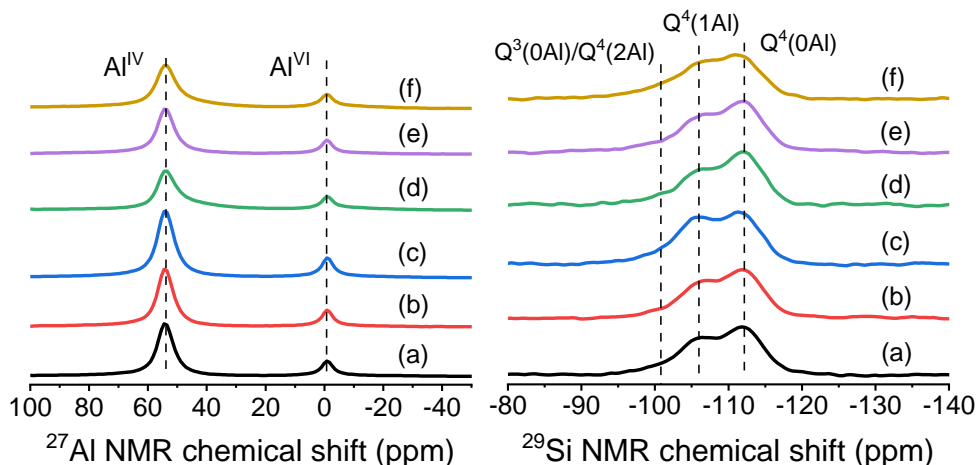


**Figure 2.5.**  $^{27}\text{Al}$  (left) and  $^{29}\text{Si}$  (right) MAS NMR spectra of the proton form of (a) MOR- $\text{NO}_3$ , (b) MOR-Cl, (c) MOR-OH, (d) MOR- $\text{NO}_3$ +CTA, (e) MOR-Cl+CTA, and (f) MOR-OH+CTA. The spectra were normalized by sample weight.

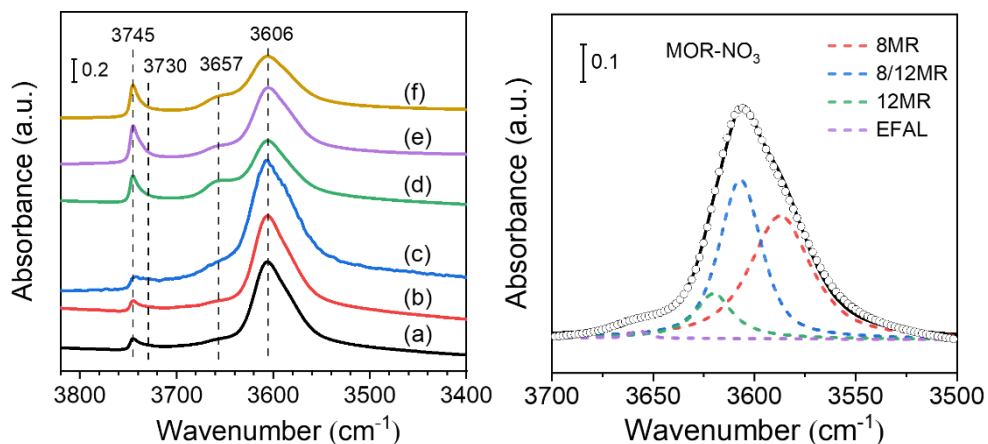


**Figure 2.6.** IR spectra of the proton form of (a) MOR-NO<sub>3</sub>, (b) MOR-Cl, (c) MOR-OH, (d) MOR-NO<sub>3</sub>+CTA, (e) MOR-Cl+CTA, and (f) MOR-OH+CTA. The right figure shows the deconvolution of a representative IR spectrum, *i.e.*, for MOR-NO<sub>3</sub>. The spectra were normalized by sample weight.

IR spectroscopy was used to investigate the nature of the hydroxyl groups of the proton form of MOR samples (Figure 2.6). The bands at 3745 cm<sup>-1</sup> and 3730 cm<sup>-1</sup> are due to the external and internal terminal silanol groups, respectively.<sup>40, 55</sup> The contribution of external silanol groups increased for the nanocrystalline zeolite samples, consistent with their larger external surface area. The band at 3657 cm<sup>-1</sup> can be assigned to hydroxyl groups connected to extraframework aluminum (EFAI) or partially bounded to the zeolite lattice. The most prominent band at 3606 cm<sup>-1</sup> is due to the vibration of hydroxyls groups bridging between aluminum and silicon.<sup>56</sup> For MOR, this band is a superposition of three bands corresponding to Brønsted acid sites (BAS) located in 12MR channels (3619 cm<sup>-1</sup>), 8MR channels (3587 cm<sup>-1</sup>) and at the intersection between these two channels (3606 cm<sup>-1</sup>).<sup>40</sup> The distribution of BAS in the MOR zeolite samples determined by deconvolution into these three contributions is shown in Table A1.<sup>57</sup> The use of different aluminum salts and the presence of CTA leads to very minor differences in the distribution of the three types of BAS in the MOR zeolites. During zeolite formation, CTA can alter the crystallization kinetics and compete with Na cations for compensation of the negative framework charges.<sup>9, 22, 58, 59</sup> An explanation for these subtle differences would require more synthesis efforts and is therefore outside the scope of this work.

— pyridine desorption at 150 °C    — pyridine desorption at 300 °C    — pyridine desorption at 400 °C  
 — pyridine desorption at 500 °C    — before pyridine adsorption

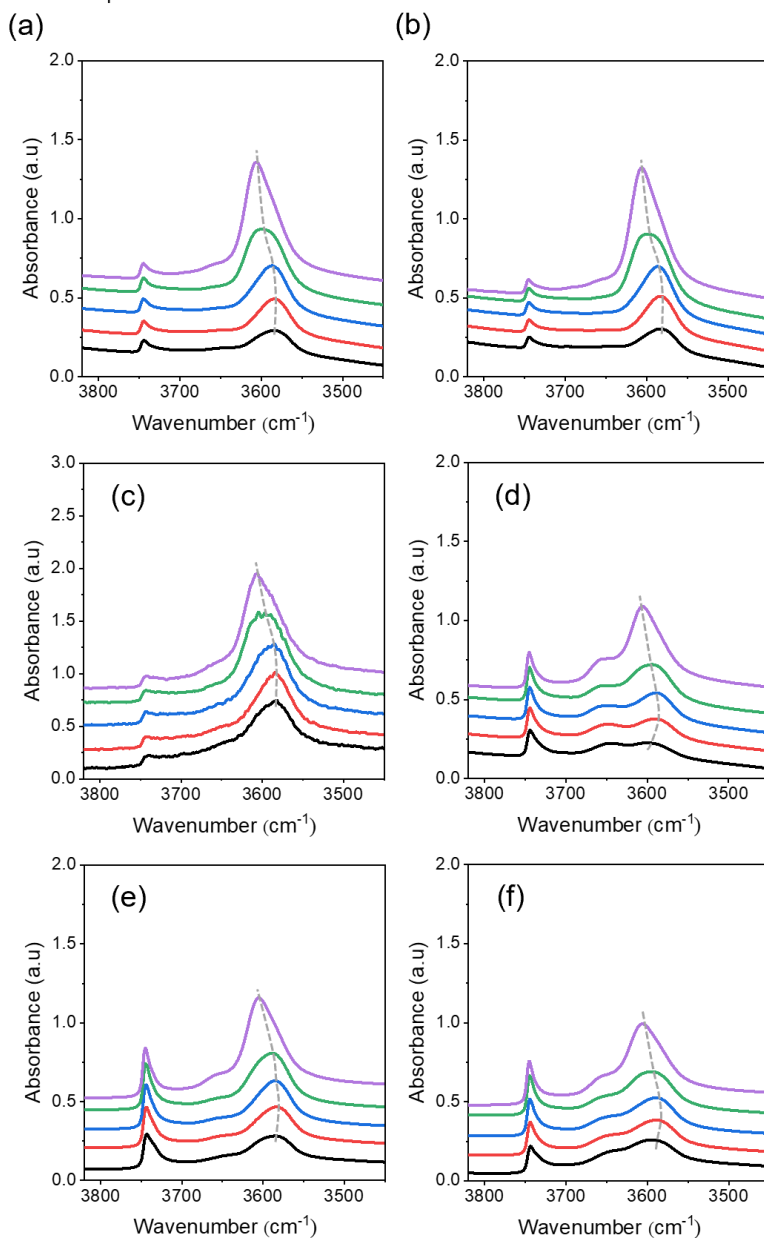


**Figure 2.7.** IR spectra of the hydroxyl region of the proton form of MOR zeolites before pyridine adsorption and after pyridine adsorption/desorption at different temperatures: (a) MOR-NO<sub>3</sub>, (b) MOR-Cl, (c) MOR-OH, (d) MOR-NO<sub>3</sub>+CTA, (e) MOR-Cl+CTA, and (f)

MOR-OH+CTA. The spectra were normalized by sample weight. The grey dashed lines indicate the peak positions attributed to bridging hydroxyl groups.

We next used pyridine as a probe molecule to investigate both the distribution and the corresponding accessibility of the acid sites. For this purpose, the vibrational OH IR spectra before pyridine adsorption and after pyridine adsorption-desorption at different temperatures are collected (Figure 2.7). Upon pyridine adsorption/desorption at 150 °C, a partial disappearance of bands corresponding to bridging hydroxyls of the samples is observed, indicating that only a part of BAS in MOR zeolites can be protonated by pyridine, which is in line with previous studies.<sup>60, 61</sup> The most likely explanation for this is that the BAS in the side pockets are not fully accessible for the large pyridine probe molecule.<sup>62</sup> For all samples, the bands corresponding to the bridging hydroxyl show a gradual recovery with increasing temperature of pyridine desorption. Notably, upon heating of the nanocrystalline samples from 150 °C to 300 °C, it is observed that the bands corresponding to bridging hydroxyls shift to lower frequencies closer to the one assigned to BAS in the side pockets. This phenomenon implies the preferential recovery of BAS in side pockets at this stage, which consequently suggests that a part of BAS located in the side pocket are even accessible for pyridine in these nanocrystalline samples. A similar phenomenon has also been observed in other studies.<sup>56, 60, 62</sup> It is likely due to defect sites in MOR framework, which can enlarge the practical window of side pockets, leading to BAS in these small pores accessible for pyridine.<sup>60</sup> Another possible explanation, well revealed in the case of MCM-22 zeolite, is that the nanocrystal morphology would make more side pockets ending up at the external surface of the crystals.<sup>63</sup> Among these samples, a larger red shift of the band corresponding to bridging hydroxyls is observed for MOR-NO<sub>3</sub>+CTA, suggesting that the side-pocket BAS in this sample are more accessible for pyridine than for the other samples. The number of BAS and LAS accessible for pyridine was determined by integrating the areas of the respective bands at 1540 cm<sup>-1</sup> and 1450 cm<sup>-1</sup> (Figure A3). As shown in Table 2.3, the nanocrystalline samples contain less BAS than their bulk counterparts.

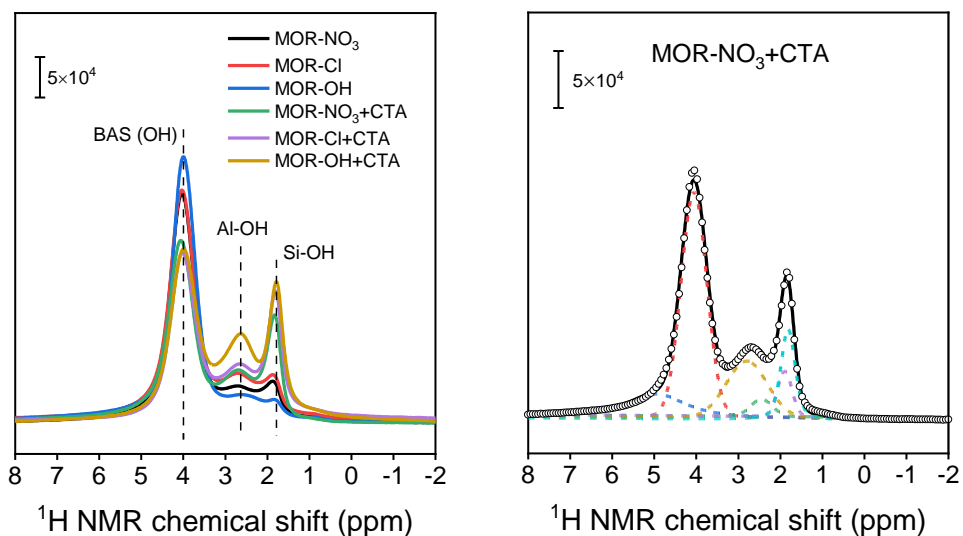


**Figure 2.8.**  $^1\text{H}$  MAS NMR spectra of dehydrated MOR zeolites. A representative fit of these spectra is shown in the right panel. The spectra were normalized by sample weight.

**Table 2.3.** Acidity of MOR zeolites.

Sample	[BAS] <sup>a</sup> ( $\mu\text{mol/g}$ )	[LAS] <sup>b</sup> ( $\mu\text{mol/g}$ )	[BAS] <sup>c</sup> ( $\mu\text{mol/g}$ )
MOR- $\text{NO}_3$	1001	32	1346
MOR-Cl	1054	39	1285
MOR-OH	1064	39	1530
MOR- $\text{NO}_3$ +CTA	704	72	1148
MOR-Cl+CTA	772	51	1071
MOR-OH+CTA	585	71	933

<sup>a</sup> Density of BAS determined by IR spectra of adsorbed pyridine after evacuation for 1 h at 150 °C.

<sup>b</sup> Density of LAS determined by IR spectra of adsorbed pyridine after evacuation for 1 h at 150 °C.

<sup>c</sup> Determined by  $^1\text{H}$  MAS NMR spectra.



As pyridine is not small enough to probe all of the acid sites, the acidity of MOR zeolite samples was further investigated by  $^1\text{H}$  NMR spectroscopy (Figure 2.8). The peak at 1.8 ppm is assigned to silanol groups, while the peaks at 2.6 ppm and 4.0 ppm are attributed to extraframework Al-OH species and BAS, respectively.<sup>64</sup> The much higher intensity of the silanol groups for the three nanocrystalline MOR zeolites can be ascribed to their higher external surface area. This result is in line with the IR data in Figure 2.6. As shown in Table 2.3, for all samples, the amount of BAS probed by pyridine is lower than the total BAS determined by  $^1\text{H}$  NMR. This is because of the existence of the inaccessible side-pocket BAS for pyridine, which has been verified in Figure 2.7. Compared to the corresponding bulk zeolites, these nanocrystalline zeolites display a lower total BAS density, in keeping with the pyridine IR data (Table 2.3). The lower acidity of nanocrystalline zeolites is likely due to the lower crystallinity and tendency to dehydroxylation.

For the purpose of n-alkane hydroconversion, the MOR zeolites were loaded with 0.5 wt% Pt. This metal loading was chosen to ensure a high enough rate of (de)hydrogenation, resulting in isomerization and cracking on acid sites being the rate-limiting steps.<sup>65</sup> ICP shows that the actual Pt loadings are all close to the targeted 0.5 wt%. ADF-STEM images of the reduced catalysts shown in Figure 2.9 demonstrate that Pt is highly dispersed in the form of nanoparticles smaller than 2 nm. This may be due to the use of the small size of  $\text{Pt}(\text{NH}_3)_4^{2+}$  ions (0.48 nm) that facilitates their diffusion into the MOR micropores during metal loading. Once in the micropores, the Pt atoms resist extensive sintering due to their confinement.<sup>66, 67</sup> Additional factors that can explain the fine dispersion are the relatively low metal loading (~0.5 wt%) and the slow heating rate during calcinations employed here (0.5 °C/min).<sup>68, 69</sup>

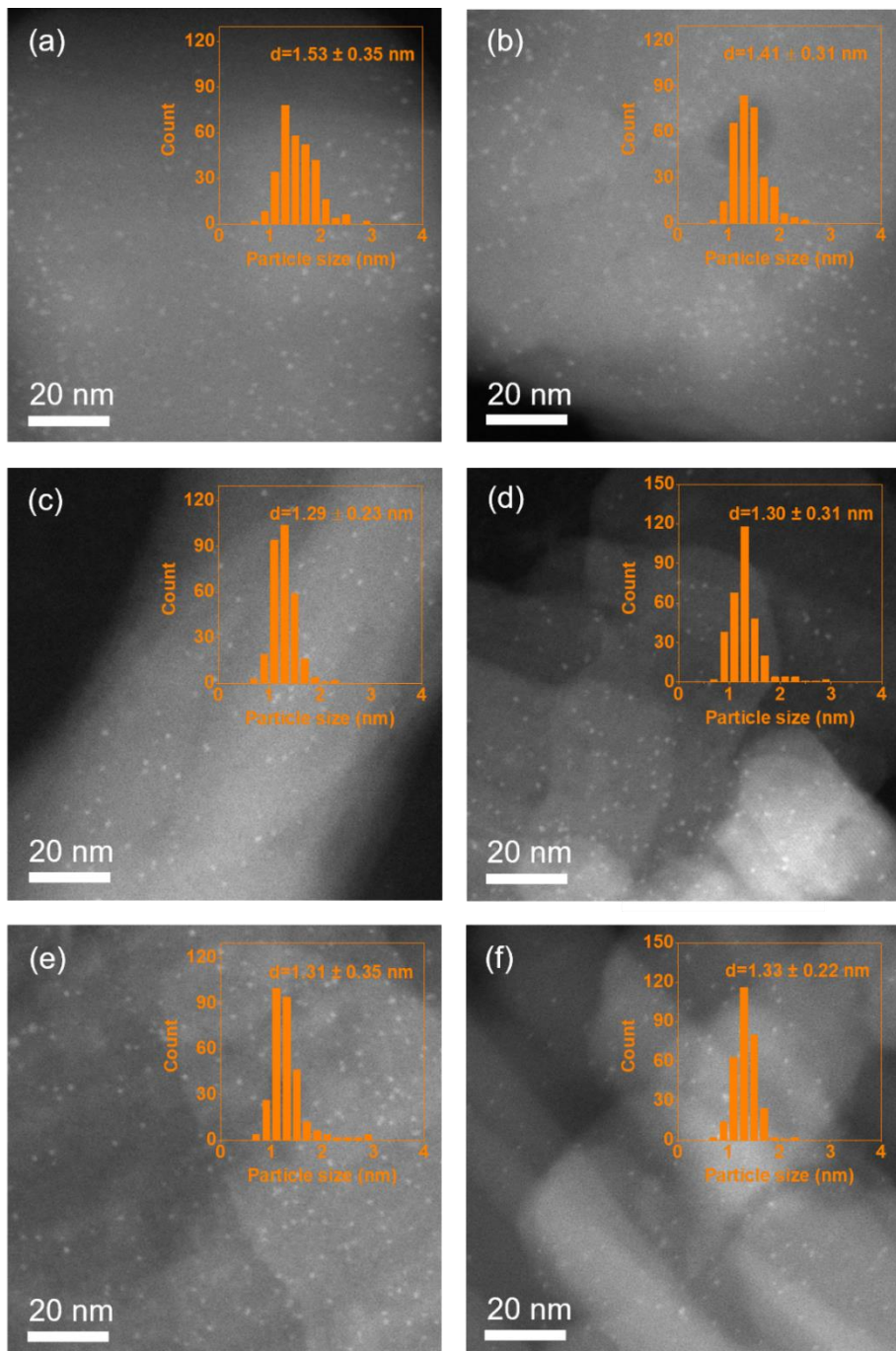
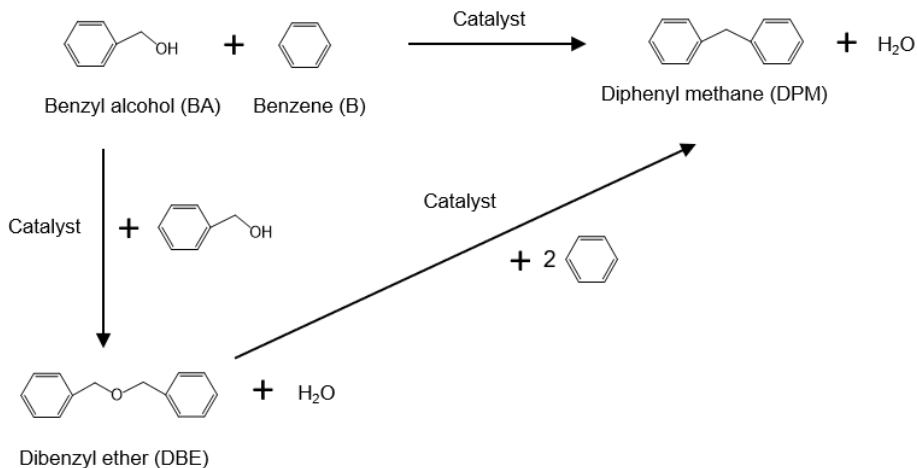


**Figure 2.9.** ADF-STEM images of reduced samples: (a) Pt/MOR-NO<sub>3</sub>, (b) Pt/MOR-Cl, (c) Pt/MOR-OH, (d) Pt/MOR-NO<sub>3</sub>+CTA, (e) Pt/MOR-Cl+CTA and (f) Pt/MOR-OH+CTA.

## 2.3.3 Catalytic activity measurements

### 2.3.3.1 Alkylation reaction of benzene with benzyl alcohol



**Scheme 2.1.** The overall reaction pathway of benzene with benzyl alcohol.

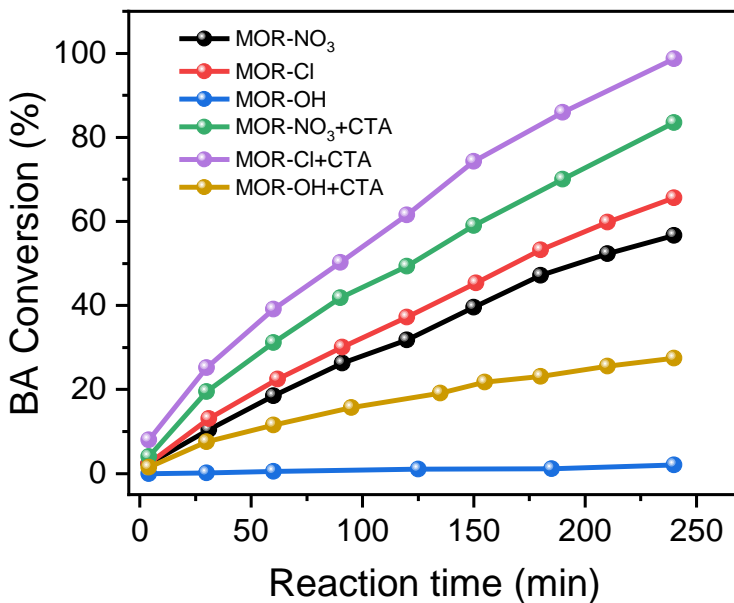


**Figure 2.10.** Catalytic conversion of liquid-phase alkylation of B with BA over MOR zeolite samples at 75 °C.

**Table 2.4.** Catalytic performance of MOR zeolite catalysts in the alkylation of B with BA after 4 h reaction.

Catalyst	BA conversion (%)	Yield (Selectivity) (%)		
		DPM	DBE	Other
MOR-NO <sub>3</sub>	57	43 (75)	3 (5)	11 (19)
MOR-Cl	66	49 (74)	3 (5)	14 (21)
MOR-OH	2	1 (50)	--	--
MOR-NO <sub>3</sub> +CTA	84	71 (85)	7 (8)	6 (7)
MOR-Cl+CTA	99	78 (79)	7 (7)	14 (14)
MOR-OH+CTA	28	18 (64)	4 (14)	6 (21)

BA: benzyl alcohol; DPM: diphenylmethane; DBE: dibenzyl ether.

The liquid-phase benzylation of benzene (B) with benzyl alcohol (BA) was chosen to probe the catalytic performance of bulk and nanocrystalline MOR zeolites in aromatics alkylation. The overall reaction pathway presented in Scheme 2.1 (more detailed schematic in Scheme A1) shows the importance of relatively large reaction intermediates and products.<sup>70</sup> The conversion of BA with reaction time for the MOR catalysts is shown in Figure 2.10. The activity of the zeolites increases in the order MOR-OH < MOR-OH+CTA < MOR-NO<sub>3</sub> < MOR-Cl < MOR-NO<sub>3</sub>+CTA < MOR-Cl+CTA. Clearly, all the nanocrystalline zeolites can convert BA faster than the corresponding bulk counterparts. The BA conversion and product distribution after 4 h reaction are collected in Table 2.4. Among the nanocrystalline zeolites, MOR-Cl+CTA provides the highest BA conversion of 99% and a DPM yield of 78% (DPM selectivity 79%) after 4 h reaction. On the other hand, the bulk MOR-OH zeolite shows the lowest catalytic activity with a BA conversion of only 2% after 4 h reaction. Notably, MOR-OH+CTA has the second highest external surface and mesopore volume among all zeolites, yet displays the second lowest activity with a BA conversion of 28% after 4 h reaction.

Typically, strong acid sites are needed to polarize BA for the reaction with benzene and BA to form DPM and DBE, respectively (Scheme A1).<sup>71</sup> The performance can therefore be expected to depend on the concentration of strong acid sites accessible to BA. Moreover, the large size of the products might also affect the catalytic performance.<sup>11</sup> The dimensions of the main channels of MOR (0.67 × 0.70 nm) can impede the diffusion of DPM (0.49 × 0.92 nm) and DBE (0.49 × 1.15 nm). These large products and the coke formed by condensation reaction can easily block the micropores. Despite their lower acidity, the nanocrystalline

zeolites exhibit a higher activity than their bulk counterparts. This difference is therefore most likely caused by the improved textural properties of the nanocrystalline zeolites. Among the nanocrystalline zeolites, it can be observed that, although MOR-NO<sub>3</sub>+CTA and MOR-Cl+CTA contain comparable amounts of acid sites, MOR-Cl+CTA is more active in line with its higher external surface area and mesopore volume. Nevertheless, MOR-Cl+CTA exhibits a nanosheet-like morphology with the main pores running along the longest particle dimension. This would mean that the diffusion length in the MOR main pores is not effectively reduced.<sup>72</sup> This may imply that also acid sites on the larger external surface can contribute to the higher activity of MOR-Cl+CTA. The role of external acid sites for this reaction has been emphasized before.<sup>72, 73</sup> However, MOR-OH+CTA has a much higher external surface area than MOR-Cl and MOR-NO<sub>3</sub> but displays a lower activity. This can be ascribed to the lower acidity of the former sample. On the contrary, MOR-OH is not very active despite its largest amount of acid sites. We attribute this to the large crystal size (Figure A1c), which most likely leads to severe diffusion limitations.<sup>12</sup> In addition, the side-pocket BAS of nanocrystalline zeolites are more accessible to pyridine than the bulk zeolites due to the more open structure of the former. It is reasonable to assume that these acid sites are therefore also more accessible for benzyl alcohol and benzene, which have a comparable size as pyridine. This can contribute to a higher activity of the nanocrystalline zeolites. From these results, it is clear that the alkylation reaction benefits from the open structure of the nanocrystalline MOR zeolite provided that sufficient acid sites are present. The combination of the use of CTA as an agent to reduce crystal size and AlCl<sub>3</sub>·6H<sub>2</sub>O as Al precursor results in the best catalyst for liquid-phase alkylation of benzene.

### 2.3.3.2 Hydroconversion of n-hexadecane

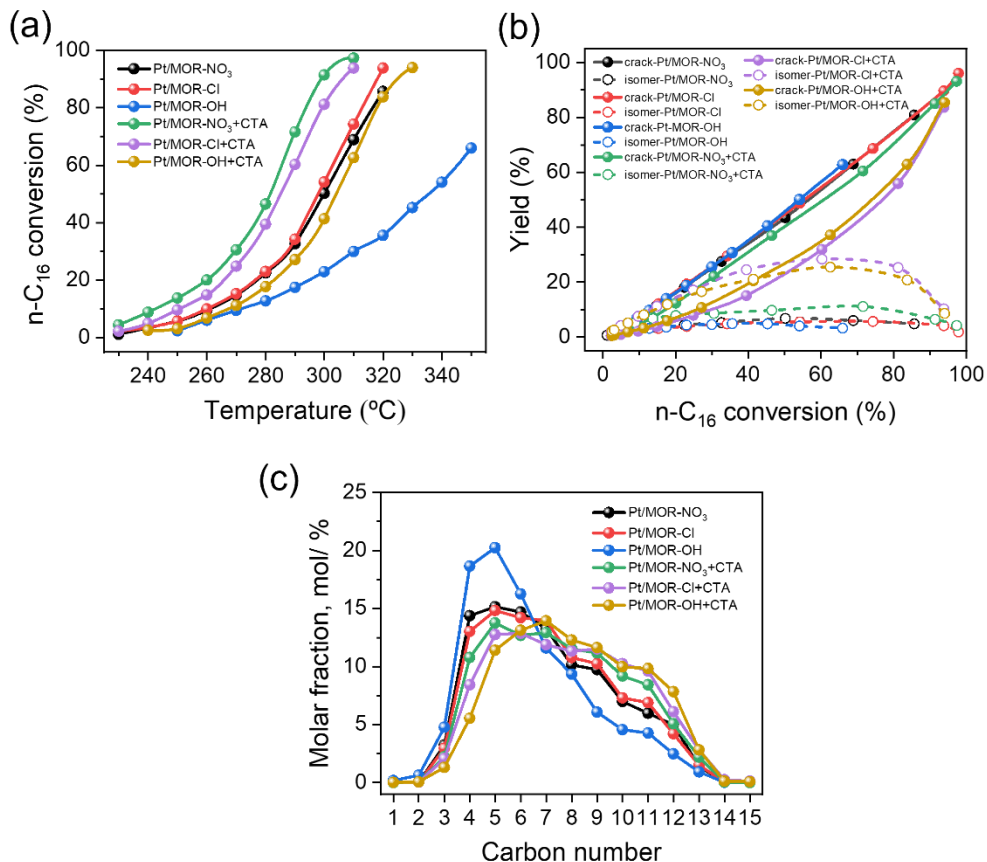


**Figure 2.11.** The catalytic performance of n-C<sub>16</sub> hydroconversion over bifunctional catalysts. (a) conversion of n-C<sub>16</sub> as a function of the reaction temperature; (b) yield of isomers and cracked products as a function of n-C<sub>16</sub> conversion and (c) distribution of cracked products at ca. 50% n-C<sub>16</sub> conversion.

The Pt/MOR catalysts were evaluated for their performance in the hydroconversion of n-C<sub>16</sub>. The bifunctional catalysts have a comparable Pt loading and Pt dispersion. Together with the high enough Pt loading to establish the alkane/alkene equilibrium, catalytic differences in n-C<sub>16</sub> hydroconversion mostly arise from differences in acidity and diffusion rates, which relate to the zeolite part of the catalysts. Figure 2.11a shows the conversion of n-C<sub>16</sub> against the reaction temperature. All nanocrystalline zeolites show improved activity compared to their corresponding bulk counterparts, despite the lower acidity of the more active nanocrystalline zeolites. It is known that BAS of medium and strong acidity can catalyze isomerization and

cracking reactions.<sup>74</sup> Therefore, the improved activity of nanocrystalline MOR zeolites can be related to the textural properties of the nanocrystalline zeolites. The role of diffusion on n-alkane hydroconversion for one-dimensional zeolites has been examined before. For instance, hierarchical ZSM-22 zeolite (TON topology) showed a higher activity than bulk ZSM-22 in the hydroisomerization of n-nonadecane, despite the lower acidity. When evaluated in n-decane hydroisomerization, the more acidic bulk ZSM-22 sample was the more active catalyst.<sup>75</sup> The lower activity of Pt/MOR-OH+CTA compared to Pt/MOR-NO<sub>3</sub>+CTA and Pt/MOR-Cl+CTA can most likely be attributed to the lower acidity of the former sample. On the contrary, the highly acidic Pt/MOR-OH sample shows a low activity, which can be attributed to the large crystal size.

The yield of isomers and cracked products is shown in Figure 2.11b. The evolution of the yields with conversion is typical for n-paraffins hydroconversion with, at a low reactant conversion, isomerization being dominant and cracking rapidly increasing at high conversion due to the formation of multibranched isomers, which are more prone to cracking.<sup>74, 76, 77</sup> Overall, the isomer yields are higher for the nanocrystalline Pt/MOR zeolites than the conventional ones. The best performing samples are Pt/MOR-Cl+CTA and Pt/MOR-OH+CTA with isomer yields of 28.4% and 25.4% at conversion levels of 60.3% and 62.6%, respectively. The more open texture of the nanocrystalline zeolites results in shorter residence time in the micropores as a consequence of the higher rate of desorption from the acidic zeolite, overall increasing the balance between hydrogenation and cracking and thus the isomer yield.<sup>78</sup>

Notably, as compared to the three bulk samples, Pt/MOR-NO<sub>3</sub>+CTA shows higher isomer yields that are still much lower than observed for the other two nanocrystalline samples. Considering that Pt/MOR-NO<sub>3</sub>+CTA has a substantially lower external surface area than Pt/MOR-Cl+CTA and Pt/MOR-OH+CTA, the low isomer yield of Pt/MOR-NO<sub>3</sub>+CTA is likely due to the lack of external acid sites. In addition, BAS in the side-pockets of Pt/MOR-NO<sub>3</sub>+CTA may also have a negative effect on the isomer yield. As pyridine IR shows that these BAS are more accessible (Figure 2.7d), they can contribute to cracking reactions. Previous studies have demonstrated that the rate of n-hexane hydroconversion/cracking in the side pocket is higher than that in main channels of MOR zeolites, which was explained by the lower free energy for reactants and intermediates due to the stronger confinement in the side pockets of MOR zeolite.<sup>47, 79</sup> The high accessibility of side-pockets, which have an intrinsically higher reaction rate due to confinement, can explain the combination of high activity and low isomer product yield for Pt/MOR-NO<sub>3</sub>+CTA.

Finally, the cracked products distribution at a conversion of ca. 50% is shown in Figure 2.11c. At this conversion level, all samples show a skewed product distribution, which is a sign of secondary cracking (overcracking).<sup>77</sup> The product distributions are most symmetric for Pt/MOR-Cl+CTA and Pt/MOR-OH+CTA. Especially, the bulk samples show a larger distribution of C<sub>4</sub>-C<sub>6</sub> paraffins due to extensive isomerization and secondary cracking of intermediate olefins already at an intermediate conversion of 50%. Comparing all samples, it can be observed that the conversion increases with the acidity, while the isomer yield increases and the cracked product distribution becomes more symmetric with an increase of the external surface area. These trends strongly suggests that shorter residence times of intermediate olefins in micropores benefit ideal hydrocracking behavior. The use of CTA to decrease the size of MOR crystals is a simple and effective approach to achieve this.

## 2.4 Conclusions

Nanocrystalline MOR zeolites were successfully synthesized by a one-step hydrothermal synthesis approach involving the commercial reagent CTAOH as the sole organic template. A typical MOR recipe was modified by using comparing aluminum sources, *i.e.*, Al(NO<sub>3</sub>)<sub>3</sub>, AlCl<sub>3</sub> and Al(OH)<sub>3</sub>. All MOR zeolites show a reduced crystal size when CTA was used. For MOR-Cl+CTA and MOR-OH+CTA, the crystal dimensions are predominantly reduced in the *a*- and *b*-direction. Besides a higher external surface area, the use of CTAOH also leads to a more defective zeolite structure in which the BAS in the side-pockets are more accessible to pyridine. This latter impact of CTAOH was most notable for MOR-NO<sub>3</sub>+CTA. Nanocrystalline MOR zeolites showed an improved catalytic performance in the alkylation of benzene with benzyl alcohol and the hydroconversion of n-C<sub>16</sub>. The CTA-templated nanocrystalline MOR zeolites show a higher activity and selectivity in these reactions than their corresponding bulk counterparts. Overall, MOR-Cl+CTA is the best-performing one due to the combination of more accessible zeolite domains and retention of acidity in the presence of CTAOH. Our findings show how CTAOH can be used to improve the performance of one-dimensional MOR zeolite.

## 2.5 References

1. D. P. Serrano, J. M. Escola and P. Pizarro, *Chem. Soc. Rev.*, 2013, **42**, 4004-4035.
2. S. Li, J. Li, M. Dong, S. Fan, T. Zhao, J. Wang and W. Fan, *Chem. Soc. Rev.*, 2019, **48**, 885-907.
3. D. Kerstens, B. Smeyers, J. Van Waeyenberg, Q. Zhang, J. Yu and B. F. Sels, *Adv. Mater.*, 2020, **32**, 2004690.
4. X.-Y. Yang, L.-H. Chen, Y. Li, J. C. Rooke, C. Sanchez and B.-L. Su, *Chem. Soc.*



- Rev.*, 2017, **46**, 481-558.
5. S. Narayanan, P. Tamizhdurai, V. L. Mangesh, C. Ragupathi, P. Santhana krishnan and A. Ramesh, *RSC Adv.*, 2021, **11**, 250-267.
  6. A. A. C. Reule, J. A. Sawada and N. Semagina, *J. Catal.*, 2017, **349**, 98-109.
  7. L. Zhang, A. N. C. v. Laak, P. E. de Jongh and K. P. de Jong, *Microporous Mesoporous Mater.*, 2009, **126**, 115-124.
  8. O. V. Shvets, K. M. Konyshева, M. V. Shamzhy, M. V. Opanasenko, P. S. Yaremov, C. Xiao, X. Zou and J. Čejka, *Catal. Today*, 2019, **324**, 115-122.
  9. Y. Li, M. Yu, K. Cai, M. Wang, J. Lv, R. F. Howe, S. Huang and X. Ma, *Phys. Chem. Chem. Phys.*, 2020, **22**, 11374-11381.
  10. J. Pérez-Ramírez, S. Abelló, A. Bonilla and J. C. Groen, *Adv. Funct. Mater.*, 2009, **19**, 164-172.
  11. K. Na, M. Choi and R. Ryoo, *Microporous Mesoporous Mater.*, 2013, **166**, 3-19.
  12. X. Li, R. Prins and J. A. van Bokhoven, *J. Catal.*, 2009, **262**, 257-265.
  13. X. Meng, F. Nawaz and F.-S. Xiao, *Nano Today*, 2009, **4**, 292-301.
  14. T. Xue, S. Li and H. Wu, *Microporous Mesoporous Mater.*, 2021, **312**, 110748.
  15. T. Xue, H. Liu, Y. Zhang, H. Wu, P. Wu and M. He, *Microporous Mesoporous Mater.*, 2017, **242**, 190-199.
  16. L. Xu, X. Ji, S. Li, Z. Zhou, X. Du, J. Sun, F. Deng, S. Che and P. Wu, *Chem. Mater.*, 2016, **28**, 4512-4521.
  17. W. Zhang, W. Ming, S. Hu, B. Qin, J. Ma and R. Li, *Materials*, 2018, **11**, 651.
  18. Z. Li, M. T. Navarro, J. Martínez-Triguero, J. Yu and A. Corma, *Catal. Sci. Technol.*, 2016, **6**, 5856-5863.
  19. M. Kumar, H. Luo, Y. Roman-Leshkov and J. D. Rimer, *J. Am. Chem. Soc.*, 2015, **137**, 13007-13017.
  20. L. Meng, B. Mezari, M. G. Goesten and E. J. M. Hensen, *Chem. Mater.*, 2017, **29**, 4091-4096.
  21. Y. Yuan, L. Wang, H. Liu, P. Tian, M. Yang, S. Xu and Z. Liu, *Chin. J. Catal.*, 2015, **36**, 1910-1919.
  22. P. He, Y. Li, K. Cai, X. Xiong, J. Lv, Y. Wang, S. Huang and X. Ma, *ACS Appl. Nano Mater.*, 2020, **3**, 6460-6468.
  23. M. Liu, W. Jia, J. Li, Y. Wang, S. Ma, H. Chen and Z. Zhu, *Catal. Lett.*, 2016, **146**, 249-254.
  24. B. P. S. Santos, N. C. Almeida, I. S. Santos, M. d. F. V. Marques and L. D. Fernandes, *Catal. Lett.*, 2018, **148**, 1870-1878.
  25. Z. Mcheik, L. Pinard, J. Toufaily, T. Hamieh and T. J. J. M. Daou, *Molecules*, 2021, **26**, 4508.

26. J. Lu, Y. Wang, C. Sun, T. Zhao, J. Zhao, Z. Wang, W. Liu, S. Wu, M. Shi and L. Bu, *New J. Chem.*, 2021, **45**, 8629-8638.
27. F. Hamidi, A. Bengueddach, F. Di Renzo and F. Fajula, *Catal. Lett.*, 2003, **87**, 149-152.
28. B. Lu, Y. Yakushi, Y. Oumi, K. Itabashi and T. Sano, *Microporous Mesoporous Mater.*, 2006, **95**, 141-145.
29. L. Zhang, S. Xie, W. Xin, X. Li, S. Liu and L. Xu, *Mater. Res. Bull.*, 2011, **46**, 894-900.
30. J. Warzywoda, A. G. Dixon, R. W. Thompson and A. Sacco, *J. Mater. Chem.*, 1995, **5**, 1019-1025.
31. B. O. Hincapie, L. J. Garces, Q. Zhang, A. Sacco and S. L. Suib, *Microporous Mesoporous Mater.*, 2004, **67**, 19-26.
32. B. N. Bhadra, P. W. Seo, J. W. Jun, J. H. Jeong, T.-W. Kim, C.-U. Kim and S. H. Jhung, *Microporous Mesoporous Mater.*, 2016, **235**, 135-142.
33. B. Lu, T. Tsuda, H. Sasaki, Y. Oumi, K. Itabashi, T. Teranishi and T. Sano, *Chem. Mater.*, 2004, **16**, 286-291.
34. X. Wang, R. Li, C. Yu, Y. Liu, L. Liu, C. Xu, H. Zhou and C. Lu, *Ind. Eng. Chem. Res.*, 2019, **58**, 18065-18072.
35. F. Hamidi, A. Bengueddach, F. Di Renzo and F. Fajula, *Catal. Lett.*, 2003, **87**, 149-152.
36. B. Lu, T. Kanai, Y. Oumi and T. Sano, *J. Porous Mater.*, 2007, **14**, 89-96.
37. E. A. Uslamin, N. A. Kosinov, E. A. Pidko and E. J. M. Hensen, *Green Chem.*, 2018, **20**, 3818-3827.
38. Y. Yang, J. Ding, C. Xu, W. Zhu and P. Wu, *J. Catal.*, 2015, **325**, 101-110.
39. Y. Li, Z. Li, S. Huang, K. Cai, Z. Qu, J. Zhang, Y. Wang and X. Ma, *ACS Appl. Mater. Interfaces*, 2019, **11**, 24000-24005.
40. A. Bolshakov, D. E. Romero Hidalgo, A. J. F. van Hoof, N. Kosinov and E. J. M. Hensen, *ChemCatChem*, 2019, **11**, 2803-2811.
41. C. Jo, J. Jung, H. S. Shin, J. Kim and R. Ryoo, *Angew. Chem. Int. Ed.*, 2013, **52**, 10014-10017.
42. Y.-J. Wang, J.-P. Cao, X.-Y. Ren, X.-B. Feng, X.-Y. Zhao, Y. Huang and X.-Y. Wei, *Fuel*, 2020, **268**, 117286.
43. B. Lu, Y. Oumi and T. Sano, *J. Cryst. Growth*, 2006, **291**, 521-526.
44. X.-d. Liu, Y.-p. Wang, X.-m. Cui, Y. He and J. Mao, *Powder Technol.*, 2013, **243**, 184-193.
45. C. Sun, Z. Liu, S. Wang, H. Pang, R. Bai, Q. Wang, W. Chen, A. Zheng, W. Yan and J. Yu, *CCS Chem.*, 2020, **3**, 189-198.

46. C. Liu, D. Kong and H. Guo, *Microporous Mesoporous Mater.*, 2014, **193**, 61-68.
47. H. Issa, J. Toufaily, T. Hamieh, J. D. Comparot, A. Sachse and L. Pinard, *J. Catal.*, 2019, **374**, 409-421.
48. S. Storck, H. Bretinger and W. F. Maier, *Appl. Catal. A*, 1998, **174**, 137-146.
49. V. J. Margarit, M. R. Díaz-Rey, M. T. Navarro, C. Martínez and A. Corma, *Angew. Chem. Int. Ed.*, 2018, **130**, 3517-3521.
50. Y. Xu, X. Shen, C. Peng, Y. Ma, L. Han, P. Wu, H. Peng and S. Che, *Sci. China Mater.*, 2018, **61**, 1185-1190.
51. M. T. J. Keene, R. D. M. Gougeon, R. Denoyel, R. K. Harris, J. Rouquerol and P. L. Llewellyn, *J. Mater. Chem.*, 1999, **9**, 2843-2849.
52. D. Xu, J. Feng and S. Che, *Dalton Trans.*, 2014, **43**, 3612-3617.
53. W. Kolodziejewski, A. Corma, M.-T. Navarro and J. Perez-Pariente, *Solid State Nucl. Magn. Reson.*, 1993, **2**, 253-259.
54. T. I. Korányi and J. B. Nagy, *J. Phys. Chem. B*, 2005, **109**, 15791-15797.
55. J. Pastvova, D. Kaucky, J. Moravkova, J. Rathousky, S. Sklenak, M. Vorokhta, L. Brabec, R. Pilar, I. Jakubec, E. Tabor, P. Klein and P. Sazama, *ACS Catal.*, 2017, **7**, 5781-5795.
56. K. Cao, D. Fan, L. Li, B. Fan, L. Wang, D. Zhu, Q. Wang, P. Tian and Z. Liu, *ACS Catal.*, 2020, **10**, 3372-3380.
57. N. Cherkasov, T. Vazhnova and D. B. Lukyanov, *Vib. Spectrosc.*, 2016, **83**, 170-179.
58. X. Wang, R. Li, C. Yu and Y. Liu, *Microporous Mesoporous Mater.*, 2021, **311**, 110665.
59. T. Yokoi, H. Mochizuki, S. Namba, J. N. Kondo and T. Tatsumi, *J. Phys. Chem. C*, 2015, **119**, 15303-15315.
60. N. S. Nesterenko, F. Thibault-Starzyk, V. Montouillout, V. V. Yuschenko, C. Fernandez, J. P. Gilson, F. Fajula and I. I. Ivanova, *Microporous Mesoporous Mater.*, 2004, **71**, 157-166.
61. X. Huang, M. Ma, M. Li and W. Shen, *Catal. Sci. Technol.*, 2020, **10**, 7280-7290.
62. F. Moreau, P. Ayrault, N. S. Gnep, S. Lacombe, E. Merlen and M. Guisnet, *Microporous Mesoporous Mater.*, 2002, **51**, 211-221.
63. P. Ayrault, J. Datka, S. Laforge, D. Martin and M. Guisnet, *J. Phys. Chem. B*, 2004, **108**, 13755-13763.
64. H. Xue, X. Huang, E. Ditzel, E. Zhan, M. Ma and W. Shen, *Ind. Eng. Chem. Res.*, 2013, **52**, 11510-11515.
65. R. Roldán, F. J. Romero, C. Jiménez-Sanchidrián, J. M. Marinas and J. P. Gómez, *Appl. Catal., A*, 2005, **288**, 104-115.
66. L. Liu, U. Diaz, R. Arenal, G. Agostini, P. Concepcion and A. Corma, *Nat. Mater.*,

- 2017, **16**, 132-138.
67. N. Kosinov, C. Liu, E. J. Hensen and E. A. Pidko, *Chem. Mater.*, 2018, **30**, 3177-3198.
68. J. de Graaf, A. J. van Dillen, K. P. de Jong and D. C. Koningsberger, *J. Catal.*, 2001, **203**, 307-321.
69. P. Yin, S. Hu, K. Qian, Z. Wei, L.-L. Zhang, Y. Lin, W. Huang, H. Xiong, W.-X. Li and H.-W. Liang, *Nat. Commun.*, 2021, **12**, 4865.
70. N. Narender, K. V. V. K. Mohan, S. J. Kulkarni and I. A. K. Reddy, *Catal. Commun.*, 2006, **7**, 583-588.
71. N. Candu, M. Florea, S. M. Coman and V. I. Parvulescu, *Appl. Catal., A*, 2011, **393**, 206-214.
72. J. Kim, C. Jo, S. Lee and R. Ryoo, *J. Mater. Chem. A*, 2014, **2**, 11905-11912.
73. J.-C. Kim, K. Cho and R. Ryoo, *Appl. Catal., A*, 2014, **470**, 420-426.
74. H. Deldari, *Appl. Catal., A*, 2005, **293**, 1-10.
75. J. A. Martens, D. Verboekend, K. Thomas, G. Vanbutsele, J. P. Gilson and J. Pérez-Ramírez, *ChemSusChem*, 2013, **6**, 421-425.
76. D. Romero, R. Rohling, L. Meng, M. Rigutto and E. J. M. Hensen, *J. Catal.*, 2021, **394**, 284-298.
77. J. Zecevic, G. Vanbutsele, K. P. de Jong and J. A. Martens, *Nature*, 2015, **528**, 245-248.
78. L. Meng, G. Vanbutsele, R. Pestman, A. Godin, D. E. Romero, A. J. van Hoof, L. Gao, T. F. Kimpel, J. Chai, J. A. Martens and E. J. M. Hensen, *J. Catal.*, 2020, **389**, 544-555.
79. H. Chiang and A. Bhan, *J. Catal.*, 2011, **283**, 98-107.

# Appendix A

**Table A1.** BAS distribution derived from deconvoluted IR spectra of MOR zeolite samples.

Sample	BAS in 8MR (%)	BAS in 8/12MR (%)	BAS in 12MR (%)
MOR-NO <sub>3</sub>	40	45	15
MOR-Cl	39	49	12
MOR-OH	43	42	15
MOR-NO <sub>3</sub> +CTA	40	50	10
MOR-Cl+CTA	44	46	10
MOR-OH+CTA	41	45	14

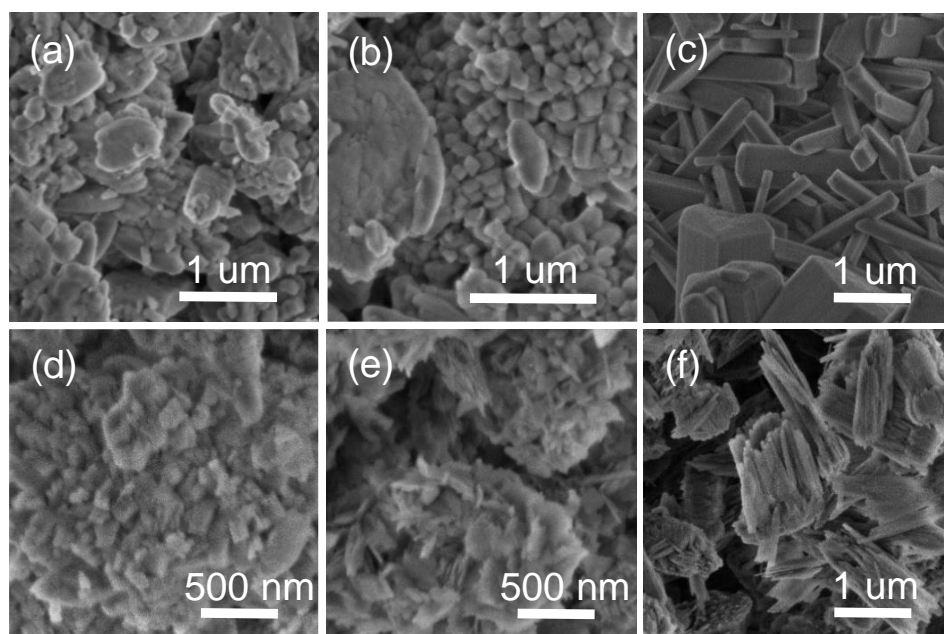


**Figure A1.** SEM images of calcined MOR zeolites: (a) MOR-NO<sub>3</sub>, (b) MOR-Cl, (c) MOR-OH, (d) MOR-NO<sub>3</sub>+CTA, (e) MOR-Cl+CTA and (f) MOR-OH+CTA.

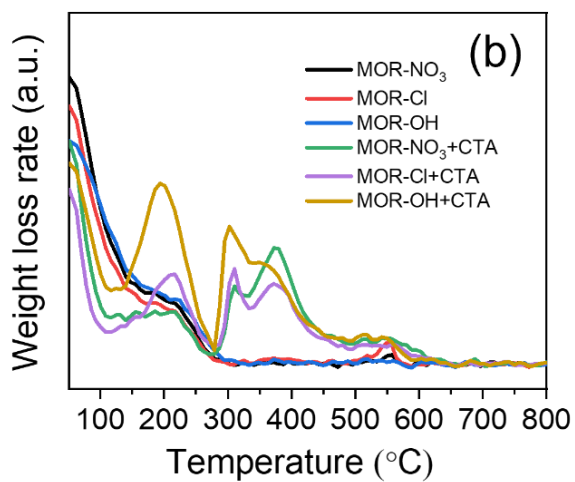
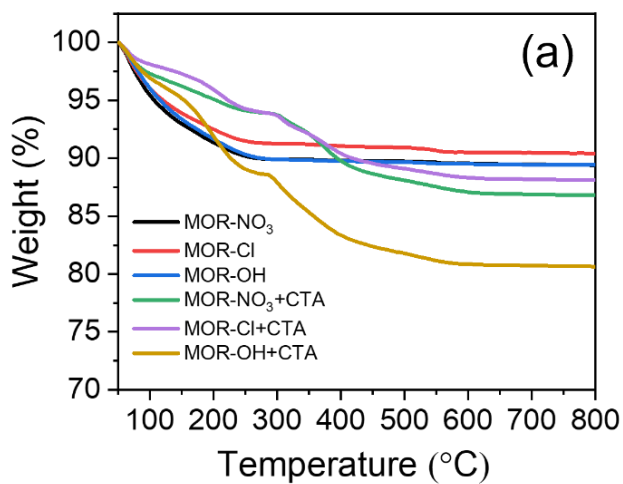


**Figure A2.** (a) TG and (b) DTG profiles of as-prepared MOR zeolites.

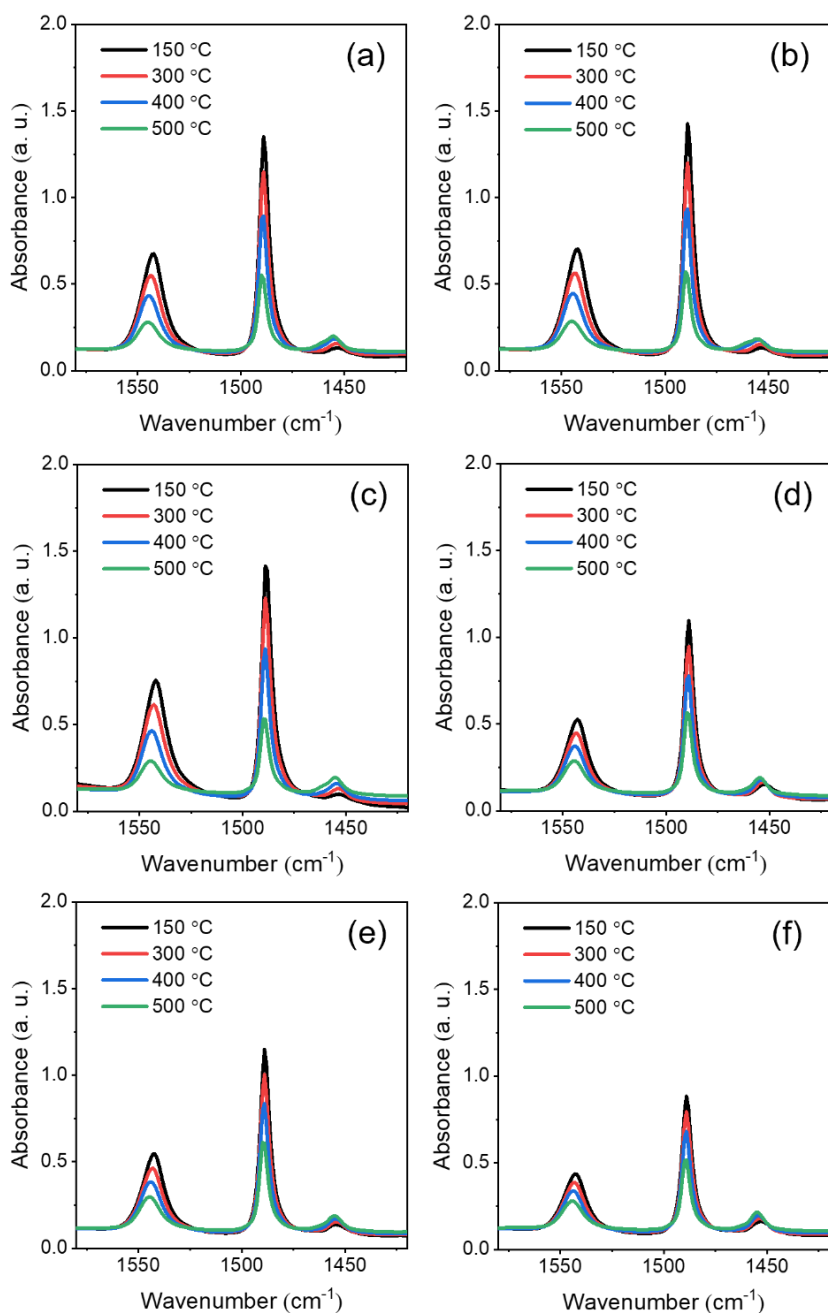
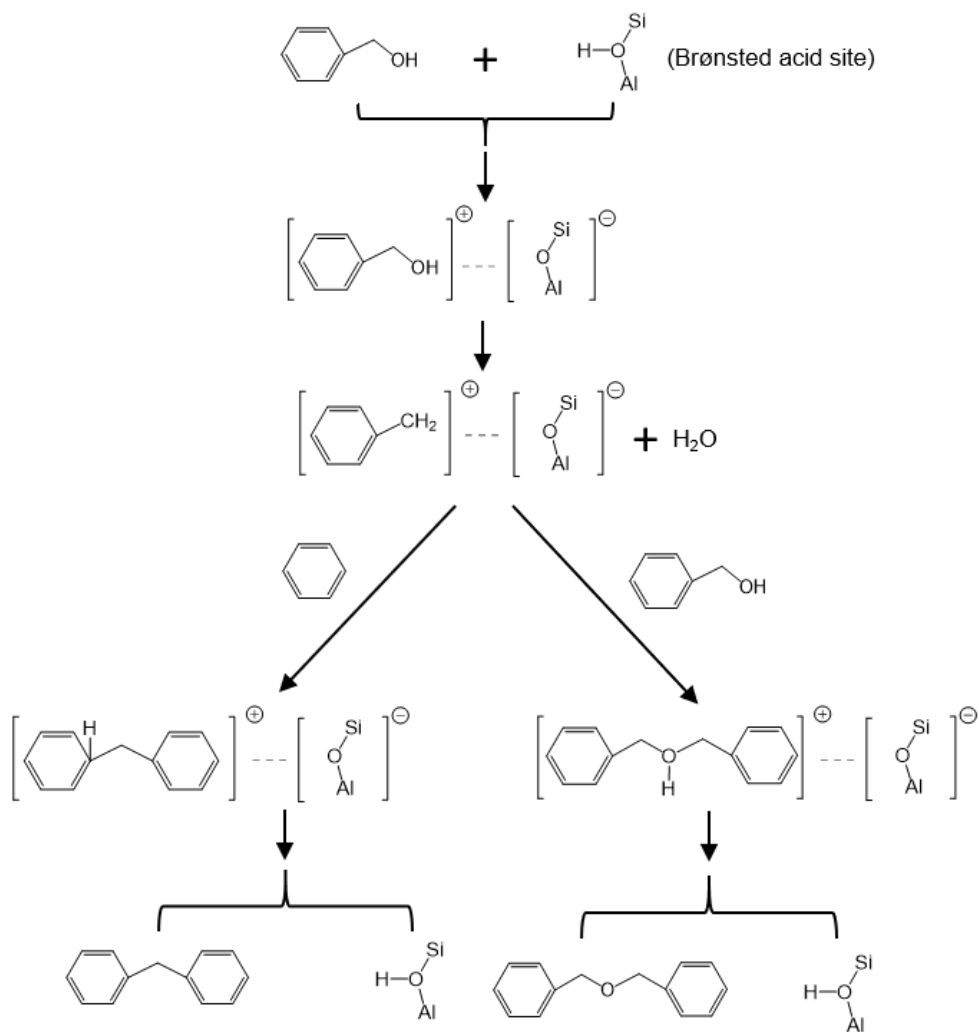


**Figure A3.** IR spectra of pyridine adsorbed on the proton form of (a) MOR-NO<sub>3</sub>, (b) MOR-Cl, (c) MOR-OH, (d) MOR-NO<sub>3</sub>+CTA, (e) MOR-Cl+CTA and (f) MOR-OH+CTA after evacuation at different temperatures. The spectra were normalized by sample weight.



**Scheme A1.** The overall reaction pathway of benzene with benzyl alcohol.





# Chapter 3

## **Facile synthesis of nanosized mordenite and Beta zeolites with improved catalytic performance: non-surfactant diquatery ammonium compounds as structure-directing agents**

### **Abstract**

Non-surfactant diquatery ammonium compounds have already been used for obtaining various zeolites in nanocrystalline form. However, facile synthesis of nanocrystals of mordenite (MOR) and Beta (BEA) in this way remains challenging. Here, we present the direct synthesis of nanosized mordenite (MOR) and Beta (BEA) zeolites with hexane- and *p*-xylene-bridged bis-methylpyrrolidinium, -methylpiperidinium and -DABCO diquats, which can be synthesized in a single step from common chemicals. Optimized recipes are presented for nanosized MOR (20-50 nm) and BEA (15-30 nm) zeolites. By investigating the solid products obtained during hydrothermal synthesis, the formation of nanocrystals can be linked to the strong interaction between diquat templates and aluminosilicate species during the induction stage, which limits the amorphous precursor particles to a size below 50 nm. Based on the textural and acidic properties, catalytic performance data are discussed evidencing the clear benefits of these nanosized zeolites over bulk reference samples in Friedel-Crafts reactions and n-alkane hydroconversion.

This chapter has been published as: S. Li, R.C.J. van de Poll, N. Kosinov and E.J.M. Hensen, *Inorganic Chemistry Frontiers*, 2022, 9, 3200-3216.

### 3.1 Introduction

Zeolites are a family of crystalline porous materials containing molecule-sized cavities and channels, which are widely used in industrial processes enabling separation, adsorption and enhanced reaction rates (catalysis).<sup>1, 2</sup> They are useful catalysts because of their tunable acidity, (hydro)thermal stability and shape selectivity.<sup>3</sup> The performance of zeolite catalysts is often hampered by the long residence times of reactants and products in the micropore network.<sup>4</sup> This can negatively affect the catalytic activity and lead to rapid deactivation due to formation of bulky products that cannot leave and therefore block the micropores. Over the last decades, many approaches have been explored to improve the rate of diffusion in zeolites.<sup>4, 5</sup> A common aspect of nearly all of these approaches is that the crystallite domain size is reduced to limit the diffusional pathways in the micropore space.<sup>6</sup> Besides introducing additional (meso)pores in zeolite crystals,<sup>7</sup> it is also effective to decrease the size of zeolite crystals below 100 nm (nanocrystals).<sup>8</sup> Another potential benefit of these nanocrystals compared to conventional, often micron-sized zeolites is the much higher external surface area that not only increases the rate of product desorption,<sup>9</sup> but also leads to higher conversion rates of reactions that take place on or close to the external surface.<sup>10</sup>

In the last two decades, considerable efforts have been made to prepare nanocrystalline zeolites. Top-down and bottom-up approaches are distinguished based on whether small crystals are obtained after or during zeolite crystallization, respectively.<sup>8</sup> Ball-milling is a physical approach of the first category, which is hampered by the need to remove amorphous debris left after subsequent recrystallization of the milled samples.<sup>11</sup> Chemical treatment is a more versatile top-down approach. For instance, Corma and co-workers prepared nanosheet zeolites, in which zeolite MWW was swelled with hexadecyltrimethylammonium bromide followed by delamination. A limitation of this approach is that it only can be used for particular zeolite topologies like MWW and FER.<sup>12, 13</sup>

Compared to top-down approaches, bottom-up methods provide more flexibility in the preparation of nanocrystalline zeolites.<sup>14</sup> Without being exhaustive, approaches may include a change in the order of mixing the reagents,<sup>15, 16</sup> replacing traditional heating by microwave irradiation,<sup>17</sup> the use of ultra-dense gels crystallized by steam treatment<sup>18</sup> and decoupling nucleation from crystal growth via a temperature-staged approach.<sup>19, 20</sup> Confined space synthesis was also employed to prepare nanosized zeolites, involving crystallization of the zeolite inside a mesoporous matrix.<sup>21</sup> Although nanocrystalline zeolites can be obtained by the above methods, major drawbacks remain, usually involving the complexity of the synthesis in the number of steps and the facilities needed. For instance, to ensure effective formation of BEA nanocrystals by using commercial TEOH, a concentrated gel utilizing

steam-assisted conversion is indispensable, which makes scale-up synthesis challenging.<sup>18</sup> Therefore, it remains highly desirable to prepare nanocrystalline zeolites via facile one-step methods.

As a more facile and effective bottom-up approach, soft-templating methods have been used to prepare nanosized zeolites. Soft templates such as surfactants or polymers can limit both crystal grain growth and Ostwald ripening by adsorbing on the growing crystal surfaces, thereby reducing crystal sizes.<sup>22, 23</sup> For instance, ferrierite nanosheets were synthesized by a dual-templating method, in which piperidine and cetyltrimethylammonium bromide acted as structure-directing agent (SDA) and morphology modifier, respectively.<sup>24</sup> Ryoo and co-workers reported the synthesis of nanocrystalline zeolites such as ZSM-5, BEA and ZSM-12 by amphiphilic surfactants that have two functions, *viz.* directing zeolite growth by their ammonium groups and limiting crystal grain growth by the long hydrophobic alkyl tails.<sup>25, 26</sup> A drawback is that synthesis of these surfactants requires multiple steps. From an industrial perspective, it is preferred to prepare nanosized zeolites with relatively cheap organic templates, such as small-sized non-surfactant molecules obtained by one-step synthesis procedure.<sup>27</sup> Such agents will not self-assemble into specific micelles, needed for obtaining (ordered) hierarchical structures or nanosized crystals. To prepare nanosized zeolites with non-surfactant molecules, a low amount of alkali together with mild crystallization temperature is often adopted to limit the aggregation of negatively charged sub-colloidal particles.<sup>8, 28</sup> This can explain the preference for organic templates in their OH form and the use of low synthesis temperatures, which usually increases the time to require fully crystalline products.<sup>29-31</sup> For example, Corma and co-workers reported the direct synthesis of nanocrystalline ZSM-5 and BEA zeolites by using non-surfactant alkyl-substituted monocationic ammonium cations as templates, which took 14 days at a high template/Si molar ratio of 0.4.<sup>32</sup>

It has been shown that diquatery ammonium compounds are better at directing nanocrystalline zeolite formation than conventional monoquatery ammonium compounds.<sup>33-35</sup> These compounds can be tailored in terms of size, functional groups and rigidity to control the crystal morphology and, in some cases, even the zeolite topology.<sup>33, 36-40</sup> The literature reveals the potential of this approach for preparing nanosized zeolites using relatively cheap non-surfactant organic templates. The synthesis of nanosized forms of commercially important MOR and BEA zeolites using non-surfactant diquatery ammonium molecules as the sole organic template has only been scarcely explored.<sup>41-46</sup> There is little understanding about the underlying crystallization mechanism, which is essential to pave the way to optimization of synthesis of nanosized forms of these zeolites and its generality for synthesis of nanosized zeolites.

In this work, we report the facile and economical synthesis of nanosized MOR and BEA zeolites by using the diquaternary ammonium compound as the sole organic template under conventional hydrothermal synthesis conditions. A total of 6 organic compounds (SDA1-6) were used varying in terms of heterocycle size and geometry of the end groups, and structural rigidity of the linkages (1,6-hexylidene and benzyl) between the quaternary ammonium centers (Figure 3.1). These organic templates were synthesized from commercial chemicals (Table B1) via a one-step procedure. Synthesis conditions for obtaining nanosized MOR and BEA zeolites with these templates were explored. For selected samples, the crystallization behavior was monitored by studying intermediate solid products. The physicochemical properties such as chemical composition, morphology, texture and acidity were extensively characterized. The benefit of nanosizing these zeolites was evaluated by comparing their catalytic performance to conventional MOR and BEA reference zeolites for several model reactions.

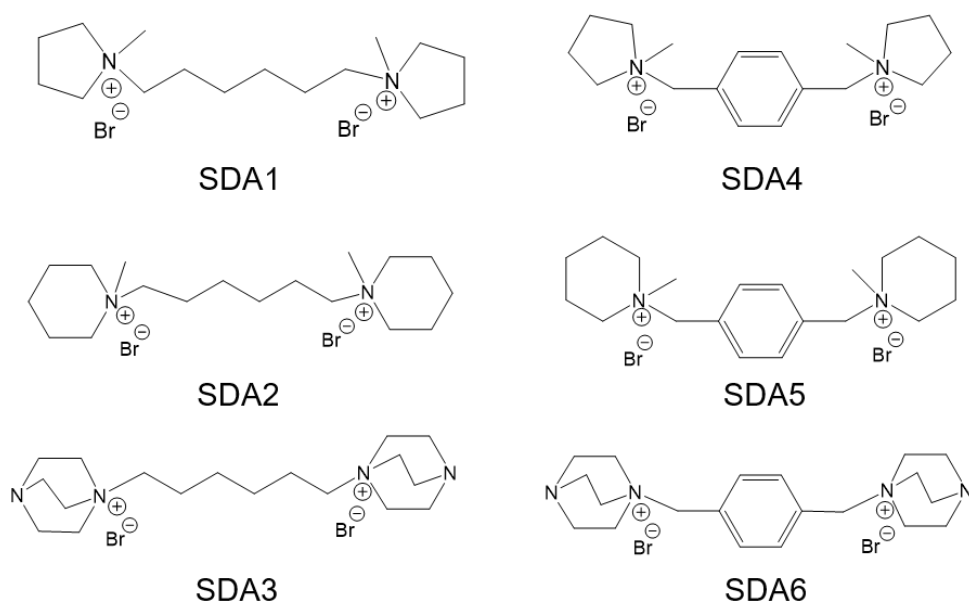


**Figure 3.1.** Organic structure-directing agents (SDAs) used in this work.

## 3.2 Experimental section

### 3.2.1 Synthesis of organic templates

1,6-bis(N-methylpyrrolidinium)hexyl dibromide (**SDA1**): 0.03 mol of 1,6-dibromohexane (TCI, > 97.0%) was dissolved in 100 ml ethanol (Biosolve, 99.9%). Then 0.09 mol of N-

methylpyrrolidine (TCI, > 98.0%) was gradually added under vigorous stirring. The reaction mixture was heated at 70 °C for 2 days under a nitrogen atmosphere. After cooling to room temperature, the solution was poured into 150 ml of diethyl ether (Biosolve, 99.5%) under stirring. The white powder precipitating out of the solution was filtered and washed with extra diethyl ether. The obtained solid product was dried at 50 °C overnight in a vacuum oven. The product yield was 91%.

1,6-bis(N-methylpiperidinium)hexyl dibromide (**SDA2**): The reaction was carried out in the same way as for SDA1, except that N-methylpiperidine (TCI, > 99.0%) was used instead of N-methylpyrrolidine. The product yield was 93%.

1,6-bis(4-aza-1-azoniabicyclo[2.2.2]octane)hexyl dibromide (**SDA3**): 0.06 mol of 1,4-diazabicyclo[2.2.2]octane (DABCO) (TCI, > 98.0%) was dissolved in 100 ml of acetone (Biosolve, 99.5%). Then 0.015 mol of 1,6-dibromohexane was added slowly under stirring. The resulting solution was reacted for 12 h under ambient conditions. After the reaction, the white precipitate was collected by filtration, followed by washing with acetone. The obtained solid product was dried at 50 °C overnight in a vacuum oven. The product yield was 88%.

*P*-phenylenedimethylene-bis(N-methylpyrrolidinium) dibromide (**SDA4**): 0.025 mol of  $\alpha,\alpha'$ -dibromo-*p*-xylene (TCI, > 98.0%) was dissolved in 100 ml of acetonitrile (Biosolve, 99.8%) at 70 °C. Then, 0.1 mol of N-methylpyrrolidine was added under stirring and kept for 2 days at 70 °C under a nitrogen atmosphere. After the reaction, the white product was separated by filtration, followed by washing with diethyl ether. The obtained solid product was dried at 50 °C overnight in a vacuum oven. The product yield was 95%.

*P*-phenylenedimethylene-bis(N-methylpiperidinium) dibromide (**SDA5**): The reaction was carried out as in the synthesis of SDA4, except for the use of N-methylpiperidine instead of N-methylpyrrolidine. The product yield was 90%.

*P*-phenylenedimethylene-bis(4-aza-1-azoniabicyclo[2.2.2]octane) dibromide (**SDA6**): 0.015 mol of  $\alpha,\alpha'$ -dibromo-*p*-xylene and 0.12 mol of DABCO were each dissolved in 100 ml of acetone. The  $\alpha,\alpha'$ -dibromo-*p*-xylene solution was added slowly into the DABCO solution under stirring. The resulting solution was reacted for 12 h under ambient conditions. After the reaction, the white precipitate was collected by filtration, followed by washing with acetone. The obtained solid product was dried at 50 °C overnight in a vacuum oven. The product yield was 90%.

The purity of the above organic templates was verified by <sup>1</sup>H NMR spectroscopy (Figure B1).

### 3.2.2 Synthesis of zeolites

All zeolite synthesis were performed in 45 ml Teflon-lined stainless-steel autoclave (Parr Instruments) under conventional hydrothermal conditions. In a typical synthesis, 0.56 g of sodium hydroxide (Sigma Aldrich,  $\geq 98\%$ ) was dissolved in 15.53 g of deionized water, followed by the addition of the required amount of organic template. After stirring for 5 min, first 0.503 g of  $\text{AlCl}_3 \cdot 6\text{H}_2\text{O}$  (Alfa Aesar, 99%) was added to the mixture, followed by 3.75 g of Ludox AS-40 (Sigma Aldrich, 40 wt%) under stirring. The resulting synthesis gel had a molar composition of 12  $\text{SiO}_2$ : 0.5  $\text{Al}_2\text{O}_3$ : 3.6  $\text{Na}_2\text{O}$ : 1.2 SDA: 480  $\text{H}_2\text{O}$ . After vigorous stirring for 3 h at room temperature, the gel was transferred into an autoclave. The autoclave was placed in an oven for hydrothermal treatment at 160 °C under rotation at 50 rpm. The resulting solid products were recovered by centrifugation, thoroughly washed with demi-water until  $\text{pH} < 8$  followed by drying at 30 °C overnight in a vacuum oven. The zeolites were calcined at 550 °C (heating rate 1 °C/min) for 8 h under flowing air to remove the organic species. The calcined zeolites were ion-exchanged three times with 1.0 M  $\text{NH}_4\text{NO}_3$  solutions, dried and calcined at 550 °C (heating rate 1 °C/min) for 4 h in  $\text{O}_2$ : $\text{N}_2$  (1:4 vol. ratio) flow. Sample notation was zeolite topology–template name–Si/Al gel ratio. For comparison, bulk reference samples were obtained using appropriate templates. The samples were indicated by the suffix -Con to the zeolite topology. A conventional BEA zeolite was synthesized with tetraethylammonium hydroxide (Sigma Aldrich, 35 wt%) by following a reported procedure.<sup>47</sup> This zeolite is denoted by BEA-12-Con.

### 3.2.3 Preparation of Pt-containing zeolites

The proton form of the zeolites were loaded with 0.5 wt% Pt using wet impregnation with an aqueous  $\text{Pt}(\text{NH}_3)_4(\text{NO}_3)_2$  solution. The resulting samples were dried in air followed by calcination at 450 °C (heating rate 0.5 °C/min) for 2 h in an  $\text{O}_2$ :  $\text{N}_2$  (1: 4 vol. ratio) flow.

### 3.2.4 Characterization

X-ray diffraction (XRD) patterns were recorded on a Bruker D2 Endeavor diffraction system using  $\text{Cu K}\alpha$  radiation. Patterns were collected in the  $2\theta$  range of 5-40°.

The elemental composition of samples was determined by inductively couple plasma optical emission spectrometry (ICP-OES). Prior to the measurement, a 1: 1: 1 (by weight) mixture of HF (40 wt% in  $\text{H}_2\text{O}$ ),  $\text{HNO}_3$  (60 wt% in  $\text{H}_2\text{O}$ ) and  $\text{H}_2\text{O}$  was used to dissolve the samples.

Textural properties were obtained from the Ar physisorption at -186 °C with a Micromeritics ASAP 2020 instrument. Prior to the measurements, samples were outgassed at 400 °C for 6

h. The total pore volume was determined at relative pressure ( $p/p_0$ ) of 0.97. The BET surface area was calculated in the  $p/p_0$  range between 0.05-0.25. The micropore volume and external surface area were calculated by  $t$ -plot method. The mesopore volume was calculated by Barrett-Joyner-Halenda (BJH) method.

Thermogravimetric analysis (TGA) was performed with a TGA/DSC 1 instrument (Mettler Toledo). The temperature was increased from 40 °C to 800 °C (heating rate 5 °C/min) in 20 ml/min O<sub>2</sub> and 40 ml/min He flow.

Scanning electron microscope (SEM) images were obtained on a FEI Quanta 200F scanning electron microscope with an accelerating voltage of 3 or 5 kV. Transmission electron microscopy (TEM) images were acquired on a FEI Tecnai 20 at 200 kV. Annular dark field scanning transmission electron microscopy (ADF-STEM) was performed on the TU/e CryoTitan (FEI, now Thermo Fischer Scientific) at 300 kV and room temperature.

IR spectra were obtained with a FTIR spectrometer (Bruker Vertex 70v). The spectra were acquired in the range of 4000-1000 cm<sup>-1</sup>, with a resolution of 2 cm<sup>-1</sup> and an average of 64 scans. The samples were pressed into thin wafers (~10 mg) and placed into a controlled-environment transmission cell. The samples were first pretreated at 550 °C for 1 h in artificial air. After pretreatment, the samples were cooled down to 150 °C and a spectrum was collected as background. Pyridine was introduced into the cell until the sample was fully saturated. Finally, spectra were collected at 150 °C after outgassing for 1h at 150 °C, 300 °C and 500 °C, respectively.

Solid-state nuclear magnetic Resonance (NMR) experiments were performed on a 11.7 Tesla Bruker DMX500 NMR spectrometer, operating at 132 MHz for <sup>27</sup>Al, 99 MHz for <sup>29</sup>Si, 125 MHz for <sup>13</sup>C and 500MHz for <sup>1</sup>H. <sup>27</sup>Al magic angle spinning (MAS) NMR measurements were performed with a Bruker 2.5 mm MAS probe head and a 2.5 mm zirconia rotor, operated at a spinning speed of 25 kHz. All other measurements were carried out with a Bruker Triple Channel 4 mm MAS probe head and a 4 mm zirconia rotor, under a spinning speed of 10 kHz. A single excitation pulse of 1 μs and a recycle delay of 1 s were used for <sup>27</sup>Al NMR measurements. <sup>27</sup>Al chemical shift was referred to Al(NO<sub>3</sub>)<sub>3</sub>. Quantitative <sup>29</sup>Si MAS NMR spectra were collected using a high-power proton decoupling direct excitation (DE) pulse sequence with a 54° pulse duration of 3 μs and a recycle delay of 120 s. <sup>29</sup>Si chemical shift was referred to tetramethylsilane (TMS). <sup>1</sup>H NMR spectra were collected using a Hahn-echo pulse sequence of  $p_1-\tau_1-p_2-\tau_2-aq$  with a 90° pulse  $p_1 = 5 \mu s$ , a 180°  $p_2 = 10 \mu s$  and  $\tau_1 = \tau_2 = 0.5 \mu s$ . A recycle delay of 120 s was applied to obtain quantitative spectra. TMS was used as reference for <sup>1</sup>H NMR chemical shift. Prior to <sup>1</sup>H NMR measurements, the samples were dehydrated at 350 °C for 6 h under vacuum and then transferred into 4 mm rotors in a



glovebox.  $^1\text{H}$ - $^{13}\text{C}$  cross-polarization (CP) MAS NMR spectra were collected with a ramped contact pulse of 3 ms and a recycle delay of 3 s. Solid adamantane was used as reference for  $^{13}\text{C}$  chemical shift. Two-dimensional (2D)  $^1\text{H}$ - $^{29}\text{Si}$  and  $^1\text{H}$ - $^{13}\text{C}$  heteronuclear correlation (HETCOR) spectra were collected with a rectangular contact pulse of 4 ms and 3 ms, respectively.

Liquid-state NMR measurements were performed on a Bruker 400 MHz spectrometer. The organic template was first dissolved in deuterated water, and the resulting solution was transferred into a 5 mm NMR tube.  $^1\text{H}$  NMR spectra were collected with a total of 32 scans and a relaxation delay of 1 s.  $^{13}\text{C}$  NMR spectra were collected with a total of 1024 scans and a relaxation delay of 2 s.

### **3.2.5 Catalytic activity measurements**

#### **3.2.5.1 Benzylation of benzene with benzyl alcohol**

The liquid-phase catalytic conversion of benzyl alcohol (BA) in benzene was performed in a round-bottom flask equipped with a reflux condenser. The flask was heated in a temperature-controlled oil bath. In a typical experiment, 26.7 ml (0.301 mol) of benzene was added to 0.1 g catalyst (activated at 500 °C for 1 h in artificial air) in a glovebox. After maintaining the reaction mixture at 80 °C for 0.5 h under stirring, 0.33 ml (0.003 mol) of BA was added. This moment was regarded as the initial reaction time. Liquid samples were taken periodically and then were separated from the solid catalyst by filtration. Afterwards, the liquid samples were analyzed by a gas chromatograph (Shimadzu GC-17A) with a flame ionization detector (FID) using a Rxi-5ms capillary column (Restek, 30 m  $\times$  0.25 mm  $\times$  0.5  $\mu\text{m}$ ).

#### **3.2.5.2 Acylation of anisole with acetic anhydride**

The liquid-phase catalytic conversion of acetic anhydride in anisole was carried out in the same equipment as described in Part 2.5.1. Typically, 20.98 ml (0.193 mol) of anisole was added to 0.2 g catalyst (activated at 500 °C for 1 h in artificial air) in a glove box. After maintaining the mixture at 70 °C for 0.5 h under stirring, 1.89 ml (0.020 mol) of acetic anhydride was added. This moment was regarded as the initial reaction time. Liquid samples were taken and analyzed following the same way used in Part 2.5.1.

#### **3.2.5.3 Hydroconversion of n-hexadecane**

The hydroconversion of n-hexadecane (n-C<sub>16</sub>) was performed in a downstream fixed-bed continuous flow reactor. Typically, the catalyst (sieve fraction 125-250  $\mu\text{m}$ ) was dried in the reactor at 200 °C for 1 h under He flow at atmospheric pressure. After cooling the reactor to

50 °C, the catalyst was reduced at 400 °C (heating rate 3 °C/min) for 1 h under H<sub>2</sub> flow at atmospheric pressure. The reactor was then cooled to 150 °C and pressurized to 60 bar with H<sub>2</sub>, followed by wetting the packed bed with n-C<sub>16</sub> flow (1 ml/min) for 10 min. The reaction was carried out at a H<sub>2</sub>/n-C<sub>16</sub> molar ratio of 20 and a weight hourly space velocity (WHSV) of 10 g<sub>n-C<sub>16</sub></sub> g<sub>cat</sub><sup>-1</sup> h<sup>-1</sup>. Before sampling, the reaction was stabilized for 5 h at each reaction temperature. The reactor effluent was analyzed using an online gas chromatography (Thermo Scientific Focus GC) equipped with an FID detector coupled with an Rtx-1 column (Restek, 30 m × 0.25 mm × 0.25 μm).

### 3.3 Results and discussion

#### 3.3.1 Zeolite synthesis

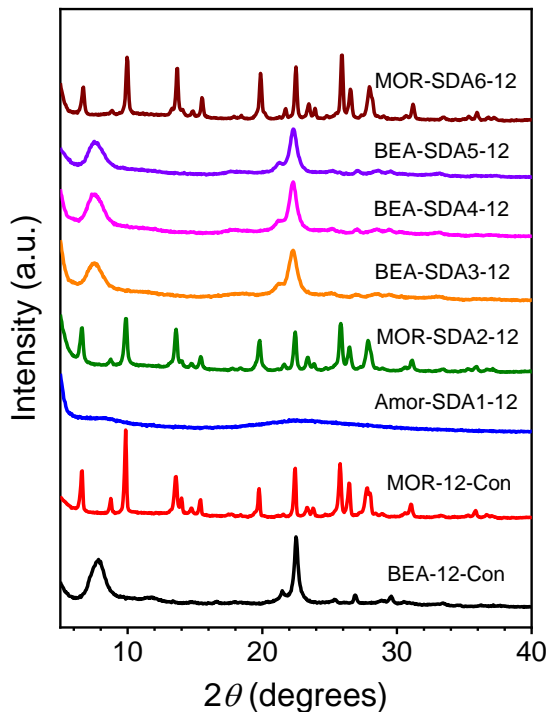


**Figure 3.2.** XRD patterns of samples synthesized using the templates shown in Figure 3.1.

Figure 3.2 shows XRD patterns of the samples obtained at a Si/Al gel ratio of 12 using various templates. Phase-pure MOR zeolite was obtained from a highly alkaline (NaOH/Si = 0.6) inorganic gel without organic templates.<sup>48</sup> Highly crystalline MOR zeolites were also

obtained with SDA2 and SDA6, whereas the use of SDA3, SDA4 and SDA5 resulted in BEA zeolites. No crystalline product was obtained with SDA1, even when the synthesis was prolonged to 6 days. The XRD patterns of the as-synthesized zeolites prepared with these SDAs display less intense and broader diffraction peaks compared to the reference MOR and BEA zeolites. This is typically attributed to reduction of the size of the crystalline zeolite domains.<sup>49</sup> Moreover, when the Si/Al ratio of the gel was raised to 30, BEA zeolites were still obtained with SDA3, SDA4 and SDA5, whereas the use of SDA2 and SDA6 resulted, respectively, in an amorphous sample and a product for which the crystal phase could not be identified (Figures B2-B4). From the inorganic gel with a Si/Al ratio of 30, MOR zeolite was obtained in a low yield, pointing to poor incorporation of silicon into the zeolite as apparent from the low final Si/Al ratio and consistent with earlier studies (Table B3).<sup>50, 51</sup>

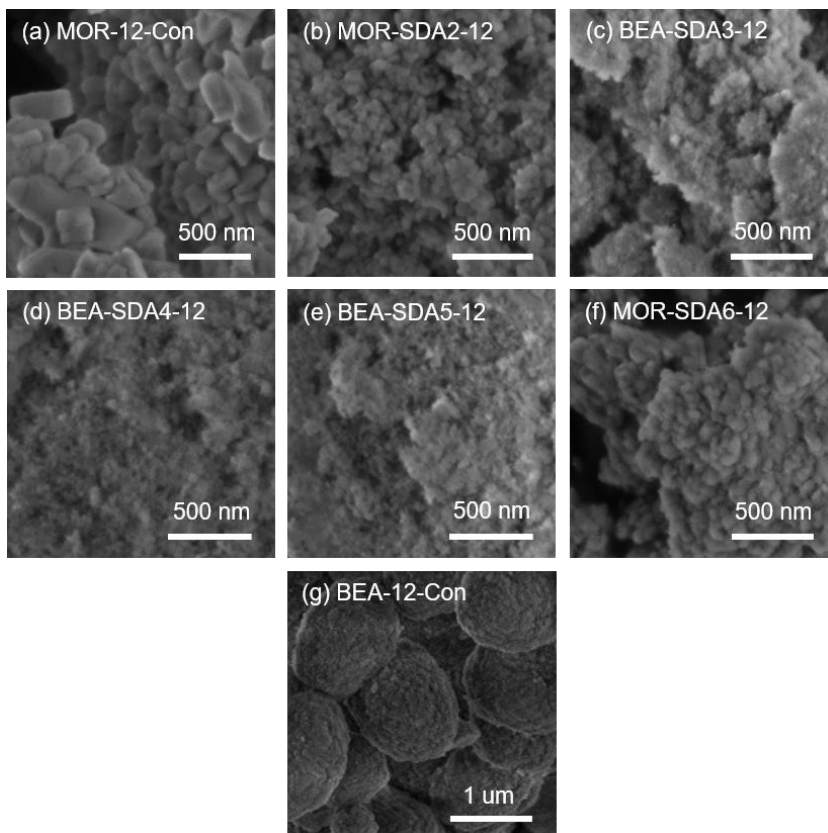


**Figure 3.3.** SEM images of calcined zeolites.

Figures 3.3 and 3.4 show SEM and TEM images of the as-prepared samples, respectively. As shown in Figures 3.3b-3.3f, the use of organic templates led to MOR and BEA zeolites in

the form of aggregates of nanosized crystals. The nanocrystalline morphology is also apparent from the TEM images. Figure 3.4 shows that the MOR-SDA2-12 and MOR-SDA6-12 samples consist of nanoparticles in the 20-50 nm range. Even smaller crystals (15-30 nm) were obtained for BEA-SDA3-12, BEA-SDA4-12 and BEA-SDA5-12. In contrast, MOR-12-Con obtained from a gel without organic template presents large (> 100 nm) crystallites. BEA-12-Con prepared using TEAOH as the SDA resulted in large spherical particles (0.5-2  $\mu\text{m}$  in diameter) with a rough surface in line with literature.<sup>47, 52</sup>

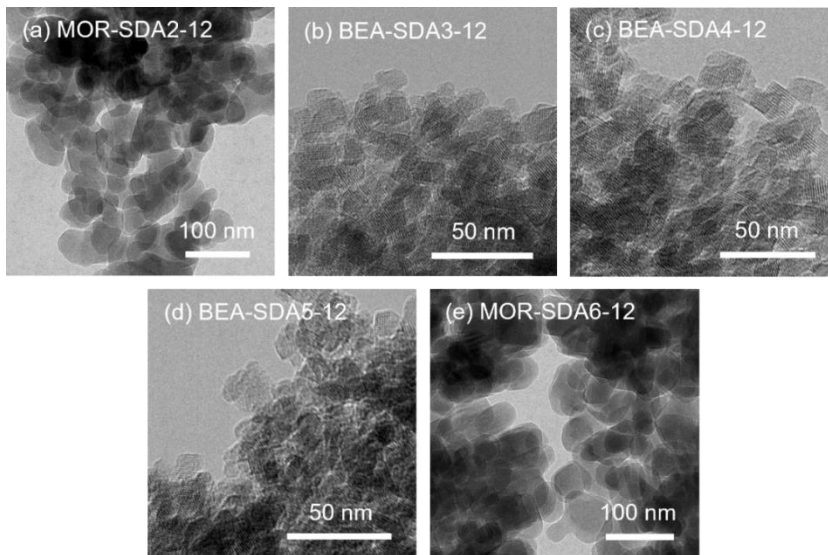


**Figure 3.4.** Representative TEM images of calcined zeolites.

The textural properties of the calcined samples were characterized by Ar physisorption. All isotherms show a steep uptake below  $P/P_0 = 0.02$ , indicating the existence of micropores (Figure 3.5).<sup>53</sup> MOR-12-Con and BEA-12-Con display type-I isotherms, which are typical for microporous materials.<sup>54</sup> Samples prepared with SDA2-6 have a type-IV isotherm with a hysteresis loop, corresponding to the interparticle capillary condensation due to the presence of small crystals.<sup>45</sup> The resulting textural properties are shown in Table 3.1. MOR-SDA2-12 and MOR-SDA6-12 present significantly higher external surfaces of 99 and 93  $\text{m}^2 \text{g}^{-1}$ , respectively, as compared to MOR-12-Con (50  $\text{m}^2 \text{g}^{-1}$ ). The external surface areas of nanosized BEA prepared with SDA3, SDA4 and SDA5 are all much higher (> 240  $\text{m}^2 \text{g}^{-1}$ ) than external surface area of the BEA-12-Con reference (65  $\text{m}^2 \text{g}^{-1}$ ). Among the BEA zeolites, BEA-SDA3-12 has the highest external surface area of 308  $\text{m}^2 \text{g}^{-1}$ . These data agree with the difference seen in the SEM and TEM images. Thus, the diquaternary ammonium compounds are effective SDAs for synthesizing nanosized MOR and BEA zeolites.

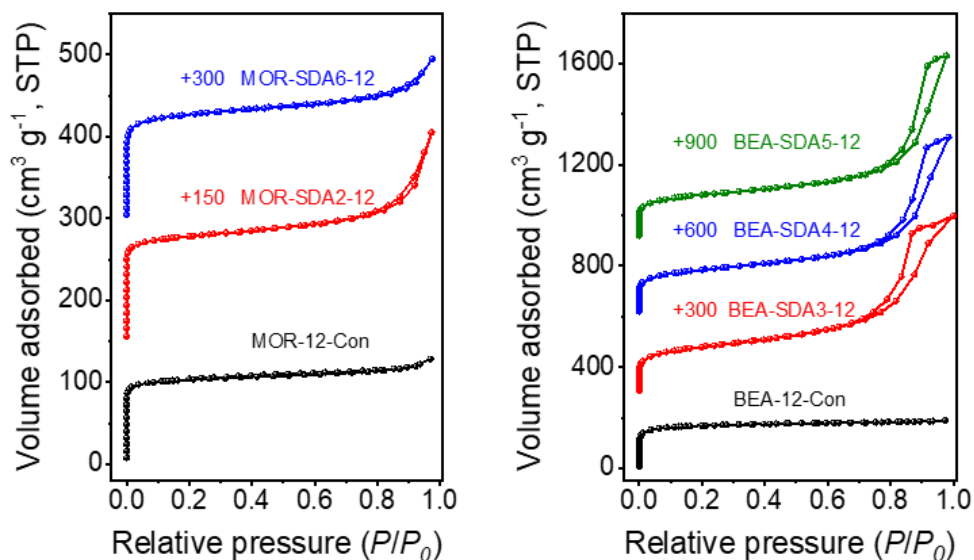


**Figure 3.5.** Ar physisorption isotherms of calcined zeolites.

**Table 3.1.** Textural properties of the calcined zeolites determined by Ar physisorption.

Zeolite	$S_{\text{BET}}$ ( $\text{m}^2 \text{g}^{-1}$ )	$V_{\text{tot}}$ ( $\text{cm}^3 \text{g}^{-1}$ )	$V_{\text{meso}}$ ( $\text{cm}^3 \text{g}^{-1}$ ) ( <i>BJH</i> )	$V_{\text{micro}}$ ( $\text{cm}^3 \text{g}^{-1}$ ) ( <i>t-plot</i> )	$S_{\text{ext}}$ ( $\text{m}^2 \text{g}^{-1}$ ) ( <i>t-plot</i> )
MOR-12-Con	315	0.16	0.04	0.11	50
MOR-SDA2-12	408	0.29	0.13	0.13	99
MOR-SDA6-12	398	0.25	0.10	0.12	93
BEA-SDA3-12	566	0.89	0.72	0.12	308
BEA-SDA4-12	539	0.89	0.72	0.12	257
BEA-SDA5-12	528	0.92	0.75	0.12	245
BEA-12-Con	520	0.24	0.04	0.17	65

$^{13}\text{C}$  NMR spectra of the 6 organic templates and the corresponding samples in their dried state are shown in Figure B5. These NMR spectra of the as-prepared samples match well with those of the pure SDAs, showing that they are stable during the crystallization process.

The TGA profiles determined in artificial air of the as-prepared samples are presented in Figure B6. For MOR-12-Con, the total weight loss below 250 °C of ~9 wt% can be related to the removal of physisorbed water (<150 °C) and water bonded to the zeolite framework (150-250 °C).<sup>55</sup> The corresponding weight loss for the other zeolites was much lower (< 4 wt%), which can be attributed to the presence of organic template in the zeolite micropores. The weight loss above 250 °C occurs in two steps due to the combustion of the organic template. The first weight-loss feature between 250-500 °C is likely due to the elimination of organic molecules on and close to external surface. The second weight loss in the range of 500-650 °C relates to the decomposition of organic species within zeolite pores. This aspect will be further investigated below. The TGA curve for Amor-SDA1-12 contains only a single feature, consistent with the absence of micropores of this amorphous material. Combined with the <sup>13</sup>C NMR data, these results demonstrate that SDA2-6 can direct the formation of nanosized MOR and BEA zeolites. Among the set of MOR and BEA zeolites, MOR-SDA2-12 and BEA-SDA3-12 were selected for further investigation of the crystallization process because of their favorable textural properties, *viz.* the largest external surface.

### 3.3.2 Crystallization process

The above results show that nanosized MOR and BEA zeolite crystals can be obtained by adding different organic templates to inorganic gels that otherwise give rise to bulk MOR. This implies a crucial role of the organic template for obtaining zeolite nanoparticles. It is therefore interesting to understand how the presence of organic template affects the precursors giving rise to zeolites with such distinctive topology and texture. For this purpose, the solid products obtained at different crystallization times were investigated.

The crystallization curves of the three zeolite samples determined by XRD are shown in Figure 3.6. The intensities of the 4 main diffraction peaks ( $2\theta = 9.8^\circ$ ,  $22^\circ$ ,  $25.6^\circ$  and  $26.2^\circ$ ) were used to calculate the relative crystallinity of the MOR zeolites. The intensities of the diffraction peaks at  $2\theta = 7.7^\circ$  and  $22.2^\circ$  were chosen to calculate the relative crystallinity of the BEA samples. MOR-12-Con-24 and BEA-SDA3-72 were used as fully crystallized references for the MOR and BEA zeolites, respectively. Crystalline MOR zeolite can be obtained in 24 h from an inorganic gel. On the other hand, it took more than 70 h to fully crystallize MOR-SDA2-12 and BEA-SDA3-12. Notably, diffraction peaks are not observed after 48 h crystallization, implying a long induction period (Figure B7). The crystal growth times for MOR-12-Con and MOR-SDA2-12 are comparable (~6 h), while the crystal growth stage of BEA-SDA3-12 was slightly longer.

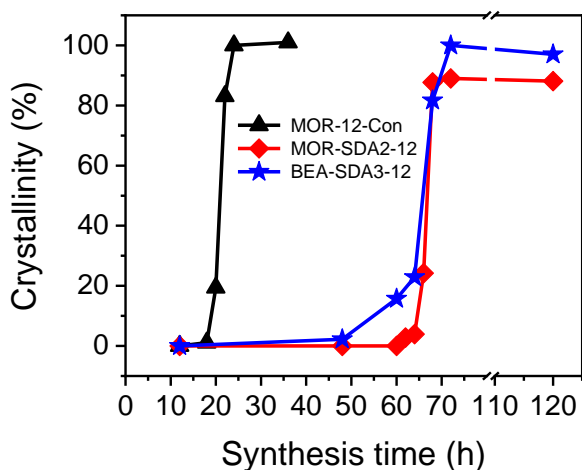


**Figure 3.6.** Relative crystallinities of obtained solid samples at different crystallization time based on XRD analysis.

The morphology of the intermediate products was determined by SEM and TEM (Figures 3.7, 3.8, B8 and B9). For MOR-12-Con, worm-like particles with a size of 0.1-2 mm were obtained after 12 h of crystallization (Figure 3.7a). This morphology has been observed before for amorphous aluminosilicates.<sup>56</sup> Prolonging the crystallization time to 18 h led to an additional phase mainly consisting of plates (Figure 3.7b). After 20 h, the fraction of this plate-like material was slightly higher (Figure 3.7c). The final MOR-12-Con material consisted of particles with a size in the 100-600 nm range with an inhomogeneous morphology (Figure 3.7e). MOR-SDA2-12 consisted of nanoparticles with a primary diameter of 20-50 nm aggregated into secondary particles with a typical size of 200 nm after 12 h hydrothermal treatment (Figure 3.8a). The significantly smaller size of the zeolite nanoparticles compared to MOR-12-Con is due to interruption of zeolite growth by the organic template. Prolonging crystallization from 12 h to 64 h did not substantially change this morphology (Figures 3.8a-3.8e and B9a). Slightly smaller nanoparticles (15-40 nm) were observed for the sample obtained after 66 h (Figure 3.8f). In the period between 66 h and 72 h, rapid crystal growth took place (Figure 3.6), resulting in the final zeolite nanoparticles with sizes between 20 and 50 nm after 72 h hydrothermal treatment (Figure 3.8h). For BEA-SDA3-12, aggregated particles with a primary size smaller than 50 nm were formed throughout the whole synthesis process. (Figures B8 and B9b). These findings show that the size of solid intermediates is significantly reduced from larger than 100 nm to less than 50 nm by the presence of the SDAs, while comparable Si/Al ratios and yields of solid products were observed throughout the synthesis for each synthetic system regardless of the presence of the SDAs (Tables B5, B6 and B7).

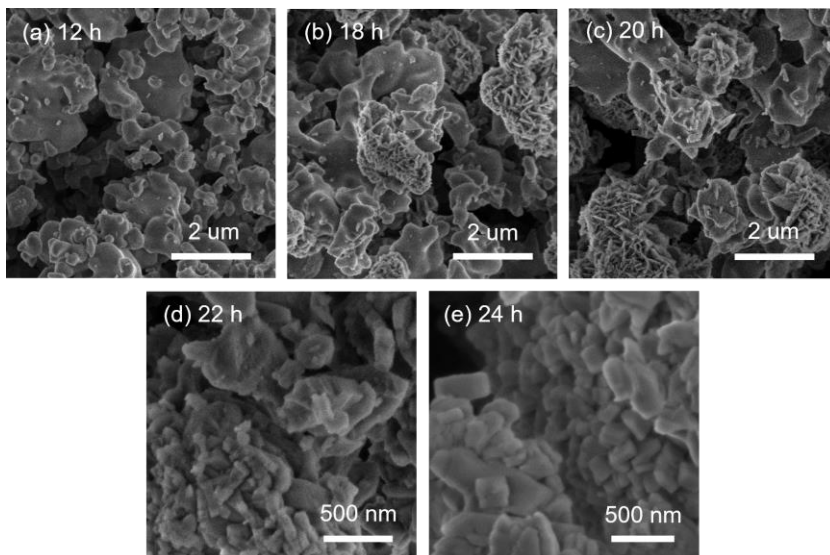


**Figure 3.7.** SEM images of solid samples obtained at different crystallization times of MOR-12-Con.

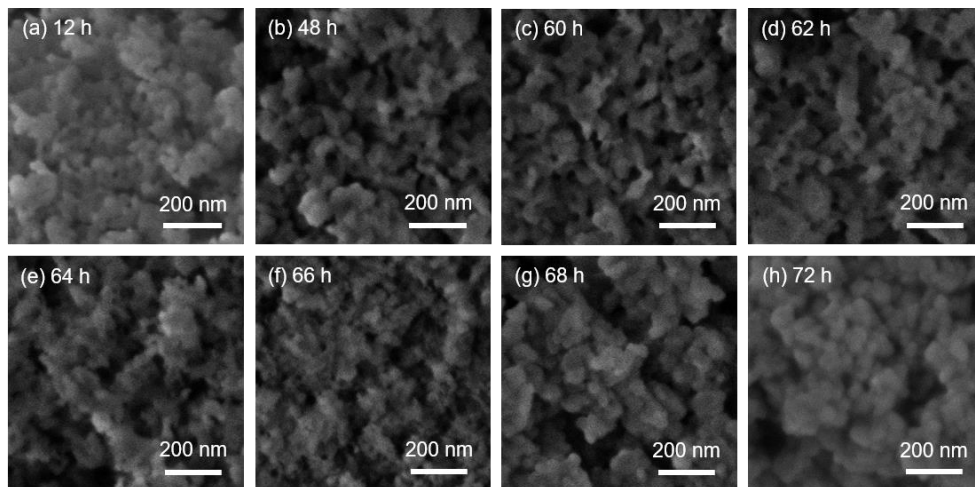


**Figure 3.8.** SEM images of solid samples obtained at different crystallization times of MOR-SDA2-12.



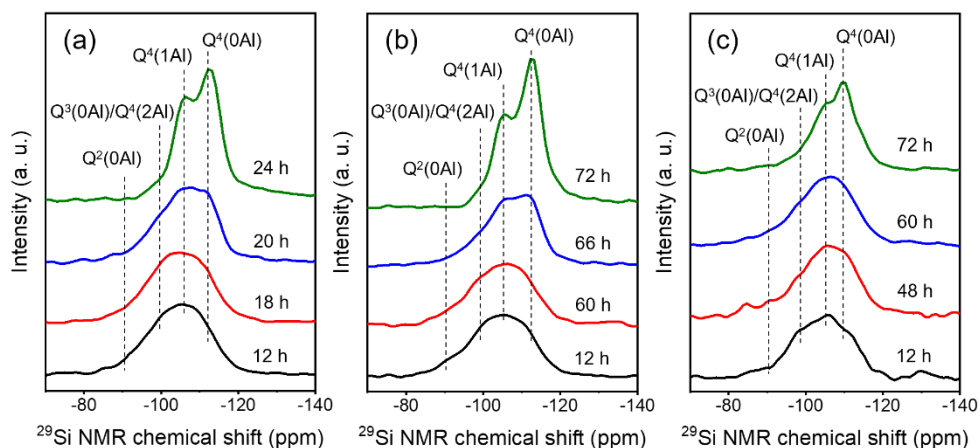


**Figure 3.9.**  $^{29}\text{Si}$  MAS NMR spectra of samples obtained at different crystallization times: (a) MOR-12-Con, (b) MOR-SDA2-12 and (c) BEA-SDA3-12.

The Si coordination in the solid products was investigated by  $^{29}\text{Si}$  MAS NMR spectroscopy. As shown in Figure 3.9, the NMR spectra of samples obtained after hydrothermal treatment for 12 h contain a broad feature in the range between -80 and -120 ppm. Main features at 91 ppm, 102 ppm, 106 ppm and 112 ppm can be observed, corresponding to  $\text{Q}^2(0\text{Al})$ ,  $\text{Q}^3(0\text{Al})/\text{Q}^4(2\text{Al})$ ,  $\text{Q}^4(1\text{Al})$  and  $\text{Q}^4(0\text{Al})$  sites, respectively.<sup>57, 58</sup> Notably, the Si coordination does not substantially change during the induction period. During crystal growth, the relative intensity of the  $\text{Q}^4(0\text{Al})$  peak gradually increased towards the final intensity observed for the fully crystallized zeolite. Together with the XRD data, these findings confirm that zeolite crystallization comprised induction and crystal growth stages with significant condensation mainly taking place during the latter stage. Similar trends in Si speciation have been observed in previous work in which the synthesis of MOR and BEA zeolites by dry gel conversion was studied in detail.<sup>59, 60</sup>

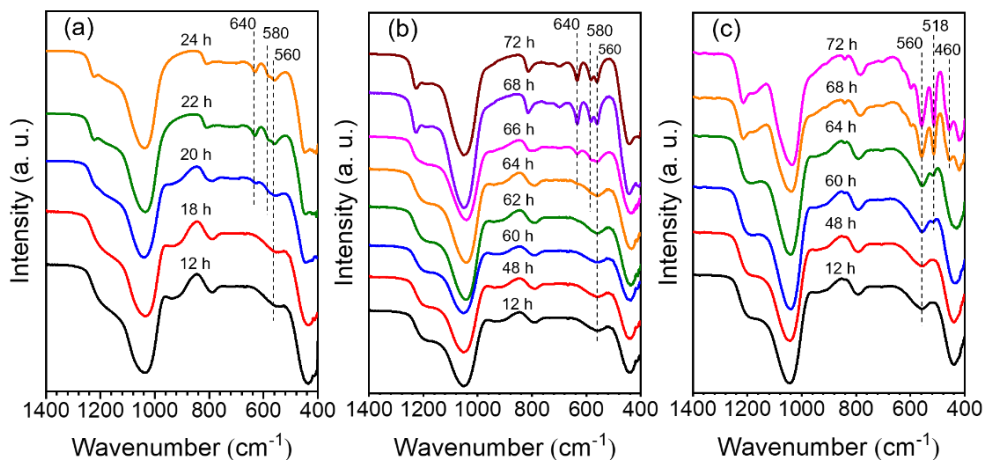


**Figure 3.10.** IR spectra of solid samples obtained at different crystallization times: (a) MOR-12-Con, (b) MOR-SDA2-12 and (c) BEA-SDA3-12.

A common view about zeolite synthesis is that precursor units formed during the induction stage assemble into zeolite crystals.<sup>58, 61, 62</sup> The presence of specific features in the solid products was investigated by IR spectroscopy (Figure 3.10). A band at  $560\text{ cm}^{-1}$  present during the whole synthesis of MOR-12-Con has been linked to five-membered rings (5MR) silicate species.<sup>63</sup> This does not necessarily mean that these species are involved in crystal growth. During the crystal growth stage (20-24 h), two other bands appear at  $580\text{ cm}^{-1}$  and  $640\text{ cm}^{-1}$  assigned to 5MR and four-membered rings (4MR), respectively.<sup>63, 64</sup> A similar trend in the IR spectra is observed for the MOR sample synthesized with SDA2, showing that the 5MR-containing motives are already present in the induction period, while formation of 4MR goes together with crystal growth. Thus, the synthesis of MOR-12-Con and MOR-SDA2-12 appears to follow a classical mechanism involving induction, nucleation and crystal growth. The longer induction period for MOR-SDA2-12 is likely due to the interactions between the organic template and the aluminosilicate precursors.<sup>61</sup> For the sample synthesized with SDA3, the band at  $560\text{ cm}^{-1}$  corresponding to 5MR is also observed during the induction period.<sup>58</sup> After prolonging the hydrothermal treatment time from 60 h to 72 h, two characteristic bands of BEA zeolite at  $460\text{ cm}^{-1}$  and  $518\text{ cm}^{-1}$  assigned to internal and external T-O-T bending vibrations, respectively, are visible,<sup>65</sup> which corresponds well with the evolution in crystallinity determined by XRD during BEA-SDA3-12 synthesis.

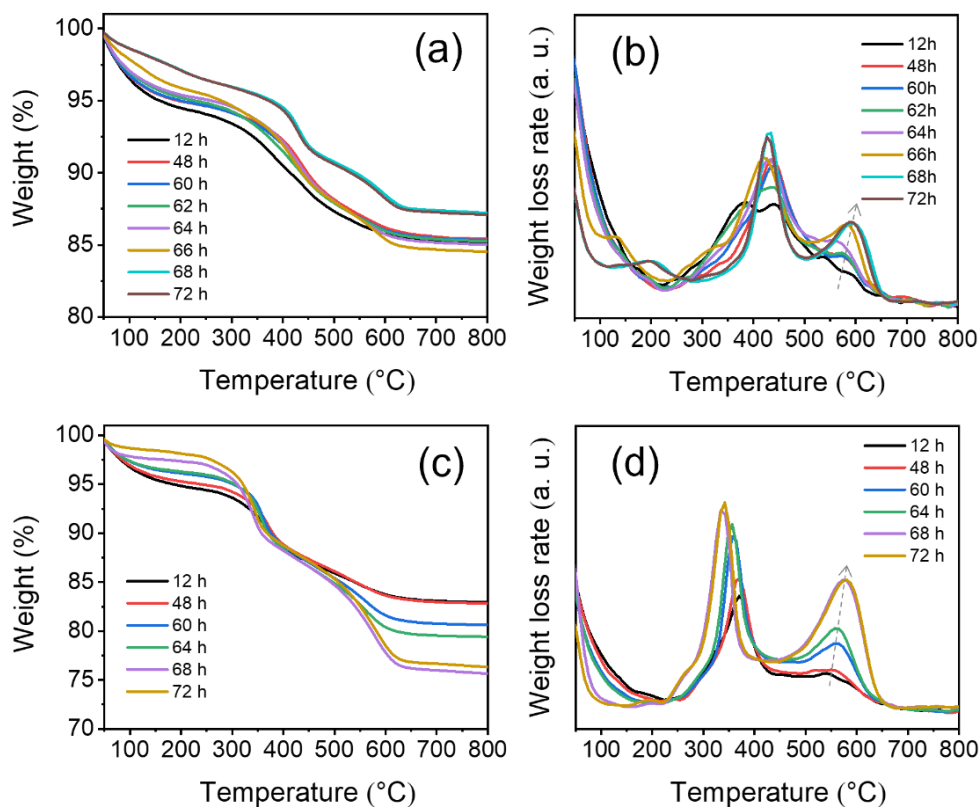


**Figure 3.11.** TG (left) and DTG (right) curves of samples obtained at different crystallization times: (a and b) MOR-SDA2-12 and (c and d) BEA-SDA3-12.

TG-DTG measurements of MOR-SDA2-12 and BEA-SDA3-12 were performed to investigate the interactions between the organic template and the aluminosilicate intermediates. The TG-DTG curves in Figure 3.11 show three weight-loss steps. The first weight-loss feature below 250 °C can be attributed to the desorption of water.<sup>55</sup> The other two weight-loss features in the 250-660 °C range are mainly due to the oxidation of organics at or close to the zeolite external surface and inside the zeolite micropores. Notably, already during the induction stage both MOR and BEA precursors contain a substantial amount of SDA (> 8.6 wt%, Tables B6 and B7), indicative of the strong interactions between the SDA and the aluminosilicate precursor species. Moreover, the third weight-loss feature becomes stronger and shifts to higher temperature during the crystallization stage. This trend is consistent with the assignment of this weight-loss feature to organics occluded in the micropores formed during crystallization. These results further underpin that SDA2 and

SDA3 were included in the micropores during SDA-directed synthesis of MOR and BEA zeolite.

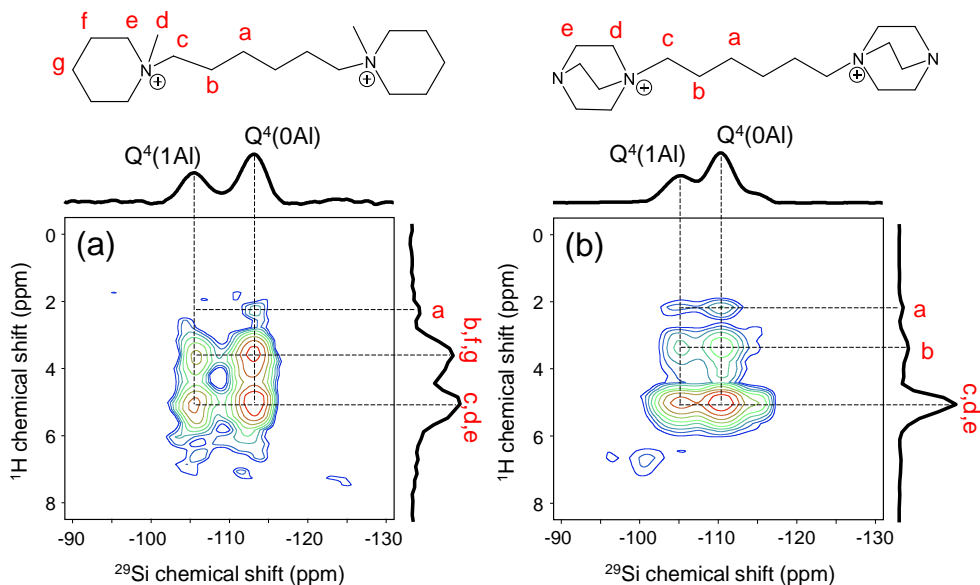


**Figure 3.12.**  $^1\text{H}$ - $^{29}\text{Si}$  HETCOR NMR spectra of as-prepared zeolites: (a) MOR-SDA2-12 and (b) BEA-SDA3-12 (assignment to different H atoms in SDA in top panels).

2D  $^1\text{H}$ - $^{29}\text{Si}$  HETCOR NMR spectroscopy measurements were carried out to investigate the zeolite-SDA interaction in more detail. This allows resolving short-range ( $< 1$  nm) interactions between  $^{29}\text{Si}$  and  $^1\text{H}$  spins.<sup>66-68</sup> The  $^{29}\text{Si}$  projection of the spectrum in Figure 3.12a contains two main peaks around -106 and -113 ppm, which are due to Q<sup>4</sup>(1Al) and Q<sup>4</sup>(0Al) zeolite framework species,<sup>57</sup> respectively. The  $^1\text{H}$  projection contains three peaks, which can all be correlated to SDA2. The  $^1\text{H}$  peaks in Figure 3.12a were identified by recording separate  $^1\text{H}$  NMR spectrum (Figure B1b),  $^1\text{H}$ - $^{13}\text{C}$  CPMAS NMR spectrum (Figure B5b) and  $^1\text{H}$ - $^{13}\text{C}$  HETCOR NMR spectrum (Figure B10a). The  $^1\text{H}$  signals at 3.7 ppm and 5.1 ppm are strongly correlated with the signals due to Q<sup>4</sup>(1Al) and Q<sup>4</sup>(0Al) framework species, resulting in 4 distinct peaks in the 2D spectrum. Besides, a weak cross-peak between a feature at 2.2 ppm in  $^1\text{H}$  dimension and a feature at -114 ppm in the  $^{29}\text{Si}$  dimension is present in the 2D spectrum. Similarly, strong correlation signals between features assigned to the various protons of SDA3 and Si atoms of the BEA zeolite framework can be distinguished in the 2D NMR spectrum in Figure 3.12b. These NMR data further underpin that SDA2 and SDA3 are predominantly present in the micropores of respectively MOR and BEA zeolites.

### 3.3.3 Acidity

Next, the acidic properties of the calcined zeolites in their proton form were characterized. The Si/Al ratios of MOR-12-Con and MOR-SDA2-12 of respectively 8.4 and 9.2 (Table 3.2) are both lower than the Si/Al ratio in the initial gels. The Si/Al ratios of BEA-12-Con and BEA-SDA3-12 of 11.3 and 11.7, on the other hand, are close to the initial gel ratio. The Al coordination was investigated by  $^{27}\text{Al}$  MAS NMR spectroscopy. The  $^{27}\text{Al}$  NMR spectra in Figure 3.13a exhibit a strong signal at  $\sim 54$  ppm assigned to tetrahedrally coordinated Al species in the zeolite framework ( $\text{Al}_F$ ), while the presence of a comparatively weak signal at  $\sim 0$  ppm is attributed to extraframework Al species in octahedral coordination.<sup>21, 67</sup> Deconvoluting these spectra shows that most Al atoms are incorporated into the zeolite framework (Table B8). The Si coordination environment was studied by  $^{29}\text{Si}$  MAS NMR spectroscopy. The relevant spectra in Figure 3.13b consist of 4 signals due to asymmetric  $\text{Q}^4(0\text{Al})$ , symmetric  $\text{Q}^4(0\text{Al})$ ,  $\text{Q}^4(1\text{Al})$  and  $\text{Q}^4(2\text{Al})/\text{Q}^3(0\text{Al})$  sites.<sup>57</sup> The fractional contributions obtained by deconvolution were used to calculate the Si/Al ratio of the zeolite framework. As shown in Table B8, MOR-12-Con has a lower framework Si/Al ratio (6.8) than MOR-SDA2-12 (8.5), while similar framework Si/Al ratios of 10.5 and 10.3 were determined for BEA-12-Con and BEA-SDA3-12, respectively. Notably, the  $\text{Si}/\text{Al}_F$  ratios determined by  $^{29}\text{Si}$  NMR are lower than the bulk Si/Al ratios. The reason for this discrepancy is that the  $\text{Q}^3(0\text{Al})$  and  $\text{Q}^4(2\text{Al})$  signals strongly overlap. For deconvolution of these spectra, we assumed that there are no  $\text{Q}^3(0\text{Al})$  sites, which can explain the lower  $\text{Si}/\text{Al}_F$  ratios. Such a systematic difference when using this assumption has been discussed by others.<sup>57, 69</sup> The presence of  $\text{Q}^3(0\text{Al})$  in these samples is supported by the relatively higher intensity of the  $\text{Q}^4(2\text{Al})/\text{Q}^3(0\text{Al})$  sites in comparison to  $\text{Q}^4(0\text{Al})$  sites in the  $^1\text{H}$ - $^{29}\text{Si}$  CPMAS NMR spectra when contrasted to  $^{29}\text{Si}$  MAS NMR spectra (Figure B11).<sup>69, 70</sup>

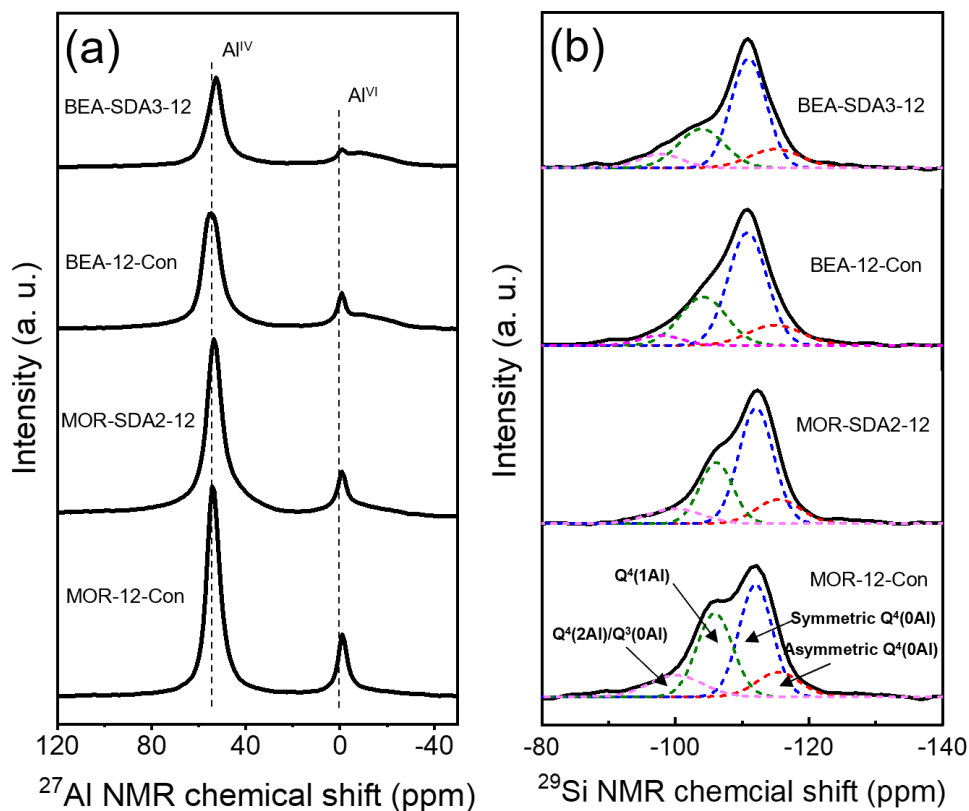


**Figure 3.13.** (a)  $^{27}\text{Al}$  MAS NMR and (b)  $^{29}\text{Si}$  MAS NMR spectra of the calcined zeolites.

**Table 3.2.** Elemental analysis and acidic properties of the calcined zeolites.

Zeolite	Si/Al (ICP)	[BAS] <sup>a</sup> ( $\mu\text{mol g}^{-1}$ )	[BAS] <sup>b</sup> ( $\mu\text{mol g}^{-1}$ )	[LAS] <sup>c</sup> ( $\mu\text{mol g}^{-1}$ )
MOR-12-Con	8.4	1291	1015	41
MOR-SDA2-12	9.2	841	753	120
BEA-12-Con	11.3	--	961	378
BEA-SDA3-12	11.7	--	704	484

<sup>a</sup> Concentration of BAS determined by  $^1\text{H}$  MAS NMR spectra.

<sup>b</sup> Concentration of BAS determined by IR spectra of adsorbed pyridine after evacuation for 1 h at 150 °C.

° Concentration of LAS determined by IR spectra of adsorbed pyridine after evacuation for 1 h at 150 °C.

The acidic properties of zeolites were characterized by IR spectroscopy after adsorption of pyridine and subsequent evacuation at 150 °C, 300 °C and 500°C. The relevant spectra given in Figure B12 contain two bands at 1455 cm<sup>-1</sup> and 1545 cm<sup>-1</sup> due to pyridine adsorbed on Lewis acid sites (LAS) and Brønsted acid sites (BAS),<sup>45,71</sup> respectively. The amount of BAS and LAS based on spectra obtained after evacuation at 150 °C are given in Table 3.2. For BEA zeolites, the corresponding numbers represent the total acidic concentration, because all the pores are accessible for pyridine. As shown in Table 2, BEA-SDA3-12 displays a lower BAS concentration but a higher LAS concentration as compared to BEA-12-Con. For the MOR zeolite, pyridine is too large to probe all of the acid sites. According, we first determined the total acidity for the MOR zeolites using <sup>1</sup>H MAS NMR spectroscopy of well-dehydrated samples (Figure B13 and Table 3.2). Compared with MOR-12-Con, MOR-SDA2-12 presents a lower total BAS concentration.

It has been demonstrated that there is a distribution of BAS in MOR zeolites related to their location in 12MR straight channels, 8MR side pockets and at the interface of these two locations (8/12MR).<sup>50, 72, 73</sup> The different confinement in these pores can profoundly impact the catalytic performance. For instance, BAS in side-pockets are very active for the carbonylation of dimethyl ether to methyl acetate due to effective stabilization of acetyl intermediates in 8MR channels, whereas BAS in 12MR channels mainly lead to the formation of coke.<sup>74, 75</sup> Reactants involving bulky reactants mainly occur in 12MR channels and at the external surface.<sup>76</sup> Therefore, the BAS distribution in MOR-12-Con and MOR-SDA2-12 were further investigated. The distribution of BAS was evaluated by deconvolution of the hydroxyl stretching region of IR spectra of the dehydrated zeolites.<sup>77</sup> As shown in Figure 3.14 right and Table B9, MOR-SDA2-12 contains a higher fraction (64%) of side-pocket BAS as compared to MOR-12-Con (49%). The accessibility of BAS was investigated by tracing the evolution of IR bands assigned to BAS sites upon pyridine adsorption and subsequent desorption at different evacuation temperatures. Figure 3.14 left shows that the relative decrease of the band due to BAS is larger for MOR-SDA2-12 as compared to MOR-12-Con. This indicates that more side-pocket BAS of MOR-SDA2-12 are accessible for pyridine. For both samples, the hydroxyl bands shift to higher wavenumbers upon pyridine desorption at 500 °C, suggesting that the recovery of BAS is mainly from 12MR channels and the 8/12MR interfaces.

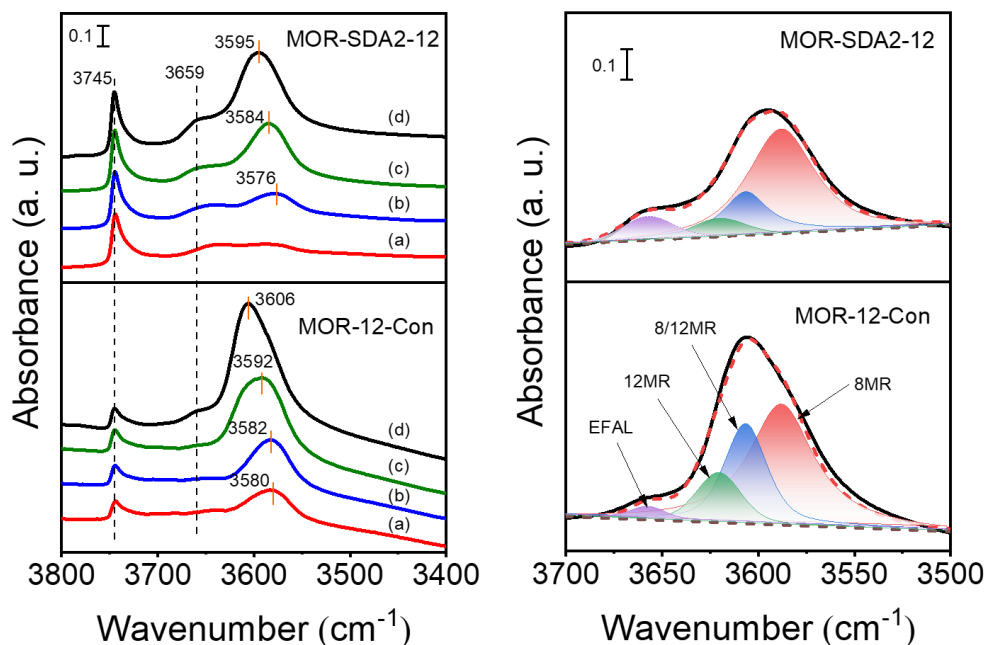


**Figure 3.14.** (Left) IR spectra of the calcined MOR zeolites: (a) after pyridine adsorption and evacuation at 150 °C, (b) evacuation at 300 °C, (c) evacuation at 500 °C and (d) hydroxyl region of IR spectra of MOR zeolites before pyridine adsorption; (right) deconvolution into contributions of hydroxyl groups due to 12MR, 8MR and 8/12MR interfaces as well as hydroxyl groups connected to EFAL species.

### 3.3.4 Catalytic activity

It has been firmly established that pore hierarchization in microporous zeolites can substantially improve the catalytic performance.<sup>4, 14</sup> Reducing the crystal size of zeolites below 100 nm is one such approach that benefits reactions with bulky reactants and reactions in which competing consecutive reactions of products can lead to lower selectivity to desired products or catalyst deactivation.<sup>8</sup> For instance, nanocrystalline zeolites perform better in Friedel-Crafts alkylation and acylation reactions than bulk zeolites.<sup>78</sup> As nanosized MOR and BEA zeolites are promising for the alkylation of benzene with benzyl alcohol and the acylation of anisole with acetic anhydride, respectively,<sup>76, 79</sup> we evaluated the optimized nanosized MOR and BEA zeolites prepared in the present study using these two model reactions compared to the bulk reference zeolites. Pt/BEA zeolite was also evaluated for the hydroconversion of *n*-C<sub>16</sub>. Paraffins hydroisomerization and hydrocracking are industrially important reactions for hydrocarbon processing.<sup>80, 81</sup>



### 3.3.4.1 Benzylation benzene with benzyl alcohol

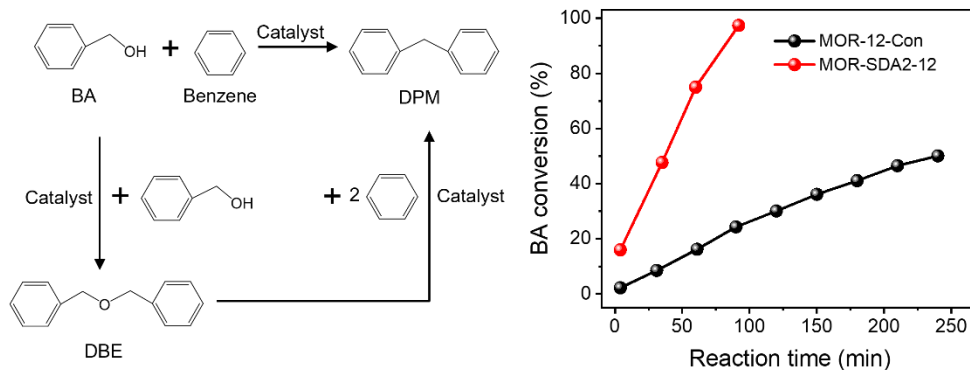


**Figure 3.15.** (Left) Reaction pathways for benzylation of benzene with benzyl alcohol (BA) and (right) catalytic conversion of BA over MOR zeolite samples at 80 °C.

The conversion of benzyl alcohol (BA) for nanosized and bulk MOR zeolite as a function of reaction time is shown in Figure 3.15. After 240 min, the BA conversion over MOR-12-Con is limited to 50% with a diphenylmethane (DPM) selectivity 72%. MOR-SDA2-12 presents a much higher catalytic activity with BA, being completely converted after 90 min at a DPM selectivity of 90%. As the benzylation of benzene with BA requires strong BAS with relatively large product molecules (Figure 3.15 left and Scheme B1), the acidity and the accessibility of the BAS are the two most important factors that determine the benzylation reaction.<sup>82, 83</sup> As the kinetic diameters of the reactants and products (~0.5 nm) are slightly smaller than the kinetic diameter of pyridine, it is reasonable to assume that the active sites for benzylation are the acid sites probed by pyridine IR. MOR-SDA2-12 presents a lower amount of such BAS than MOR-12-Con (Table 3.2). Thus, the higher activity and DPM selectivity of MOR-SDA2-12 can be ascribed to the significantly smaller zeolite crystal size.

### 3.3.4.2 Acylation anisole with acetic anhydride

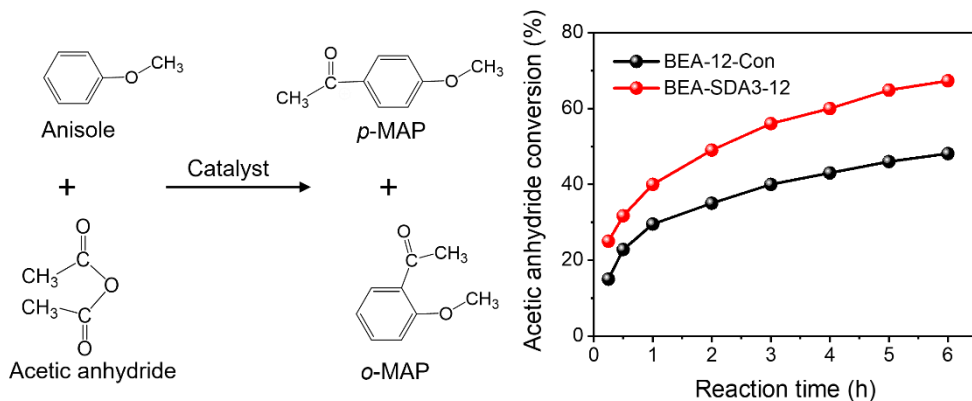


**Figure 3.16.** (Left) The mechanism of anisole acylation and (right) catalytic conversion of acetic anhydride over BEA zeolite samples at 70 °C.

The acylation of anisole with acetic anhydride was chosen as a model reaction to evaluate the catalytic performance of BEA zeolites. The formation of *p*-methoxyacetophenone (*p*-MAP) over *o*-methoxyacetophenone (*o*-MAP) is strongly favored for BEA-12-Con and BEA-SDA3-12 with a selectivity over 98%. Such a high *p*-MAP selectivity is generally observed for a wide range of catalysts with little influence of confinement of the active sites.<sup>84</sup> Figure 3.16 right shows that BEA-SDA3-12 exhibits a higher activity than BEA-12-Con, providing an *p*-MAP yield of 57% (*p*-MAP selectivity 85%) after 6 h reaction. BEA-12-Con shows a lower yield of 39% (*p*-MAP selectivity 81%) after 6 h reaction (Table B10). Strong BAS are required for the activation of the nucleophilic carbonyl group of acetic anhydride to form the acylium intermediates, which will further react with anisole to form *p*-MAP (Figure 3.16 left and Scheme B2).<sup>85</sup> The large *p*-MAP product is strongly adsorbed to the surface and tends to form products that can be considered as coke decreasing the accessibility of the acid sites.<sup>86, 87</sup> Considering that BEA-SDA3-12 contains less BAS than Con-BEA-12 (Table 3.2), the higher catalytic activity of BEA-SDA3-12 can be attributed to the better accessibility of the active sites. Thus, the shorter diffusion pathways in the zeolite domains lead to a higher activity.

### 3.3.4.3 Hydroconversion of n-hexadecane

The two BEA zeolites were also evaluated for the hydroconversion of n-C<sub>16</sub> after loading 0.5 wt% Pt. This metal loading amount is generally deemed sufficient to ensure isomerization/cracking reactions of intermediate olefins on the BAS as the rate-determining

step during n-alkane hydroconversion reactions.<sup>9</sup> Elemental analysis confirms that the actual Pt loading is close to the targeted value for both catalysts. ADF-STEM images (Figure B14) demonstrate a high Pt dispersion with average particle sizes of  $1.3 \pm 0.2$  nm and  $1.1 \pm 0.2$  nm for Pt/BEA-12-Con and Pt/BEA-SDA3-12, respectively. Thus, based on the similar metal function for the two bifunctional catalysts, differences in the catalytic performance can be attributed to differences in the acidic zeolite component.

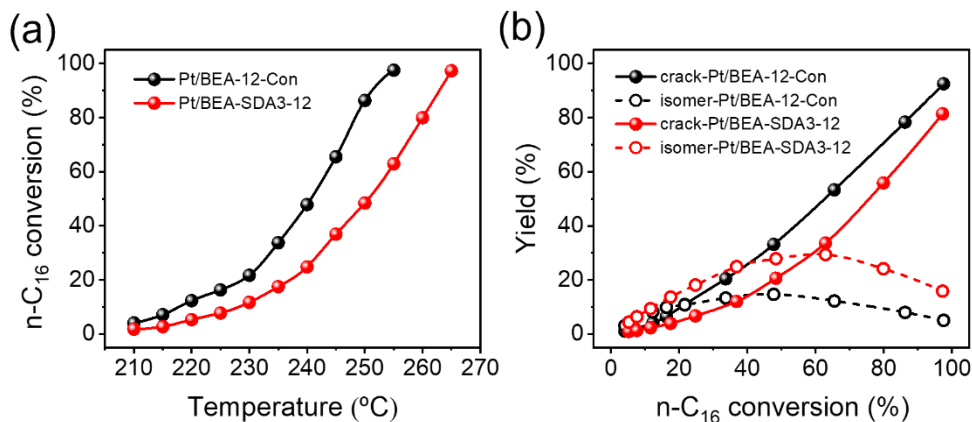


**Figure 3.17.** (a) Conversion of n-C<sub>16</sub> as a function of the reaction temperature and (b) yield of isomers and cracked hydrocarbon products as a function of n-C<sub>16</sub> conversion.

Figure 3.17a shows the conversion of n-C<sub>16</sub> as a function of reaction temperature. The less acidic Pt/BEA-SDA3-12 displays a lower reaction activity than Pt/BEA-12-Con. Astafan *et al.* reported that the activity of n-C<sub>16</sub> hydroconversion over Pt/BEA was proportional to the concentration of BAS probed by pyridine at 150 °C, regardless of the zeolite crystal size.<sup>90</sup> This can most likely be explained by the fact that the n-C<sub>16</sub> hydroconversion reaction is not limited by mass transport under the given reaction conditions. It is also common that pore hierarchization of BEA zeolite impedes the amount of BAS and, thus, the activity for hydroconversion of n-alkanes.<sup>89</sup> Therefore, the lower reaction activity of Pt/BEA-SDA3-12 can be attributed to the lower acidity of the nanosized sample in line with the activity in n-alkane hydroisomerization reactions being proportional to the intrinsic acidity.<sup>88</sup> Figure 3.17b shows the differences in the product distribution between the two catalysts. For both catalysts, the yield of isomers gradually increases with reactant conversion until a maximum is reached, after which cracking becomes the dominant route. The origin of this dependence of the product distribution is well understood in terms of skeletal isomerization of linear alkanes, leading to multibranched isomers whose olefinic counterparts are easier to crack.<sup>81</sup> Notably, the maximum isomer yield of 29.3% for Pt/BEA-SDA3-12 is much higher than the

corresponding yield of 14.6% for Pt/BEA-12-Con. The work of Astafan *et al.* showed that the maximum yield of isomer can be correlated to the BEA zeolite crystal size.<sup>90</sup> Reducing the zeolite crystal size reduces the residence time of olefinic intermediates within the zeolite domains and, therefore, limits consecutive reactions.<sup>9</sup> As the activity comparison excludes diffusion limitations, it is more likely that the selectivity is improved by the larger external surface, which benefits the desorption of intermediate olefins from the zeolite domains.<sup>10, 91</sup> Thus, the higher yield of isomers over Pt/BEA-SDA2-12 can be explained by the smaller crystal size. The beneficial effect of nanosizing BEA zeolite is also clear from the more symmetric cracked product distribution for Pt/BEA-SDA2-12 (Figure B15).

### 3.4 Conclusions

This work describes the facile and economical synthesis of nanosized MOR and BEA zeolites by using simple bromide-form diquatary ammonium compound as the sole organic template. The specific formation of MOR or BEA zeolites strongly depends on the size, geometry, and structural rigidity of organic templates. SDA2 and SDA6 give MOR zeolites, while SDA3-5 give BEA zeolites. The optimized nanosized zeolites are MOR-SDA2-12 (Si/Al = 9.2, 20-50 nm) and BEA-SDA3-12 (Si/Al = 11.7, 15-30 nm). While bulk MOR-12-Con (> 100 nm) can be obtained within 24 h from a completely inorganic gel, the strong interaction between organic templates and aluminosilicate precursors results in an extended induction period (~48 h) for SDA2 and SDA3, effectively decreasing the aluminosilicate precursor size below 50 nm. MOR-12-Con and MOR-SDA2-12 display a similar crystal growth behavior, *viz.* a quick crystal growth (~6 h) via reorganization in the solid state. Specific strong framework stabilization by the pore-filling template molecules is decisive for the final zeolite topology. Despite their lower acidity, nanocrystalline MOR-SDA2-12 and BEA-SDA3-12 are more active than their corresponding bulk counterparts in the alkylation of benzene with benzyl alcohol and the acylation of anisole with acetic anhydride, respectively, due to the enhanced mass transport ability and better accessibility of the Brønsted acid sites. In hydroconversion of *n*-C<sub>16</sub>, Pt/BEA-SDA3-12 shows much higher isomer yield than Pt/BEA-12-Con, which is explained by shorter residence times of olefinic intermediates in the smaller zeolite crystals. Overall, this work not only shows a facile route to synthesize nanosized MOR and BEA zeolites with excellent catalytic performance by using simple organic molecules, but also provides better insight into the crystallization behavior.

### 3.5 References

1. J. Li, A. Corma and J. Yu, *Chem. Soc. Rev.*, 2015, **44**, 7112-7127.
2. N. Kosinov, J. Gascon, F. Kapteijn and E. J. M. Hensen, *J. Membr. Sci.*, 2016, **499**, 65-79.
3. J. Přečh, P. Pizarro, D. P. Serrano and J. Čejka, *Chem. Soc. Rev.*, 2018, **47**, 8263-8306.
4. D. Kerstens, B. Smeyers, J. Van Waeyenberg, Q. Zhang, J. Yu and B. F. Sels, *Adv. Mater.*, 2020, **32**, 2004690.
5. X.-Y. Yang, L.-H. Chen, Y. Li, J. C. Rooke, C. Sanchez and B.-L. Su, *Chem. Soc. Rev.*, 2017, **46**, 481-558.
6. S. Mintova, J.-P. Gilson and V. Valtchev, *Nanoscale*, 2013, **5**, 6693-6703.
7. L.-H. Chen, M.-H. Sun, Z. Wang, W. Yang, Z. Xie and B.-L. Su, *Chem. Rev.*, 2020, **120**, 11194-11294.
8. S. Mintova, M. Jaber and V. Valtchev, *Chem. Soc. Rev.*, 2015, **44**, 7207-7233.
9. L. Meng, G. Vanbutsele, R. Pestman, A. Godin, D. E. Romero, A. J. van Hoof, L. Gao, T. F. Kimpel, J. Chai, J. A. Martens and E. J. M. Hensen, *J. Catal.*, 2020, **389**, 544-555.
10. T. Blasco, A. Chica, A. Corma, W. J. Murphy, J. Agúndez-Rodríguez and J. Pérez-Pariente, *J. Catal.*, 2006, **242**, 153-161.
11. J. Wang, S. Xu, J. Li, Y. Zhi, M. Zhang, Y. He, Y. Wei, X. Guo and Z. Liu, *RSC Adv.*, 2015, **5**, 88928-88935.
12. A. Corma, U. Diaz, M. E. Domine and V. Fornés, *Angew. Chem. Int. Ed.*, 2000, **39**, 1499-1501.
13. A. Corma, V. Fornes, S. Pergher, T. L. Maesen and J. Buglass, *Nature*, 1998, **396**, 353-356.
14. K. Na, M. Choi and R. Ryoo, *Microporous Mesoporous Mater.*, 2013, **166**, 3-19.
15. Z. Chen, Z. Li, Y. Zhang, D. Chevella, G. Li, Y. Chen, X. Guo, J. Liu and J. Yu, *Chem. Eng. J.*, 2020, **388**, 124322.
16. B. O. Hincapie, L. J. Garces, Q. Zhang, A. Sacco and S. L. Suib, *Microporous Mesoporous Mater.*, 2004, **67**, 19-26.
17. M. Ansari, A. Aroujalian, A. Raisi, B. Dabir and M. Fathizadeh, *Adv. Powder Technol.*, 2014, **25**, 722-727.
18. A. Sakthivel, A. Iida, K. Komura, Y. Sugi and K. V. R. Chary, *Microporous Mesoporous Mater.*, 2009, **119**, 322-330.
19. G. Zhang, Y. Fan, J. Huang, L. Wang, C. Yang, M. Lyu, H. Liu and Y. Ma, *Dalton Trans.*, 2020, **49**, 7258-7266.

20. C. J. Van Oers, K. Góra-Marek, K. Sadowska, M. Mertens, V. Meynen, J. Datka and P. Cool, *Chem. Eng. J.*, 2014, **237**, 372-379.
21. M. H. Sun, L. H. Chen, S. Yu, Y. Li, X. G. Zhou, Z. Y. Hu, Y. H. Sun, Y. Xu and B. L. Su, *Angew. Chem. Int. Ed.*, 2020, **59**, 19582-19591.
22. C. Jo, J. Jung, H. S. Shin, J. Kim and R. Ryoo, *Angew. Chem. Int. Ed.*, 2013, **52**, 10014-10017.
23. H. Zhu, Z. Liu, D. Kong, Y. Wang and Z. Xie, *J. Phys. Chem. C*, 2008, **112**, 17257-17264.
24. T. Xue, S. Li and H. Wu, *Microporous Mesoporous Mater.*, 2021, **312**, 110748.
25. W. Kim, J.-C. Kim, J. Kim, Y. Seo and R. Ryoo, *ACS Catal.*, 2013, **3**, 192-195.
26. M. Choi, K. Na, J. Kim, Y. Sakamoto, O. Terasaki and R. J. N. Ryoo, *Nature*, 2009, **461**, 246-249.
27. W. Schwieger, A. G. Machoke, T. Weissenberger, A. Inayat, T. Selvam, M. Klumpp and A. Inayat, *Chem. Soc. Rev.*, 2016, **45**, 3353-3376.
28. Y. Xu, X. Shen, C. Peng, Y. Ma, L. Han, P. Wu, H. Peng and S. Che, *Sci. China Mater.*, 2018, **61**, 1185-1190.
29. L. Ding and Y. Zheng, *Microporous Mesoporous Mater.*, 2007, **103**, 94-101.
30. E. M. Gallego-Sánchez, C. Li, C. Paris, N. Martín-García, J. Martínez-Triguero, M. Boronat Zaragoza, M. Moliner Marin and A. J. C.-A. E. J. Corma Canós, *Chem. Eur. J.*, 2018, **24**, 14631-14635.
31. X. Zhang, D. Liu, D. Xu, S. Asahina, K. A. Cychosz, K. V. Agrawal, Y. Al Wahedi, A. Bhan, S. Al Hashimi and O. J. S. Terasaki, *Science*, 2012, **336**, 1684-1687.
32. E. M. Gallego, C. Paris, M. R. Díaz-Rey, M. E. Martínez-Armero, J. Martínez-Triguero, C. Martínez, M. Moliner and A. Corma, *Chem. Sci.*, 2017, **8**, 8138-8149.
33. X. Jia, Y. Zhang, Z. Gong, B. Wang, Z. Zhu, J. Jiang, H. Xu, H. Sun, L. Han, P. Wu and S. Che, *J. Phys. Chem. C*, 2018, **122**, 9117-9126.
34. Y. Zhao, Z. Ye, L. Wang, H. Zhang, F. Xue, S. Xie, X.-M. Cao, Y. Zhang and Y. Tang, *Cryst. Growth Des.*, 2018, **18**, 1101-1108.
35. A. Molino, K. A. Łukaszuk, D. Rojo-Gama, K. P. Lillerud, U. Olsbye, S. Bordiga, S. Svelle and P. Beato, *Chem. Commun.*, 2017, **53**, 6816-6819.
36. S. H. Keoh, W. Chaikittisilp, K. Muraoka, R. R. Mukti, A. Shimojima, P. Kumar, M. Tsapatsis and T. Okubo, *Chem. Mater.*, 2016, **28**, 8997-9007.
37. A. Jackowski, S. I. Zones, S.-J. Hwang and A. W. Burton, *J. Am. Chem. Soc.*, 2009, **131**, 1092-1100.
38. X. Hong, W. Chen, G. Zhang, Q. Wu, C. Lei, Q. Zhu, X. Meng, S. Han, A. Zheng, Y. Ma, A.-N. Parvulescu, U. Müller, W. Zhang, T. Yokoi, X. Bao, B. Marler, D. E. De Vos, U. Kolb and F.-S. Xiao, *J. Am. Chem. Soc.*, 2019, **141**, 18318-18324.

39. M. Moliner, F. Rey and A. Corma, *Angew. Chem. Int. Ed.*, 2013, **52**, 13880-13889.
40. S. B. Hong, *Catal. Surv. Asia*, 2008, **12**, 131-144.
41. H. Xue, X. Huang, E. Ditzel, E. Zhan, M. Ma and W. Shen, *Ind. Eng. Chem. Res.*, 2013, **52**, 11510-11515.
42. S. Inagaki, Y. Watanabe, Y. Nishita and Y. Kubota, *Chem. Lett.*, 2013, **42**, 186-188.
43. K. Na, M. Choi and R. Ryoo, *J. Mater. Chem.*, 2009, **19**, 6713-6719.
44. K. Zhang, Z. Liu, X. Yan, X. Hao, M. Wang, C. Li and H. Xi, *Langmuir*, 2017, **33**, 14396-14404.
45. R. Martínez-Franco, C. Paris, M. E. Martínez-Armero, C. Martínez, M. Moliner and A. Corma, *Chem. Sci.*, 2016, **7**, 102-108.
46. R. Kore and R. Srivastava, *RSC Adv.*, 2012, **2**, 10072-10084.
47. J. Zhang, P. Cao, H. Yan, Z. Wu and T. Dou, *Chem. Eng. J.*, 2016, **291**, 82-93.
48. L. Zhang, A. N. C. v. Laak, P. E. de Jongh and K. P. de Jong, *Microporous Mesoporous Mater.*, 2009, **126**, 115-124.
49. R. Kore, B. Satpati and R. Srivastava, *Chem. Eur. J.*, 2011, **17**, 14360-14365.
50. A. Bolshakov, D. E. Romero Hidalgo, A. J. F. van Hoof, N. Kosinov and E. J. M. Hensen, *ChemCatChem*, 2019, **11**, 2803-2811.
51. Y. Yuan, L. Wang, H. Liu, P. Tian, M. Yang, S. Xu and Z. Liu, *Chin. J. Catal.*, 2015, **36**, 1910-1919.
52. J. Zhang, L. Wang, G. Wang, F. Chen, J. Zhu, C. Wang, C. Bian, S. Pan and F.-S. Xiao, *ACS Sustainable Chem. Eng.*, 2017, **5**, 3123-3131.
53. S. Storck, H. Bretinger and W. F. Maier, *Appl. Catal. A*, 1998, **174**, 137-146.
54. L. Meng, X. Zhu, W. Wannapakdee, R. Pestman, M. G. Goesten, L. Gao, A. J. F. van Hoof and E. J. M. Hensen, *J. Catal.*, 2018, **361**, 135-142.
55. K. Zhang, S. Luo, Z. Liu, C. Li, Z. Ke, X. Yan, Y. Wu and H. Xi, *Chem. Eur. J.*, 2018, **24**, 8133-8140.
56. M. Pan, J. Zheng, Y. Ou, Q. Wang, L. Zhang and R. Li, *Microporous Mesoporous Mater.*, 2021, **316**, 110983.
57. T. I. Korányi and J. B. Nagy, *J. Phys. Chem. B*, 2005, **109**, 15791-15797.
58. T. Ikuno, W. Chaikittisilp, Z. Liu, T. Iida, Y. Yanaba, T. Yoshikawa, S. Kohara, T. Wakihara and T. Okubo, *J. Am. Chem. Soc.*, 2015, **137**, 14533-14544.
59. W. Gao, C. C. Amoo, G. Zhang, M. Javed, B. Mazonde, C. Lu, R. Yang, C. Xing and N. Tsubaki, *Microporous Mesoporous Mater.*, 2019, **280**, 187-194.
60. S. Inagaki, K. Nakatsuyama, Y. Saka, E. Kikuchi, S. Kohara and M. Matsukata, *J. Phys. Chem. C*, 2007, **111**, 10285-10293.
61. J. Twu, P. K. Dutta and C. T. Kresge, *J. Phys. Chem.*, 1991, **95**, 5267-5271.

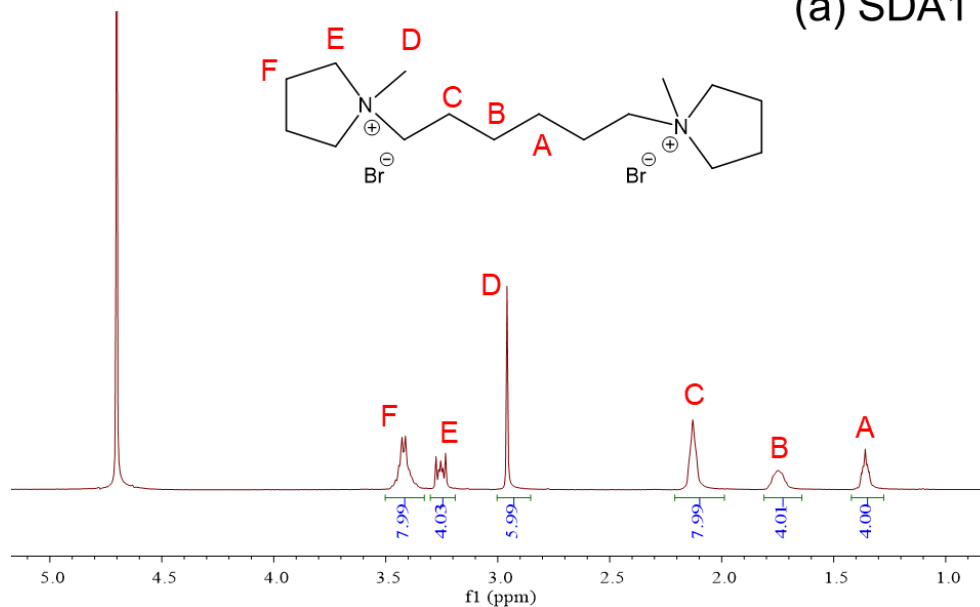
62. X. Zhu, M. G. Goesten, A. J. J. Koekkoek, B. Mezari, N. Kosinov, G. Filonenko, H. Friedrich, R. Rohling, B. M. Szyja, J. Gascon, F. Kapteijn and E. J. M. Hensen, *Chem. Sci.*, 2016, **7**, 6506-6513.
63. P. Van Geem, K. Scholle and G. Van der Velden, *J. Phys. Chem.*, 1988, **92**, 1585-1589.
64. M. Cui, L. Wang, Y. Zhang, Y. Wang and C. Meng, *Microporous Mesoporous Mater.*, 2015, **206**, 52-57.
65. D. Zhao, W. Chu, Y. Wang, X. Zhu, X. Li, S. Xie, J. An, W. Xin, S. Liu and L. Xu, *J. Mater. Chem. A*, 2018, **6**, 24614-24624.
66. K. Na, C. Jo, J. Kim, K. Cho, J. Jung, Y. Seo, R. J. Messinger, B. F. Chmelka and R. Ryoo, *Science*, 2011, **333**, 328-332.
67. K. Lu, J. Huang, L. Ren, C. Li, Y. Guan, B. Hu, H. Xu, J. Jiang, Y. Ma and P. Wu, *Angew. Chem. Int. Ed.*, 2020, **59**, 6258-6262.
68. M. Kumar, Z. J. Berkson, R. J. Clark, Y. Shen, N. A. Prisco, Q. Zheng, Z. Zeng, H. Zheng, L. B. McCusker, J. C. Palmer, B. F. Chmelka and J. D. Rimer, *J. Am. Chem. Soc.*, 2019, **141**, 20155-20165.
69. H.-M. Kao, C.-Y. Yu and M.-C. Yeh, *Microporous Mesoporous Mater.*, 2002, **53**, 1-12.
70. R. Hajjar, Y. Millot, P. P. Man, M. Che and S. Dzwigaj, *J. Phys. Chem. C*, 2008, **112**, 20167-20175.
71. X. Wang, R. Li, C. Yu, Y. Liu, L. Liu, C. Xu, H. Zhou and C. Lu, *Ind. Eng. Chem. Res.*, 2019, **58**, 18065-18072.
72. S. H. Meixia Wang, Jing Lü, Zaizhe Cheng, Ying Li, Shengping Wang, Xinbin Ma, *Chin. J. Catal.*, 2016, **37**, 1530-1538.
73. Y. Li, M. Yu, K. Cai, M. Wang, J. Lv, R. F. Howe, S. Huang and X. Ma, *Phys. Chem. Chem. Phys.*, 2020, **22**, 11374-11381.
74. Z. Cheng, S. Huang, Y. Li, K. Cai, Y. Wang, M.-y. Wang, J. Lv and X. Ma, *ACS Catal.*, 2021, **11**, 5647-5657.
75. A. Bhan, A. D. Allian, G. J. Sunley, D. J. Law and E. Iglesia, *J. Am. Chem. Soc.*, 2007, **129**, 4919-4924.
76. M.-N. Liu, Z.-X. Xie, Q.-X. Luo, J. Zhang, H. Chen, L. Xu, M. Sun, X. Ma and Q.-Q. Hao, *Ind. Eng. Chem. Res.*, 2022, **61**, 1078-1088.
77. N. Cherkasov, T. Vazhnova and D. B. Lukyanov, *Vib. Spectrosc.*, 2016, **83**, 170-179.
78. G. Sartori and R. Maggi, *Chem. Rev.*, 2006, **106**, 1077-1104.
79. E. G. Derouane, I. Schmidt, H. Lachas and C. J. H. Christensen, *Catal. Lett.*, 2004, **95**, 13-17.
80. W. Wang, C.-J. Liu and W. Wu, *Catal. Sci. Technol.*, 2019, **9**, 4162-4187.



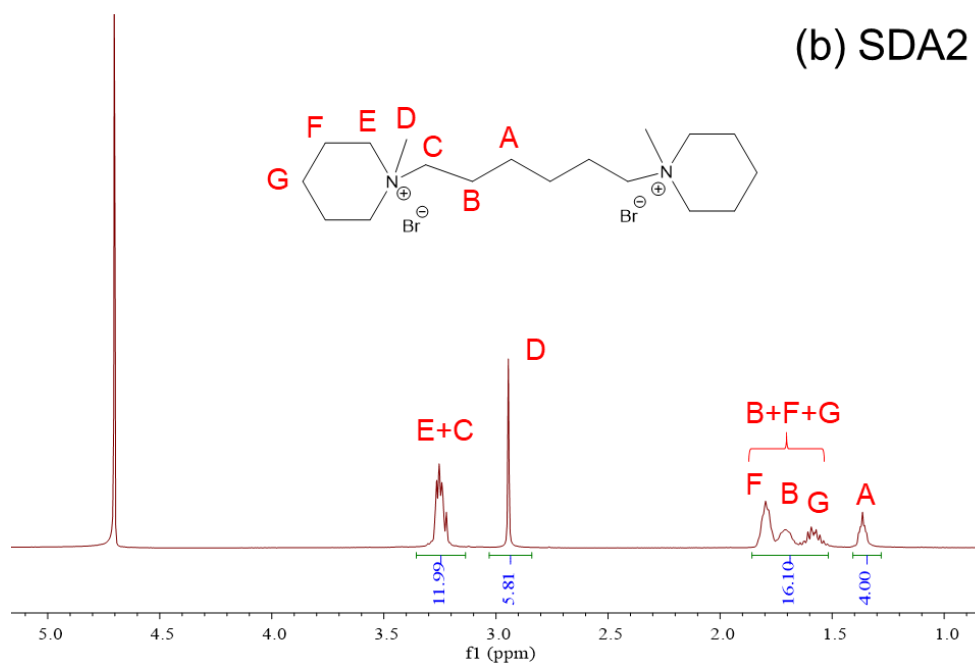
81. J. Weitkamp, *ChemCatChem*, 2012, **4**, 292-306.
82. K. Leng, Y. Wang, C. Hou, C. Lancelot, C. Lamonier, A. Rives and Y. J. J. o. c. Sun, *J. Catal.*, 2013, **306**, 100-108.
83. Y. Li, C. Sun, W. Fan, Y. Wang, A. Lan, P. Han, X. Li and T. Dou, *J. Mater. Sci.*, 2015, **50**, 5059-5067.
84. M. Guidotti, C. Canaff, J.-M. Coustard, P. Magnoux and M. Guisnet, *J. Catal.*, 2005, **230**, 375-383.
85. U. Freese, F. Heinrich and F. Roessner, *Catal. Today*, 1999, **49**, 237-244.
86. E. G. Derouane, C. J. Dillon, D. Bethell and S. B. Derouane-Abd Hamid, *J. Catal.*, 1999, **187**, 209-218.
87. G. Huang, P. Ji, H. Xu, J.-G. Jiang, L. Chen and P. Wu, *Microporous Mesoporous Mater.*, 2017, **248**, 30-39.
88. E. J. M. Hensen, D. G. Poduval, V. Degirmenci, D. A. J. M. Ligthart, W. Chen, F. Maugé, M. S. Rigutto and J. A. R. v. Veen, *J. Phys. Chem. C*, 2012, **116**, 21416-21429.
89. H. Sammoury, J. Toufaily, K. Cherry, Y. Pouilloux, T. Hamieh and L. Pinard, *Catal. Lett.*, 2018, **148**, 3051-3061.
90. A. Astafan, Y. Pouilloux, J. Patarin, N. Bats, C. Bouchy, T. Jean Daou and L. Pinard, *New J. Chem.*, 2016, **40**, 4335-4343.
91. J. Zecevic, G. Vanbutsele, K. P. de Jong and J. A. Martens, *Nature*, 2015, **528**, 245-248.

# Appendix B

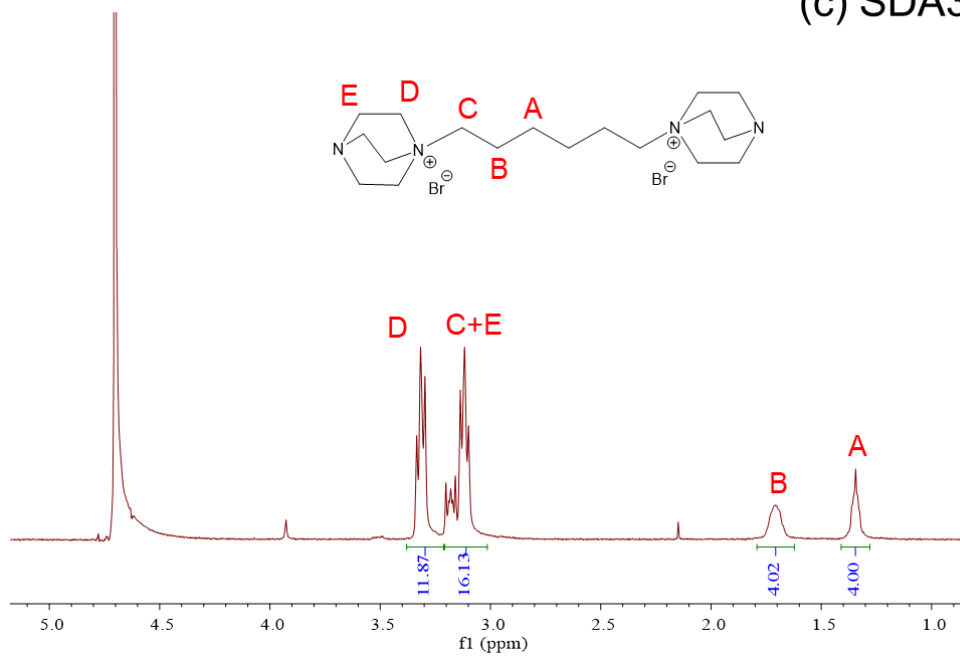
(a) SDA1



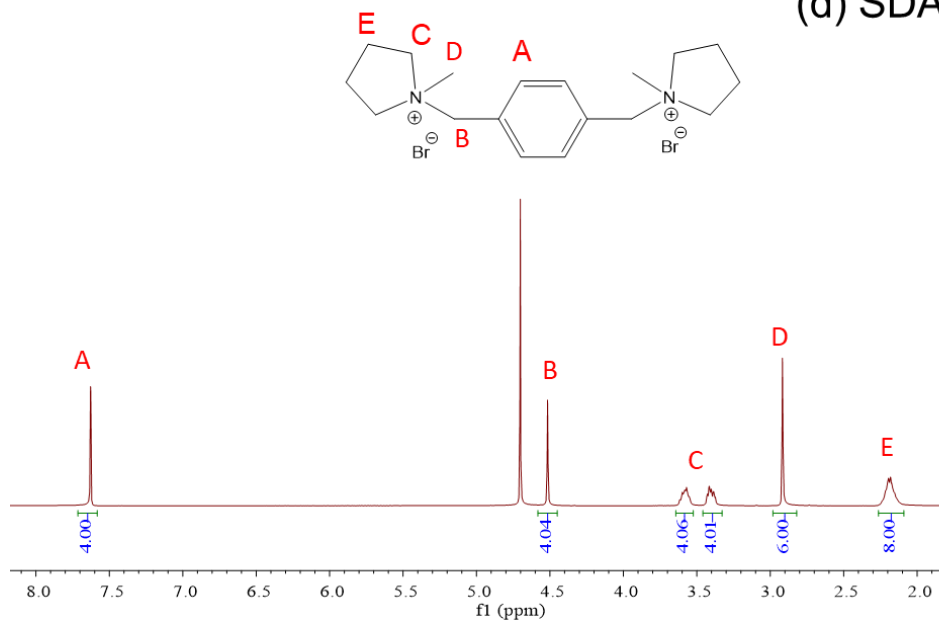
(b) SDA2



(c) SDA3



(d) SDA4



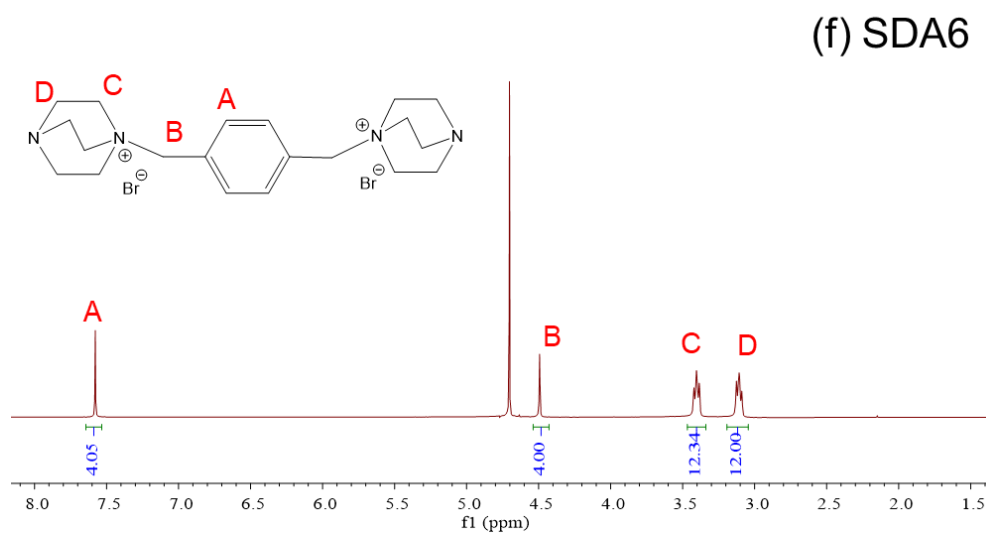
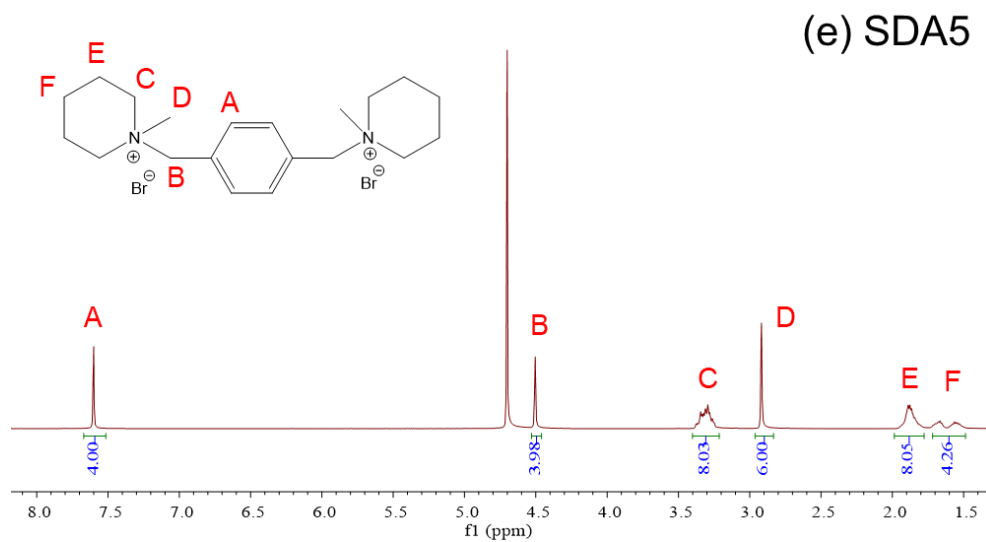


**Figure B1.** Liquid-state  $^1\text{H}$  NMR spectra of organic structure-directing agents (SDA) used in this work.

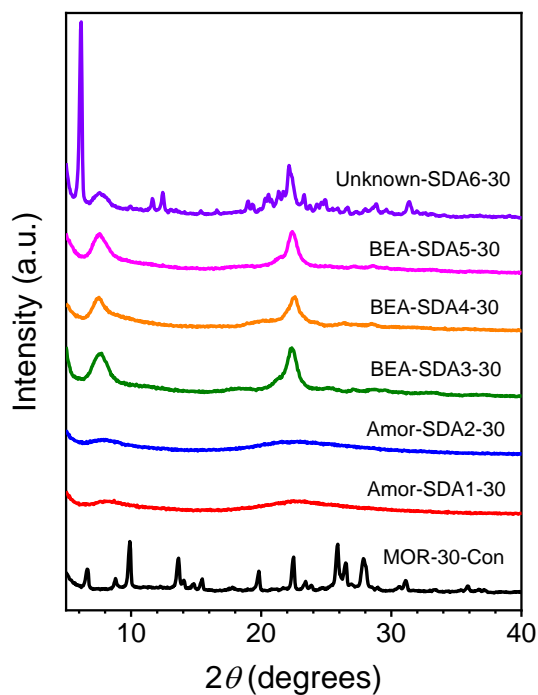


**Figure B2.** XRD patterns of samples synthesized using the templates shown in Figure 3.1 (recipe: Si/Al = 30).

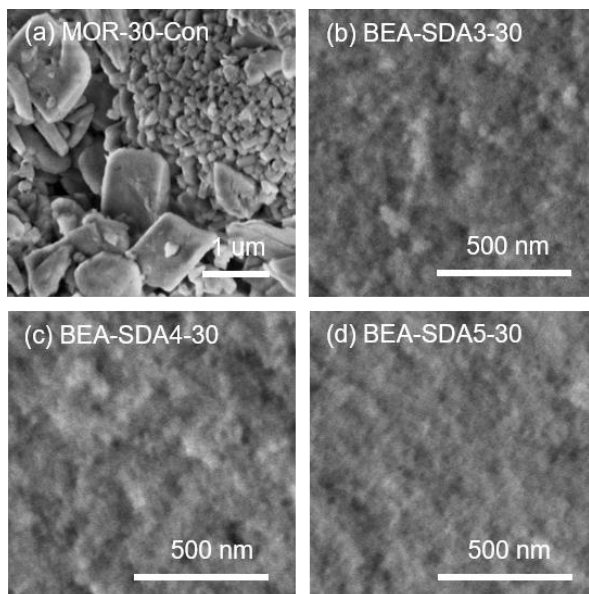


**Figure B3.** SEM images of calcined zeolites (recipe: Si/Al=30).

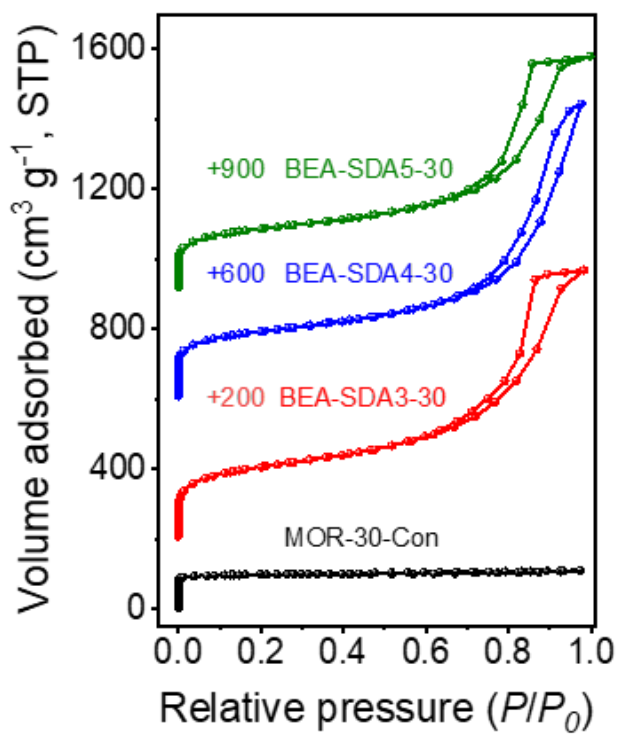


**Figure B4.** Ar physisorption isotherms of calcined zeolites (recipe: Si/Al=30).

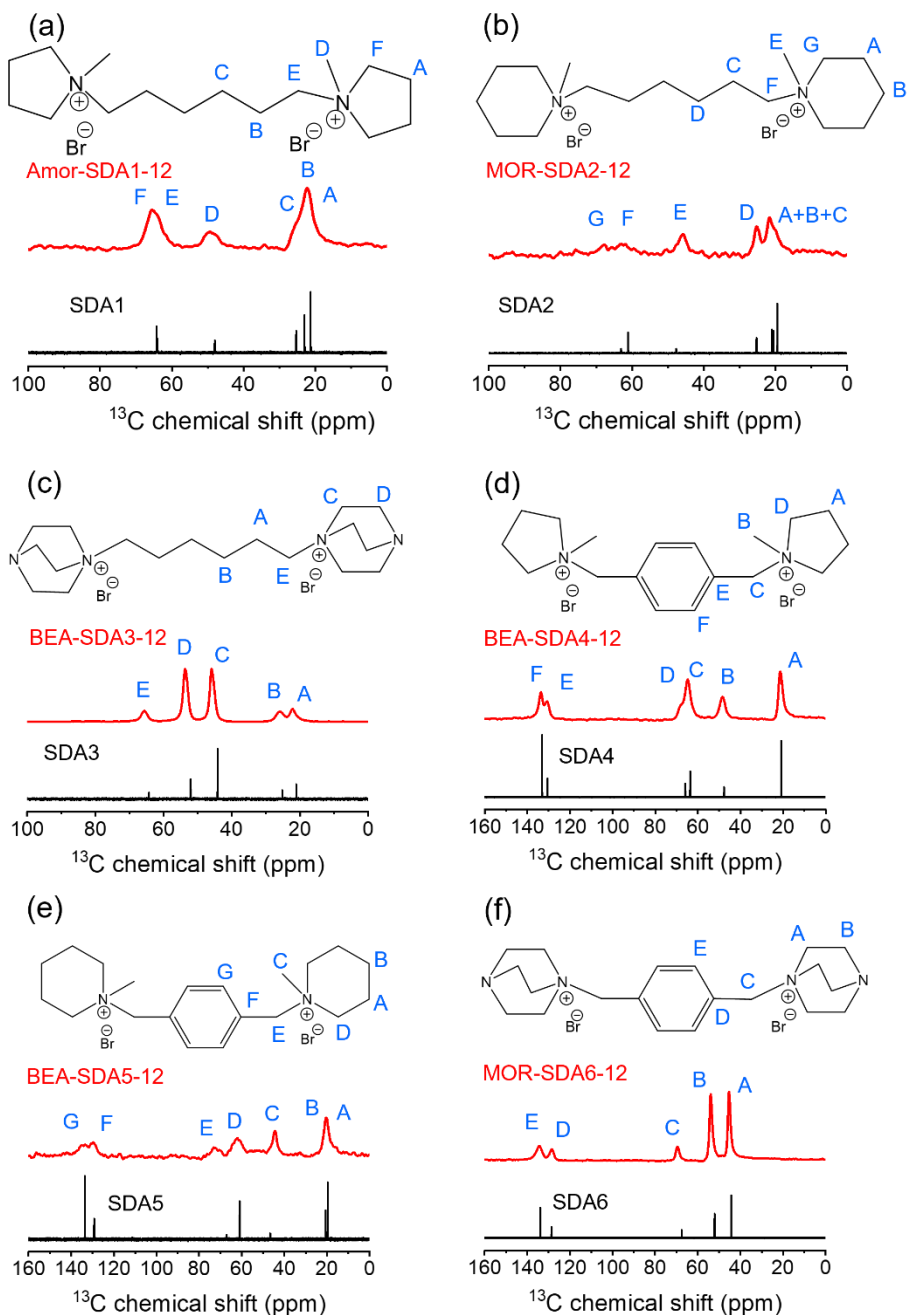


**Figure B5.** Liquid-state  $^{13}\text{C}$  NMR spectra (red line) of SDA in  $\text{D}_2\text{O}$  solution: (a) SDA1, (b) SDA2, (c) SDA3, (d) SDA4, (e) SDA5 and (f) SDA6; Solid-state  $^1\text{H}$ - $^{13}\text{C}$  CPMAS NMR spectra (black line) of as-prepared samples: (a) Amor-SDA1-12; (b) MOR-SDA2-12; (c) BEA-SDA3-12; (d) BEA-SDA4-12; (e) BEA-SDA5-12 and (f) MOR-SDA6-12.

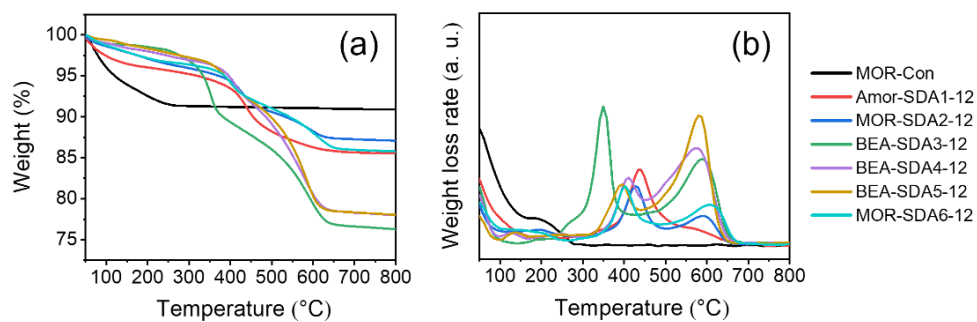


**Figure B6.** (a) TG and (b) DTG of as-prepared samples.

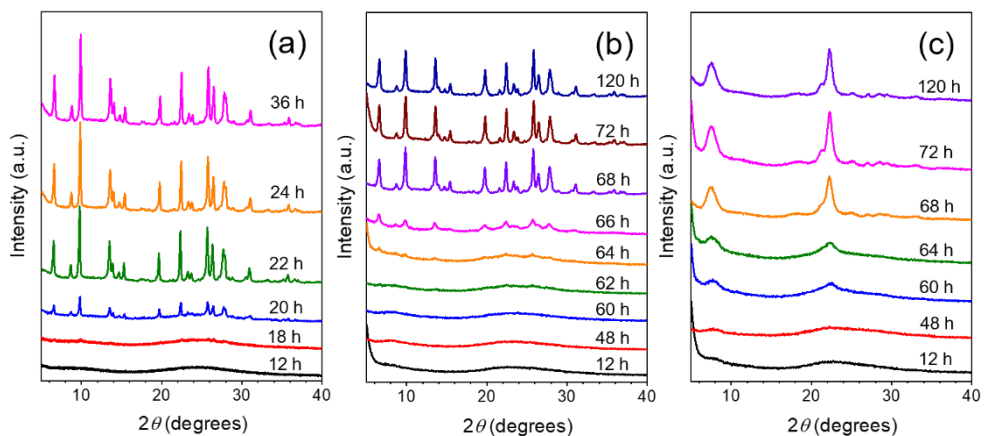


**Figure B7.** XRD patterns of solid samples obtained at different crystallization times: (a) MOR-12-Con, (b) MOR-SDA2-12 and (c) BEA-SDA3-12.



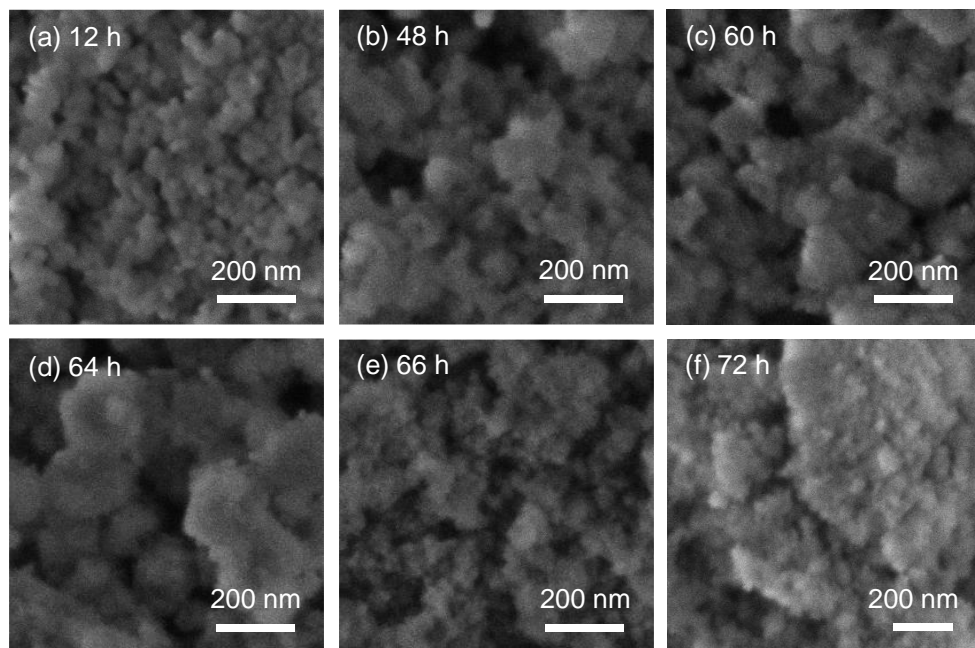


**Figure B8.** SEM images of solid samples obtained at different crystallization times of BEA-SDA3-12.

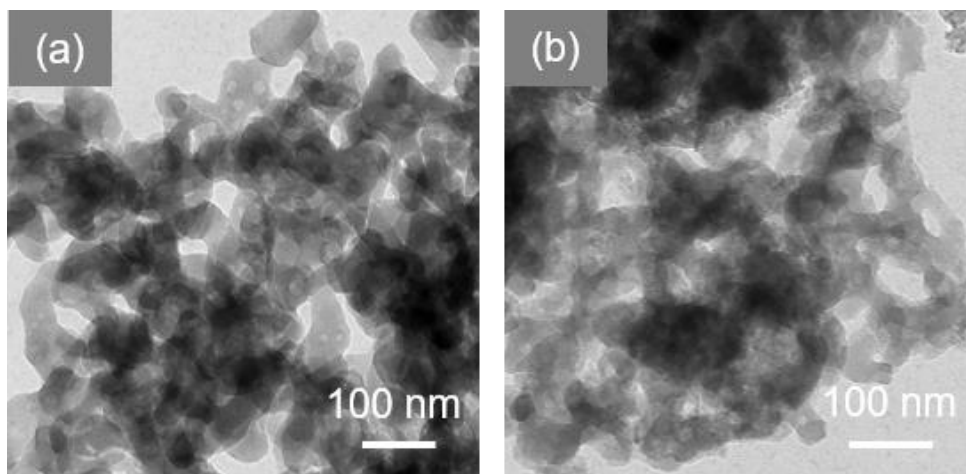


**Figure B9.** TEM images of solid products: (a) MOR-SDA2-12-(48 h) and (b) BEA-SDA3-12-(48 h).

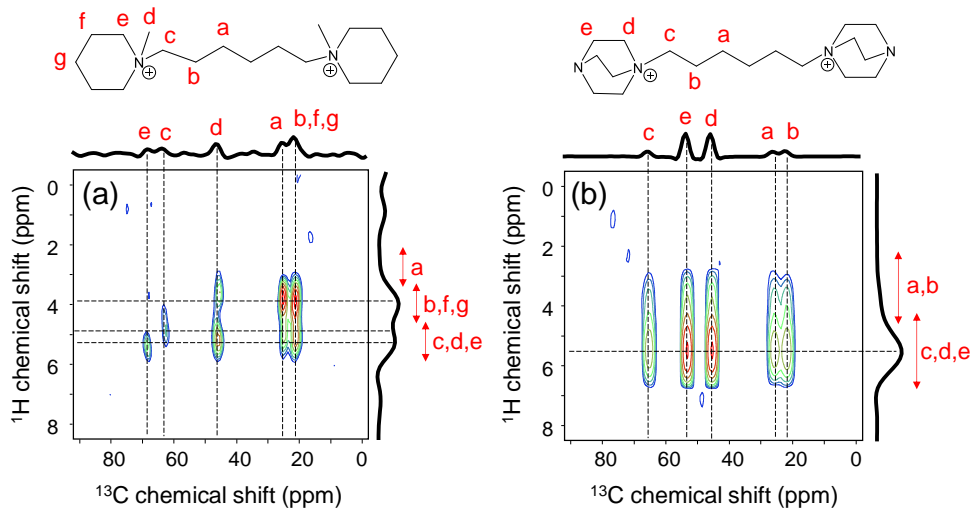


**Figure B10.**  $^1\text{H}$ - $^{13}\text{C}$  HETCOR NMR spectra of as-prepared zeolites: (a) MOR-SDA2-12 and (b) BEA-SDA3-12 (assignment to different H atoms in SDA in top panels).

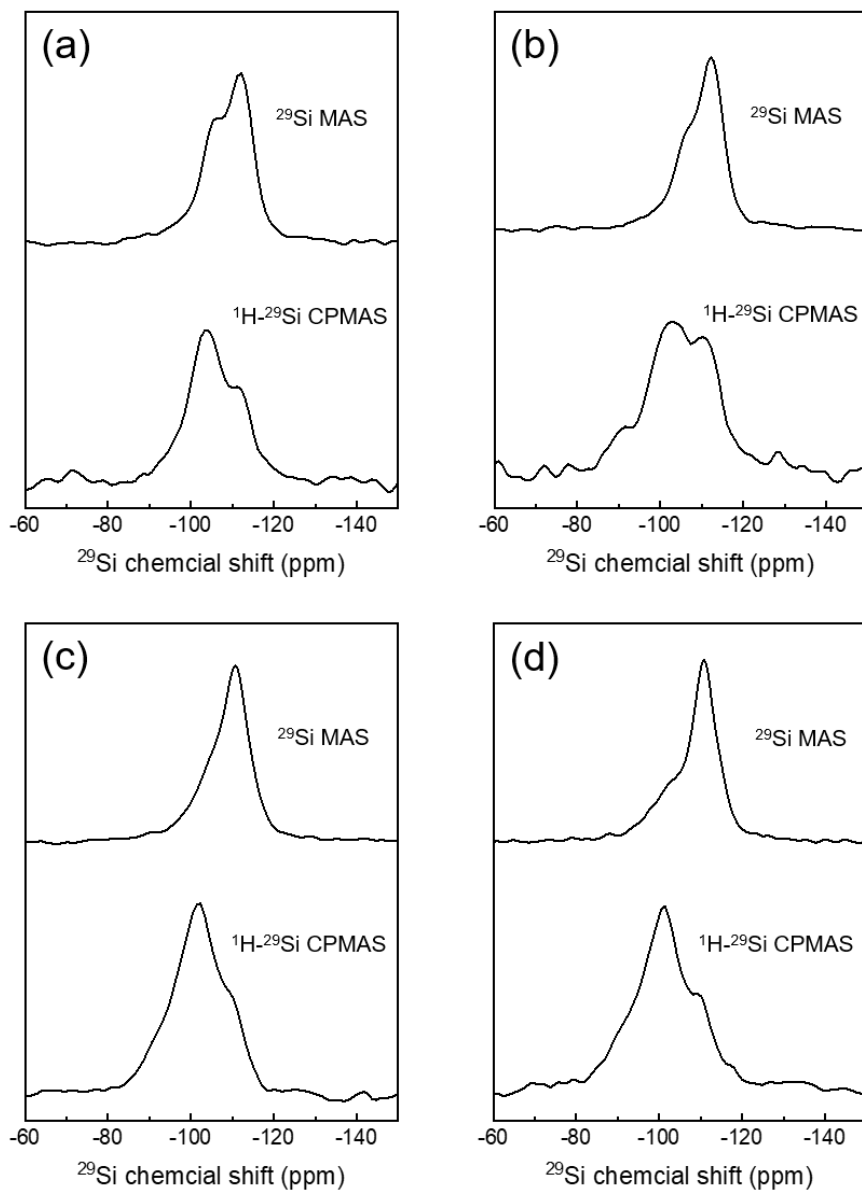


**Figure B11.**  $^{29}\text{Si}$  MAS NMR and  $^1\text{H}$ - $^{29}\text{Si}$  CPMAS spectra of the calcined zeolites: (a) MOR-12-Con, (b) MOR-SDA2-12, (c) BEA-12-Con and (d) BEA-SDA3-12.

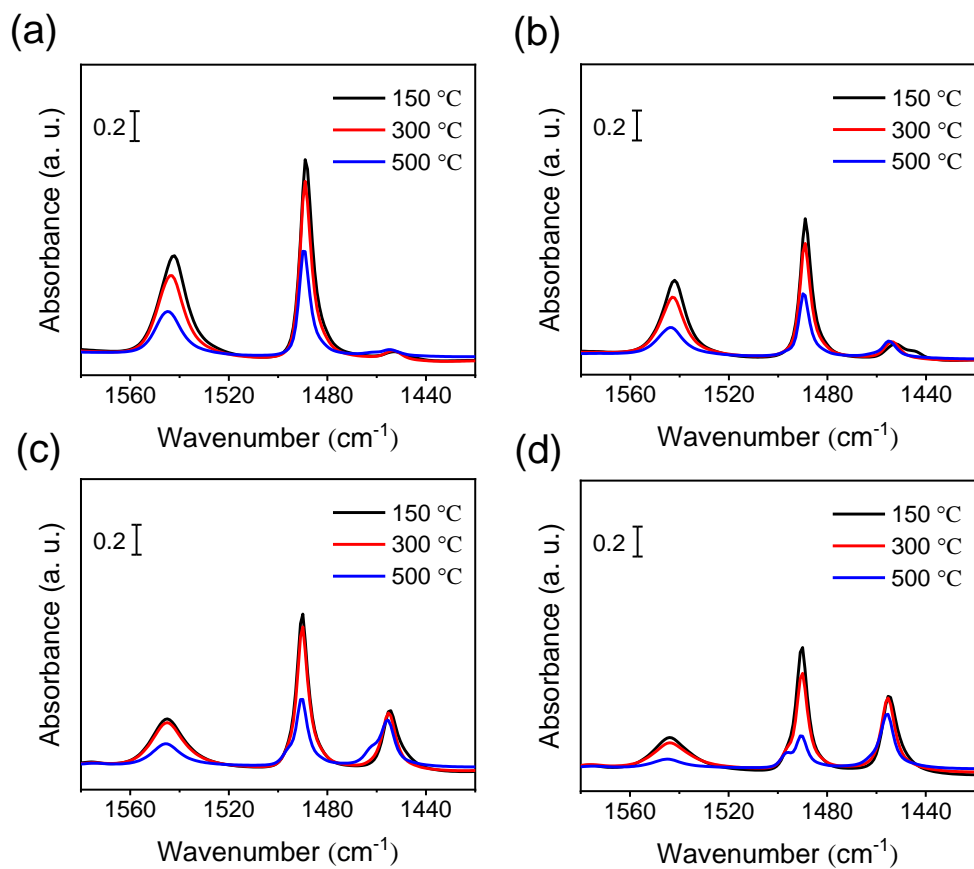


**Figure B12.** IR spectra of pyridine adsorbed on zeolites: (a) MOR-12-Con, (b) MOR-SDA2-12, (c) BEA-12-Con and (d) BEA-SDA3-12.

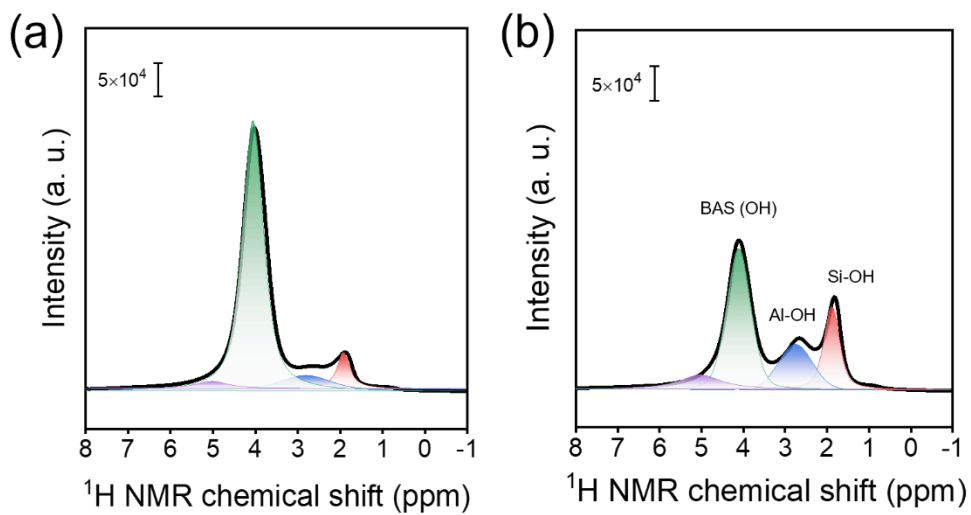


**Figure B13.**  $^1\text{H}$  NMR spectra of dehydrated samples: (a) MOR-12-Con and (b) MOR-SDA2-12.

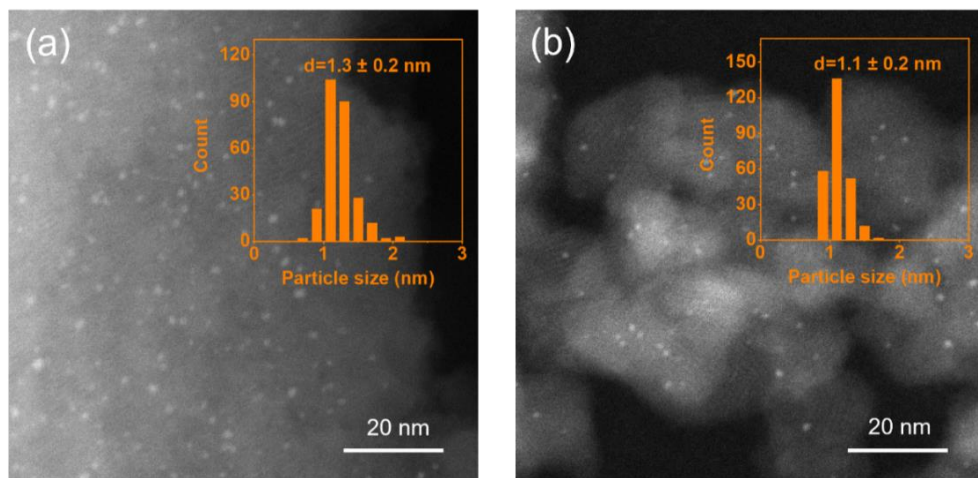


**Figure B14.** ADF-STEM images of reduced samples: (a) Pt/BEA-12-Con and (b) Pt/BEA-SDA3-12.

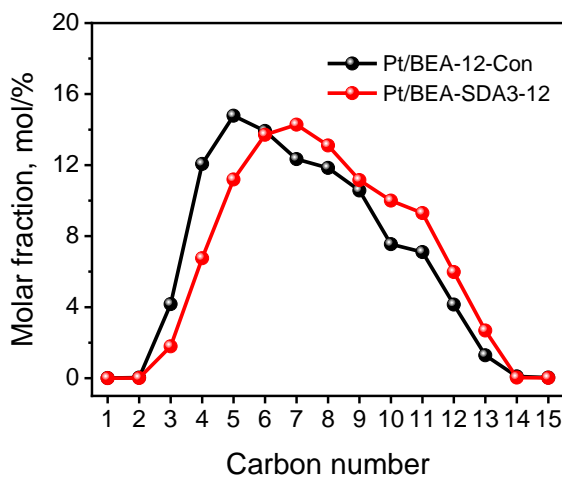


**Figure B15.** The distribution of cracked products at ca. 50% n-C<sub>16</sub> conversion.

**Table B1.** Prices of chemicals used for organic template synthesis.

Chemical	Supplier	Price
1,6-dibromohexane	TCI, > 97.0%	52.00 €/500 g
$\alpha,\alpha'$ -dibromo- <i>p</i> -xylene	TCI, > 98.0%	64.00 €/25 g
N-methylpyrrolidine	TCI, > 98.0%	80.00 €/500 ml
N-methylpiperidine	TCI, > 99.0%	90.00 €/500 ml
1,4-diazabicyclo[2.2.2]octane	TCI, > 98.0%	91.00 €/500 g

**Table B2.** Solid yields and Si/Al ratios of zeolite samples obtained at a Si/Al gel ratio of 12.

Zeolite	Si/Al	Yield (%) <sup>a</sup>
MOR-12-Con	8.4	69.9
MOR-SDA2-12	9.2	76.6
MOR-SDA6-12	9.8	81.1
BEA-SDA3-12	11.7	75.3
BEA-SDA4-12	11.9	60.3
BEA-SDA5-12	12.0	64.1
BEA-12-Con	11.3	59.7

<sup>a</sup> Based on the inorganic sources introduced in the initial gel.

**Table B3.** Solid yields and Si/Al ratios of zeolite samples obtained at a Si/Al gel ratio of 30.

Zeolite	Si/Al	Yield (%) <sup>a</sup>
MOR-30-Con	13.4	43.4
BEA-SDA3-12	14.3	35.1
BEA-SDA4-12	15.8	51.4
BEA-SDA5-12	14.9	41.7

<sup>a</sup> Based on the inorganic sources introduced in the initial gel.

**Table B4.** Textural properties of calcined zeolites determined by Ar physisorption.

Zeolite	$S_{\text{BET}}$ ( $\text{m}^2 \text{g}^{-1}$ )	$V_{\text{tot}}$ ( $\text{cm}^3 \text{g}^{-1}$ )	$V_{\text{meso}}$ ( $\text{cm}^3 \text{g}^{-1}$ ) ( <i>BJH</i> )	$V_{\text{micro}}$ ( $\text{cm}^3 \text{g}^{-1}$ ) ( <i>t-plot</i> )	$S_{\text{ext}}$ ( $\text{m}^2 \text{g}^{-1}$ ) ( <i>t-plot</i> )
MOR-30-Con	303	0.14	0.02	0.12	37
BEA-SDA3-30	648	0.98	0.79	0.10	370
BEA-SDA4-30	604	1.08	0.90	0.11	313
BEA-SDA5-30	549	0.85	0.69	0.10	295

**Table B5.** Changes in the solid yield and chemical compositions along with the synthesis time for MOR-12-Con.

Synthesis time (h)	Solid yield (wt %) <sup>a</sup>	Si/Al
12	77.3	9.0
18	77.1	9.1
20	75.0	8.8
24	69.9	8.4

<sup>a</sup> Based on the inorganic sources introduced in the initial gel.

**Table B6.** Changes in the solid yield and chemical compositions along with the synthesis time for MOR-SDA2-12.

Synthesis time (h)	Solid yield (wt %) <sup>a</sup>	Si/Al	Organic content (wt %)
12	75.1	9.1	8.7
60	74.7	9.2	9.2
66	76.0	9.1	9.6
72	76.6	9.2	9.1

<sup>a</sup> Based on the inorganic sources introduced in the initial gel.

**Table B7.** Changes in the solid yield and chemical compositions along with the synthesis time for BEA-SDA3-12.

Synthesis time (h)	Solid yield (wt %) <sup>a</sup>	Si/Al	Organic content (wt %)
12	76.2	9.2	11.8
48	78.2	9.4	12.3
60	79.5	10.1	15.4
72	75.3	11.7	21.5

<sup>a</sup> Based on the inorganic sources introduced in the initial gel.

**Table B8.** Al and Si distributions of the proton form zeolites.

Zeolite	<sup>27</sup> Al NMR <sup>a</sup>		<sup>29</sup> Si NMR			Si/Al <sub>F</sub> <sup>b</sup>
	Al <sup>IV</sup>	Al <sup>VI</sup>	Q <sup>4</sup> (2Al) and Q <sup>3</sup> (0Al)	Q <sup>4</sup> (1Al)	Q <sup>4</sup> (0Al)	
MOR-12-Con	80	20	13	33	54	6.8
MOR-SDA2-12	83	17	10	27	63	8.5
BEA-12-Con	74	26	5	28	67	10.5
BEA-SDA3-12	70	30	7	25	68	10.3

<sup>a</sup> Al<sup>IV</sup> determined by integration of NMR signal between 20 and 100 ppm; Al<sup>VI</sup> determined by integration of NMR signal between 20 and -50 ppm.



<sup>b</sup> Framework Si/Al=2  $\Sigma$  ISi(nAl)/  $\Sigma$ 0.25·n-ISi(nAl) with assuming that Q<sup>3</sup>(0Al) does not contribute to the intensity of Q<sup>4</sup>(2Al)/ Q<sup>3</sup>(0Al), n = 0-4.

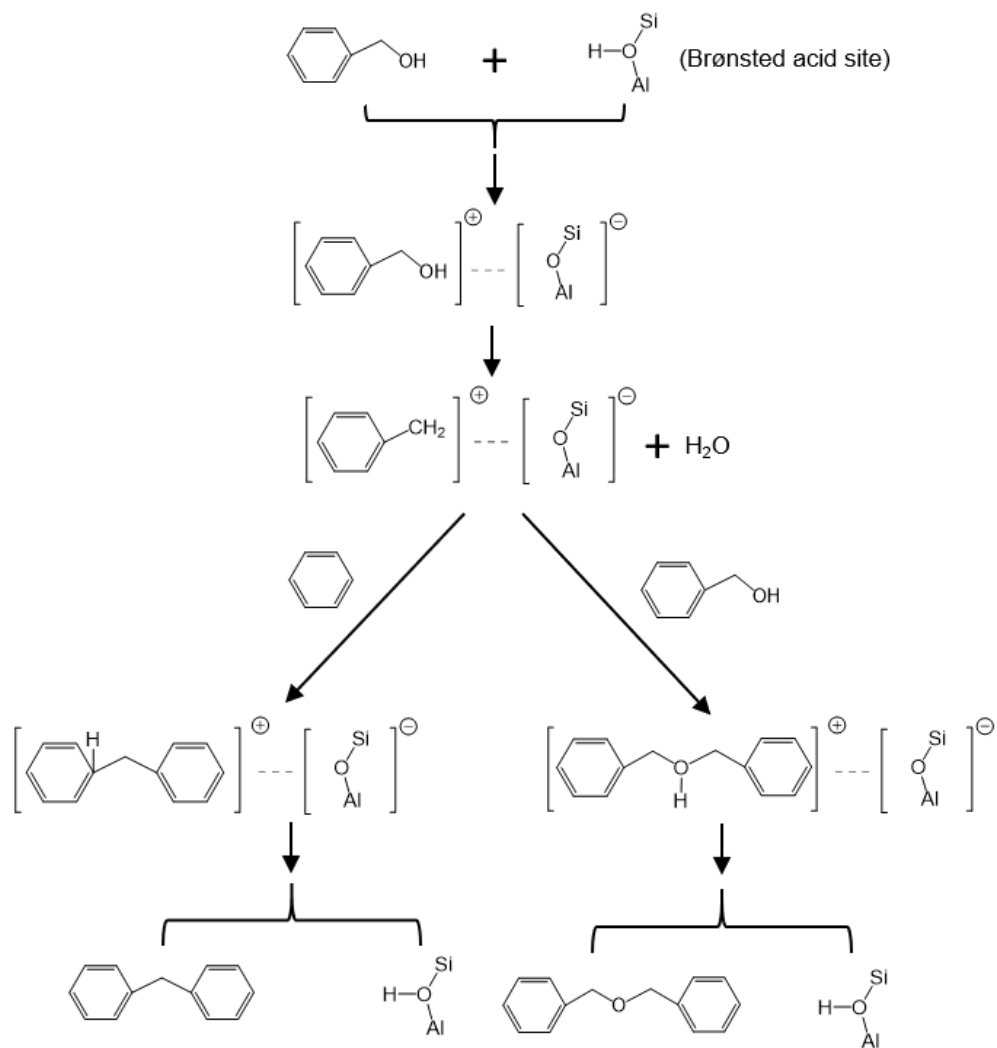
**Table B9.** BAS distribution derived from deconvoluted IR spectra of MOR zeolites.

Zeolite	BAS in 8MR (%)	BAS in 8/12MR (%)	BAS in 12MR (%)
MOR-12-Con	49	30	21
MOR-SDA2-12	64	25	11

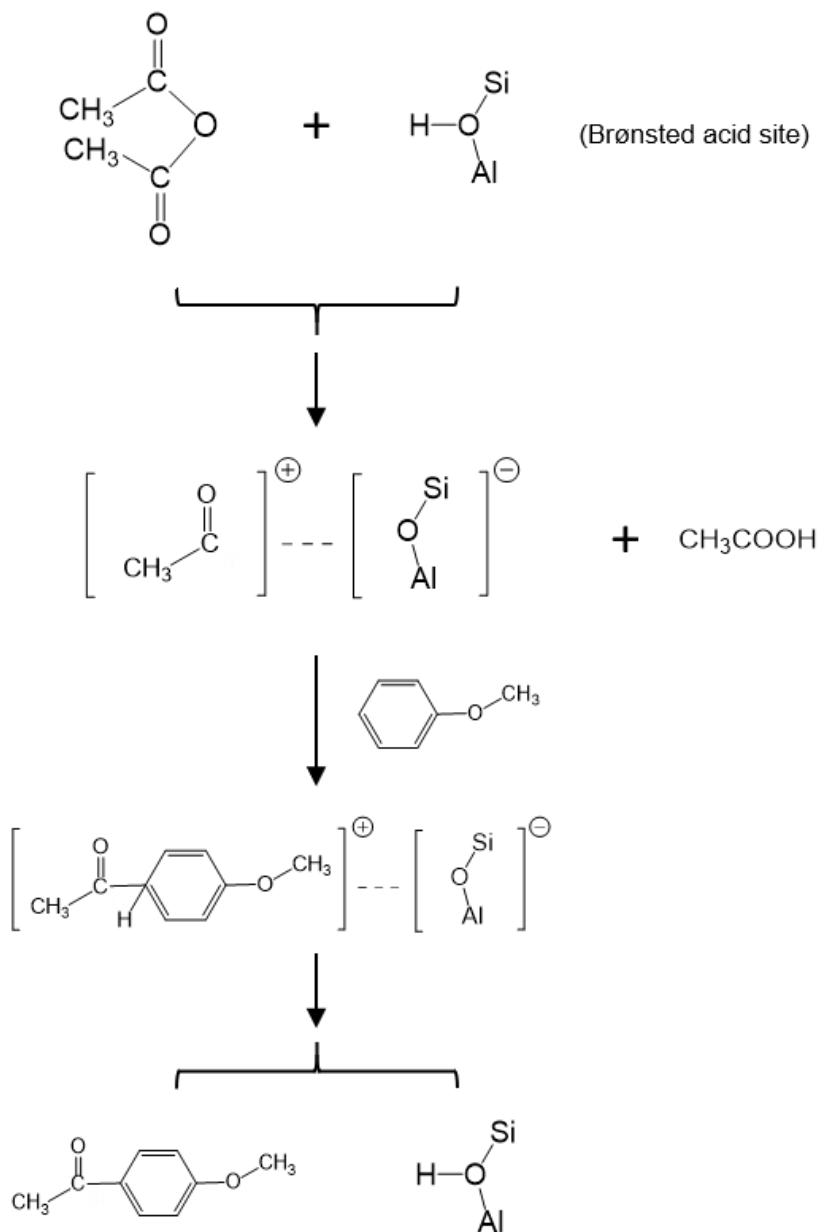
**Table B10.** Catalytic performance of the acylation of anisole with anhydride over BEA zeolites after 6 h reaction.

Zeolite	Acetic anhydride conversion (%)	<i>p</i> -MAP yield (selectivity) (%)
BEA-12-Con	48	39 (81)
BEA-SDA3-12	67	57 (85)

*p*-MAP: *p*-methoxyacetophenone.



**Scheme B1.** Reaction pathways for benzylation of benzene with benzyl alcohol.



**Scheme B2.** Reaction pathway for acylation of anisole with acetic anhydride (*p*-methoxyacetophenone as the product).

# Chapter 4

## Direct synthesis of Al-rich ZSM-5 nanocrystals with improved performance in aromatics formation from methane and methanol

### Abstract

Nanosized ZSM-5 (< 100 nm) zeolites with high acidity (Si/Al < 15) can bring distinct advantages in their use as catalysts for the synthesis of valuable aromatics in C1 chemistry. Synthesis of such nanosized zeolites in a cheap and scalable manner remains a challenge. Herein, nanosized ZSM-5 (20-50 nm) with high acidity (Si/Al = 10.9) was hydrothermally synthesized in excellent yield using *p*-phenylenedimethylene-bis(tripropylammonium) (Pr<sub>3</sub>N-benzyl-NPr<sub>3</sub>) as the sole organic structure-directing agent (OSDA). By investigating the solid products formed during zeolite synthesis, it was found that crystallization follows a solid-state transformation mechanism. An in-depth NMR study combined with TGA measurements reveals that, after early electrostatic interaction between condensed aluminosilicate and the head groups of OSDA, ZSM-5 crystallizes around the OSDA. Owing to the high acidity and improved mass transfer, such nanosized ZSM-5 demonstrates enhanced productivity in the formation of aromatics by methanol dehydration and non-oxidative dehydroaromatization of methane reactions in comparison to reference bulk ZSM-5.

## 4.1 Introduction

Zeolites are crystalline porous aluminosilicates possessing channels and cavities with size in the range of molecules.<sup>1-3</sup> ZSM-5 is widely used as heterogeneous catalyst in environmental chemistry, fine chemistry and petrochemistry.<sup>4-6</sup> Its MFI topology contains zigzag channels along the *a*-axis (0.51 nm × 0.55 nm) and straight channels along the *b*-axis (0.53 nm × 0.56 nm). The broad application of ZSM-5 zeolite catalysts in industrial chemical processes is related to its high (hydro)thermal stability, suitable shape selectivity and tunable acidity.<sup>7</sup> Among the many aspects that affect the performance of zeolites, the realization that the crystal size has a profound impact on the performance has led to many approaches to control the zeolite domain/crystal size.<sup>8,9</sup> For instance, Ryoo and co-workers demonstrated that, by reducing ZSM-5 crystal thickness to the single unit cell dimension, catalyst deactivation by coke deposition during methanol-to-hydrocarbons (MTH) reaction can be substantially suppressed.<sup>10</sup> The reduced crystallite size not only facilitates diffusion of coke precursors out of the micropores but also increases the micropore utilization degree.<sup>11</sup> By varying the Si/Al ratio of ZSM-5 zeolite, the acid site density can be controlled as an effective strategy to optimize the selectivity, activity and stability in many catalytic reactions such as the MTH reaction.<sup>12-14</sup> Another example is the optimization of ZSM-5 zeolite promoted by metals such as Mo for the non-oxidative dehydroaromatization of methane.<sup>15,16</sup> As demonstrated for the MTH reaction, highly acidic ZSM-5 (Si/Al < 15) is effective to achieve a high aromatics selectivity.<sup>17</sup> However, the high acidity will also lead to increased coke formation and faster catalyst deactivation.<sup>18,19</sup> To resolve these issue, Al-rich ZSM-5 nanocrystals (< 100 nm) can be used where the decreased diffusion length can improve the catalytic stability.<sup>20,21</sup>

The synthesis of phase-pure ZSM-5 zeolite with a low Si/Al ratio (< 12) with the most commonly employed tetrapropylammonium (TPA) template is difficult.<sup>22-25</sup> Al-rich ZSM-5 zeolites can only be obtained in a narrow window of synthesis conditions with the risk of forming impurity phases such as mordenite and amorphous material.<sup>26</sup> Such challenges in obtaining nanosized Al-rich ZSM-5 crystals has motivated the development of alternative synthesis strategies.<sup>27-29</sup> For instance, Valtchev and co-workers investigated the synthesis of nanosized ZSM-5 zeolite with a low Si/Al ratio (~10) by using a seed-induced crystallization method. The nanosized crystals (30-70 nm) obtained at low crystallization temperatures (100 and 120 °C) displayed relatively low crystallinity.<sup>27</sup> Okubo and co-workers investigated the synthesis of hierarchically intergrown ZSM-5 from an initial gel at Si/Al ratio of 11 by using a dimer of TPA, *i.e.* N, N,N,N',N',N'-hexapropylpentanediammonium cations (Pr<sub>6</sub>-diquat-5), as the organic structure-directing agent (OSDA). Although the XRD pattern of the as-synthesized sample showed intense diffraction peaks corresponding to the MFI zeolite, a

large fraction of extraframework Al was observed after calcination, suggesting a poor incorporation of Al into the zeolite framework.<sup>28, 30</sup> Overall, despite considerable efforts, synthesis of nanosized Al-rich ZSM-5 zeolites remains a challenge.

In this work, we demonstrate a one-step hydrothermal synthesis of nanosized ZSM-5 from initial gels with different Si/Al ratios (11, 13 and 15) and a high NaOH/Si ratio (0.6) by using *p*-phenylenedimethylene-bis(tripropylammonium) (Pr<sub>3</sub>N-benzyl-NPr<sub>3</sub>) (Figure 4.4a) as the OSDA. Nanosized ZSM-5 crystals (20-50 nm) with high yield (99%) and low Si/Al molar ratio of 10.9 were successfully synthesized. The crystallization behavior was investigated via characterizing the obtained solid products throughout the crystallization process. The physicochemical properties of the nanosized ZSM-5 with Si/Al ratio of 10.9 were extensively characterized. Finally, this nanosized Al-rich ZSM-5 zeolite was tested in MTH reaction and, upon impregnation with 2 wt.% Mo, in non-oxidative dehydroaromatization of methane (MDA) and displayed significantly improved catalytic performance as compared to a commercial bulk ZSM-5 zeolite.

## 4.2 Experimental section

### 4.2.1 Synthesis of OSDA

0.02 mol of 1,4-bis(chloromethyl)benzene (Sigma Aldrich, 98%) was dissolved in 100 ml acetonitrile (Biosolve, 99.8%) and 30 ml ethanol (Biosolve, 99.9%). Then 0.08 mol of tripropylamine (Sigma Aldrich, ≥ 98%) was added dropwise into the solution under vigorous stirring. The reaction solution was heated in a round-bottom flask in an oil bath kept at 70 °C for 3 days under a nitrogen atmosphere. After cooling to room temperature, the solution was poured into 200 ml of diethyl ether (Biosolve, 99.5%) under stirring. The precipitated white powder was collected by filtration and washed with diethyl ether. The obtained solid product was dried under evacuation at 50 °C for 12 h. The successful synthesis of the OSDA was confirmed by <sup>1</sup>H NMR and <sup>13</sup>C NMR spectra (Figures C1 and C2). The product yield was 92%.

### 4.2.2 Synthesis of zeolites

Hydrothermal synthesis of zeolites was performed in a 45 ml Teflon-lined stainless-steel autoclave (Parr Instruments). In a typical synthesis, 0.6 g of sodium hydroxide (Sigma Aldrich, ≥ 98%) was dissolved in 15.51 g of deionized water, followed by addition of 1.15 g OSDA. After stirring for 5 min, AlCl<sub>3</sub>·6H<sub>2</sub>O (Alfa Aesar, 99%) was added to the mixture. After further stirring for 5 min, 3.75 g Ludox AS-40 (Sigma Aldrich, 40 wt%) was added slowly to the mixture under stirring. The final mixture had a molar composition of 12 SiO<sub>2</sub> :

$x \text{ Al}_2\text{O}_3 : 3.6 \text{ Na}_2\text{O} : 1.2 \text{ OSDA} : 480 \text{ H}_2\text{O}$  ( $x = 0.4\text{-}0.6$ ). After vigorous stirring for 24 h at room temperature, the mixture was transferred to the autoclave and heated at 160 °C for 7 days under tumbling in an oven (50 rpm). After hydrothermal treatment, the solid product was collected by centrifugation and washed with deionized water until  $\text{pH} < 8$ , followed by drying at 30 °C overnight under evacuation. The organic template was removed by calcination at 550 °C for 8 h in air. The calcined samples were converted to the ammonium form by triple ion exchange with 1.0 M  $\text{NH}_4\text{NO}_3$  at 70 °C. The ion-exchanged samples were dried at 30 °C overnight under evacuation followed by calcination at 550 °C for 4 h in a  $\text{O}_2/\text{N}_2$  (1/4 by volume) flow to obtain the final proton form. Samples were named as ZSM-5- $x$ , where  $x$  is the Si/Al ratio. A commercial ZSM-5 zeolite (Si/Al = 13, Süd-Chemie, now Clariant) was used as reference material and named ZSM-5-Con.

Mo/ZSM-5 catalysts were prepared by wet impregnation of an aqueous solution of ammonium heptamolybdate tetrahydrate  $(\text{NH}_4)_6\text{Mo}_7\text{O}_{24}\cdot 4\text{H}_2\text{O}$ , Merck) on ZSM-5 zeolite. After impregnation, the samples were dried overnight at 110 °C and calcined in air at 550 °C for 8 h (rate 2 °C/min).

### 4.2.3 Characterization

X-ray diffraction (XRD) patterns were recorded with a Bruker D2 Phase powder diffractometer with  $\text{Cu K}\alpha$  radiation. The chemical composition of the samples were determined by inductively couple plasma optical emission spectrometry (ICP-OES) after solid dissolution in  $\text{HF}/\text{HNO}_3$  aqueous solution. Textural properties were analyzed by Ar physisorption at -186 °C on a Micromeritics ASAP 2020 instrument. Prior to the sorption measurement, the samples were outgassed at 400 °C for 6 h. The relative pressure in the range of 0.05-0.25 was chosen to calculate BET surface area. The  $t$ -plot method was used to calculate the micropore volume and external surface area, while the Barrett-Joyner-Halenda (BJH) method was used to calculate the mesopore volume. Thermogravimetric analysis (TGA) was performed on a TGA/DSC 1 instrument (Mettler Toledo) from 40 °C to 800 °C at a heating rate of 5 °C/min in a flow of 20 ml/min  $\text{O}_2$  and 40 ml/min He.

Scanning electron microscopy (SEM) images were taken on a FEI Quanta 200F scanning electron microscope at an accelerating voltage of 3 kV. Transmission electron microscopy (TEM) images were obtained on a FEI Tecnai 20 at 200kV. Prior to the measurement, the samples were suspended in ethanol and dispersed over a holey Cu grid coated with a carbon film.

The acidity of samples was determined by IR spectroscopy of adsorbed pyridine and 2,4,6-collidine. IR spectra were collected in the range of 1000-4000  $\text{cm}^{-1}$  on a Bruker Vertex 70v

spectrometer. The sample in the form of a pressed wafer (~10 mg, diameter 13 mm) was pretreated in artificial air at 550 °C for 1 h. After cooling to 150 °C, a background spectrum was collected. Pyridine or 2,4,6-collidine was then introduced into the IR cell until saturation of the IR spectra was observed. Finally, the sample was outgassed for 1 h at 150 °C, 300 °C and 500 °C. After each step, a corresponding spectrum was collected after cooling to 150 °C.

Solid-state nuclear magnetic resonance (NMR) spectroscopy was carried out on a 11.7 Tesla Bruker DMX500 NMR spectrometer. The measurements were performed at 132 MHz for  $^{27}\text{Al}$ , 99 MHz for  $^{29}\text{Si}$ , 125 MHz for  $^{13}\text{C}$  nuclei.  $^{27}\text{Al}$  magic angle spinning (MAS) NMR measurements were carried out using a Bruker 2.5 mm MAS probe head and a 2.5 mm zirconia rotor with a spinning speed of 25 kHz. Prior to the  $^{27}\text{Al}$  NMR measurements, the samples were hydrated in a desiccator containing water overnight. All other measurements were performed using a Bruker triple channel 4 mm MAS probe head and a 4 mm zirconia rotor with a spinning speed of 10 kHz. Quantitative  $^{29}\text{Si}$  MAS NMR spectra were recorded with a high-power proton decoupling direct excitation (DE) pulse sequence during which a 54° pulse duration of 3  $\mu\text{s}$  and a recycle delay of 120 s were used.  $^1\text{H}$ - $^{13}\text{C}$  cross-polarization (CP) MAS NMR spectra were recorded by using a ramped contact pulse of 3 ms and a recycle delay of 3 s. Two-dimensional (2D)  $^1\text{H}$ - $^{13}\text{C}$  heteronuclear correlation (HETCOR) spectra were recorded by using a rectangular contact pulse of 1 ms.  $^1\text{H}$ - $^{29}\text{Si}$  HETCOR spectra were recorded by using a rectangular contact pulse of 4 ms. Liquid-state NMR experiments were carried out on a Bruker 400 MHz spectrometer. The as-synthesized OSDA was dissolved in deuterated water. Then, the solution was transferred into a 5 mm NMR tube.  $^1\text{H}$  NMR spectra were recorded with a total of 32 scans and a relaxation delay of 1 s.  $^{13}\text{C}$  NMR spectra were recorded with a total of 1024 scans and a relaxation delay of 2 s.

## 4.2.4 Catalytic activity measurements

### 4.2.4.1 Methanol to hydrocarbons

The catalytic activity of the samples for MTH reaction was tested in a fixed-bed downstream reactor. Samples were pressed, and then crushed and sieved to obtain particles in the range of 250-500  $\mu\text{m}$ . An amount of 15 mg of the catalyst (sieve fraction 250-500  $\mu\text{m}$ ) was loaded into a quartz reactor with an internal diameter of 4 mm. Prior to the reaction, the catalyst was pretreated *in situ* in artificial air at 550 °C for 1 h, followed by cooling to the reaction temperature of 450 °C in the same artificial air. Methanol was fed to the reactor at a weight hourly velocity (WHSV) of 10  $\text{h}^{-1}$  by flowing He through a saturator containing methanol, which was kept at 6.6 °C. The products were analyzed by online gas chromatography (Interscience Compact GC) equipped with 2 pre-columns, 3 columns and 3 detectors. A



thermal conductivity detector (TCD) coupled with an RT-Q-Bond pre-column (length 3 m; i.d. 0.32 mm; thickness 10  $\mu\text{m}$ ) and a Molsieve 5A column (length 10 m; i.d. 0.32 mm; thickness 30  $\mu\text{m}$ ) was used for the analysis of  $\text{H}_2$  and  $\text{CH}_4$ . A TCD coupled with an RT-Q-Bond pre-column (length 3 m; i.d. 0.32 mm; thickness 10  $\mu\text{m}$ ) and an RT-Q-Bond column (length 10 m; i.d. 0.32 mm; thickness 10  $\mu\text{m}$ ) was used for the analysis of  $\text{C}_2$ - $\text{C}_3$  hydrocarbons, water and oxygenates. Heavier hydrocarbons ( $\text{C}_4$  to naphthalene) were separated on an Rtx-1 column (length 15 m; i.d. 0.32 mm; thickness 1  $\mu\text{m}$ ) and analyzed with a flame ionization detector (FID). Dimethyl ether was considered as a reactant.

#### **4.2.4.2 Non-oxidative dehydroaromatization of methane**

The MDA reaction was performed in a fix-bed downstream reactor. Samples were pressed, and then crushed and sieved to obtain particles in the range of 250-500  $\mu\text{m}$ . An amount of 300 mg of catalyst (sieve fraction 250-500  $\mu\text{m}$ ) was loaded into a quartz reactor with an internal diameter of 4 mm. The catalyst was pretreated by heating to 450  $^\circ\text{C}$  at a rate of 10  $^\circ\text{C}/\text{min}$  in a flow of  $\text{CH}_4/\text{N}_2$  (95/5) followed by an isothermal dwell of 45 min. Then the temperature was increased to 700  $^\circ\text{C}$  (15  $^\circ\text{C}/\text{min}$ ). The moment when the final temperature was reached was regarded as the start of the reaction. The reaction was carried out at 700  $^\circ\text{C}$  for 16 h in a 30 ml/min  $\text{CH}_4/\text{N}_2$  (95/5) flow. The reaction products were analyzed by online gas chromatography (Interscience Compact GC) equipped with 2 pre-columns, 3 columns and 3 detectors. A TCD coupled with an RT-Q-Bond pre-column (length 3 m; i.d. 0.32 mm; thickness 10  $\mu\text{m}$ ) and a Molsieve 5A column (length 10 m; i.d. 0.32 mm; thickness 30  $\mu\text{m}$ ) was used for the analysis of  $\text{H}_2$ ,  $\text{N}_2$ ,  $\text{CH}_4$  and  $\text{CO}$ . A TCD coupled with an RT-Q-Bond pre-column (length 3 m; i.d. 0.32 mm; thickness 10  $\mu\text{m}$ ) and an RT-Q-Bond column (length 10 m; i.d. 0.32 mm; thickness 10  $\mu\text{m}$ ) was used for the analysis of ethane and ethylene. Heavier hydrocarbons (benzene, toluene and naphthalene) were analyzed with FID coupled with an Rtx-1 column (length 15 m; i.d. 0.32 mm; thickness 1  $\mu\text{m}$ ).

## 4.3 Results and discussion

### 4.3.1 Zeolite synthesis

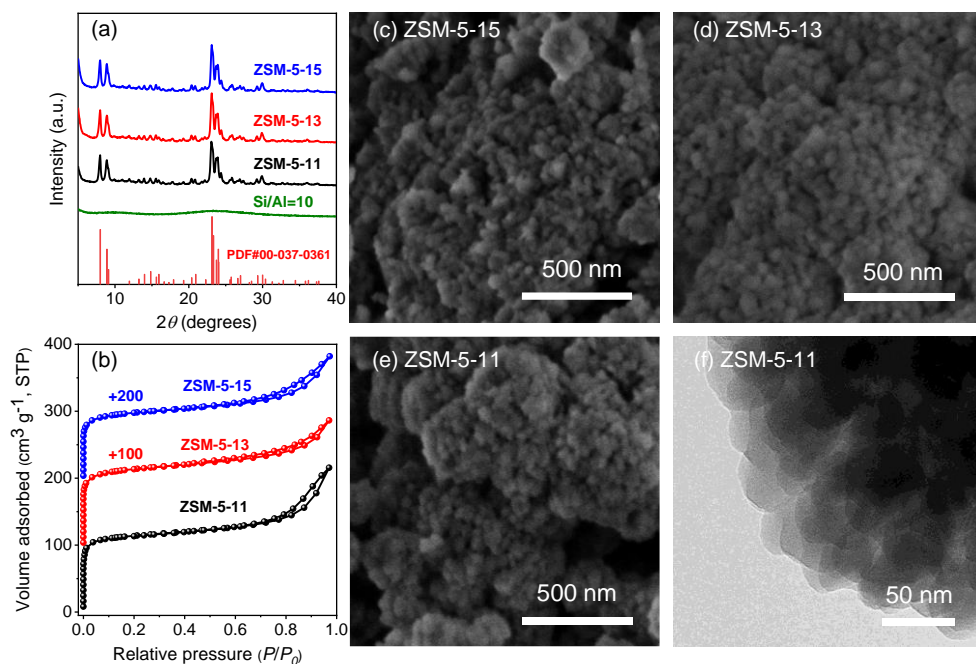


**Figure 4.1.** (a) XRD patterns of as-synthesized samples, (b) Ar physisorption isotherms of calcined samples, (c-e) SEM images of calcined samples and (f) representative TEM image of calcined ZSM-5-11.

Various ZSM-5 zeolites were hydrothermally synthesized from initial gels with different Si/Al ratios (*i.e.*, 15, 13, 11, and 10) at 160 °C for 7 days. The XRD patterns, Ar physisorption isotherms and representative SEM and TEM images of the solid products are shown in Figure 4.1. XRD patterns in Figure 4.1a show that phase-pure ZSM-5 zeolites with high crystallinity are obtained from gels with Si/Al ratios of 11, 13, and 15, while no crystalline product was obtained at a Si/Al ratio of 10. The high crystallinity is also evident from the steep Ar uptake at low relative pressure ( $p/p_0 < 0.01$ ) due to the filling of the zeolite micropores (Figure 4.1b).<sup>31</sup> SEM and TEM images (Figures 4.1c-4.1f) show agglomerates composed of nanosized crystals (20-50 nm). The nanocrystalline morphology of these ZSM-5 zeolites is consistent with their high external surface area in the 86-93  $\text{m}^2 \text{g}^{-1}$  range (Table C1). Elemental analysis shows that the Si/Al ratio of the zeolites is very similar to the ratio in the

corresponding starting gels, which suggests proper incorporation of Al and Si nutrients, consistent with the high synthesis yields (94-99%) (Table C1).

The effect of the NaOH/Si molar ratio (0.5, 0.6 and 0.7) in the initial gel was also investigated. The results in Figure C3 show that phase-pure ZSM-5 can only be obtained at a NaOH/Si molar ratio of 0.6 at a Si/Al ratio of 11. It should be noted that in previous studies the initial synthesis gel had a lower NaOH/Si molar ratio of around 0.3, because higher alkalinity typically leads to impurity phases such as MOR.<sup>26, 32</sup> Although this is not the case here with Pr<sub>3</sub>N-benzyl-NPr<sub>3</sub> as the OSDA, we verified the formation of a mixture of ZSM-5 and MOR when this OSDA was replaced by TPABr at a NaOH/Si gel ratio of 0.6 (Figure C4). Pure MOR zeolite was obtained in the absence of the OSDA already after 1 day hydrothermal synthesis (Figure C5), consistent with previous studies.<sup>33</sup> Overall, the above results demonstrate that Pr<sub>3</sub>N-benzyl-NPr<sub>3</sub> is an effective OSDA for synthesizing nanosized Al-rich ZSM-5 with high yield. Therefore, our synthesis extends the scope of the use of Pr<sub>3</sub>N-benzyl-NPr<sub>3</sub> as OSDA in directing more valuable aluminum-containing zeolite for acidic catalysis. So far, this OSDA has only been reported for directing all-silica zeolites (Silicate-1 and IDM-1) in fluoride media by the group of Cambor.<sup>3, 34</sup>

In order to understand the crystallization behavior of ZSM-5-11, the solids obtained at different crystallization time were characterized in terms of crystallinity, chemical composition, morphology and textural properties. The XRD results (Figures 4.2a and C6) show that the crystallization process starts with a long induction period (~5 days) followed by a fast crystal growth stage (~1 day). Notably, a high solid yield (> 87%) is maintained throughout the whole crystallization process (Figure 4.2a). Consistent with this, the solid products are similar in both bulk and surface Si/Al ratios (~11). Electron microscopy was used to determine the morphology of the solid products. The SEM image in Figure 4.1d shows the presence of worm-like particles (> 100 nm) with an irregular morphology in the solid product obtained after 1 day synthesis. Supported by XRD (Figure C6) and physisorption data (Figure C7 and Table C2), these worm-like particles represent amorphous aluminosilicate species. Similar worm-like features have also been observed for amorphous zeolite precursors in ZSM-5 synthesis with TPA.<sup>35, 36</sup> After hydrothermal treatment for 2 days, a decrease in the size of the particles is observed, which then remains constant until the onset of crystallization. After 5 days synthesis, the SEM image shows the formation of embedded tiny particles on the outer surface of the worm-like particles (Figure 4.2h). The corresponding TEM image presents clear lattice fringes, indicating that these small particles (< 30 nm) are crystalline in nature (Figure 4.2c). The formation of such crystalline particles is also consistent with the XRD patterns, where already MFI features can be discerned (Figure C6). As indicated by XRD (Figure S6), further hydrothermal treatment until 6 days resulted in fast

crystal growth and formation of aggregated particles with a size of 20-50 nm (Figure 4.2i). After 7 days, no significant change in the morphology of the particles was observed anymore, while the corresponding XRD pattern indicates that ZSM-5 with high crystallinity is obtained. This is also confirmed by the Ar physisorption isotherms of the calcined samples, in which the highest Ar adsorption capacity in the low-pressure region ( $p/p_0 < 0.01$ ) is observed for the sample synthesized for 7 days (Figure C7). Prolonging the synthesis to 9 days has a negligible effect on the crystallinity (Figure 4.2a) and textural properties of the zeolite (Figures 4.2k and C6, Table C2).

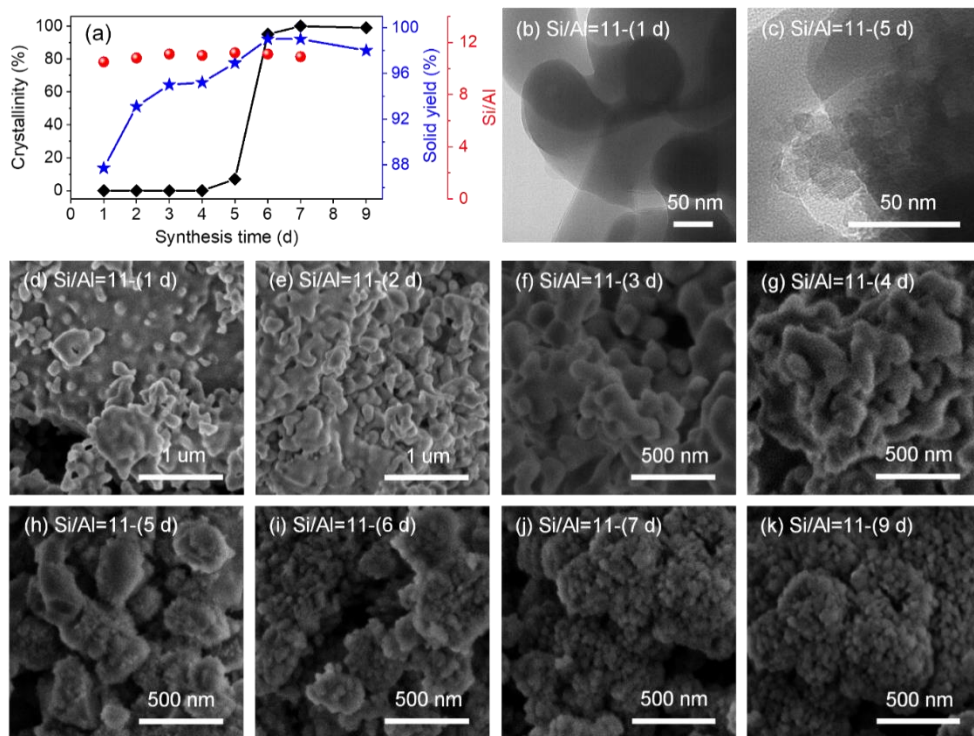


**Figure 4.2.** (a) Relative crystallinities, Si/Al molar ratios and yields of solid synthesis products; (b-c) TEM images and (d-k) SEM images of obtained solid products during the synthesis of ZSM-5-11.

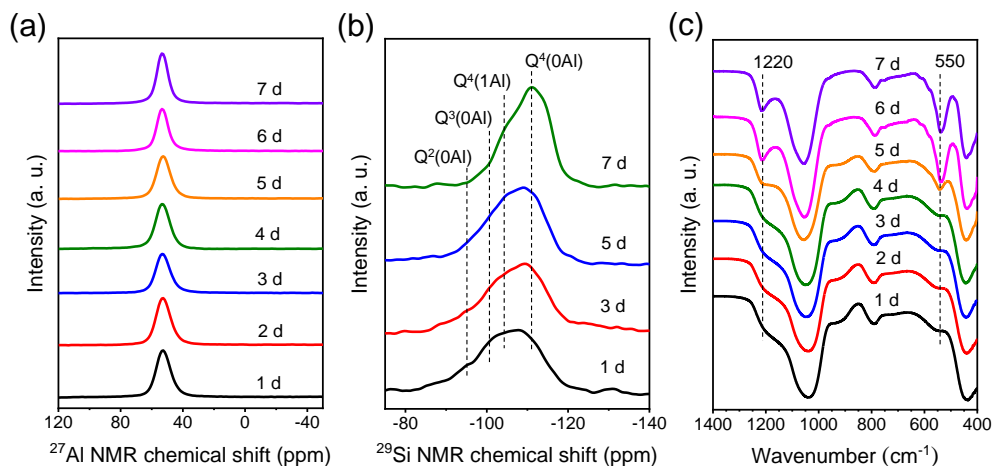


**Figure 4.3.** (a)  $^{27}\text{Al}$  MAS NMR spectra; (b)  $^{29}\text{Si}$  MAS NMR spectra and (c) IR spectra of solid products obtained during the synthesis of ZSM-5-11.

Besides the evolution of crystallinity, the chemical composition, the morphology and textural properties as well as the structural evolution of the solid products was investigated with  $^{27}\text{Al}$  MAS NMR,  $^{29}\text{Si}$  MAS NMR and IR spectroscopy. The  $^{27}\text{Al}$  MAS NMR spectra in Figure 4.3a show a single intense signal at 54 ppm assigned to four-coordinated Al species for all samples obtained as a function of hydrothermal synthesis time.<sup>37</sup> This indicates that the aluminum precursor is dissolved well and reacts with silicates to form the aluminosilicates composed of four-coordinated Al at the beginning of the synthesis.<sup>38</sup> As shown in Figure C8, the full width at half maximum (FWHM) of the peak at 54 ppm decreases gradually during the induction period (< 5 days), which indicates an improved structural order of the amorphous precursor.<sup>39</sup> After the onset of crystal growth, a substantial decrease of the FWHM of the relevant NMR peak is observed in line with the increased crystallinity. The coordination environment of Si atoms was investigated by  $^{29}\text{Si}$  MAS NMR spectroscopy. As shown for the solid product after 1 day synthesis in Figure 4.3b, the  $^{29}\text{Si}$  MAS NMR spectrum shows a broad peak between -80 and -120 ppm. According to a previous study, this broad peak mainly consists of resonances centered at around -95 ppm, -102 ppm, -105 ppm and -111 ppm, which correspond to  $\text{Q}^2(0\text{Al})$ ,  $\text{Q}^3(0\text{Al})$ ,  $\text{Q}^4(1\text{Al})$  and  $\text{Q}^4(0\text{Al})$ , respectively.<sup>40</sup> Upon hydrothermal treatment up to 5 days, the resonances assigned to  $\text{Q}^2(0\text{Al})$  and  $\text{Q}^3(0\text{Al})$  gradually decrease in intensity, while an increased intensity in the signal assigned to  $\text{Q}^4(0\text{Al})$  is observed, suggesting the gradual condensation of silicates during the induction period.<sup>41</sup> After full crystallization (7 days), a sharp peak at -111 ppm is observed, while the feature at -95 ppm is absent, indicating the high condensation degree of silicates and well-ordered structure of

the obtained ZSM-5 zeolite. Finally, the various samples were investigated by IR spectroscopy. Figure 4.3c shows that the spectrum for the solid sample obtained after 1 day synthesis contains a weak band at  $550\text{ cm}^{-1}$ , which can be related to double-5-membered ring (D5R) units.<sup>42</sup> After formation of highly crystalline ZSM-5 zeolite after 7 days synthesis, the band at  $550\text{ cm}^{-1}$  is more intense, which is usually explained by the more rigid environment in the zeolite framework.<sup>43</sup>

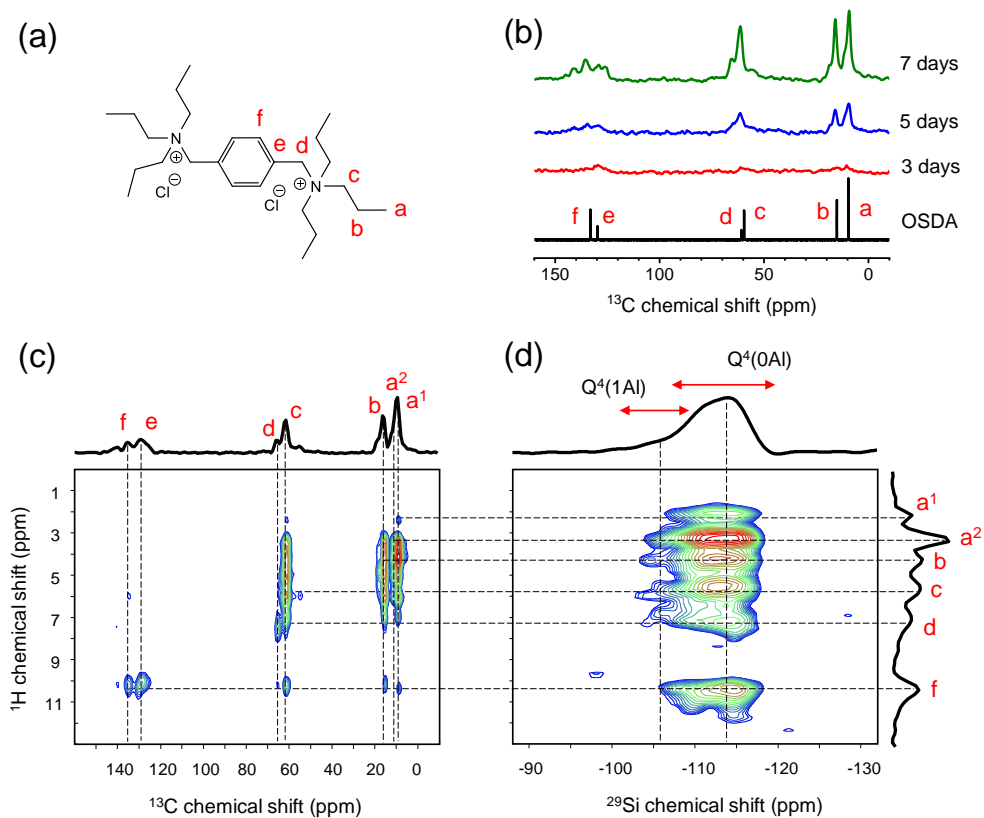


**Figure 4.4.** (a) Structural formula of  $\text{Pr}_3\text{N-benzyl-NPr}_3$ ; (b) Solid-state  $^1\text{H-}^{13}\text{C}$  CP/MAS NMR spectra of solid samples synthesized as a function of the hydrothermal synthesis time (top) and liquid-state  $^{13}\text{C}$  NMR spectrum of  $\text{Pr}_3\text{N-benzyl-NPr}_3$  in  $\text{D}_2\text{O}$  (bottom); (c)  $^1\text{H-}^{13}\text{C}$  HETCOR NMR spectrum of as-synthesized ZSM-5-11 and (d)  $^1\text{H-}^{29}\text{Si}$  HETCOR NMR spectrum of as-synthesized ZSM-5-11.

We also investigated the interaction between the solid aluminosilicate intermediates and the OSDA during hydrothermal synthesis by TGA,  $^1\text{H-}^{13}\text{C}$  CP/MAS NMR spectroscopy,  $^1\text{H-}^{13}\text{C}$  HETCOR NMR spectroscopy and 2D  $^1\text{H-}^{29}\text{Si}$  HETCOR NMR spectroscopy. The TGA

results in Table C3 show that the content of occluded OSDAs in the solid product obtained after 1 day synthesis is 4.2 wt%. This amount is the same as after prolonged synthesis until the end of the induction period. However, the amount of occluded OSDA substantially increases to values larger than 8 wt% for the crystalline samples, which implies that the interaction between the OSDA and aluminosilicate precursors in amorphous products differs from that in the crystalline end product. Such differences were also reported in previous studies involving ZSM-5 synthesis with TPA in which the incorporation of a particular amount of TPA into the amorphous phase during the induction stage was argued to be an essential prerequisite for the subsequent disorder-to-order solid transformation.<sup>44, 45</sup> Other synthesis strategies, *e.g.* ultrasonication, have also been employed to facilitate the incorporation of TPA into the amorphous inorganic substrates, resulting in a shorter induction stage.<sup>44, 46</sup> We also investigated the obtained solid samples by <sup>1</sup>H-<sup>13</sup>C CP/MAS NMR spectroscopy. As shown in Figure 4.4b, the <sup>13</sup>C NMR spectrum of sample obtained after 7 days synthesis matches well with that of the pure Pr<sub>3</sub>N-benzyl-NPr<sub>3</sub>, indicating that the OSDA is stable during hydrothermal synthesis. Notably, the spectra of the two samples obtained after 3 and 5 days synthesis show a much lower intensity than the spectrum of the highly crystalline sample obtained after 7 days. Considering the relatively small differences in the amount of occluded OSDA between samples (Table C3), the intensity changes can be correlated to a higher mobility of the occluded organic molecules, explaining the less intense correlation signals.<sup>47</sup> It is reasonable to expect that the OSDA interacting with amorphous solid intermediates during the induction period are more mobile than the OSDA in the final condensed zeolite framework.

To further reveal guest-host interactions between the OSDA and the inorganic part, 2D <sup>1</sup>H-<sup>13</sup>C and <sup>1</sup>H-<sup>29</sup>Si HETCOR NMR experiments were carried out. First, the proton chemical shift assignment was determined on the basis of the 2D <sup>1</sup>H-<sup>13</sup>C HETCOR NMR spectrum. As shown in Figure 4.4c, two correlated signals between protons and carbon atoms in the terminal methyl groups (-CH<sub>3</sub>) are observed. An additional shoulder is observed for the resonance assigned to -CH<sub>3</sub> in the <sup>13</sup>C dimension projection. These findings are in qualitative agreement with the <sup>13</sup>C NMR spectrum for TPA occluded in ZSM-5 zeolite in previous studies, where the splitting of the signal due to terminal -CH<sub>3</sub> was attributed to differences in confinement and electrostatic interactions between TPA in zigzag and straight channels.<sup>47-49</sup> Another supporting evidence for this is that a symmetric <sup>13</sup>C NMR signal without splitting is observed for the terminal -CH<sub>3</sub> in the <sup>13</sup>C projection of 2D <sup>1</sup>H-<sup>13</sup>C HETCOR NMR spectrum of Pr<sub>3</sub>N-benzyl-NPr<sub>3</sub> itself (Figure C10). The proximity between the occluded OSDA and the zeolite framework can be deduced from the <sup>1</sup>H-<sup>29</sup>Si HETCOR NMR spectrum. The strongly correlated signals in Figure 4.4d between the various protons of the OSDA and the

framework Si species, *i.e.* Q<sup>4</sup>(1Al) and Q<sup>4</sup>(0Al), evidence the inclusion of the OSDA in the ZSM-5 micropores. For the amorphous solid sample after 3 days synthesis, additional correlation signals are observed between the propyl moieties of the OSDA and Q<sup>4</sup> sites, while cross-peaks between aromatic protons and Q<sup>4</sup> sites are absent (Figure C11a). These findings indicate that the formation of the inorganic-organic composites at the initial induction stage is mainly driven by the electrostatic interactions between the positive-charged head groups of the OSDA and the negatively charged Al-rich aluminosilicate matrix. The appearance of correlation signals between the aromatic protons of the OSDA and Si atoms goes together with the formation of crystalline ZSM-5, which is likely due to the complete confinement of the OSDA by the micropores (Figure C11b).

On the basis of the above, we propose a scheme for the formation of the nanocrystalline ZSM-5-11 sample. During the initial stages of the synthesis, rapid condensation of silica including aluminum results in dense amorphous particles with a limited amount of OSDA incorporated. A high NaOH/Si molar ratio (0.6) is essential to initiate these condensation reactions. A high concentration of sodium cations leads to competition with the OSDA for compensation of the negative charges of the inorganic matrix (due to deprotonated silanol groups and Al for Si substitutions), which we speculate could hinder the incorporation of OSDAs into the inorganic matrix. This can explain the longer induction period. Comparable Si/Al ratios and high yields of the solid products are already achieved after 1 day synthesis. Once tiny crystals on the outer surface of the amorphous solid gel (solid-liquid) interface are formed, crystal growth proceeds fast within 1 day via a non-conventional solid-solid transformation mechanism. These observations suggest the importance of autocatalytic nucleation.<sup>50-53</sup> During the crystal growth stage, Pr<sub>3</sub>N-benzyl-NPr<sub>3</sub> has a strong templating function for MFI by fitting in the forming MFI channels. The formation of aggregated small crystals is likely related to capping of the growing crystals by the OSDA. Specifically, this may stem from the strong electrostatic interaction between the highly negatively charged surface of Al-rich crystals and the positively charged OSDA.<sup>54</sup> It has also been mentioned that  $\pi$ - $\pi$  stacking interaction of the OSDA in the liquid phase is beneficial to limit Ostwald ripening, thus avoiding small crystals transforming into larger ones.<sup>55, 56</sup>

### 4.3.2 Acidity

ZSM-5-Con was chosen as a reference catalyst for evaluating the acidity and catalytic performance of nanosized ZSM-5-11, ZSM-5-13 and ZSM-5-15. Basic characterization data are presented in the Supporting Information (Figure C12 for SEM image, Ar physisorption isotherm and XRD pattern; Table C4 for textural properties). The <sup>27</sup>Al NMR spectra in Figure 4.5 show that both ZSM-5-Con and three nanosized ZSM-5 zeolites have a high fraction of



framework Al (> 83%). ZSM-5-11 exhibits lower bulk (10.9) and framework (13.4) Si/Al ratios than ZSM-5-Con (Si/Al<sub>bulk</sub> = 12.9, Si/Al<sub>F</sub> = 16.1). ZSM-5-11 with a higher density of framework Al atoms also shows a larger amount of Brønsted acid sites (BAS) as compared to the other samples (Table 4.1). Notably, a substantially larger amount of external BAS is determined for ZSM-5-11, which can be correlated to the much higher external surface area. Next, the catalytic performance of nanosized ZSM-5 samples was determined in comparison to ZSM-5-Con in the MTH and MDA reactions, both of which are promising for the production of aromatic building blocks.<sup>57, 58</sup>

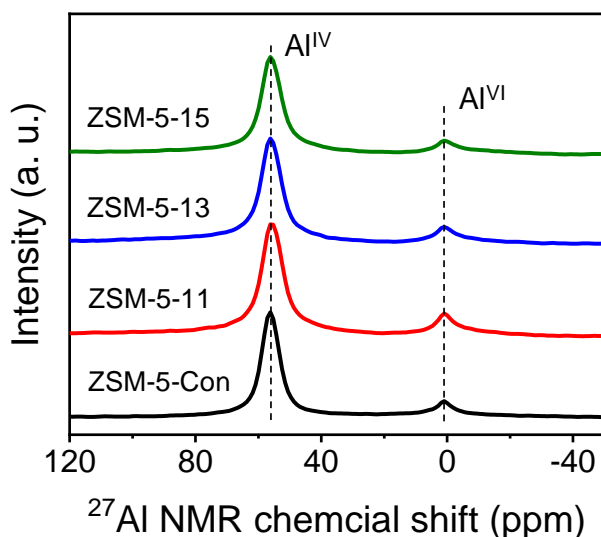


**Figure 4.5.** <sup>27</sup>Al MAS NMR spectra of calcined ZSM-5-Con, ZSM-5-11, ZSM-5-13 and ZSM-5-15.

**Table 4.1.** Si/Al ratio, fraction of framework Al, and acidity of the ZSM-5 zeolites.

Zeolite	Si/Al (ICP)	Si/Al <sup>a</sup> (NMR)	Al <sub>F</sub> (%) <sup>b</sup>	[BAS] <sup>c</sup> (μmol g <sup>-1</sup> )	[LAS] <sup>d</sup> (μmol g <sup>-1</sup> )	[BAS <sub>ext</sub> ] <sup>e</sup> (μmol g <sup>-1</sup> )
ZSM-5-Con	12.9	16.1	83.5	948	165	18
ZSM-5-11	10.9	13.4	86.0	1226	159	63
ZSM-5-13	13.1	--	88.3	1101	148	56
ZSM-5-15	14.8	--	88.7	966	134	47

<sup>a</sup> Framework Si/Al ratio determined by <sup>29</sup>Si NMR.

<sup>b</sup> Fraction of framework Al determined by <sup>27</sup>Al NMR.

<sup>c</sup> Density of Brønsted acid sites (BAS) determined by IR spectra of adsorbed pyridine after evacuation for 1 h at 150 °C.

<sup>d</sup> Density of Lewis acid sites (LAS) determined by IR spectra of adsorbed pyridine after evacuation for 1 h at 150 °C.

<sup>e</sup> Density of BAS on the external surface determined by IR spectra of adsorbed 2,4,6-collidine after evacuation for 1 h at 150 °C.

### 4.3.3 Catalytic activity

#### 4.3.3.1 Methanol to hydrocarbons

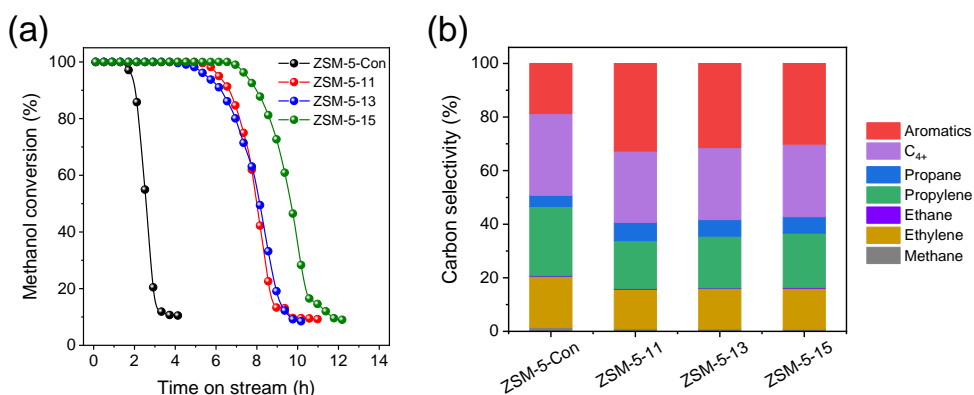


**Figure 4.6.** MTH performance of ZSM-5 catalysts: (a) methanol conversion as a function of reaction time and (b) product selectivity after 0.5 h time on stream.

First, the catalytic performance of the nanosized and conventional ZSM-5 zeolites in the MTH reaction was investigated. The catalyst lifetime is defined as the time at which the initially complete methanol conversion decreased to 50%. Figure 4.6a shows that methanol can be fully converted over all catalysts during the initial stages of the MTH reaction. With longer time on stream, these three nanosized ZSM-5 zeolites exhibits a better catalytic stability than ZSM-5-Con and a significant decline in activity is only observed after 5 h with a much longer lifetime of longer than 8 h for nanosized samples in comparison to that of ~2 h for ZSM-5-Con. Figure C15 shows that the coke contents are much higher in the used ZSM-5-11, ZSM-5-13 and ZSM-5-15 samples (14.5%, 15.5% and 15.6%, respectively) than in the used ZSM-5-Con sample (8.9%). Therefore, the significantly longer lifetime of nanosized ZSM-5 samples can be attributed to a better utilization of the micropore space due to the reduction of the crystal size<sup>59, 60</sup>. Inspection of the product distribution given in Figure 4.6b shows a much larger aromatics selectivity of 32.7% for ZSM-5-11 in comparison to ZSM-5-

Con (18.7%). A more detailed analysis of the products (Figure C16) shows that the heavier aromatics, such as tetra-methylbenzene and indane, contribute significantly to the improved aromatic yield of ZSM-5-11, whereas they are negligible in the products of ZSM-5-Con. We explain such substantial differences in product distribution to the higher rate of desorption for nanocrystalline samples. This can be evidenced by the comparable productivity distributions of these three nanosized ZSM-5 zeolites. A comparison of the  $C_2/C_2^-$  and  $C_3/C_3^-$  ratios (Table C6) points to a higher hydrogen transfer rate for nanosized ZSM-5-11, ZSM-5-13 and ZSM-5-15.<sup>61</sup> The higher hydrogen transfer rate of the less acidic ZSM-5-15 than ZSM-5-Con suggests likely the more amount of available acid sites during the reaction.<sup>17</sup> Thus, the longer catalytic lifetime of nanocrystalline ZSM-5 zeolites is due to better utilization of the zeolite micropore space, while differences in product distribution is mainly from improved desorption of heavier products for the smaller crystals.

#### 4.3.3.2 Methane dehydroaromatization

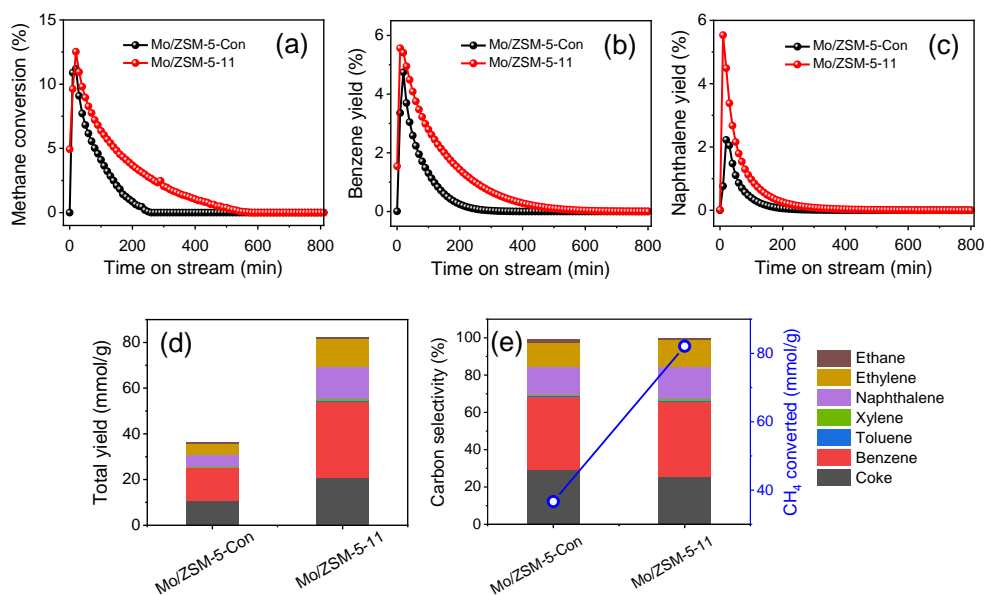


**Figure 4.7.** Dehydroaromatization of methane over Mo/ZSM-5 catalysts: (a) methane conversion, (b) yield of benzene, (c) yield of naphthalene, (d) total yields of products and (e) overall product distribution and total amount of converted methane.

For evaluating the performance of the ZSM-5 zeolites in the MDA reaction, the zeolites were loaded with 2 wt% Mo via wet impregnation. A previous study demonstrated that at such a

loading nearly all Mo atoms are atomically dispersed by anchoring on double framework Al sites of high-acidity ZSM-5 zeolites ( $\text{Si}/\text{Al} < 15$ ).<sup>62</sup> The catalytic results (Figures 4.7 and C17 and Tables C6 and C7) demonstrate the improved performance of Mo/ZSM-5-11 over Mo/ZSM-5-Con. The nanocrystalline zeolite deactivates slower during the methane conversion reaction, which can be appreciated from the evolution of the methane conversion and the benzene and naphthalene yield. The accumulated product yields are more than twice those obtained with the reference zeolite, similar to the relative difference in the total amount of methane converted which increases from 36.6 mmol/g<sub>cat</sub> for Mo/ZSM-5-Con to 82.1 mmol/g<sub>cat</sub> for Mo/ZSM-5-11. The amount of benzene and naphthalene obtained for Mo/ZSM-5-11 increased to 33.4 mmol/g<sub>cat</sub> and 13.7 mmol/g<sub>cat</sub>, respectively, from values of 14.2 mmol/g<sub>cat</sub> and 5.4 mmol/g<sub>cat</sub> for Mo/ZSM-5-Con (Table C6). Relatively speaking, the product distributions over the total reaction time were comparable (Figure 4.7e and Table C7). TGA data (Figure C18) show that the coke content in used Mo/ZSM-5-11 (22%) is much higher than in used Mo/ZSM-5-Con (13%). We attribute this difference to the better utilization of the micropore space of the nanocrystalline zeolite.<sup>63, 64</sup> The corresponding DTG profiles in Figure C18 shows that the coke combustion for used Mo/ZSM-5-Con occurs in two steps. According to our previous study, the weight loss in the low temperature range (450-550 °C) corresponds to the combustion of coke close to Mo-centers, which can catalyze coke combustion upon reoxidation to the oxide, while the weight loss at high temperatures (550-650 °C) is due to the diffusion-limited combustion of coke further away from Mo-centers.<sup>65</sup> In contrast, coke combustion in used Mo/ZSM-5-11 occurs in a single step, which we tentatively attribute to strong diffusion limitations for oxygen because of the dense filling of coke in the micropores of used Mo/ZSM-5-11.<sup>66</sup> Overall, the enhanced productivity of valuable ethylene and aromatics products over Mo/ZSM-5-11 can be mainly ascribed to the better utilization of zeolite micropores.

## 4.4 Conclusions

In summary, this work describes the direct synthesis of nanosized Al-rich ZSM-5 zeolites by a one-step hydrothermal synthesis approach using Pr<sub>3</sub>N-benzyl-NPr<sub>3</sub> as the sole OSDA. The most acidic sample is ZSM-5-11 ( $\text{Si}/\text{Al} = 10.9$ , 20-50 nm, yield = 99%). A high NaOH/Si molar ratio of 0.6 is crucial for the successful zeolite synthesis. The crystallization process of ZSM-5-11 shows a long induction period (~5 days) and a fast crystal growth step (~1 day) involving a solid-state transformation, which can be described by the autocatalytic model. A systematic NMR study, together with TGA, reveals that, after electrostatic interaction between condensed aluminosilicate and the head groups of OSDA during the induction stage, ZSM-5 crystallizes around the OSDA. <sup>27</sup>Al NMR spectroscopy reveals that 86% of

aluminum species are in the framework of calcined ZSM-5-11. Nanosized ZSM-5-11 shows significantly improved aromatics productivity in MTH and MDA reactions as compared to a commercial ZSM-5 (Si/Al = 12.9). The improved catalytic performance of ZSM-5-11 is ascribed to the high acidity and enhanced mass-transfer ability. Finally, we expect that nanosized ZSM-5-11 zeolite could also be a promising catalyst for other reactions relevant to the clean energy transition.

## 4.5 References

1. C. S. Cundy and P. A. Cox, *Chem. Rev.*, 2003, **103**, 663-702.
2. A. Korde, B. Min, E. Kapaca, O. Knio, I. Nezam, Z. Wang, J. Leisen, X. Yin, X. Zhang, D. S. Sholl, X. Zou, T. Willhammar, C. W. Jones and S. Nair, *Science*, 2022, **375**, 62-66.
3. L. A. Villaescusa, J. Li, A. Mayoral, Z. R. Gao and M. A. Camblor, *Chem. Mater.*, 2021, **33**, 7869-7877.
4. R. Zhang, N. Liu, Z. Lei and B. Chen, *Chem. Rev.*, 2016, **116**, 3658-3721.
5. L. B. Pierella, C. Saux, S. C. Caglieri, H. R. Bertorello and P. G. Bercoff, *Appl. Catal., A*, 2008, **347**, 55-61.
6. E. T. Vogt and B. M. Weckhuysen, *Chem. Soc. Rev.*, 2015, **44**, 7342-7370.
7. T. F. Degnan, G. K. Chitnis and P. H. Schipper, *Microporous Mesoporous Mater.*, 2000, **35-36**, 245-252.
8. A. Martínez and C. Lopez, *Appl. Catal., A*, 2005, **294**, 251-259.
9. M. Firoozi, M. Baghalha and M. Asadi, *Catal. Commun.*, 2009, **10**, 1582-1585.
10. M. Choi, K. Na, J. Kim, Y. Sakamoto, O. Terasaki and R. Ryoo, *Nature*, 2009, **461**, 246-249.
11. H. Dai, Y. Shen, T. Yang, C. Lee, D. Fu, A. Agarwal, T. T. Le, M. Tsapatsis, J. C. Palmer, B. M. Weckhuysen, P. J. Dauenhauer, X. Zou and J. D. Rimer, *Nat. Mater.*, 2020, **19**, 1074-1080.
12. Y. Gao, B. Zheng, G. Wu, F. Ma and C. Liu, *RSC Adv.*, 2016, **6**, 83581-83588.
13. C. Engtrakul, C. Mukarakate, A. K. Starace, K. A. Magrini, A. K. Rogers and M. M. Yung, *Catal. Today*, 2016, **269**, 175-181.
14. T. Fu, J. Shao and Z. Li, *Appl. Catal., B*, 2021, **291**, 120098.
15. M. Rahman, A. Infantes-Molina, A. S. Hoffman, S. R. Bare, K. L. Emerson and S. J. Khatib, *Fuel*, 2020, **278**, 118290.
16. J.-P. Tessonnier, B. Louis, S. Rigolet, M. J. Ledoux and C. Pham-Huu, *Appl. Catal., A*, 2008, **336**, 79-88.

17. D. Mores, J. Kornatowski, U. Olsbye and B. M. Weckhuysen, *Chem. Eur. J.*, 2011, **17**, 2874-2884.
18. Z. Wan, W. Wu, G. Li, C. Wang, H. Yang and D. Zhang, *Appl. Catal., A*, 2016, **523**, 312-320.
19. I. Yarulina, A. D. Chowdhury, F. Meirer, B. M. Weckhuysen and J. Gascon, *Nat. Catal.*, 2018, **1**, 398-411.
20. S. Li, J. Li, M. Dong, S. Fan, T. Zhao, J. Wang and W. Fan, *Chem. Soc. Rev.*, 2019, **48**, 885-907.
21. K. Sun, D. M. Ginosar, T. He, Y. Zhang, M. Fan and R. Chen, *Ind. Eng. Chem. Res.*, 2018, **57**, 1768-1789.
22. M. A. Ali, B. Brisdon and W. J. Thomas, *Appl. Catal., A*, 2003, **252**, 149-162.
23. B. Burger, K. Haas-Santo, M. Hunger and J. Weitkamp, *Chem. Eng. Technol.*, 2000, **23**, 322-324.
24. M. M. Pereira, E. S. Gomes, A. V. Silva, A. B. Pinar, M.-G. Willinger, S. Shanmugam, C. Chizallet, G. Laugel, P. Losch and B. Louis, *Chem. Sci.*, 2018, **9**, 6532-6539.
25. Y. Jiao, L. Forster, S. Xu, H. Chen, J. Han, X. Liu, Y. Zhou, J. Liu, J. Zhang, J. Yu, C. D'Agostino and X. Fan, *Angew. Chem. Int. Ed.*, 2020, **59**, 19478-19486.
26. V. N. Romannikov, V. M. Mastikhin, S. Hočevár and B. Držaj, *Zeolites*, 1983, **3**, 311-320.
27. G. Majano, A. Darwiche, S. Mintova and V. Valtchev, *Ind. Eng. Chem. Res.*, 2009, **48**, 7084-7091.
28. W. Chaikittisilp, Y. Suzuki, R. R. Mukti, T. Suzuki, K. Sugita, K. Itabashi, A. Shimojima and T. Okubo, *Angew. Chem. Int. Ed.*, 2013, **52**, 3355-3359.
29. R. Jain, A. Chawla, N. Linares, J. García Martínez and J. D. Rimer, *Adv. Mater.*, 2021, **33**, 2100897.
30. S. H. Keoh, W. Chaikittisilp, K. Muraoka, R. R. Mukti, A. Shimojima, P. Kumar, M. Tsapatsis and T. Okubo, *Chem. Mater.*, 2016, **28**, 8997-9007.
31. L. Meng, X. Zhu, W. Wannapakdee, R. Pestman, M. G. Goesten, L. Gao, A. J. F. van Hoof and E. J. M. Hensen, *J. Catal.*, 2018, **361**, 135-142.
32. F. Crea, R. Aiello, A. Nastro and J. B. Nagy, *Zeolites*, 1991, **11**, 521-527.
33. L. Zhang, A. N. C. v. Laak, P. E. d. Jongh and K. P. d. Jong, *Microporous Mesoporous Mater.*, 2009, **126**, 115-124.
34. L. A. Villaescusa, J. Li, Z. Gao, J. Sun and M. A. Camblor, *Angew. Chem. Int. Ed.*, 2020, **132**, 11379-11382.
35. M. Pan, J. Zheng, Y. Ou, Q. Wang, L. Zhang and R. Li, *Microporous Mesoporous Mater.*, 2021, **316**, 110983.

36. N. Ren, B. Subotić, J. Bronić, Y. Tang, M. Dutour Sikirić, T. Mišić, V. Svetličić, S. Bosnar and T. Antonić Jelić, *Chem. Mater.*, 2012, **24**, 1726-1737.
37. D. P. Serrano, J. Aguado, G. Morales, J. M. Rodríguez, A. Peral, M. Thommes, J. D. Epping and B. F. Chmelka, *Chem. Mater.*, 2009, **21**, 641-654.
38. T. Jiang, F. Wang, X. Zhang, Y. Zhai, G. Lv, Y. Shen and Y. Wu, *Microporous Mesoporous Mater.*, 2021, **321**, 111112.
39. T. Ikuno, W. Chaikittisilp, Z. Liu, T. Iida, Y. Yanaba, T. Yoshikawa, S. Kohara, T. Wakihara and T. Okubo, *J. Am. Chem. Soc.*, 2015, **137**, 14533-14544.
40. L. Meng, X. Zhu, B. Mezari, R. Pestman, W. Wannapakdee and E. J. M. Hensen, *ChemCatChem*, 2017, **9**, 3942-3954.
41. R. Van Grieken, J. Sotelo, J. Menendez and J. Melero, *Microporous Mesoporous Mater.*, 2000, **39**, 135-147.
42. R. Zhang, P. Zhao, L. Han, J. Wang and L. Zhao, *Microporous Mesoporous Mater.*, 2021, **312**, 110754.
43. K. F. M. G. J. Scholle, W. S. Veeman, P. Frenken and G. P. M. van der Velden, *Appl. Catal.*, 1985, **17**, 233-259.
44. C.-T. Chen, K. Iyoki, Y. Yonezawa, T. Okubo and T. Wakihara, *J. Phys. Chem. C*, 2020, **124**, 11516-11524.
45. S. L. Burkett and M. E. Davis, *J. Phys. Chem. B*, 1994, **98**, 4647-4653.
46. G. Feng, P. Cheng, W. Yan, M. Boronat, X. Li, J.-H. Su, J. Wang, Y. Li, A. Corma, R. Xu and J. Yu, *Science*, 2016, **351**, 1188-1191.
47. M. Kovalakova, B. Wouters and P. Grobet, *Microporous Mesoporous Mater.*, 1998, **22**, 193-201.
48. X. Liu and Q. Luo, *J. Phys. Chem. C*, 2017, **121**, 13211-13217.
49. J. B. Nagy, Z. Gabelica and E. G. Derouane, *Zeolites*, 1983, **3**, 43-49.
50. V. P. Valtchev and K. N. Bozhilov, *J. Am. Chem. Soc.*, 2005, **127**, 16171-16177.
51. V. Valtchev, S. Rigoleto and K. N. Bozhilov, *Microporous Mesoporous Mater.*, 2007, **101**, 73-82.
52. B. Subotić and A. Graovac, in *Stud. Surf. Sci. Catal.*, eds. B. Držaj, S. Hočevar and S. Pejovnik, Elsevier, 1985, vol. 24, pp. 199-206.
53. A. Palčić, J. Bronić, Đ. Brlek and B. Subotić, *CrystEngComm*, 2011, **13**, 1215-1220.
54. C. Jo, J. Jung, H. S. Shin, J. Kim and R. Ryoo, *Angew. Chem. Int. Ed.*, 2013, **52**, 10014-10017.
55. M. Peng, Z.-Q. Wang, J. Huang, M. Shen, J. Jiang, H. Xu, Y. Ma, B. Hu, X.-Q. Gong, H.-H. Wu and P. Wu, *Chem. Mater.*, 2021, **33**, 6934-6941.
56. D. Xu, Y. Ma, Z. Jing, L. Han, B. Singh, J. Feng, X. Shen, F. Cao, P. Oleynikov, H. Sun, O. Terasaki and S. Che, *Nat. Commun.*, 2014, **5**, 4262.

57. U. Olsbye, S. Svelle, K. Lillerud, Z. Wei, Y. Chen, J. Li, J. Wang and W. Fan, *Chem. Soc. Rev.*, 2015, **44**, 7155-7176.
58. N. Kosinov and E. J. M. Hensen, *Adv. Mater.*, 2020, **32**, 2002565.
59. F. Schmidt, C. Hoffmann, F. Giordano, S. Bordiga, P. Simon, W. Carrillo-Cabrera and S. Kaskel, *J. Catal.*, 2013, **307**, 238-245.
60. J. Kim, M. Choi and R. Ryoo, *J. Catal.*, 2010, **269**, 219-228.
61. S. Ilias and A. Bhan, *ACS Catal.*, 2013, **3**, 18-31.
62. N. Kosinov, A. S. G. Wijkema, E. Uslamin, R. Rohling, F. J. A. G. Coumans, B. Mezari, A. Parastayev, A. S. Poryvaev, M. V. Fedin, E. A. Pidko and E. J. M. Hensen, *Angew. Chem. Int. Ed.*, 2018, **57**, 1016-1020.
63. D. Kerstens, B. Smeyers, J. Van Waeyenberg, Q. Zhang, J. Yu and B. F. Sels, *Adv. Mater.*, 2020, **32**, 2004690.
64. Y. Wu, L. Emdadi, S. C. Oh, M. Sakbodin and D. Liu, *J. Catal.*, 2015, **323**, 100-111.
65. N. Kosinov, E. A. Uslamin, L. Meng, A. Parastayev, Y. Liu and E. J. M. Hensen, *Angew. Chem. Int. Ed.*, 2019, **58**, 7068-7072.
66. M. Milanesio, G. Artioli, A. F. Gualtieri, L. Palin and C. Lamberti, *J. Am. Chem. Soc.*, 2003, **125**, 14549-14558.



# Appendix C

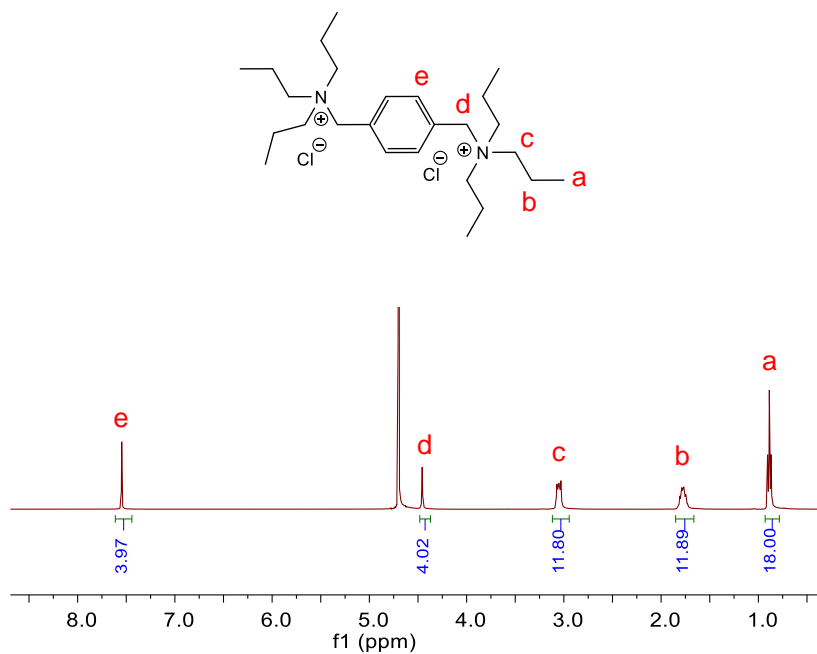


**Figure C1.** Liquid-state  $^1\text{H}$  NMR spectrum of  $\text{Pr}_3\text{N-benzyl-NPr}_3$  in  $\text{D}_2\text{O}$ .

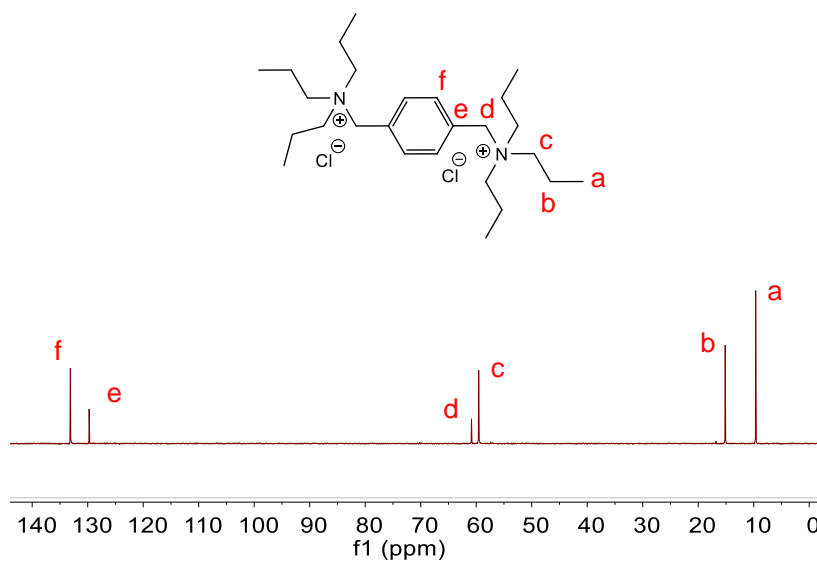


**Figure C2.** Liquid-state  $^{13}\text{C}$  NMR spectrum of  $\text{Pr}_3\text{N-benzyl-NPr}_3$  in  $\text{D}_2\text{O}$ .

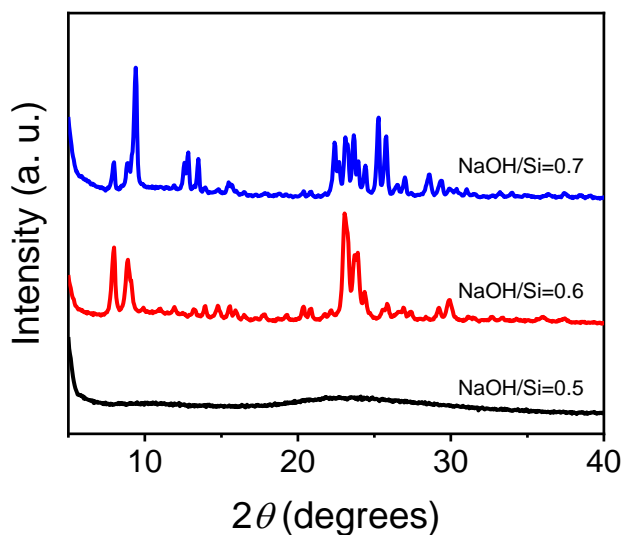


**Figure C3.** XRD patterns of solid products obtained at different NaOH/Si molar ratios. The initial gel molar composition: 12 SiO<sub>2</sub>: 0.545 Al<sub>2</sub>O<sub>3</sub>: x Na<sub>2</sub>O: 1.2 OSDA: 480 H<sub>2</sub>O (Si/Al=11; x=3-4.2). All the syntheses were performed at 160 °C for 7 days under tumbling (50 rpm).

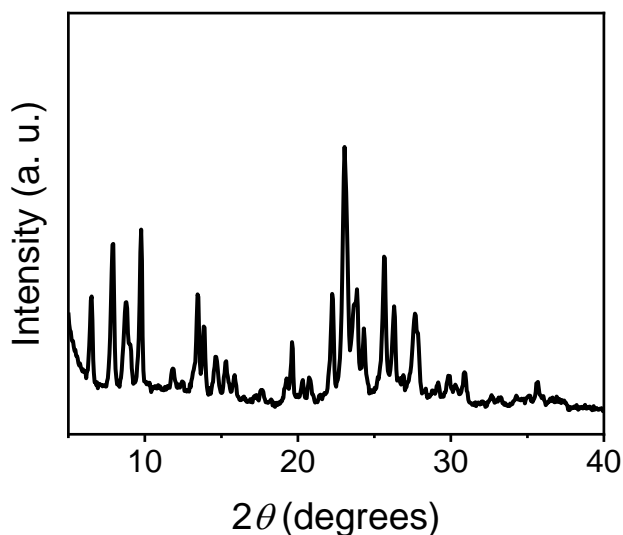


**Figure C4.** The XRD pattern of solid product obtained by using TPABr. The initial gel molar composition: 12 SiO<sub>2</sub>: 0.545 Al<sub>2</sub>O<sub>3</sub>: 3.6 Na<sub>2</sub>O: 2.4 TPABr: 480 H<sub>2</sub>O (Si/Al=11). The synthesis was performed at 160 °C for 7 days under tumbling (50 rpm).

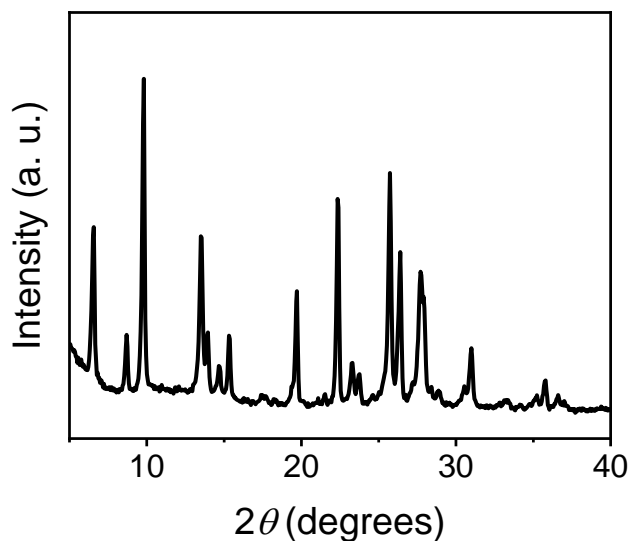


**Figure C5.** The XRD pattern of solid product obtained in the absence of OSDA. The initial gel molar composition: 12 SiO<sub>2</sub>: 0.545 Al<sub>2</sub>O<sub>3</sub>: 3.6 Na<sub>2</sub>O: 480 H<sub>2</sub>O (Si/Al=11). The synthesis was performed at 160 °C for 1 day under tumbling (50 rpm).

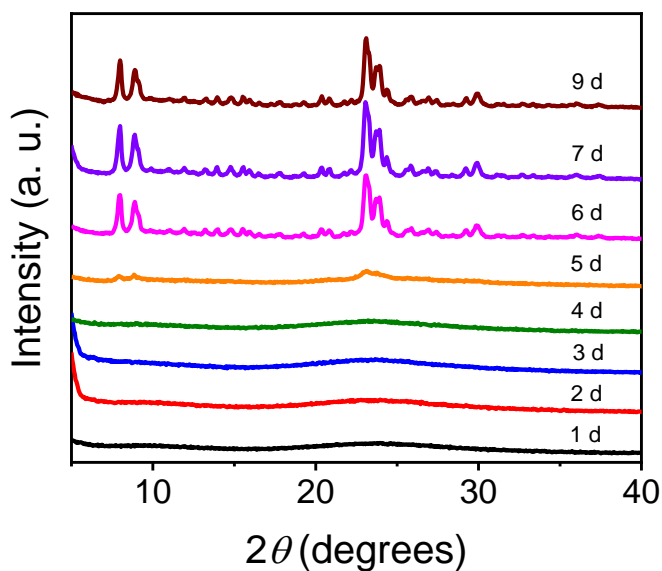


**Figure C6.** XRD patterns of solid products obtained at different crystallization time. The initial gel molar composition: 12 SiO<sub>2</sub>: 0.545 Al<sub>2</sub>O<sub>3</sub>: 3.6 Na<sub>2</sub>O: 1.2 OSDA: 480 H<sub>2</sub>O (Si/Al=11). All the syntheses were performed at 160 °C under tumbling (50 rpm).

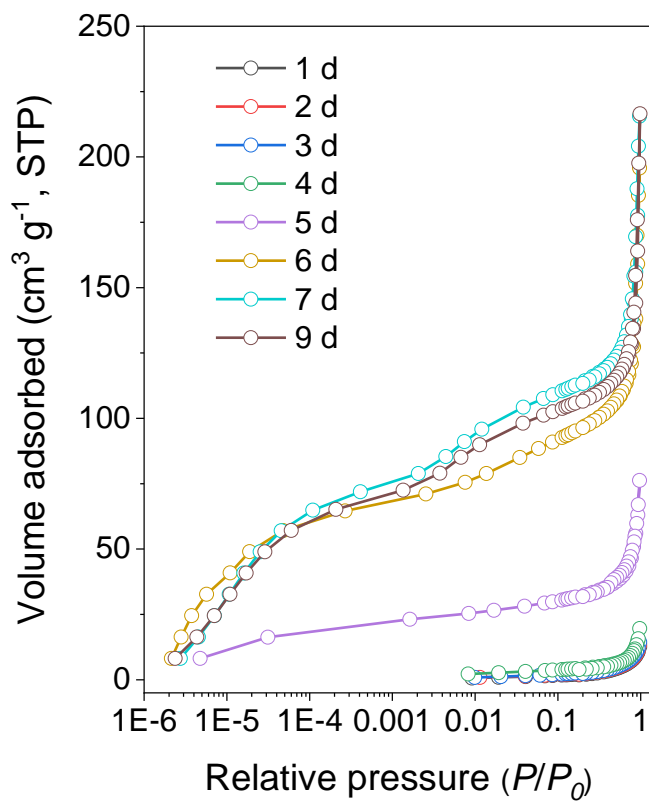


**Figure C7.** Ar physisorption isotherms of calcined solid products obtained at different crystallization time during the synthesis of ZSM-5-11.

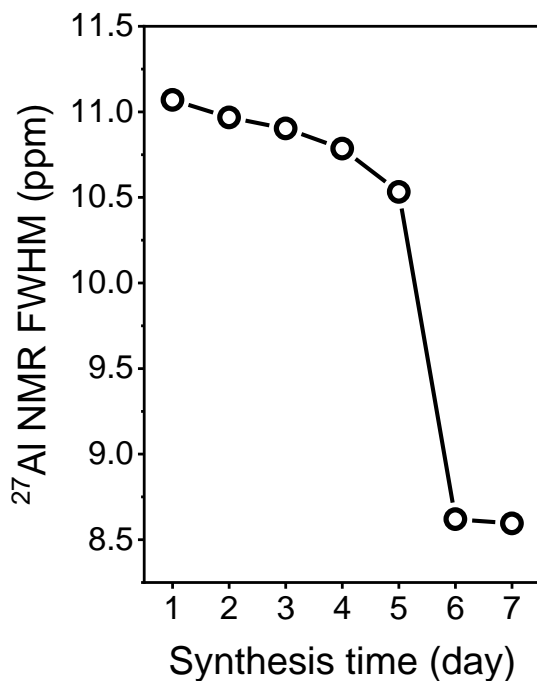


**Figure C8.** Full width at half-maximum (FWHM) of  $^{27}\text{Al}$  NMR spectra of solid products obtained at different crystallization time during the synthesis of ZSM-5-11.

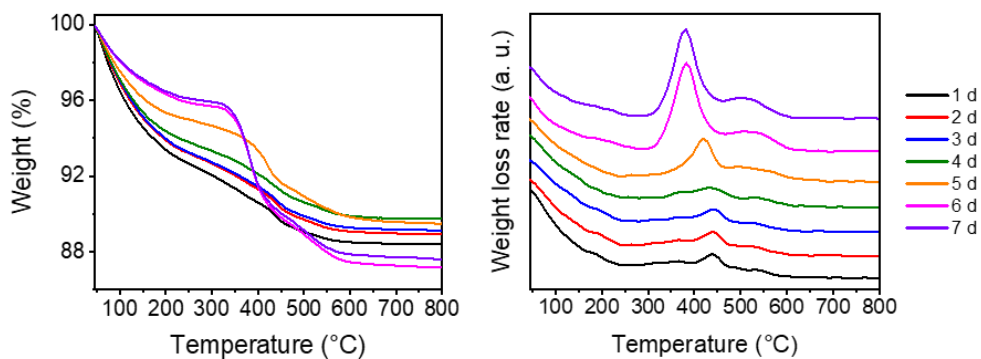


**Figure C9.** TG (left) and DTG (right) curves of samples obtained at different crystallization time during the synthesis of ZSM-5-11.

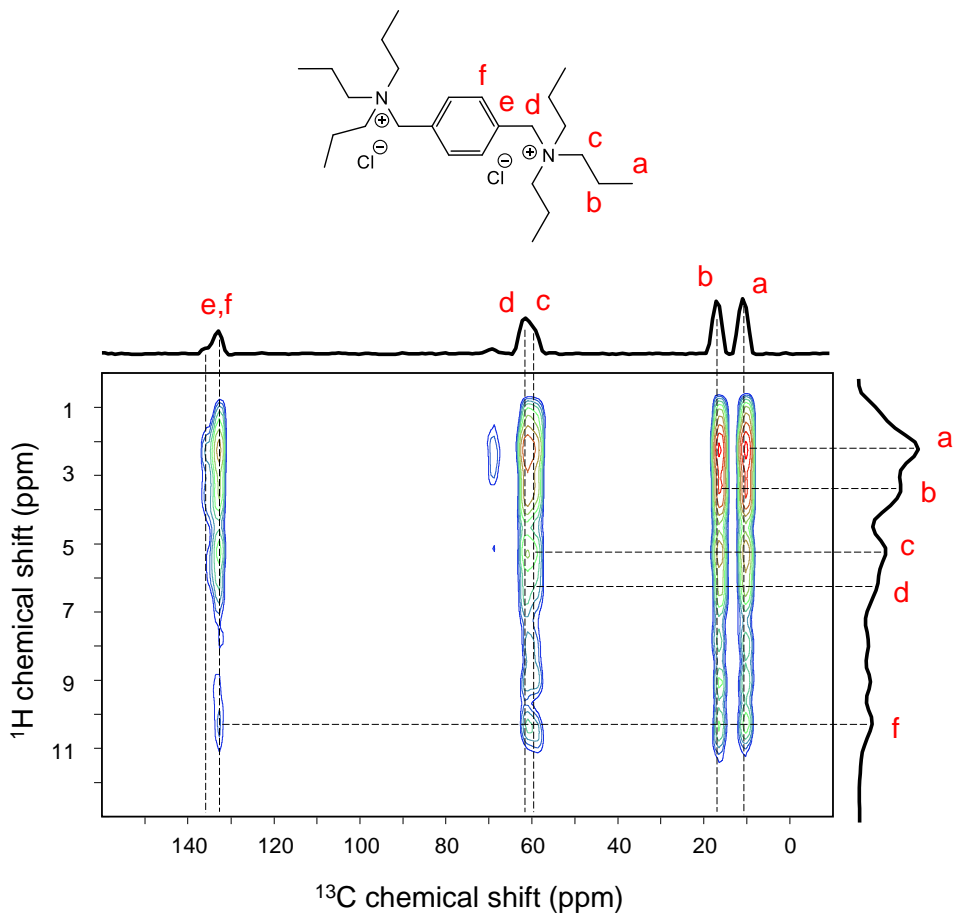


**Figure C10.**  $^1\text{H}$ - $^{13}\text{C}$  HETCOR NMR spectrum of  $\text{Pr}_3\text{N-benzyl-NPr}_3$ .

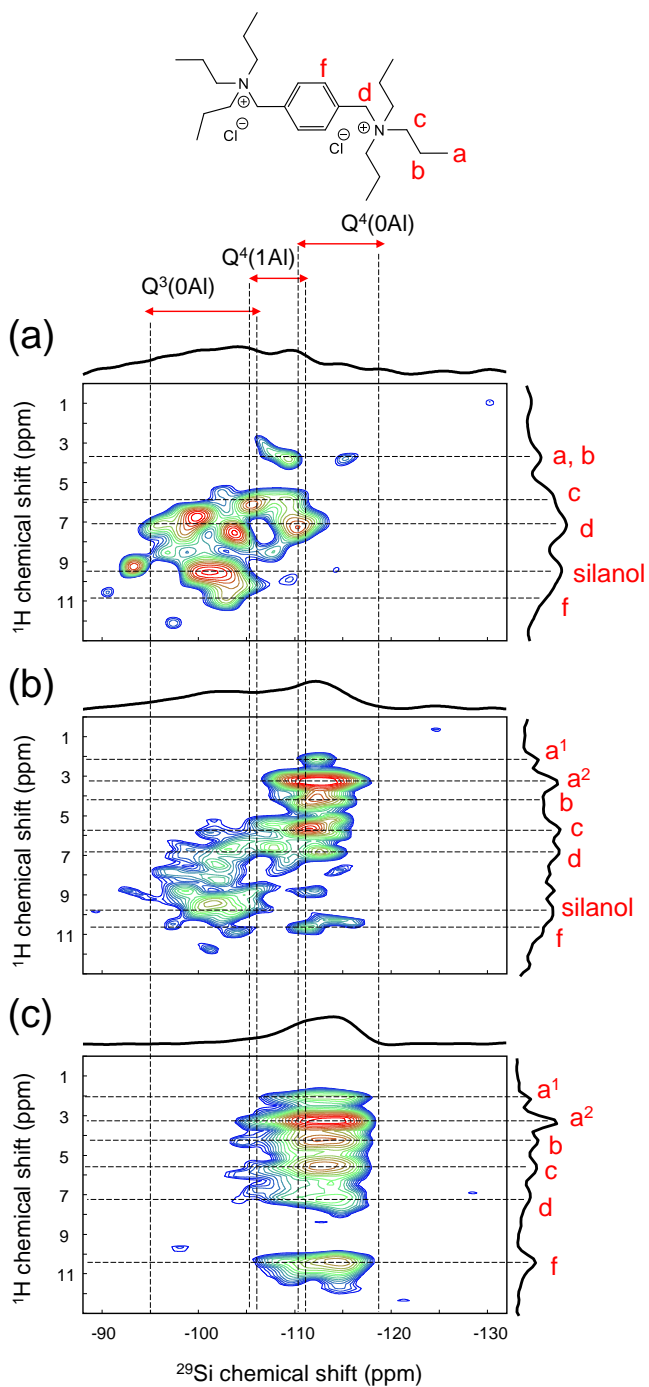


**Figure C11.**  $^1\text{H}$ - $^{29}\text{Si}$  HETCOR NMR spectra of obtained samples during the synthesis of ZSM-5-11: (a) ZSM-5-11-(3 d); (b) ZSM-5-11-(5 d); (c) ZSM-5-11-(7 d).

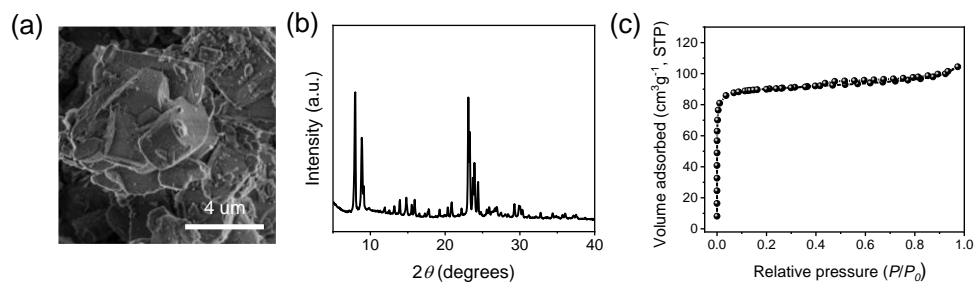


**Figure C12.** (a) SEM image, (b) XRD pattern and (c) Ar physisorption isotherm of calcined ZSM-5-Con.

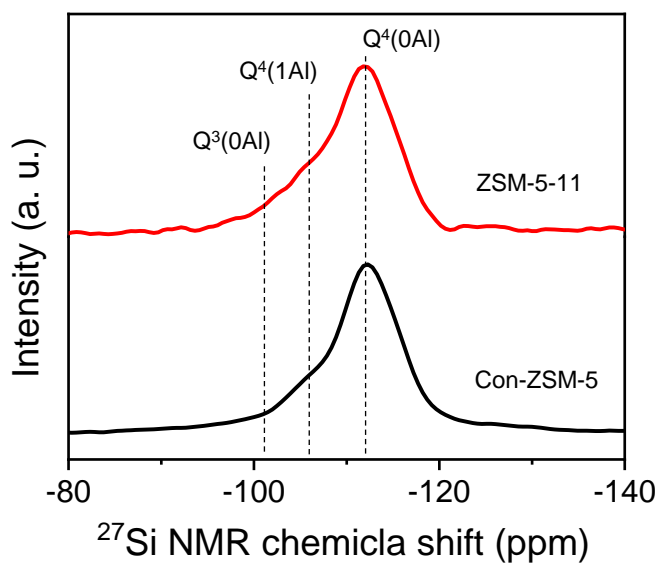


**Figure C13.**  $^{29}\text{Si}$  MAS NMR spectra of calcined ZSM-5-11 and ZMM-5-Con.



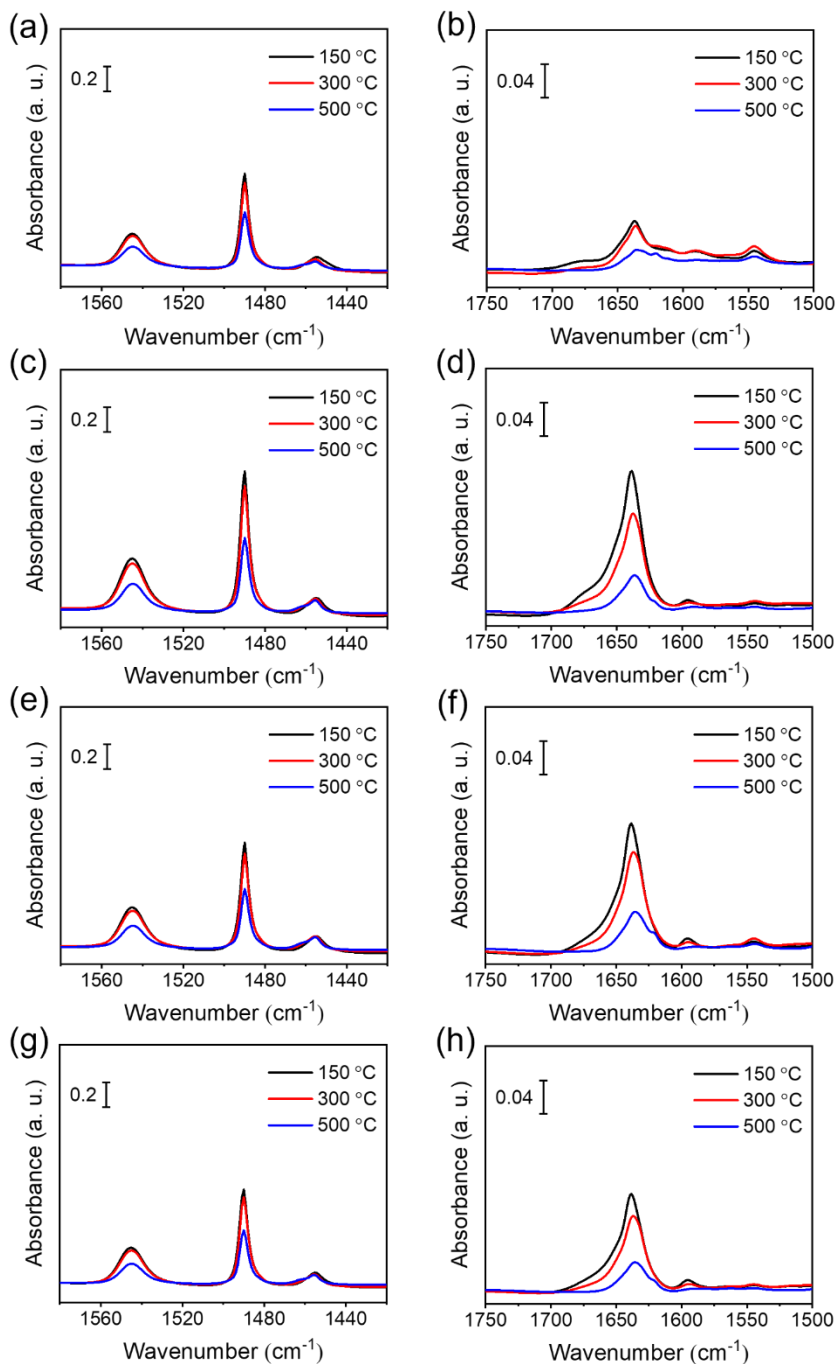


**Figure C14.** IR spectra of pyridine (left) and 2,4,6-collidine (right) adsorbed on: (a and b) ZSM-5-Con, (c and d) ZSM-5-11, (e and f) ZSM-5-13 and (g and h) ZSM-5-15.

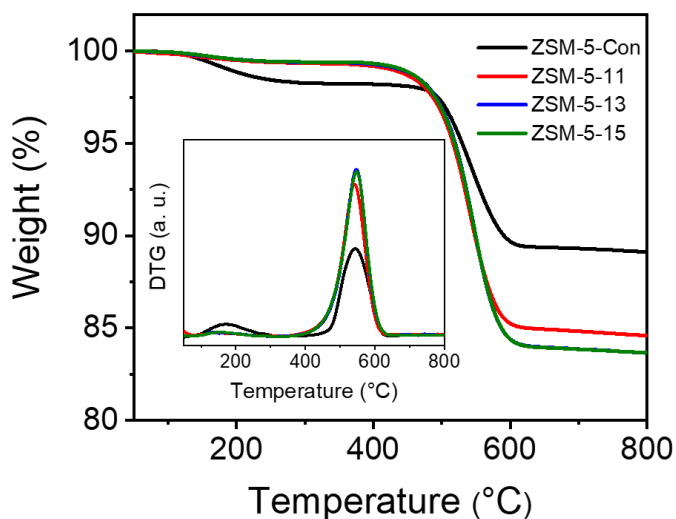


**Figure C15.** TG and DTG (inset) profiles of spent catalysts after methanol-to-hydrocarbons (MTH) reaction.

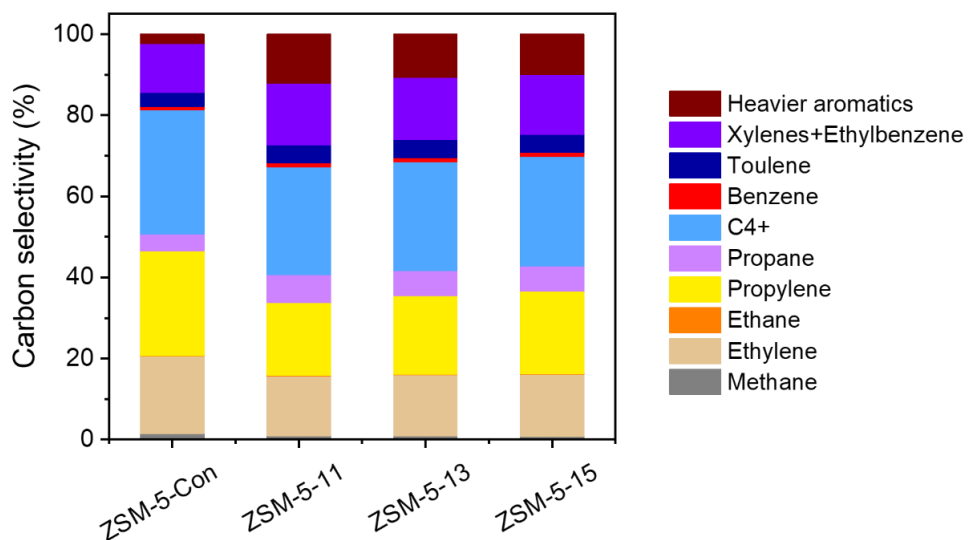


**Figure C16.** Product selectivity of ZSM-5 catalysts for MTH reaction after 0.5 h time on stream. The heavier aromatics include n-propylbenzene, 1,3,5-trimethylbenzene, indane and other unidentified heavy aromatics.

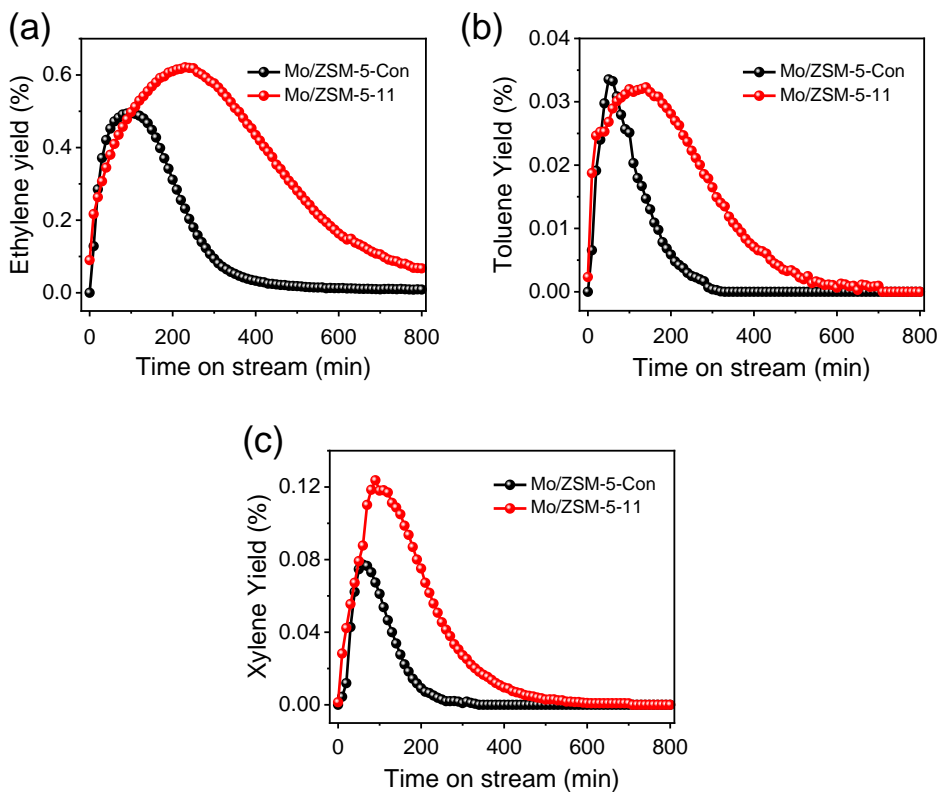


**Figure C17.** Non-oxidative dehydroaromatization of methane (MDA) over Mo/ZSM-5 catalysts: (a) yield of ethylene and (b) yield of toluene and (c) yield of xylene.

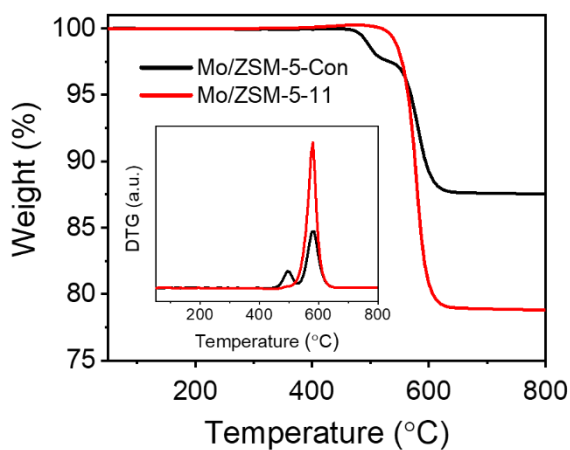


**Figure C18.** TG and DTG (inset) profiles of spent catalysts after MDA reaction.

**Table C1.** Product yields and textural properties of calcined ZSM-5 zeolites with different Si/Al ratios.

Sample	Yield (%) <sup>a</sup>	S <sub>BET</sub> (m <sup>2</sup> g <sup>-1</sup> )	V <sub>tot</sub> (cm <sup>3</sup> g <sup>-1</sup> )	V <sub>micro</sub> (cm <sup>3</sup> g <sup>-1</sup> ) ( <i>t</i> -plot)	V <sub>meso</sub> (cm <sup>3</sup> g <sup>-1</sup> ) ( <i>BJH</i> )	S <sub>ext</sub> (m <sup>2</sup> g <sup>-1</sup> ) ( <i>t</i> -plot)
ZSM-5-15	94	325	0.24	0.10	0.12	86
ZSM-5-13	96	362	0.25	0.11	0.11	93
ZSM-5-11	99	349	0.27	0.11	0.14	87

<sup>a</sup> Based on the inorganic sources introduced in the initial gel.

**Table C2.** Textural properties of calcined solid products obtained at different crystallization time during the synthesis of ZSM-5-11.

Sample	S <sub>BET</sub> (m <sup>2</sup> g <sup>-1</sup> )	V <sub>micro</sub> (cm <sup>3</sup> g <sup>-1</sup> ) ( <i>t</i> -plot)
1 d	8	0
2 d	10	0
3 d	10	0
4 d	14	0
5 d	100	0.02
6 d	299	0.08
7 d	349	0.11
9 d	328	0.11

**Table C3.** Organic template content within solid products obtained at different crystallization time during the synthesis of ZSM-5-11.

Sample	Organic template content (wt%) <sup>a</sup>
1 d	4.2
2 d	4.2
3 d	4.1
4 d	4.1
5 d	5.4
6 d	8.6
7 d	8.4

<sup>a</sup> Determined by the weight loss between 250 °C and 700 °C of TG results.

**Table C4.** Textural properties ZSM-5-Con.

Sample	S <sub>BET</sub> (m <sup>2</sup> g <sup>-1</sup> )	V <sub>tot</sub> (cm <sup>3</sup> g <sup>-1</sup> )	V <sub>micro</sub> (cm <sup>3</sup> g <sup>-1</sup> ) ( <i>t</i> -plot)	V <sub>meso</sub> (cm <sup>3</sup> g <sup>-1</sup> ) ( <i>BJH</i> )	S <sub>ext</sub> (m <sup>2</sup> g <sup>-1</sup> ) ( <i>t</i> -plot)
ZSM-5-Con	294	0.14	0.10	0.02	29

**Table C5.** Productivity selectivity of MTH reaction after 0.5 h on stream over ZSM-5 catalysts.

Sample	Selectivity (%)							C <sub>2</sub> / C <sub>2=</sub>	C <sub>3</sub> / C <sub>3=</sub>
	CH <sub>4</sub>	C <sub>2</sub> H <sub>4</sub>	C <sub>2</sub> H <sub>6</sub>	C <sub>3</sub> H <sub>6</sub>	C <sub>3</sub> H <sub>8</sub>	C <sub>4+</sub>	Aromatics		
ZSM-5-Con	1.5	19.1	0.1	25.9	4.2	30.5	18.7	0.006	0.160
ZSM-5-11	1.0	14.7	0.2	18.0	6.8	26.6	32.7	0.014	0.380
ZSM-5-13	0.9	15.1	0.2	19.3	6.2	26.9	31.4	0.012	0.320
ZSM-5-15	0.8	15.3	0.2	20.4	6.1	27.1	30.1	0.011	0.300

**Table C6.** Total product yields of MDA reaction over Mo/ZSM-5 catalysts.

Sample	Total yield (mmol/g <sub>cat</sub> )						
	C <sub>2</sub> H <sub>4</sub>	C <sub>2</sub> H <sub>6</sub>	C <sub>6</sub> H <sub>6</sub>	C <sub>7</sub> H <sub>8</sub>	C <sub>8</sub> H <sub>10</sub>	C <sub>10</sub> H <sub>8</sub>	Coke
Mo/ZSM-5-Con	4.8	0.7	14.2	0.2	0.4	5.4	10.8
Mo/ZSM-5-11	12.3	0.5	33.4	0.4	1.1	13.7	20.7

**Table C7.** Overall product selectivity and total amounts of converted methane of MDA reaction over Mo/ZSM-5 catalysts.

Sample	Carbon selectivity (%)							Total methane converted (mmol/g <sub>cat</sub> )
	C <sub>2</sub> H <sub>4</sub>	C <sub>2</sub> H <sub>6</sub>	C <sub>6</sub> H <sub>6</sub>	C <sub>7</sub> H <sub>8</sub>	C <sub>8</sub> H <sub>10</sub>	C <sub>10</sub> H <sub>8</sub>	Coke	
Mo/ZSM-5-	13.2	1.9	38.9	0.5	1.0	14.8	29.7	36.6
Mo/ZSM-5-	15.0	0.6	40.7	0.5	1.3	16.7	25.2	82.1



# Chapter 5

## **Rigid diquat structure-directing agents for synthesis of ZSM-12 nanocrystals with improved performance in n-paraffins hydroconversion and methanol-to-hydrocarbons reactions**

### **Abstract**

ZSM-12 is an important zeolite used as a catalyst in several industrial hydrocarbon conversion reactions. Facile synthesis of nanocrystalline ZSM-12 with sufficient acidity (low Si/Al ratio) remains a challenge. Here we report the successful synthesis of nanosized ZSM-12 from flexible aluminosilicate initial gels (Si/Al = 20, 50 and 100) using rigid diquatery ammonium compounds (*p*-xylene-bridged bis-methylpyrrolidinium, -methylpiperidinium and -1,2-dimethylimidazolium -) as the organic structure-directing agents (OSDAs). The effective structure-directing ability of these OSDAs for nanocrystalline ZSM-12 synthesis is due to the strong interaction between the OSDA and the growing zeolite framework. The resulting nanocrystalline ZSM-12 zeolites exhibit improved catalytic performance in hydroconversion of n-hexadecane (n-C<sub>16</sub>) and methanol-to-hydrocarbons reactions. TGA analysis of used catalysts and *in situ* IR spectroscopy of intra-zeolite organic species during the MTH reaction revealed that the smaller crystals result in lighter aromatics and less coke deposition due to the higher rate of desorption attributed to the larger external surface.



## 5.1 Introduction

Zeolites are a family of crystalline porous materials with well-defined channels and cavities in the molecular range.<sup>1</sup> Depending on their pore topology and chemical composition, these materials can be useful in many technological applications, mainly in separation, adsorption and catalysis.<sup>2, 3</sup> Despite the many zeolite available from a synthetic point of view, only relatively few of them are used on a commercial scale. ZSM-12 with its one-dimensional system of 12-membered ring (12-MR) pores is used as a shape-selective acid catalyst in petroleum refining reactions such as alkylation and disproportionation of aromatics, hydroisomerization of n-paraffins and cracking of hydrocarbons.<sup>4</sup> The pores in ZSM-12 have a size of  $5.7 \text{ \AA} \times 6.1 \text{ \AA}$  and run in the *b*-direction of the crystal. While the one-dimensional pore topology endows ZSM-12 unique shape-selective properties, it also leads to severe diffusion limitations for reactants and products, lowering the catalytic activity and inefficient use of acid sites in the micropores.<sup>5, 6</sup> The long residence times in such crystals can lead to undesired secondary reactions, giving rise to decreased selectivity or deactivation.<sup>7, 8</sup> A well-known strategy to overcome transport limitations is to decrease the path length of diffusion by reducing the crystal domain size of zeolites, which can be achieved by introducing intracrystalline mesopores or by reducing the size of the zeolite crystal.<sup>9-11</sup> For acid catalysis, the Si/Al ratio is the most important chemical property of zeolites.<sup>12, 13</sup> For instance, highly acidic ZSM-12 (Si/Al < 20) is desirable for the n-decane cracking to achieve high activity,<sup>14</sup> while a specific acidic density is needed to achieve a high isomer yields in the hydroisomerization of n-paraffins.<sup>15, 16</sup>

Various approaches have been devoted to prepare hierarchical ZSM-12 zeolites, such as modification of the synthesis condition, introduction of growth modifiers, employment of new OSDAs or post-synthetic modification.<sup>17-21</sup> However, it still remains a challenge to synthesize hierarchical ZSM-12 zeolites with Si/Al ratios outside the normal 35-100 range. The main reason is that, for conventional ZSM-12 zeolites synthesized with the most commonly employed OSDAs, *i.e.* tetraethylammonium (TEA), methyltriethylammonium (MTEA) and benzytrimethylammonium (BTMA), the lowest Si/Al ratio is ~25.<sup>22-25</sup> The more expensive TEA in the hydroxide form (instead of the bromide) is required to synthesize nanocrystalline ZSM-12 zeolites. Besides, to ensure effective formation of nanosized ZSM-12 by using TEAOH, a highly concentrated gel ( $\text{H}_2\text{O}/\text{Si} < 15$ ) is indispensable to favor nucleation, which makes scale-up synthesis even more challenging.<sup>8, 26</sup> Recently, diquatery ammonium compounds have been demonstrated to be effective templates for the facile synthesis of hierarchical ZSM-12 zeolites due to the strong interaction between the two ammonium centers and the negatively charged aluminosilicate precursors. However, the

effective utilization of these templates for hierarchical ZSM-12 synthesis has been limited to relatively typical Si/Al ratios between 40 and 100.<sup>5, 10, 27-30</sup> Therefore, it is highly desirable to fabricate more effective OSDAs in order to synthesize hierarchical ZSM-12 zeolites with a wider range of Si/Al ratios, especially at the more acidic compositions.

Although zeolite crystallization is a very complex process involving numerous solid-liquid equilibria and silica condensation steps, it has been demonstrated that the highly flexible OSDA allows the synthesis of zeolites with different topologies.<sup>31-34</sup> For example, Weckhuysen and co-workers demonstrated that the occluded TEA can adopt two distinct conformations with different fractions depending on the templated zeolitic topology (BEA and MOR) as well as the framework heteroatoms.<sup>35</sup> However, the molecular flexibility in terms of conformation of OSDA can impede host-guest specificity, therefore resulting in mixtures of different zeolite phases. This can be illustrated by the formation of Beta zeolite when synthesizing ZSM-12 at Si/Al gel ratios lower than 30 with TEOH as the OSDA.<sup>22</sup> The use of conformationally rigid and bulky organic molecule as OSDA can lead to the selective formation of particular zeolites due to a host-guest specificity.<sup>36</sup> As an example, Xiao and co-workers reported the direct synthesis of IWR zeolite using *p*-phenylenedimethylene-bis(N-methylpyrrolidinium), which is more rigid than the commonly used and flexible hexamethonium OSDA.<sup>37</sup> Motivated by these previous studies, we explored the use of rigid OSDA for the synthesis of nanocrystalline ZSM-12 zeolites in a wider range of Si/Al ratios.

In this work, we investigated the direct synthesis of nanosized ZSM-12 zeolites using diquaternary ammonium compounds in conventional hydrothermal synthesis in a broad range of Si/Al ratios. Our starting point was to employ inexpensive diquaternary ammonium compounds more rigid than those multiquaternary ammonium salts used before in ZSM-12 synthesis (Table D1). Another important consideration was that the OSDA should fit MTW channels. This led to the identification of three organic compounds in which *p*-xylene forms the linkage between two quaternary ammonium centers and nitrogen-containing cycles as the end groups (Figure 5.1). These organic compounds were synthesized via a one-step procedure from commercial chemicals and used to prepare zeolites from initial gels with Si/Al ratios ranging from 15 to infinity. The resulting zeolites were extensively characterized for their physicochemical properties and evaluated for their catalytic performance in the hydroconversion of *n*-hexadecane (*n*-C<sub>16</sub>) after loading with Pt and in the methanol-to-hydrocarbons (MTH). *In situ* IR spectroscopy was employed to identify the intra-zeolite organic deposits during the MTH reaction.

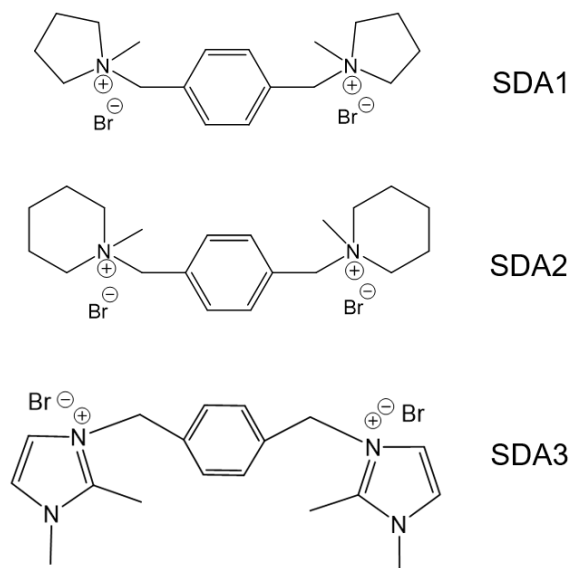


**Figure 5.1.** Organic structure-directing agents (OSDAs) used in this work.

## 5.2 Experimental section

### 5.2.1 Synthesis of OSDA

*P*-phenylenedimethylene-bis(N-methylpyrrolidinium) dibromide (**SDA1**): 0.025 mol of  $\alpha,\alpha'$ -dibromo-*p*-xylene (TCI, > 98.0%) was dissolved in a solution of 100 ml of acetonitrile (Biosolve, 99.8%) and 50 ml of toluene (Alfa Aesar, anhydrous, 99.8%) at 70 °C. Then, 0.1 mol of N-methylpyrrolidine (TCI, > 98.0%) was added under stirring and kept at 70 °C for 2 days under a nitrogen atmosphere. After the reaction, the white product was separated by filtration, followed by washing with diethyl ether (Biosolve, 99.9%). The obtained solid product was dried at 50 °C overnight in a vacuum oven. The product yield was 95%.

*P*-phenylenedimethylene-bis(N-methylpiperidinium) dibromide (**SDA2**): The reaction was carried out as in the synthesis of SDA1, except for the use of N-methylpiperidine (TCI, > 99.0%) instead of N-methylpyrrolidine. The product yield was 90%.

*P*-phenylenedimethylene-bis(1,2-dimethylimidazolium) dibromide (**SDA3**): The reaction was carried out as in the synthesis of SDA1, except for the use of 1,2-dimethylimidazole (TCI, > 98.0%) instead of N-methylpyrrolidine. The product yield was 91%.

The purity of the above three organic templates were verified by liquid-state  $^1\text{H}$  NMR (Figure D1).

## 5.2.2 Synthesis of zeolites

Taking the hydrothermal synthesis with a Si/Al gel ratio of 50 and SDA1 as an example, 0.3 g of sodium hydroxide (Sigma Aldrich,  $\geq 98\%$ ) was dissolved in 15.7 g H<sub>2</sub>O, followed by the addition of 1.09 g SDA1. After sodium hydroxide and organic template were fully dissolved, 0.121 g AlCl<sub>3</sub>·6H<sub>2</sub>O (Alfa Aesar, 99%) was added to the mixture, followed by the addition of 3.75 g of Ludox AS-40 (Sigma Aldrich, 40 wt%) under stirring. The resulting gel had a molar composition of 12 SiO<sub>2</sub>: 0.12 Al<sub>2</sub>O<sub>3</sub>: 1.8 Na<sub>2</sub>O: 1.2 SDA: 480 H<sub>2</sub>O. After vigorous stirring for 3 h at room temperature, the gel was transferred into a 45 ml Teflon-lined stainless-steel autoclave (Parr Instruments). The autoclave was heated in an oven at 160 °C for 4 days under tumbling (50 rpm). After crystallization, the solid product was recovered by centrifugation, washed with demi-water until pH < 8 and dried at 30 °C overnight in a vacuum oven. The organic species in the as-synthesized zeolite was removed by calcination under flowing air at 550 °C for 8 h. To obtain the proton-form, the calcined sample was ion-exchanged with 1.0 M NH<sub>4</sub>NO<sub>3</sub> solution followed by calcination at 550 °C (heating rate 1 °C/min) for 4 h in a O<sub>2</sub> flow (20 vol% in N<sub>2</sub>). Samples are denoted by zeolite topology(x, SDAY) with x indicating the Si/Al gel ratio and y indicating number of SDA. For comparison, a conventional ZSM-12 zeolite was synthesized with methyltriethylammonium chloride (MTEACl, Alfa Aesar, 98%) by following a procedure from the literature.<sup>28</sup> This zeolite was denoted as MTW-Con.

## 5.2.3 Preparation of Pt-containing zeolites

The proton-form of the zeolites were loaded with 0.5 wt% Pt using wet impregnation with an aqueous solution of tetraammineplatinum(II) nitrate (Pt(NH<sub>3</sub>)<sub>4</sub>(NO<sub>3</sub>)<sub>2</sub>, Alfa Aesar). The impregnated zeolites were dried in air followed by calcination at 450 °C (heating rate 0.5 °C/min) for 2 h under O<sub>2</sub> (20 vol% in N<sub>2</sub>).

## 5.2.4 Characterization

The chemical compositions of samples were determined by inductively couple plasma optical emission spectrometry (ICP-OES) performed on a Spectro Blue ICP instrument, after solid dissolution in HF/HNO<sub>3</sub> aqueous solution.

Powder X-ray diffraction (XRD) patterns of samples were recorded on a Bruker D2 Endeavor diffraction system using Cu K $\alpha$  radiation.

Ar physisorption measurements were performed on a Micromeritics ASAP 2020 instrument in static mode at -186 °C. Prior to measurements, the samples were outgassed at 400 °C for 6 h.

Thermogravimetric analyses (TGA) experiments were carried on a TGA/DSC 1 instrument (Mettler Toledo). The sample was heated from 40 °C to 800 °C at a rate of 5 °C/min in 20 ml/min O<sub>2</sub> and 40 ml/min He flow.

Scanning electron microscopy (SEM) and transmission electron microscopy (TEM) images were obtained, respectively, on a FEI Quanta 200F (3 kV) and a FEI Tecnai 20 (200 kV). Annular dark field scanning transmission electron microscopy (ADF-STEM) images were recorded on a TU/e CryoTitan (FEI, now Thermo Fischer Scientific) electron microscope at 300 kV and room temperature.

The acidity of samples was determined by IR spectroscopy on a Bruker Vertex 70v spectrometer by studying the adsorption of pyridine and 2,4,6-collidine. Samples were prepared as a pressed round wafer with a diameter of 13 mm (~10 mg) and pretreated *in situ* at 550 °C for 1 h in artificial air. After pretreatment, the cell was cooled to 150 °C and outgassed until the residual pressure was below  $1 \times 10^{-4}$  mbar. A background spectrum was collected. Pyridine or 2,4,6-collidine was then introduced into the cell until the sample was fully saturated as judged from the IR spectra. Finally, IR spectra were recorded at 150 °C after outgassing for 1 h at 150 °C, 300 °C and 500 °C.

The nature of carbon deposits formed on the catalyst during the MTH reaction was monitored on a Nicolet spectrometer with a MCT detector. Prior to the reaction, self-support wafers (~10 mg) were pretreated *in situ* in He flow at 450 °C for 1 h, followed by cooling to the reaction temperature of 400 °C and taking a background. Then, methanol was fed into the *in situ* IR cell by flowing He (30 ml/min) through a saturator containing methanol (VWR Chemical, ≥ 99.8%) at -10.4 °C. Time-resolved spectra were recorded with a resolution of 4 cm<sup>-1</sup> and a total scan of 64.

Solid-state <sup>27</sup>Al, <sup>29</sup>Si and <sup>13</sup>C MAS NMR measurements were performed on a 11.7 Tesla Bruker DMX500 NMR spectrometer at a frequency of 132, 99 and 125 MHz, respectively. <sup>27</sup>Al NMR spectra were recorded with a 2.5 mm MAS probe at a spinning rate of 25 kHz. <sup>29</sup>Si and <sup>13</sup>C NMR spectra were recorded with a 4 mm MAS probe at a spinning rate of 10 kHz. Two-dimensional <sup>1</sup>H-<sup>29</sup>Si and <sup>1</sup>H-<sup>13</sup>C heteronuclear correlation (HETCOR) NMR spectra were recorded with a contact time of 1 ms and 4 ms, respectively. <sup>27</sup>Al, <sup>29</sup>Si and <sup>13</sup>C chemical shifts were referred to Al(NO<sub>3</sub>)<sub>3</sub>, tetramethylsilane and solid adamantane, respectively.

Liquid-state  $^1\text{H}$  and  $^{13}\text{C}$  NMR measurements were performed on a Bruker 400 MHz spectrometer. Prior to measurements, the organic template was dissolved in deuterated water and transferred into a 5 mm NMR tube.  $^1\text{H}$  and  $^{13}\text{C}$  NMR spectra were collected with a total scans of 32 and 1024, respectively.

## 5.2.5 Catalytic activity measurements

### 5.2.5.1 Hydroconversion of n-hexadecane

The activity of Pt/ZSM-12 catalysts in the hydroconversion of hexadecane ( $n\text{-C}_{16}$ ) were evaluated in a downstream fixed-bed reactor. Typically, the catalyst (sieve fraction 125-250  $\mu\text{m}$ ) was dried in the reactor at 200  $^\circ\text{C}$  for 1 h at atmospheric pressure under flowing He. After cooling the reactor to 50  $^\circ\text{C}$ , the catalyst was reduced *in situ* at 400  $^\circ\text{C}$  using a rate 3  $^\circ\text{C}/\text{min}$  for 1 h in flowing  $\text{H}_2$  at atmospheric pressure. The reactor was then cooled to 150  $^\circ\text{C}$  and pressurized to 60 bar with  $\text{H}_2$ , followed by wetting the packed bed in a liquid  $n\text{-C}_{16}$  flow of 1 ml/min for 10 min. The reaction was carried out at a  $\text{H}_2/n\text{-C}_{16}$  molar ratio of 20 and a weight hourly space velocity (WHSV) of  $\text{g}_{n\text{-C}_{16}} \text{g}_{\text{cat}}^{-1} \text{h}^{-1}$ . The reactor effluent was analyzed every 10  $^\circ\text{C}$  with steady-state activities obtained after  $\sim 5$  h. Products were analyzed using an online gas chromatograph (Thermo Scientific Focus GC) equipped with an FID detector coupled with an Rtx-1 column.

### 2.5.2. Methanol to hydrocarbons

The catalytic performance of the ZSM-12 samples in MTH reactions were tested in a downstream fixed-bed reactor. Samples were pressed, and then crushed and sieved to obtain particles in the range of 250-500  $\mu\text{m}$ . An amount of 45 mg of catalyst (sieve fraction 250-500  $\mu\text{m}$ ) was loaded into a quartz reactor. First, the catalyst was pretreated *in situ* in artificial air at 550  $^\circ\text{C}$  for 1 h, followed by cooling to the reaction temperature of 400  $^\circ\text{C}$ . Methanol was fed to the reactor at a WHSV of 1.1  $\text{h}^{-1}$  by flowing He (30 ml/min) through a saturator containing methanol (VWR Chemicals,  $\geq 99.8\%$ ) at -10.4  $^\circ\text{C}$ . The effluent was analyzed by an online gas chromatograph (Interscience Compact GC). A thermal conductivity detector (TCD) coupled with an RT-Q-Bond pre-column (Restek, 3 m  $\times$  0.32 mm  $\times$  10  $\mu\text{m}$ ) and a Molsieve 5A column (Restek, 10 m  $\times$  0.32 mm  $\times$  30  $\mu\text{m}$ ) was used for the analysis of  $\text{H}_2$  and  $\text{CH}_4$ . A TCD coupled with an RT-Q-Bond pre-column (Restek, 3 m  $\times$  0.32 mm  $\times$  10  $\mu\text{m}$ ) and an RT-Q-Bond column (Restek, 10 m  $\times$  0.32 mm  $\times$  10  $\mu\text{m}$ ) for the analysis of  $\text{C}_2\text{-C}_3$  hydrocarbons. A FID detector coupled with Rtx-1 column (Restek, 15 m  $\times$  0.32 mm  $\times$  1  $\mu\text{m}$ ) was used to analyze heavier hydrocarbons ( $\text{C}_{4+}$ ). Dimethyl ether was considered as a reactant.

## 5.3 Results and discussion

### 5.3.1 Zeolite synthesis and characterization

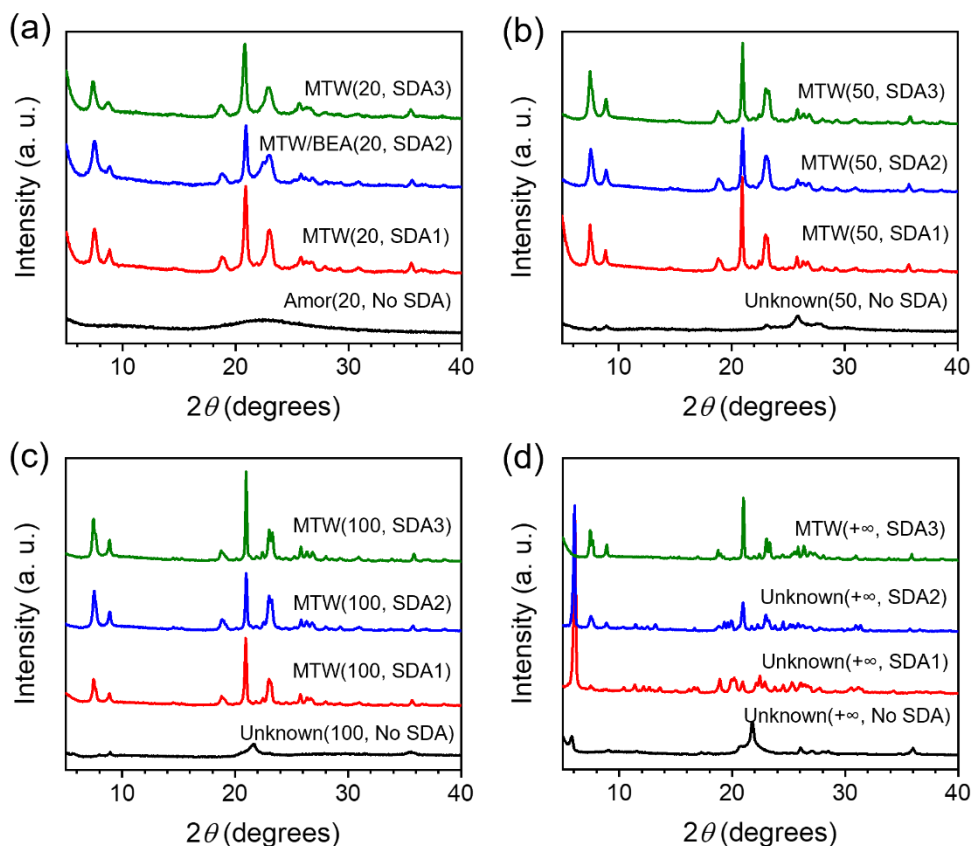


**Figure 5.2.** XRD patterns of as-synthesized samples.

Figure 5.2 shows XRD patterns of the samples obtained at different Si/Al gel ratios (from 20 to  $+\infty$ ) using the selected OSDAs. At Si/Al gel ratios of 50 and 100, phase-pure ZSM-12 zeolite was obtained in all cases (Figures 5.2b and 5.2c). At a lower Si/Al gel ratio of 20, the use of SDA1 and SDA3 also led to phase-pure ZSM-12 zeolite, whereas a mixture of ZSM-12 and Beta zeolite was formed with SDA2 (Figure 5.2a). Only amorphous product was obtained when the Si/Al gel ratio was decreased to 15 (Figure D2). Starting from a gel without Al, only SDA3 was able to direct ZSM-12 zeolite (Figure 5.2d). We also verified that no ZSM-12 zeolite is formed when organic template was omitted from the synthesis gel.

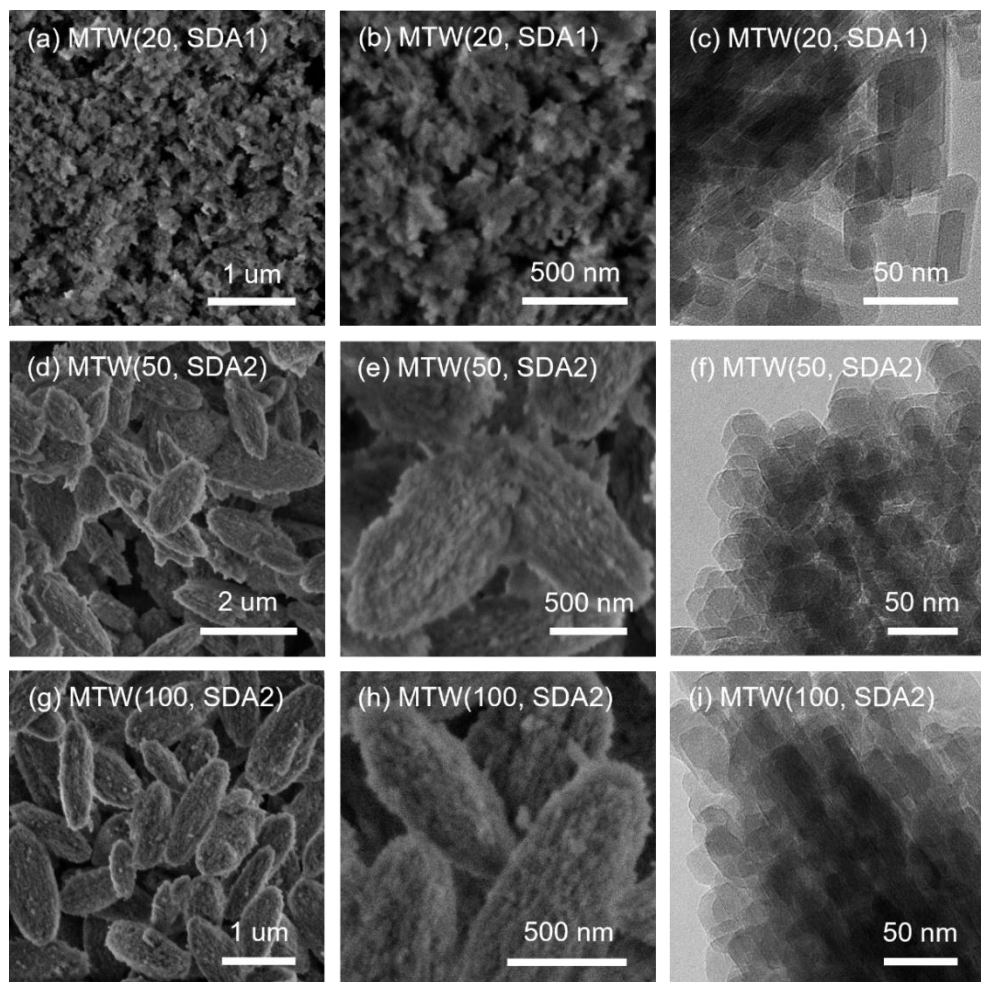


**Figure 5.3.** SEM and TEM images of calcined zeolites: (a-c) MTW(20, SDA1), (d-f) MTW(50, SDA2) and (g-i) MTW(100, SDA2).

Figure 5.3 contains representative SEM and TEM images of the calcined zeolites (additional images in Figures D3-D6). At a Si/Al gel ratio of 20, the zeolite was made up of loosely aggregated crystals with a size less than 50 nm (Figures 5.3a-c and D3). At Si/Al ratios of 50 and 100, the zeolites obtained with SDA2 consisted of rugby-like aggregates of nanoparticles with size smaller than 50 nm (Figures 5.3d-i). More dense aggregation of nanoparticles was observed for MTW(50, SDA1), MTW(50, SDA3), MTW(100, SDA1) and MTW(100, SDA3) (Figures D4 and D5). The all-silica ZSM-12 zeolite, MTW(+∞, SDA3), consists of large micron-sized crystals (Figure D6).



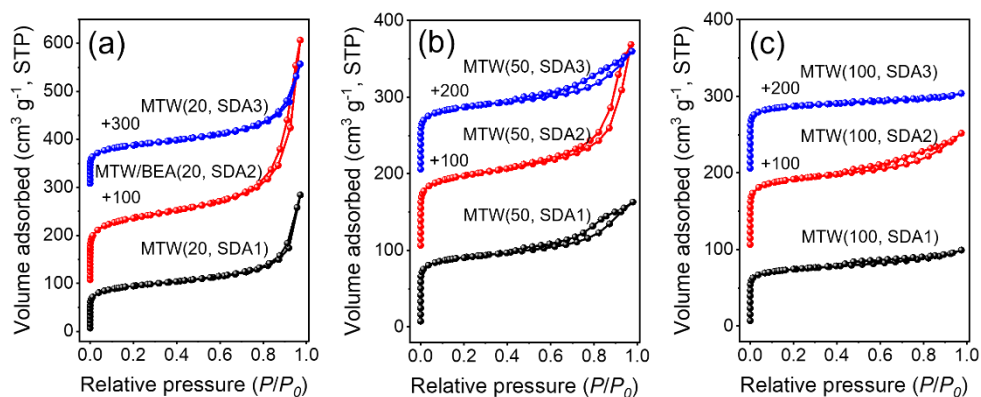


**Figure 5.4.** Ar physisorption isotherms of calcined zeolites.

The textural properties of the calcined samples were determined by Ar physisorption. The Ar physisorption isotherms and micropore size distributions (PSD) are shown in Figures 5.4, D7 and D8. All the isotherms exhibit a steep Ar adsorption below  $P/P_0 = 0.02$ , indicating the presence of micropores.<sup>38</sup> The zeolites synthesized at Si/Al gel ratios of 20 and 50 display the type IV isotherm with a hysteresis loop in the relative pressure higher than 0.6, implying the existence of both micropores and mesopores (Figures 5.4a and 5.4b).<sup>6</sup> A type IV isotherm with a clear hysteresis loop is also observed for MTW(100, SDA2), whereas MTW(100, SDA1) and MTW(100, SDA3) present the typical type I isotherms with limited uptake at higher relative pressure. The characteristic size of 0.55 nm micropores of ZSM-12 can be appreciated from the PSDs given in the supporting information (Figure D7).<sup>26</sup> Notably, besides the main peak at 0.55 nm, the PSD of MTW/BEA(20, SDA2) shows an additional peak at 0.60 nm, which is typical for BEA zeolite.<sup>39</sup> Therefore, consistent with the XRD data, the PSD data confirm the phase purity of the ZSM-12 zeolites except for the zeolite MTW/BEA(20, SDA2), which contained both MTW and BEA. The corresponding textural properties are summarized in Table 5.1. MTW(20, SDA1) shows a large mesopore volume and external surface area ( $0.26 \text{ cm}^3 \text{ g}^{-1}$  and  $116 \text{ m}^2 \text{ g}^{-1}$ , respectively). Comparable data were observed for MTW(20, SDA3) ( $0.24 \text{ cm}^3 \text{ g}^{-1}$  and  $104 \text{ m}^2 \text{ g}^{-1}$ , respectively), which goes along with the rather similar SEM and TEM images for these samples. For synthesis at a Si/Al gel ratio of 50, MTW(50, SDA2) presents a much larger mesopore volume and external surface area ( $0.24 \text{ cm}^3 \text{ g}^{-1}$  and  $103 \text{ m}^2 \text{ g}^{-1}$ , respectively) than MTW(50, SDA1) and MTW(50, SDA3). At a Si/Al gel ratio of 100, MTW(100, SDA2) has the larger mesopore volume and external surface ( $0.09 \text{ cm}^3 \text{ g}^{-1}$  and  $74 \text{ m}^2 \text{ g}^{-1}$ , respectively). In contrast, a substantially lower contribution of mesopores was found for MTW(100, SDA1) and MTW(100, SDA3). This is likely due to the dense aggregation of nanoparticles as observed by SEM characterization.

MTW(+∞, SDA3) also has a small mesopore volume and external surface (0.04 cm<sup>3</sup> g<sup>-1</sup> and 36 m<sup>2</sup> g<sup>-1</sup>, respectively), consistent with its bulky morphology. Thus, the textural data are qualitatively consistent with XRD, SEM and TEM characterization, demonstrating that selective diquatery ammonium compound can be effective templates to direct nanocrystalline ZSM-12 zeolites in a wide range of Si/Al gel ratios from 20 to 100.

**Table 5.1.** Textural properties of calcined zeolites determined by Ar physisorption.

Sample	S <sub>BET</sub> (m <sup>2</sup> g <sup>-1</sup> )	V <sub>tot</sub> (cm <sup>3</sup> g <sup>-1</sup> )	V <sub>micro</sub> (cm <sup>3</sup> g <sup>-1</sup> ) ( <i>t</i> -plot)	V <sub>meso</sub> (cm <sup>3</sup> g <sup>-1</sup> ) ( <i>BJH</i> )	S <sub>ext</sub> (m <sup>2</sup> g <sup>-1</sup> ) ( <i>t</i> -plot)
MTW(20, SDA1)	297	0.37	0.09	0.26	116
MTW/BEA(20, SDA2)	426	0.65	0.10	0.51	178
MTW(20, SDA3)	275	0.33	0.08	0.24	104
MTW(50, SDA1)	283	0.21	0.10	0.10	70
MTW(50, SDA2)	306	0.34	0.09	0.24	103
MTW(50, SDA3)	274	0.21	0.09	0.11	77
MTW(100, SDA1)	230	0.13	0.08	0.04	47
MTW(100, SDA2)	287	0.20	0.10	0.09	74
MTW(100, SDA3)	273	0.14	0.10	0.03	43
MTW(+∞, SDA3)	278	0.15	0.10	0.04	36
MTW-Con	253	0.12	0.10	0.02	33

Next, TGA and <sup>13</sup>C NMR measurements were performed to investigate the inclusion and intactness of OSDAs in the as-synthesized ZSM-12 zeolites, respectively. TG-DTG curves in Figure D9 show a major weight loss at 200-750 °C due to the combustion of the OSDAs within the zeolite samples. Notably, for each OSDA, the combustion peaks shift to higher temperature with decreasing Si/Al ratio, which can be attributed to the stronger interaction between the positively charged OSDA and negatively charged framework Al sites.<sup>40</sup> The <sup>13</sup>C NMR spectra of as-synthesized zeolites are similar to those of the pure OSDAs, indicating that they are stable during the hydrothermal synthesis (Figure D10). The spatial proximity

between the occluded OSDA and the zeolite framework was investigated by 2D  $^1\text{H}$ - $^{13}\text{C}$  and  $^1\text{H}$ - $^{29}\text{Si}$  HETCOR NMR spectra.<sup>41</sup> The proton chemical shift assignments in Figure 5.5b were determined by collecting separate  $^1\text{H}$  NMR spectrum (Figure D1a),  $^1\text{H}$ - $^{13}\text{C}$  CPMAS NMR spectrum (Figure D10a) and  $^1\text{H}$ - $^{13}\text{C}$  HETCOR NMR spectrum (Figure 5.5a). As shown in Figure 5.5b,  $\text{Q}^4(1\text{Al})$  and  $\text{Q}^4(0\text{Al})$  framework species of MTW(50, SDA1) exhibit strongly correlated signals with both ammonium head groups and the benzyl group of SDA1, suggesting strong intermolecular interactions between the zeolite framework and the organic molecule. Therefore, this observation reveals the structure-directing role of the embedded organic template SDA1. In a similar way, the 2D NMR spectra in Figures D11 and D12 also evidence the essential role of SDA2 and SDA3 in directing MTW(50, SDA2) and MTW(50, SDA3), respectively.

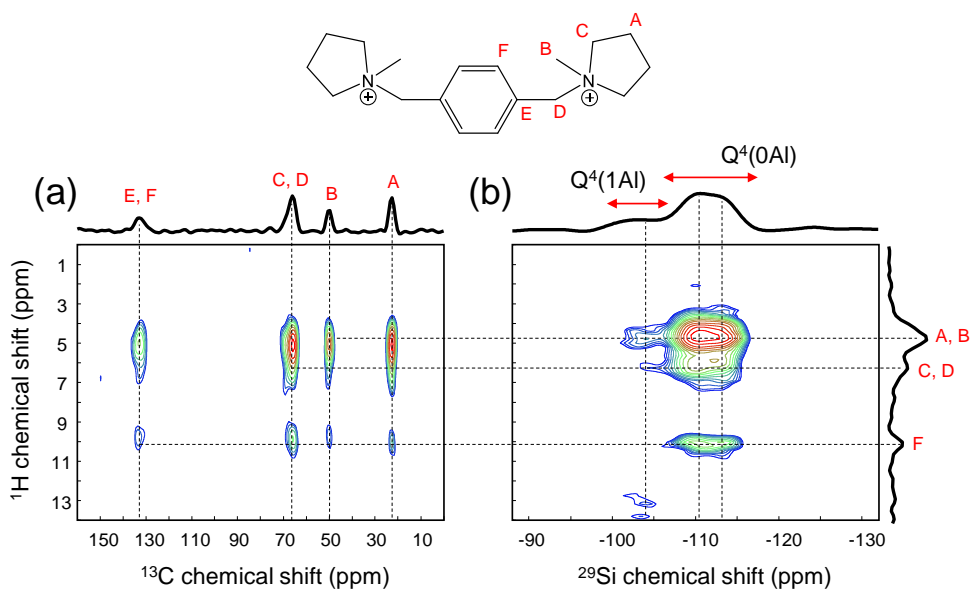


**Figure 5.5.**  $^1\text{H}$ - $^{13}\text{C}$  (a) and  $^1\text{H}$ - $^{29}\text{Si}$  (b) HETCOR NMR spectra of as-synthesized MTW(50, SDA1) zeolite. The assignment to different H atoms in organic molecule SDA1 is indicated in the top panel.

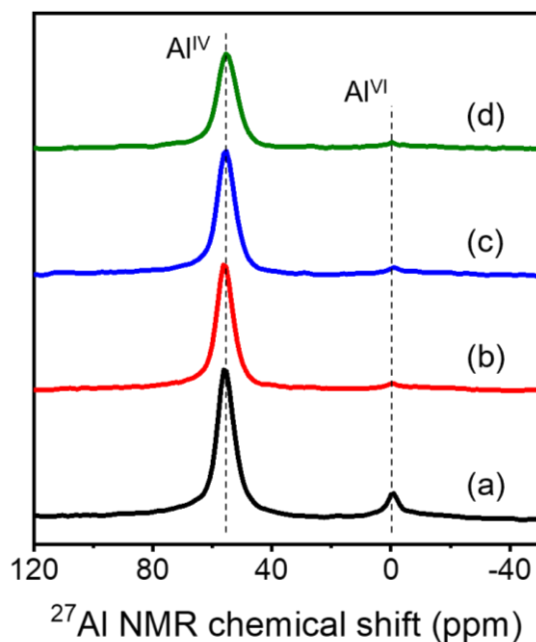


**Figure 5.6.**  $^{27}\text{Al}$  MAS NMR spectra of calcined zeolites: (a) MTW(20, SDA1), (b) MTW(50, SDA2), (c) MTW-Con and (d) MTW(100, SDA2).

Among the set of ZSM-12 zeolites synthesized with different Si/Al gel ratios, MTW(20, SDA1), MTW(50, SDA2) and MTW(100, SDA2) were selected for further study because of their favorable textural properties, *viz.* the largest the external surface. The Si/Al ratios of calcined ZSM-12 zeolites were determined by ICP elemental analysis. The Si/Al ratio of MTW(20, SDA1) is 18.3, which is close to the initial gel ratio of 20. MTW(50, SDA2) and MTW(100, SDA2) have Si/Al ratios of 40.1 and 68.8, respectively. It is observed that the discrepancy between the Si/Al ratios of the initial gel and the zeolite product increases with the increase of the Si/Al gel ratio. A similar phenomenon has also been observed in ZSM-12 synthesis with TEAOH, which is mainly due to the low utilization for silica source.<sup>22</sup> The chemical environment of Al atoms in ZSM-12 zeolites was investigated by  $^{27}\text{Al}$  NMR spectroscopy. The  $^{27}\text{Al}$  NMR spectra in Figure 5.6 are dominated with a main resonance at  $\sim 54$  ppm for all samples, corresponding to framework Al atoms in tetrahedral coordination ( $\text{Al}^{\text{IV}}$ ), while the weak peak at 0 ppm is attributed to extraframework Al atoms in octahedral coordination ( $\text{Al}^{\text{VI}}$ ).<sup>14</sup> Deconvolution of these spectra shows that the Al atoms are mainly incorporated into the zeolite framework ( $> 85\%$ ). Among these samples, MTW(20, SDA1) shows a slightly lower fraction (86%) of  $\text{Al}^{\text{IV}}$ . This is in line with previous studies and due to Al-rich zeolites being more prone to develop extraframework Al species.<sup>42</sup>

**Table 5.2.** Si/Al ratios, fractions of framework Al and acidic properties of the calcined zeolite samples.

Zeolite	Si/Al <sup>a</sup>	Al <sub>F</sub> <sup>b</sup> (%)	[BAS] <sup>c</sup> ( $\mu\text{mol g}^{-1}$ )	[LAS] <sup>d</sup> ( $\mu\text{mol g}^{-1}$ )	[BAS] <sup>e</sup> ( $\mu\text{mol g}^{-1}$ )
MTW(20, SDA1)	18.3	86	736	162	283
MTW(50, SDA2)	40.1	92	436	114	176
MTW-Con	40.0	93	478	97	86
MTW(100, SDA2)	68.8	93	253	48	88

<sup>a</sup> Determined by ICP-OES analysis.

<sup>b</sup> Fraction of framework Al determined by <sup>27</sup>Al NMR.

<sup>c</sup> Density of BAS determined by IR spectra of adsorbed pyridine after evacuation for 1 h at 150 °C.

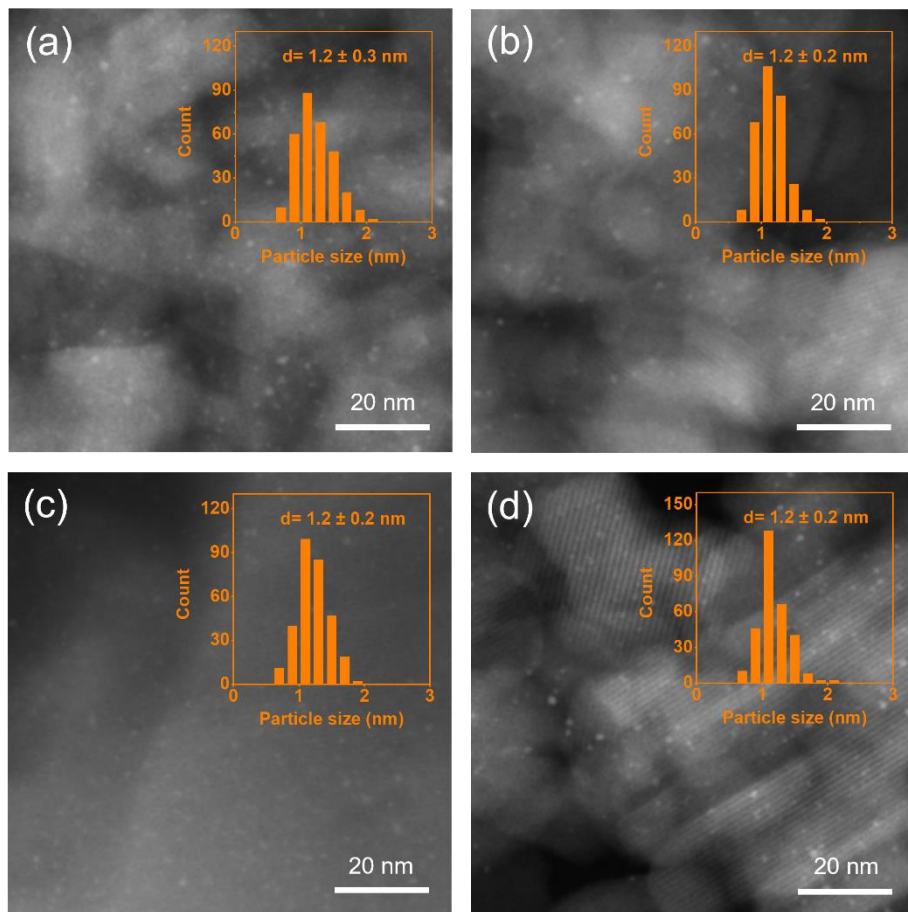
<sup>d</sup> Density of LAS determined by IR spectra of adsorbed pyridine after evacuation for 1 h at 150 °C.

<sup>e</sup> Density of external BAS determined by IR spectra of adsorbed 2,4,6-collidine after evacuation for 1 h at 150 °C.

The total acidity of the zeolites was characterized by IR spectroscopy after pyridine adsorption and subsequent desorption at 150 °C, 300 °C and 500 °C. Quantification of Brønsted acid sites (BAS) and Lewis acid sites (LAS) was determined by the integrated areas of the bands at 1540 cm<sup>-1</sup> and 1450 cm<sup>-1</sup>, respectively.<sup>43</sup> The total BAS density of zeolites follow the sequence MTW(20, SDA1) > MTW-Con > MTW(50, SDA2) > MTW(100, SDA2). MTW(20, SDA1) displays the highest BAS density as expected because of its highest Al content. In addition, the density of BAS on the external zeolite surface was determined by IR spectroscopy of adsorbed 2,4,6-collidine. The quantification of these data are given in Table 5.2. The density of external BAS follows the sequence MTW(20, SDA1) > MTW(50, SDA2) > MTW(100, SDA2) ≈ MTW-Con. Notably, MTW(50, SDA2) displays a much higher external BAS density than MTW-Con, although they present comparable total BAS densities. The most reasonable explanation for this is the much higher external surface area of MTW(50, SDA2).

## 5.3.2 Catalytic activity

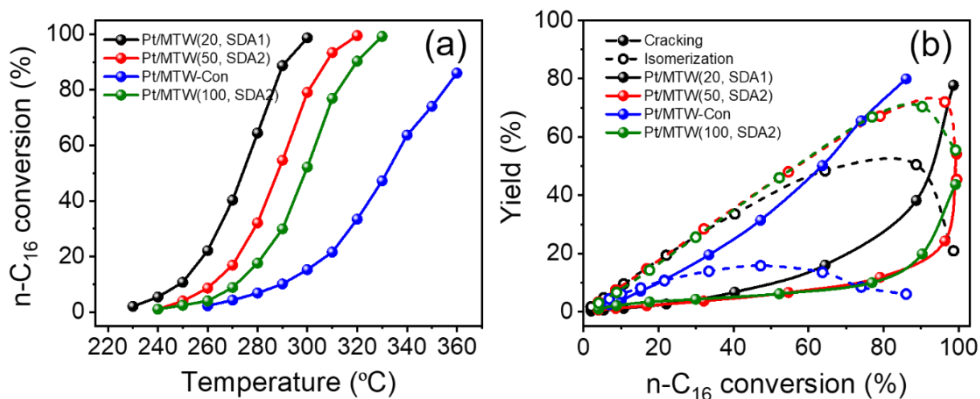
### 5.3.2.1 Hydroconversion of n-hexadecane



**Figure 5.7.** ADF-STEM images of reduced samples: (a) Pt/MTW(20, SDA1), (b) Pt/MTW(50, SDA2), (c) Pt/MTW-Con and (d) Pt/MTW(100, SDA2).

The ZSM-12 zeolites were evaluated for the hydroconversion of n-C<sub>16</sub> after loading 0.5 wt% Pt. This metal loading is generally deemed sufficient to ensure a high enough rate of (de)hydrogenation for the isomerization/cracking reactions on acid sites to limit the overall rate.<sup>44</sup> Element analysis shows that the actual Pt loading amounts are all close to the targeted 0.5 wt%. ADF-STEM images in Figure 5.7 demonstrate that Pt is highly dispersed on all samples with average particle sizes smaller than 2 nm. Therefore, based on the similar metal function for the 4 bifunctional catalysts, catalytic differences in n-C<sub>16</sub> hydroconversion can

be attributed to differences in intrazeolite residence times and acidities, which are related to the acidic zeolite component.



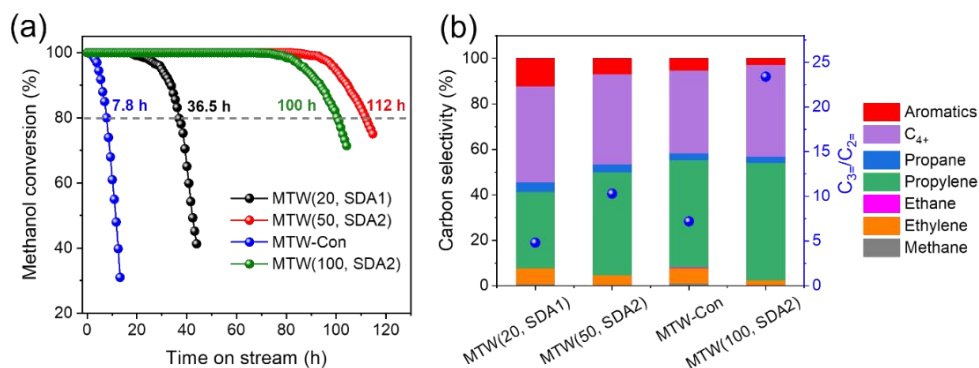
**Figure 5.8.** (a) Conversion of n-C<sub>16</sub> as a function of the reaction temperature and (b) the product yield as a function of n-C<sub>16</sub> conversion.

Figure 5.8a shows the conversion of n-C<sub>16</sub> as a function of reaction temperature. The activity increases in the order Pt/MTW-Con < Pt/MTW(100, SDA2) < Pt/MTW(50, SDA2) < Pt/MTW(20, SDA1). Among the three nanocrystalline zeolites, it can be observed that their activities follow their acidities. Nevertheless, both Pt/MTW(50, SDA2) and Pt/MTW(100, SDA2) are substantially more active than Pt/MTW-Con despite the lower acidity of the nanosized zeolites. As it has been demonstrated that medium and strong BAS are required to catalyze isomerization and cracking reactions,<sup>45</sup> the improved activity of Pt/MTW(50, SDA2) and Pt/MTW(100, SDA2) can be due to favorable texture of the nanocrystalline zeolites. The role of the crystal size on long chain n-paraffin hydroconversion for one-dimensional zeolites has been widely investigated before.<sup>19, 46, 47</sup> For instance, our previous study showed that nanocrystalline MOR zeolite was more active than bulk MOR in the hydroconversion of n-C<sub>16</sub>.<sup>48</sup> Therefore, the lower activity of Pt/MTW-Con can be attributed to a lower accessibility of BAS as a result of the larger crystal size.

Figure 5.8b shows the yield of isomers and cracked products as a function of n-C<sub>16</sub> conversion. For all catalysts, the yield of isomers gradually increases with n-C<sub>16</sub> conversion until a maximum after which cracking rapidly increases. This typical dependence of the product distribution is due to the isomerization of n-alkanes, resulting in the formation of more reactive multibranched isomers, which are prone to cracking.<sup>49</sup> Maximum isomer yields increase in the order Pt/MTW-Con (15.8%) < Pt/MTW(20, SDA1) (50.5%) < Pt/MTW(100, SDA1) (70.4%) < Pt/MTW(50, SDA2) (72.0%). The maximum isomer yields for

nanocrystalline ZSM-12 zeolites are much higher than for bulk Pt/MTW-Con. According to previous studies, reducing the zeolite crystal sizes results in shorter residence time of olefinic intermediates in the micropores as a consequence of the faster desorption from the acidic zeolite, which limits overcracking and henceforth increases the isomer yield.<sup>26, 44</sup> The beneficial effect of nanocrystalline ZSM-12 zeolite is also clear from the more symmetric cracked product distribution as compared to that of Pt/MTW-Con (Figure D16). Among the nanocrystalline zeolites, Pt/MTW(20, SDA1) shows a lower isomer yield than the other two samples. Considering that Pt/MTW(20, SDA1) has the highest external surface area, the lower highest isomer yield is likely due to the high acidity, which impairs the balance between hydrogenation and cracking.<sup>16</sup> Notably, the isomers distribution in Figure D17 shows that the ratio of multi- to mono-branched isomers of 2.8 for Pt/MTW(50, SDA2) higher than the value of 1.8 for Pt/MTW(100, SDA2), although the maximum isomers yield is comparable for these two catalysts. The higher ratio of multi- to mono-branched isomers for Pt/MTW(50, SDA2) is likely due to the higher acidity, which favours the formation of multi-branched products.<sup>45</sup>

### 5.3.2.2 Methanol to hydrocarbons



**Figure 5.9.** (a) MTH performance of ZSM-12 catalysts: (a) methanol conversion as a function of reaction time and (b) product selectivity after 0.5 h time on stream.

The catalytic performance of the nanosized and conventional ZSM-12 zeolites were evaluated in the MTH reaction at a temperature of 400 °C and a WHSV of 1.1 h<sup>-1</sup>. We defined the catalyst lifetime ( $t_{80}$ ) as the time at which the methanol conversion decreases to 80%. Figure 5.9a shows the conversion of methanol as a function of time on stream. Initially, the methanol feed can be fully converted over all catalysts. Deactivation of MTW-Con is rapid with a lifetime of only 7.8 h. Compared to MTW-Con, these three nanosized zeolites exhibit significantly enhanced catalyst lifetime. The lifetime of the catalyst increases in the order



MTW-Con (7.8 h) < MTW(20, SDA1) (36.5 h) < MTW(100, SDA2) (100 h) < MTW(50, SDA2) (112 h). The TG results in Figure D18 show that the coke contents are much higher in used MTW(20, SDA1), MTW(50, SDA2) and MTW(100, SDA2) (7.4%, 7.8% and 6.6%, respectively) than in the used MTW-Con (4.8%), whereas the average coke formation rate of MTW-Con ( $0.172 \text{ mg mg}^{-1} \text{ h}^{-1}$ ) is much higher than these nanosized zeolites ( $0.030\text{-}0.082 \text{ mg mg}^{-1} \text{ h}^{-1}$ ) (Table D3). Compared to MTW-Con, the less acidic MTW(50, SDA2) and MTW(100, SDA2) containing more coke still maintain higher catalytic activity. This indicates a better coke tolerance, which can be attributed to the improved accessibility of acid sites as a consequence of the reduced crystal size.<sup>50</sup> ZSM-12 possesses one-dimensional channels and the acid sites in each micropore are only accessible by the two end of the crystals. This can not only result in rapid coke formation within the zeolite channels, but also easily render the acid sites inaccessible by coke deposition.<sup>21</sup> Therefore, it can be concluded that the significantly longer lifetime of MTW(50, SDA2) and MTW(100, SDA2) than MTW-Con is due to a lower coke formation rate and a higher pore utilization. Notably, MTW(20, SDA2) has a shorter lifetime compared to MTW(50, SDA1) and MTW(100, SDA2), despite its higher external surface area. It is known that a higher acidity can increase the rate of formation of aromatics, which are typically coke precursors.<sup>51</sup> Therefore, the shorter lifetime of MTW(20, SDA1) can be related to the higher acidity, which explains the higher coke formation rate of  $0.082 \text{ mg mg}^{-1} \text{ h}^{-1}$  than MTW(50, SDA2) and MTW(100, SDA2) ( $0.033 \text{ mg mg}^{-1} \text{ h}^{-1}$  and  $0.030 \text{ mg mg}^{-1} \text{ h}^{-1}$ , respectively). The product distribution given in Figure 5.9b and Table D4 shows a much higher aromatics selectivity of 12.1% for MTW(20, SDA1) in comparison to MTW-Con (5.1%), which can be attributed to the higher acidity and the faster desorption of aromatics from smaller crystals. Notably, MTW(100, SDA2) shows a high propylene selectivity (51.6%) and remarkably high  $C_{3=}/C_{2=}$  ratio (23.4) in comparison to the other samples, which is most likely related to the low acidity and short diffusional pathways for this sample.

To better understand the substantial difference in catalytic performance between samples, the intra-zeolite organic compounds formed during the MTH reaction were investigated by *in situ* IR spectroscopy. For this purpose, a wafer (~10 mg) of zeolite sample was placed in an *in situ* cell and exposed to 2 kPa methanol in He (flow of  $30 \text{ ml min}^{-1}$ ). Although the contact time is not accurately determined in this approach, it is expected to be shorter than in the catalytic activity measurements discussed above. Time-resolved spectra recorded at  $400 \text{ }^{\circ}\text{C}$  are depicted in Figure 5.10. For all samples, bands at  $2800\text{-}3100 \text{ cm}^{-1}$  due to C-H stretching vibrations, bands between  $1430\text{-}1650 \text{ cm}^{-1}$  due to C=C vibrations of aromatics and bands at  $1358 \text{ cm}^{-1}$  due to C-H bending vibrations of unsaturated species are observed, indicating the formation of intra-zeolite organic species.<sup>52, 53</sup> The intensity of these bands increases with the

progress of the MTH reaction. The slower change of these bands intensity for MTW(50, SDA1) and MTW(100, SDA2) upon starting the reaction points to a slower formation of such organic species, consistent with the lower coke formation rate determined by TG. In addition, negative bands at  $3580\text{ cm}^{-1}$  in the hydroxyl stretching region appear due to BAS interacting with adsorbates.<sup>54</sup> Notably, for MTW-Con, the strong absorption band at  $1591\text{ cm}^{-1}$  is more prominent than the band at  $1358\text{ cm}^{-1}$ , which is not the case for the three nanosized zeolites. These differences suggest that the intra-zeolite organic species formed over nanosized zeolites contain a substantial amount of highly alkylated aromatic species, which are less condensed than those formed over MTW-Con. The formation of less condensed coke over nanosized zeolites can be due to the faster desorption of aromatics from smaller crystals, whereas such species would easily condense into heavier deposits due to the longer residence time in larger crystals.<sup>51</sup>

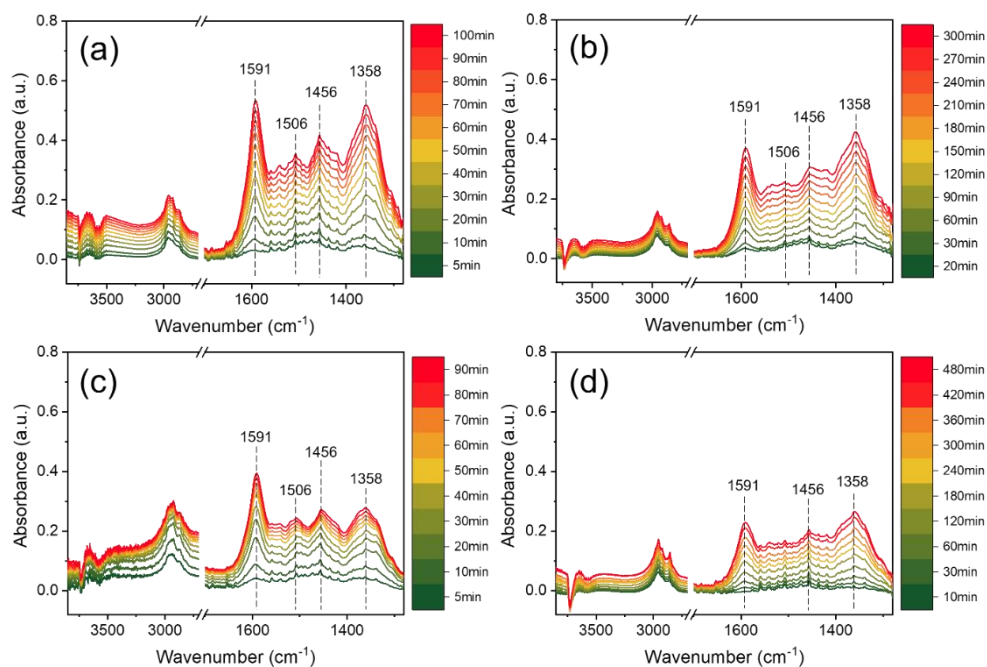


**Figure 5.10.** *In situ* IR spectra recorded during the MTH reaction at  $400\text{ }^{\circ}\text{C}$  over ZSM-12 zeolites: (a) MTW(20, SDA1), (b) MTW(50, SDA2), (c) MTW-Con and (d) MTW(100, SDA2). The spectra were normalized by the weight of the samples.

## 5.4 Conclusions

This work describes the effective synthesis of ZSM-12 in a wide range of Si/Al ratios from 20 to  $+\infty$  by one-step hydrothermal synthesis using rigid non-surfactant diquatery ammonium compounds as the sole OSDA. Nanosized ZSM-12 zeolites were obtained from aluminosilicate gels (Si/Al = 20, 50 and 100), while a reference bulk ZSM-12 sample was obtained from an all-silica gel with SDA3. Strong interaction between the OSDA and the zeolite framework was confirmed by solid-state NMR and TGA. The nanosized ZSM-12 samples show higher activity and significantly improved isomer yields in the hydroconversion of n-C<sub>16</sub> than bulk ZSM-12. The improved performance of nanosized ZSM-12 is due to the reduced residence time in zeolite pores, rendering acid sites more accessible for primary conversion reactions of olefins and at the same time limiting secondary conversion reactions. In the MTH reaction (T = 400 °C and WHSV = 1.1 h<sup>-1</sup>), the nanosized ZSM-12 samples display significantly improved lifetime over bulk ZSM-12. A high propylene selectivity (51.6%) and remarkably high C<sub>3=</sub>/C<sub>2=</sub> ratio (23.4) were obtained over MTW(100, SDA2). TGA analysis of the used catalysts and *in situ* IR spectroscopy of intra-zeolite organic species revealed that nanosizing zeolites leads to a lower concentration of aromatics, reducing the extent of heavy deposits formation. Thus, rigid diquats can be used to obtain ZSM-12 nanocrystals with tunable acidity with a significantly improved catalytic performance.

## 5.5 References

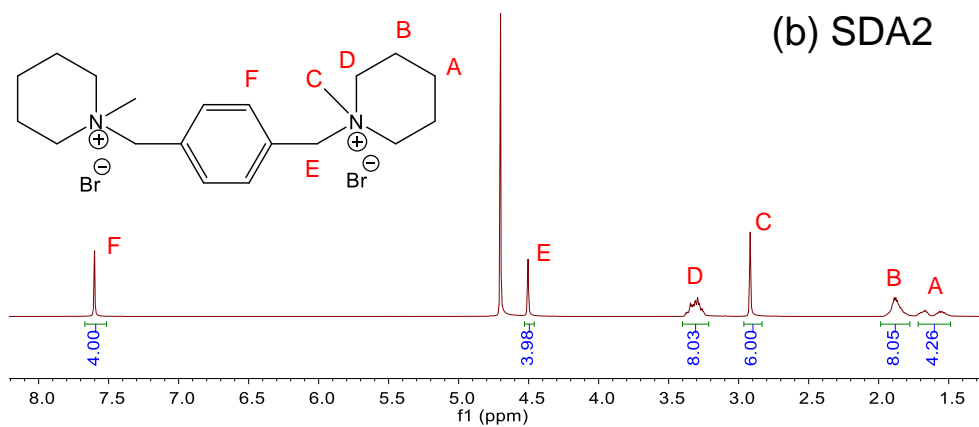
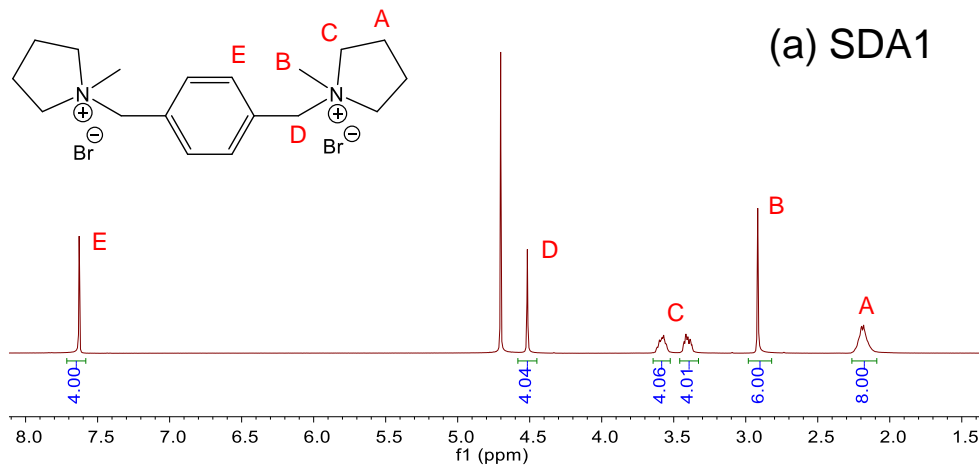
1. J. Li, A. Corma and J. Yu, *Chem. Soc. Rev.*, 2015, **44**, 7112-7127.
2. M. Dusselier and M. E. Davis, *Chem. Rev.*, 2018, **118**, 5265-5329.
3. N. Masoumifard, R. Guillet-Nicolas and F. Kleitz, *Adv. Mater.*, 2018, **30**, 1704439.
4. G. Feng, Z.-H. Wen, J. Wang, Z.-H. Lu, J. Zhou and R. Zhang, *Microporous Mesoporous Mater.*, 2021, **312**, 110810.
5. X. Jia, Y. Zhang, Z. Gong, B. Wang, Z. Zhu, J. Jiang, H. Xu, H. Sun, L. Han, P. Wu and S. Che, *J. Phys. Chem. C*, 2018, **122**, 9117-9126.
6. K. T. G. Carvalho and E. A. Urquieta-Gonzalez, *Catal. Today*, 2015, **243**, 92-102.
7. X. Lu, Y. Guo, Y. Zhang, R. Ma, Y. Fu and W. Zhu, *Microporous Mesoporous Mater.*, 2020, **306**, 110459.
8. Y. Hou, N. Wang, J. Zhang and W. Qian, *RSC Adv.*, 2017, **7**, 14309-14313.
9. S. Mintova, M. Jaber and V. Valchev, *Chem. Soc. Rev.*, 2015, **44**, 7207-7233.
10. K. Zhang, S. Luo, Z. Liu, C. Li, Z. Ke, X. Yan, Y. Wu and H. Xi, *Chem. Eur. J.*, 2018, **24**, 8133-8140.

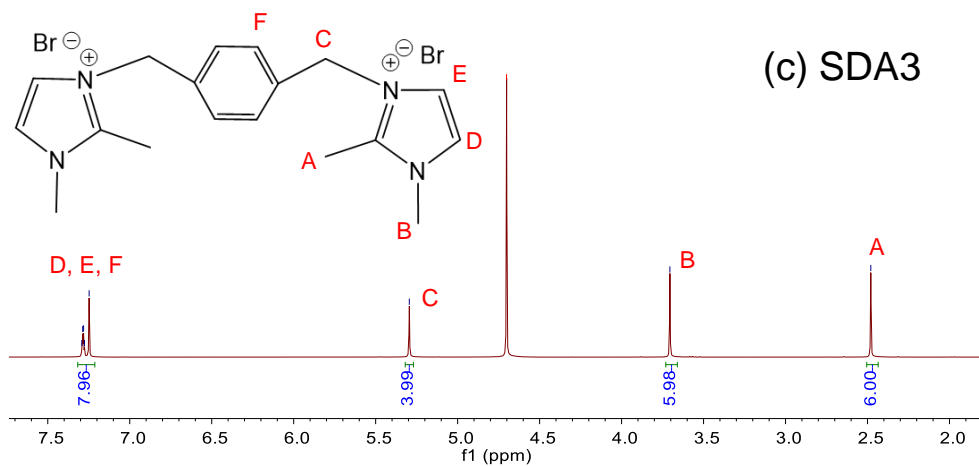
11. L.-H. Chen, M.-H. Sun, Z. Wang, W. Yang, Z. Xie and B.-L. Su, *Chem. Rev.*, 2020, **120**, 11194-11294.
12. C. Vogt and B. M. Weckhuysen, *Nat. Rev. Chem.*, 2022, **6**, 89-111.
13. E. Derouane, J. C. Vedrine, R. R. Pinto, P. Borges, L. Costa, M. Lemos, F. Lemos and F. R. Ribeiro, *Catal. Rev.*, 2013, **55**, 454-515.
14. C. Paris, N. Martín, J. Martínez-Triguero, M. Moliner and A. Corma, *New J. Chem.*, 2016, **40**, 4140-4145.
15. S. Mehla, K. R. Krishnamurthy, B. Viswanathan, M. John, Y. Niwate, S. A. Kishore Kumar, S. M. Pai and B. L. Newalkar, *Microporous Mesoporous Mater.*, 2013, **177**, 120-126.
16. S. Mehla, K. Krishnamurthy, B. Viswanathan, M. John, Y. Niwate, K. Kumar, S. M. Pai and B. Newalkar, *J. Porous Mater.*, 2013, **20**, 1023-1029.
17. X. Wei and P. G. Smirniotis, *Microporous Mesoporous Mater.*, 2006, **89**, 170-178.
18. S. Jegatheeswaran, C.-M. Cheng and C.-H. Cheng, *Microporous Mesoporous Mater.*, 2015, **201**, 24-34.
19. S. Wang, C. Wang, H. Liu, D. Wang, L. Yang, X. Wang, W. Qu, H. Ma and Z. Tian, *Microporous Mesoporous Mater.*, 2022, **331**, 111652.
20. Y. Zhao, H. Zhang, P. Wang, F. Xue, Z. Ye, Y. Zhang and Y. Tang, *Chem. Mater.*, 2017, **29**, 3387-3396.
21. K. T. G. Carvalho, D. S. Araújo Silva and E. A. Urquieta-Gonzalez, *Ind. Eng. Chem. Res.*, 2019, **58**, 7044-7051.
22. S. Gopal, K. Yoo and P. G. Smirniotis, *Microporous Mesoporous Mater.*, 2001, **49**, 149-156.
23. K. Yoo, R. Kashfi, S. Gopal, P. G. Smirniotis, M. Gangoda and R. N. Bose, *Microporous Mesoporous Mater.*, 2003, **60**, 57-68.
24. S. Ernst, P. A. Jacobs, J. A. Martens and J. Weitkamp, *Zeolites*, 1987, **7**, 458-462.
25. A. S. Araujo, A. O. Silva, M. J. Souza, A. C. Coutinho, J. M. Aquino, J. A. Moura and A. M. Pedrosa, *Adsorption*, 2005, **11**, 159-165.
26. D. Romero, R. Rohling, L. Meng, M. Rigutto and E. J. M. Hensen, *J. Catal.*, 2021, **394**, 284-298.
27. Y. Zhao, Z. Ye, L. Wang, H. Zhang, F. Xue, S. Xie, X.-M. Cao, Y. Zhang and Y. Tang, *Cryst. Growth Des.*, 2018, **18**, 1101-1108.
28. W. Kim, J.-C. Kim, J. Kim, Y. Seo and R. Ryoo, *ACS Catal.*, 2013, **3**, 192-195.
29. K. Na, M. Choi and R. Ryoo, *J. Mater. Chem.*, 2009, **19**, 6713-6719.
30. P. Wang, Y. Zhao, H. Zhang, T. Yu, Y. Zhang and Y. Tang, *RSC Adv.*, 2017, **7**, 23272-23278.
31. M. Moliner, F. Rey and A. Corma, *Angew. Chem. Int. Ed.*, 2013, **52**, 13880-13889.

32. M. Moliner, M. J. Díaz-Cabañas, V. Fornés, C. Martínez and A. Corma, *J. Catal.*, 2008, **254**, 101-109.
33. A. Jackowski, S. I. Zones, S.-J. Hwang and A. W. Burton, *J. Am. Chem. Soc.*, 2009, **131**, 1092-1100.
34. S.-H. Lee, C.-H. Shin, D.-K. Yang, S.-D. Ahn, I.-S. Nam and S. B. Hong, *Microporous Mesoporous Mater.*, 2004, **68**, 97-104.
35. J. E. Schmidt, D. L. Fu, M. W. Deem and B. M. Weckhuysen, *Angew. Chem. Int. Ed.*, 2016, **55**, 16044-16048.
36. A. W. Burton and S. I. Zones, in *Stud. Surf. Sci. Catal.*, eds J. Čejka, H. van Bekkum, A. Corma and F. Schüth, Elsevier, 2007, vol. 168, pp. 137-179.
37. X. Hong, W. Chen, G. Zhang, Q. Wu, C. Lei, Q. Zhu, X. Meng, S. Han, A. Zheng, Y. Ma, A.-N. Parvulescu, U. Müller, W. Zhang, T. Yokoi, X. Bao, B. Marler, D. E. De Vos, U. Kolb and F.-S. Xiao, *J. Am. Chem. Soc.*, 2019, **141**, 18318-18324.
38. S. Storck, H. Bretinger and W. F. Maier, *Appl. Catal., A*, 1998, **174**, 137-146.
39. M. H. Sun, L. H. Chen, S. Yu, Y. Li, X. G. Zhou, Z. Y. Hu, Y. H. Sun, Y. Xu and B. L. Su, *Angew. Chem. Int. Ed.*, 2020, **59**, 19582-19591.
40. T. Ikuno, W. Chaikittisilp, Z. Liu, T. Iida, Y. Yanaba, T. Yoshikawa, S. Kohara, T. Wakihara and T. Okubo, *J. Am. Chem. Soc.*, 2015, **137**, 14533-14544.
41. M. Kumar, Z. J. Berkson, R. J. Clark, Y. Shen, N. A. Prisco, Q. Zheng, Z. Zeng, H. Zheng, L. B. McCusker, J. C. Palmer, B. F. Chmelka and J. D. Rimer, *J. Am. Chem. Soc.*, 2019, **141**, 20155-20165.
42. Z. Wan, W. Wu, G. Li, C. Wang, H. Yang and D. Zhang, *Appl. Catal., A*, 2016, **523**, 312-320.
43. W. Wu, W. Wu, O. V. Kikhtyanin, L. Li, A. V. Toktarev, A. B. Ayupov, J. F. Khabibulin, G. V. Echevsky and J. Huang, *Appl. Catal., A*, 2010, **375**, 279-288.
44. L. Meng, G. Vanbutsele, R. Pestman, A. Godin, D. E. Romero, A. J. van Hoof, L. Gao, T. F. Kimpel, J. Chai, J. A. Martens and E. J. M. Hensen, *J. Catal.*, 2020, **389**, 544-555.
45. H. Deldari, *Appl. Catal., A*, 2005, **293**, 1-10.
46. J. A. Martens, D. Verboekend, K. Thomas, G. Vanbutsele, J. P. Gilson and J. Pérez-Ramírez, *ChemSusChem*, 2013, **6**, 421-425.
47. T. Blasco, A. Chica, A. Corma, W. J. Murphy, J. Agúndez-Rodríguez and J. Pérez-Pariente, *J. Catal.*, 2006, **242**, 153-161.
48. S. Li, H. Wu, R. C. J. van de Poll, R. R. M. Joosten, N. Kosinov and E. J. M. Hensen, *ChemCatChem*, 2022, **14**, e202101852.
49. J. Weitkamp, *ChemCatChem*, 2012, **4**, 292-306.

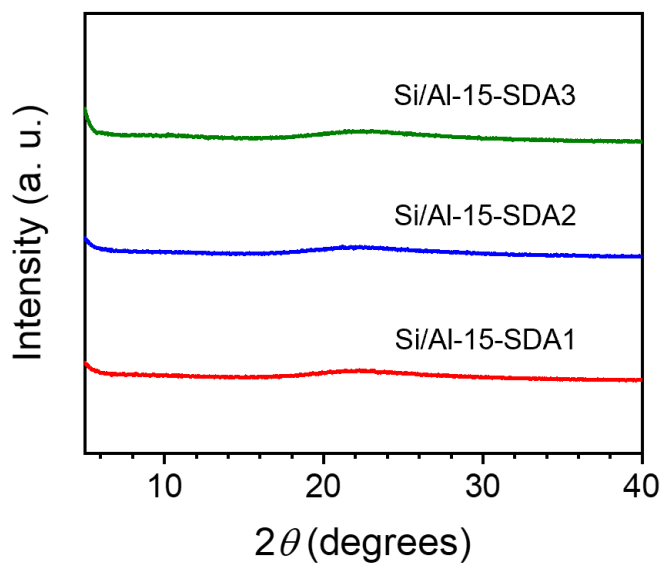
50. J. Zhang, L. Ren, A. Zhou, W. Li, S. Shang, Y. Liu, Z. Jia, W. Liu, A. Zhang, X. Guo and C. Song, *Chem. Mater.*, 2022, **34**, 3217-3226.
51. D. Mores, J. Kornatowski, U. Olsbye and B. M. Weckhuysen, *Chem. Eur. J.*, 2011, **17**, 2874-2884.
52. E. A. Uslamin, N. Kosinov, G. A. Filonenko, B. Mezari, E. Pidko and E. J. M. Hensen, *ACS Catal.*, 2019, **9**, 8547-8554.
53. W. Dai, X. Wang, G. Wu, L. Li, N. Guan and M. Hunger, *ChemCatChem*, 2012, **4**, 1428-1435.
54. J. Valecillos, G. Elordi, A. T. Aguayo and P. Castaño, *Catal. Sci. Technol.*, 2021, **11**, 1269-1281.
55. K. Zhang, S. Luo, Z. Liu, C. Li, Z. Ke, X. Yan, Y. Wu and H. Xi, *Chem. Eur. J.*, 2018, **24**, 8133-8140.
56. R. Kore and R. Srivastava, *RSC Adv.*, 2012, **2**, 10072-10084.

# Appendix D



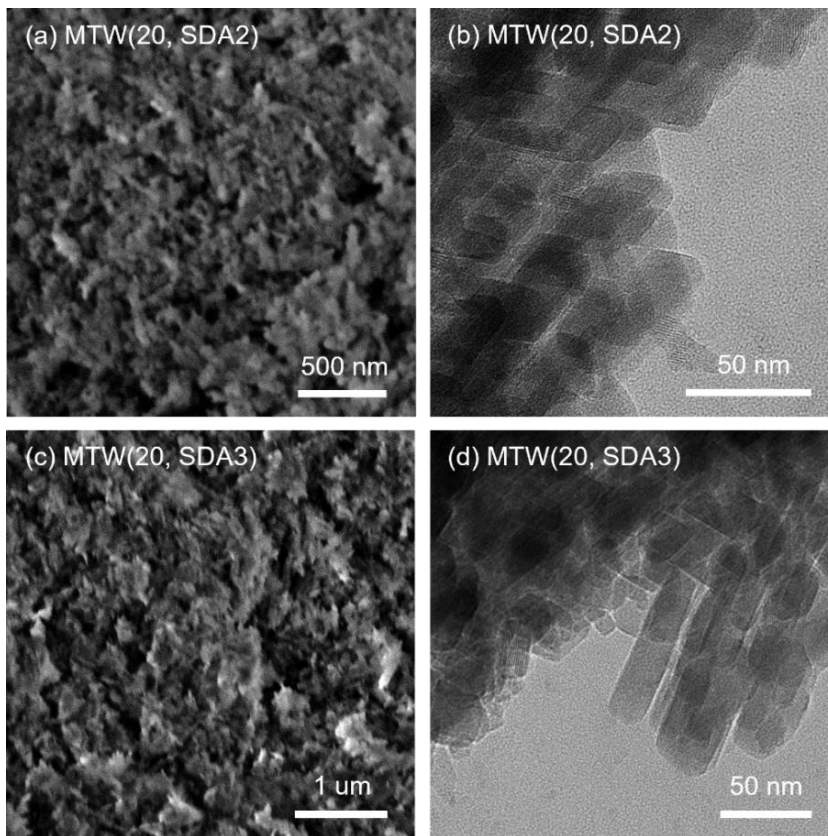


**Figure D1.** <sup>1</sup>H NMR spectra of organic templates used in this work.

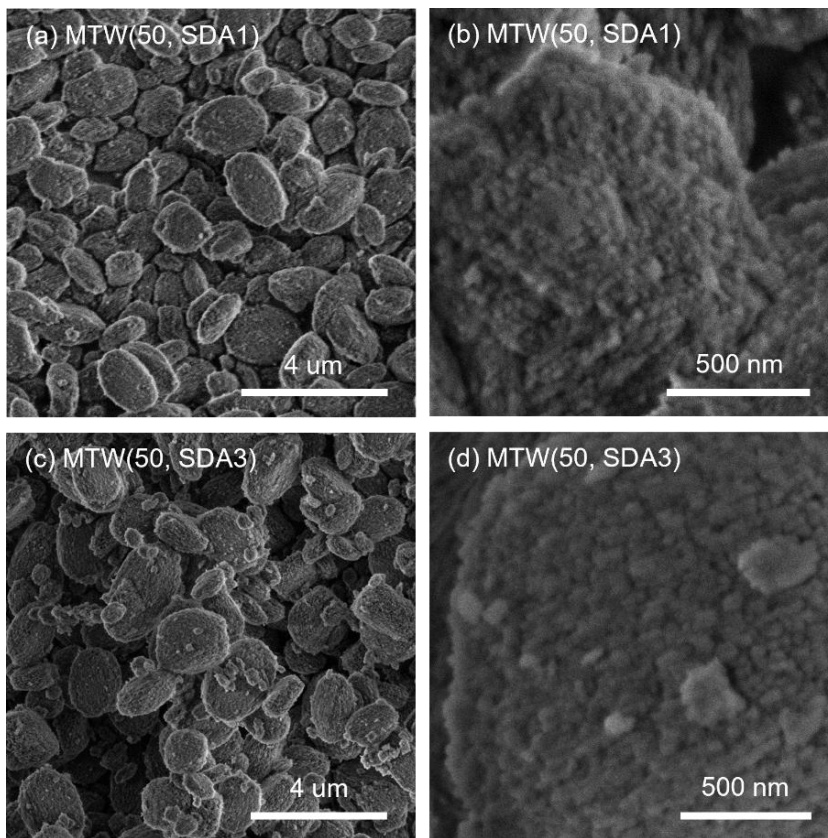


**Figure D2.** XRD patterns of as-synthesized samples (Si/Al=15).

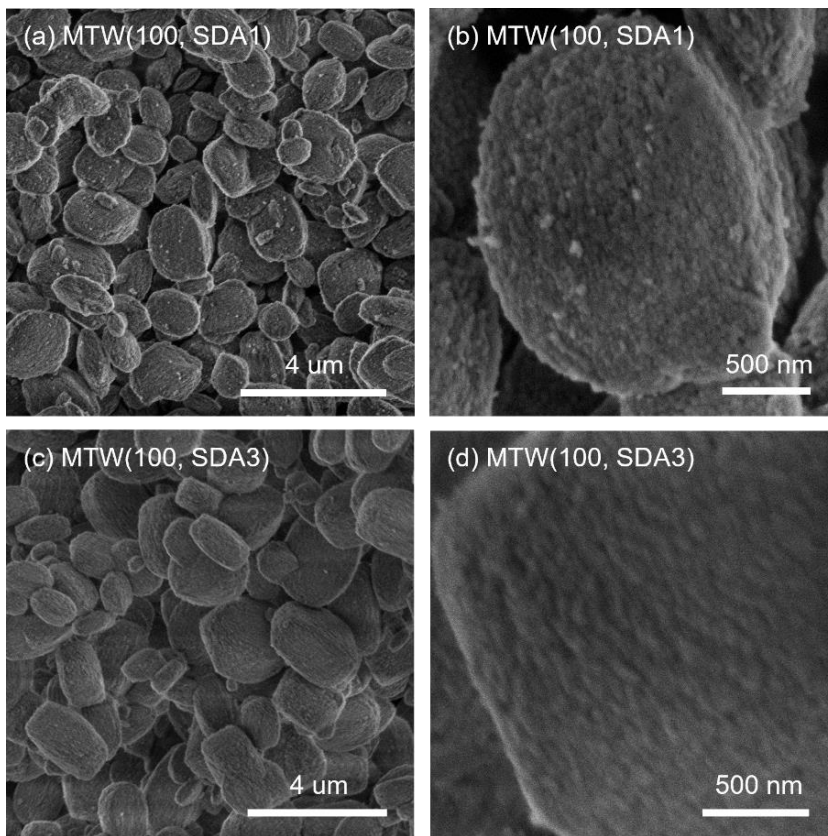




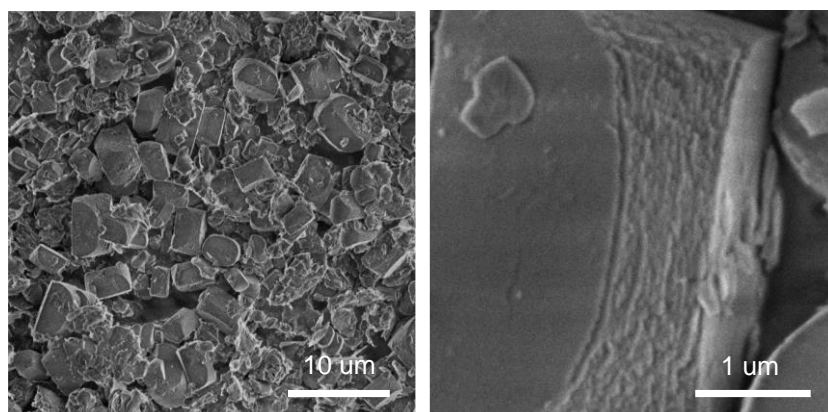
**Figure D3.** SEM and TEM images of calcined zeolites: (a and b) MTW/BEA(20, SDA2) and (c and d) MTW(20, SDA3).



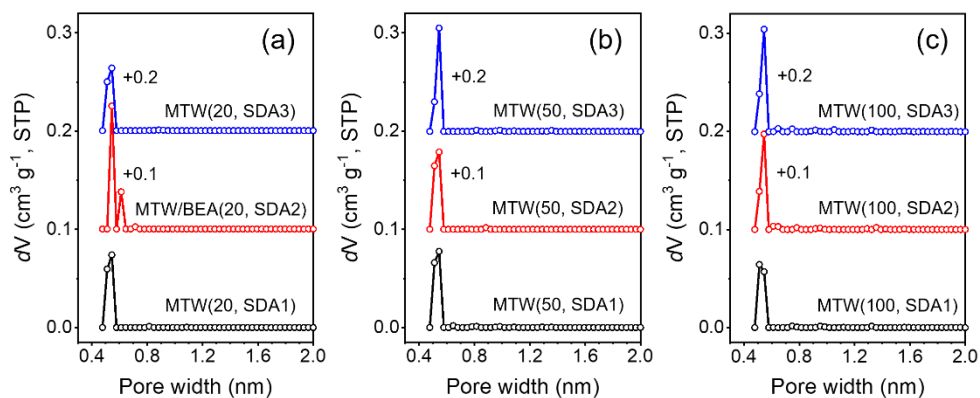
**Figure D4.** SEM images of calcined zeolites: (a and b) MTW(50, SDA1) and (c and d) MTW(50, SDA3).



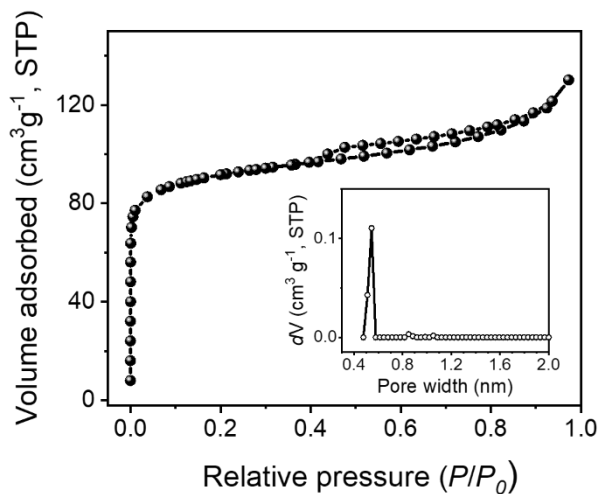
**Figure D5.** SEM and TEM images of calcined zeolites: (a and b) MTW(100, SDA1) and (c and d) MTW(100, SDA3).



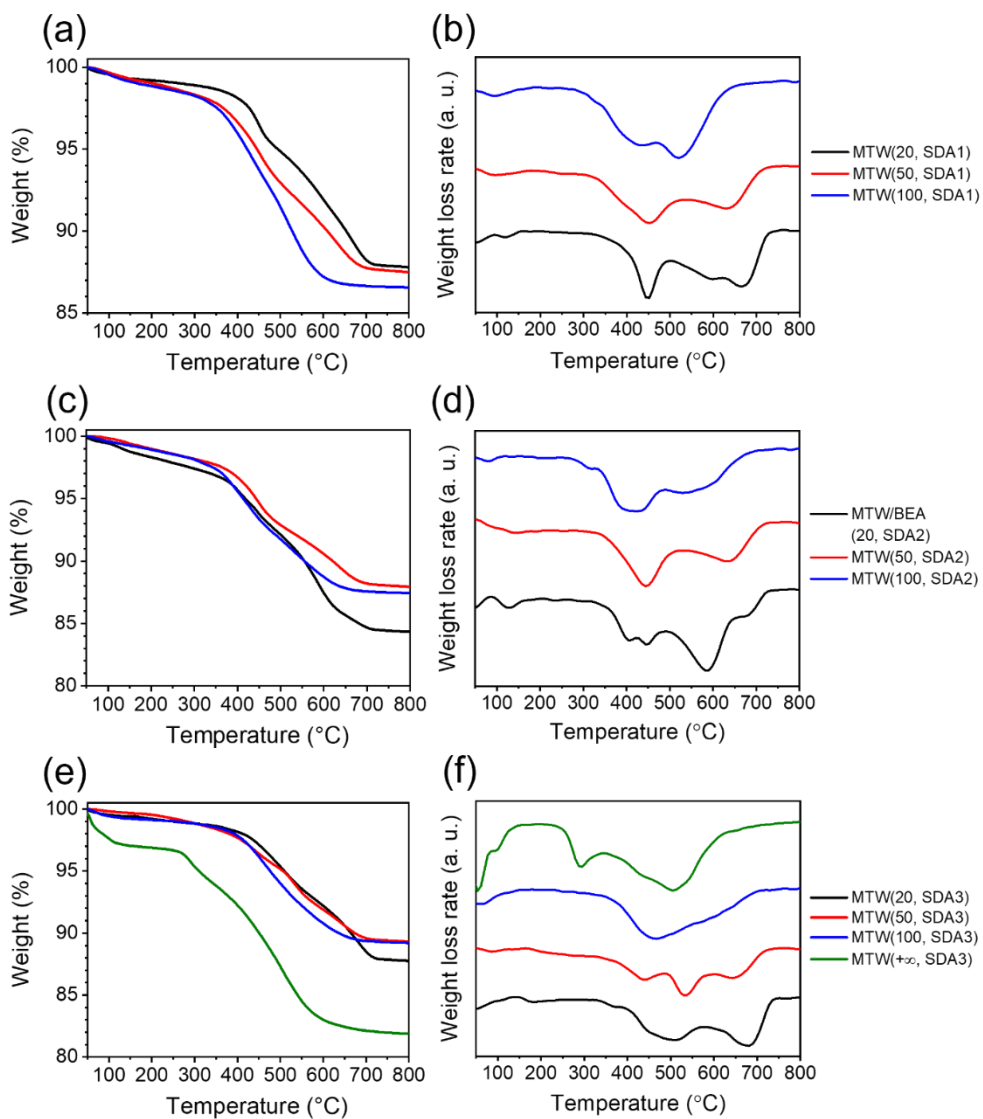
**Figure D6.** SEM images of calcined zeolite MTW(+∞, SDA3).



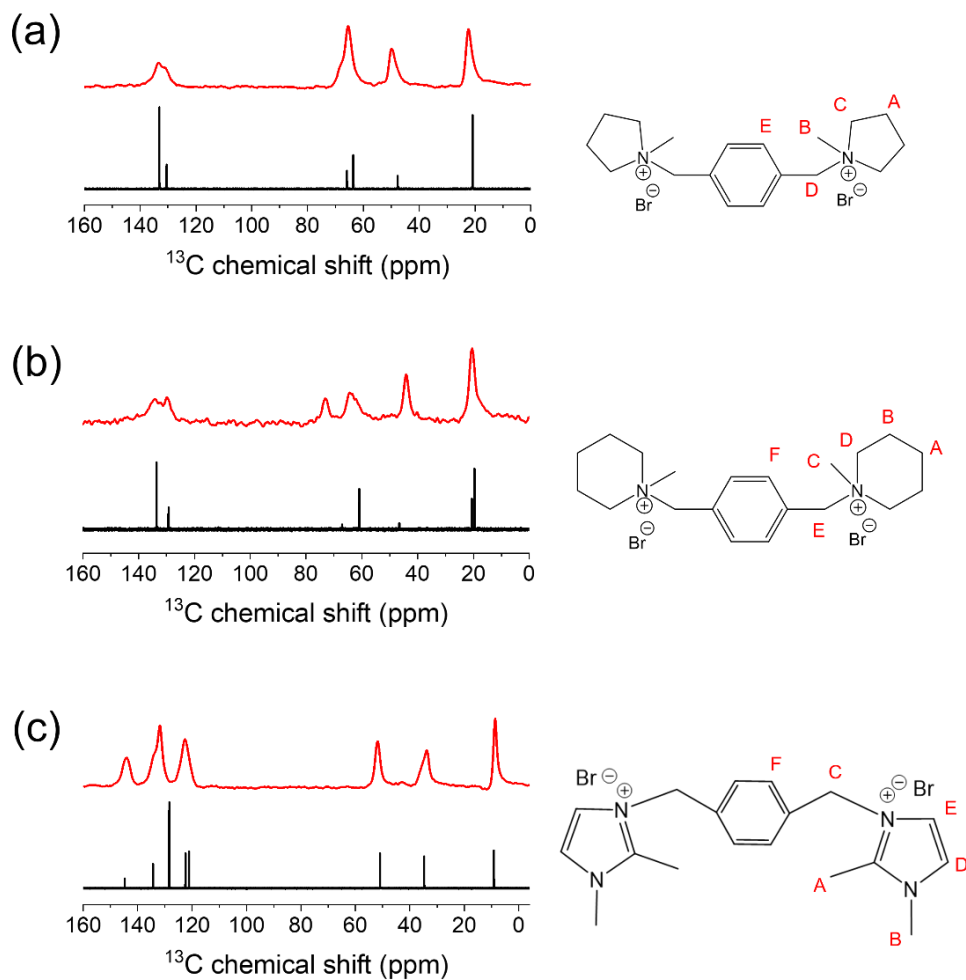
**Figure D7.** Micropore size distributions of calcined zeolites.



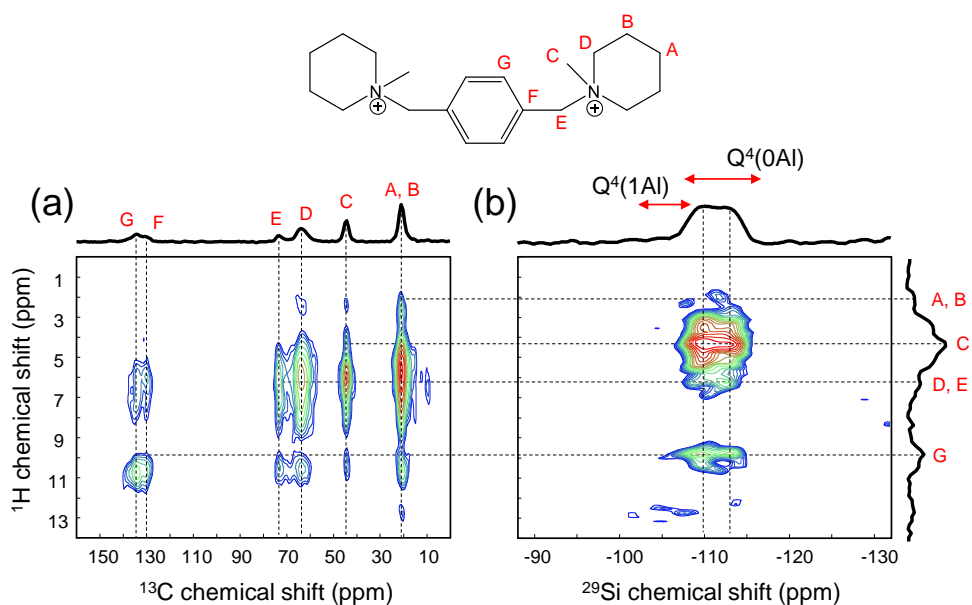
**Figure D8.** Ar physisorption isotherm and micropore size distribution (inset) of calcined zeolite MTW(+ $\infty$ , SDA3).



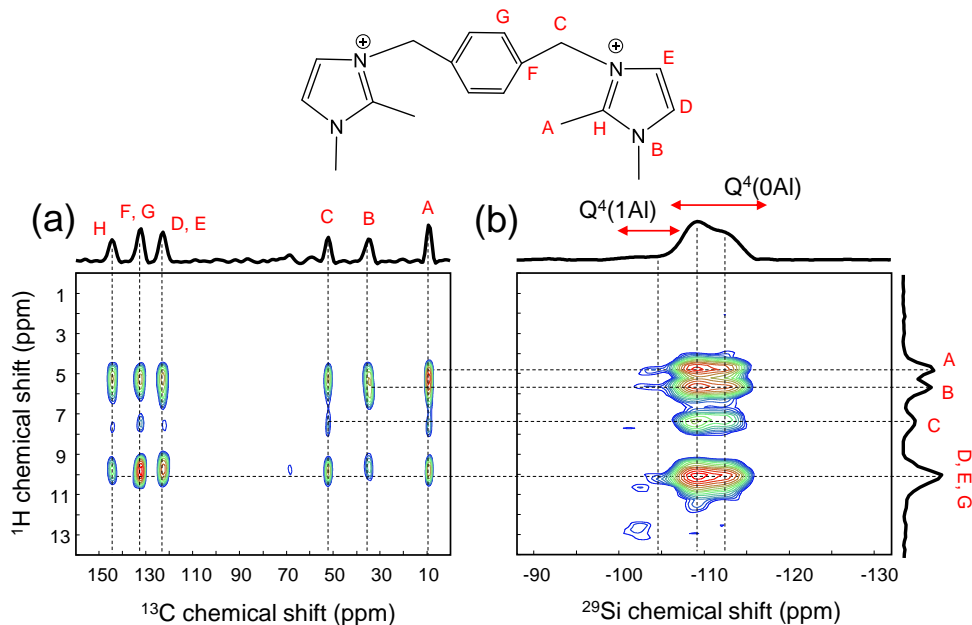
**Figure D9.** TG (left) and DTG (right) profiles of as-synthesized zeolites.



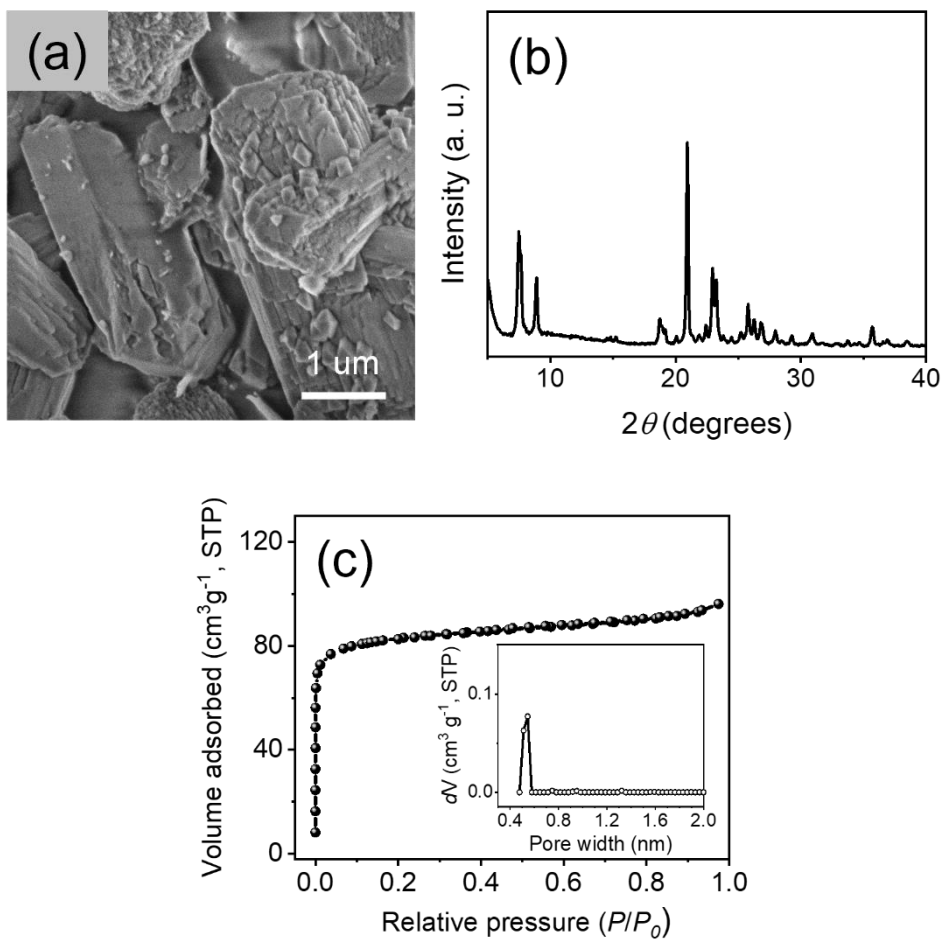
**Figure D10.**  $^{13}\text{C}$  NMR spectra (black line) of OSDA in  $\text{D}_2\text{O}$  solution: (a) SDA1, (b) SDA2 and (c) SDA3;  $^1\text{H}$ - $^{13}\text{C}$  CP/MAS NMR spectra (red line) of as-synthesized samples: (a) MTW(50, SDA1), (b) MTW(50, SDA2) and (c) MTW(50, SDA3).



**Figure D11.**  $^1\text{H}$ - $^{13}\text{C}$  (a) and  $^1\text{H}$ - $^{29}\text{Si}$  (b) HETCOR NMR spectra of as-synthesized MTW(50, SDA2) zeolite. The assignment to different H atoms in template is indicated in the top panel.

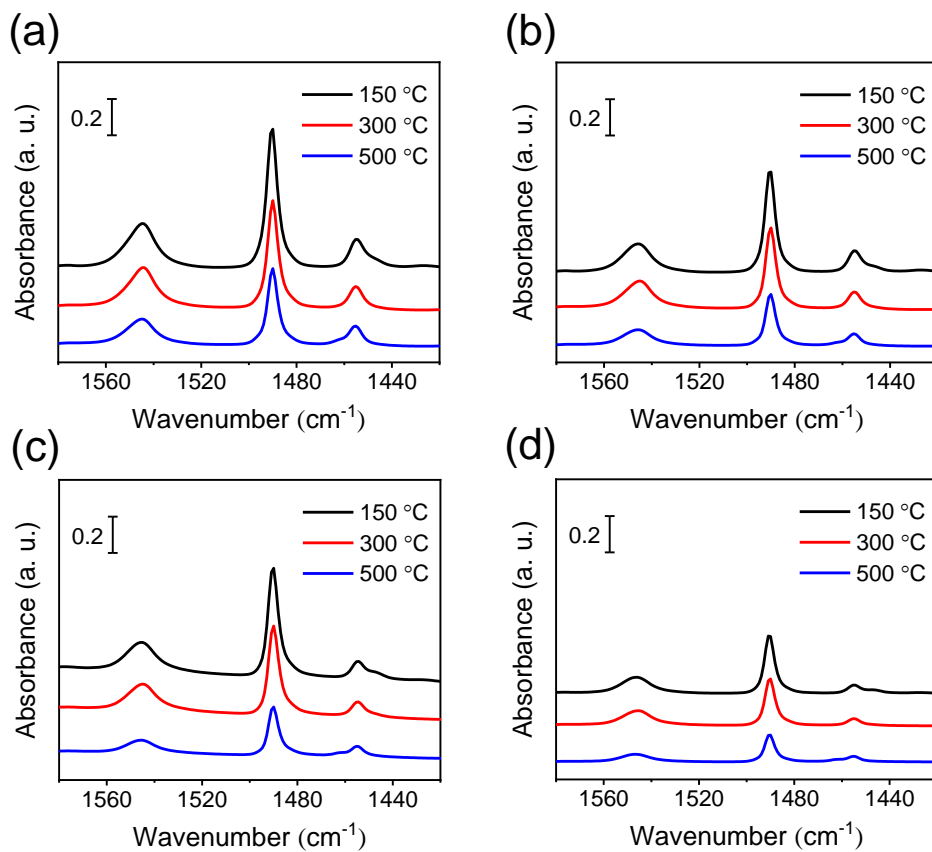


**Figure D12.**  $^1\text{H}$ - $^{13}\text{C}$  (a) and  $^1\text{H}$ - $^{29}\text{Si}$  (b) HETCOR NMR spectra of as-synthesized MTW(50, SDA3) zeolite. The assignment to different H atoms in template is indicated in the top panel.

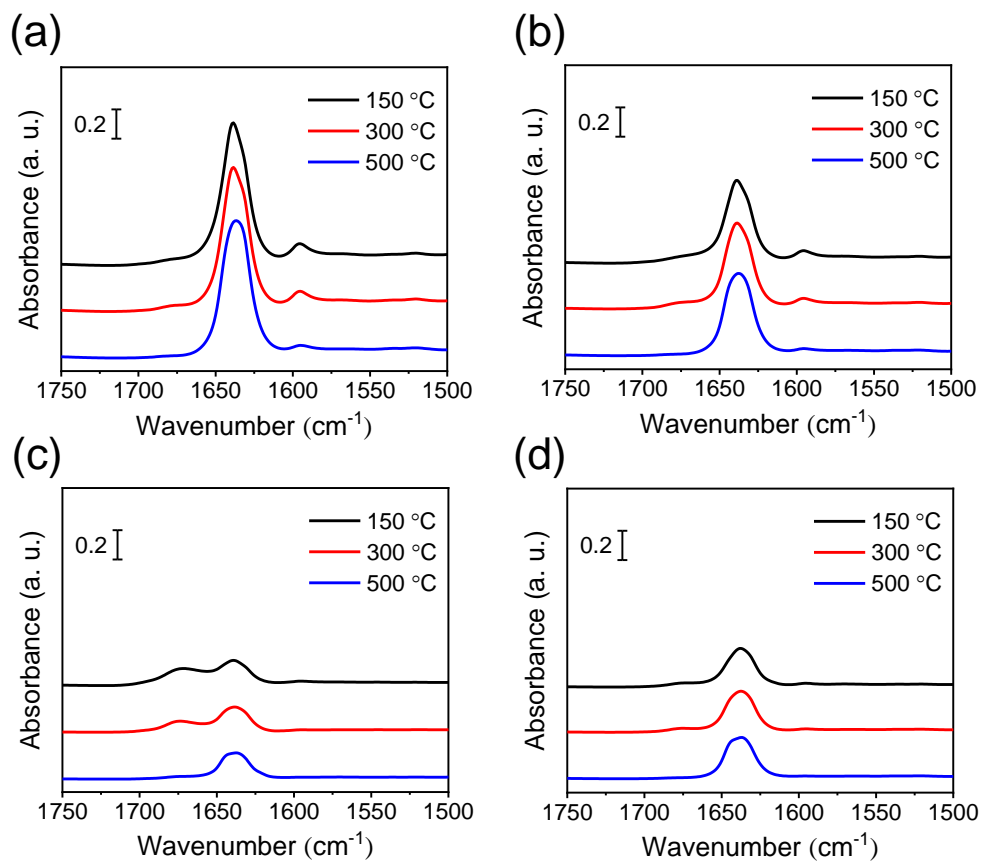


**Figure D13.** (a) SEM image, (b) XRD pattern and (c) Ar physisorption isotherm and micropore size distribution (inset) of MTW-Con.

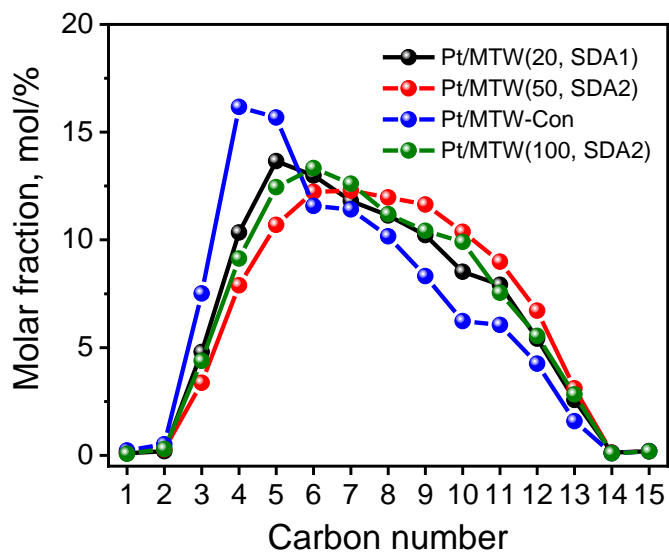




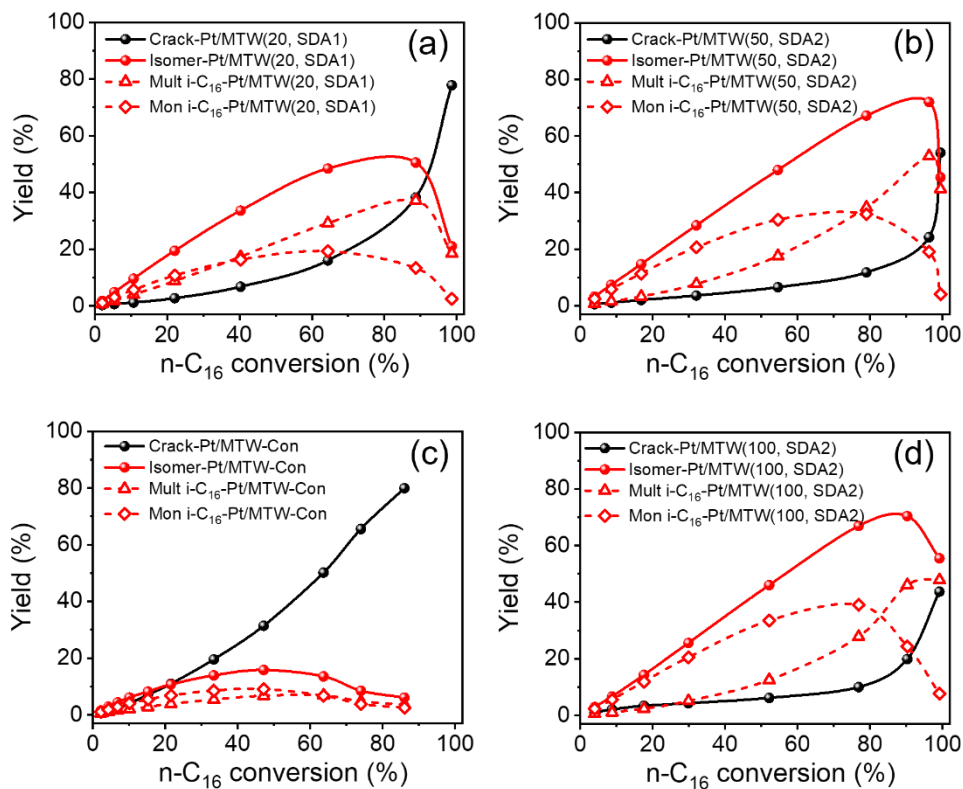
**Figure D14.** IR spectra of pyridine adsorbed on the calcined zeolites: (a) MTW(20, SDA1), (b) MTW(50, SDA2), (c) MTW-Con and (d) MTW(100, SDA2). The spectra were normalized by the weight of the samples.



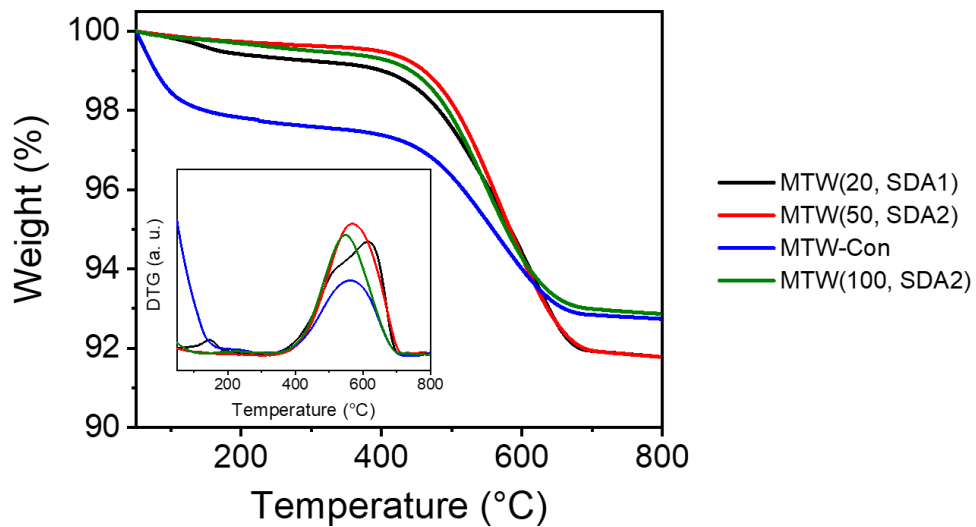
**Figure D15.** IR spectra of 2,4,6-collidine adsorbed on the calcined zeolites: (a) MTW(20, SDA1), (b) MTW(50, SDA2), (c) MTW-Con and (d) MTW(100, SDA2). The spectra were normalized by the weight of the samples.



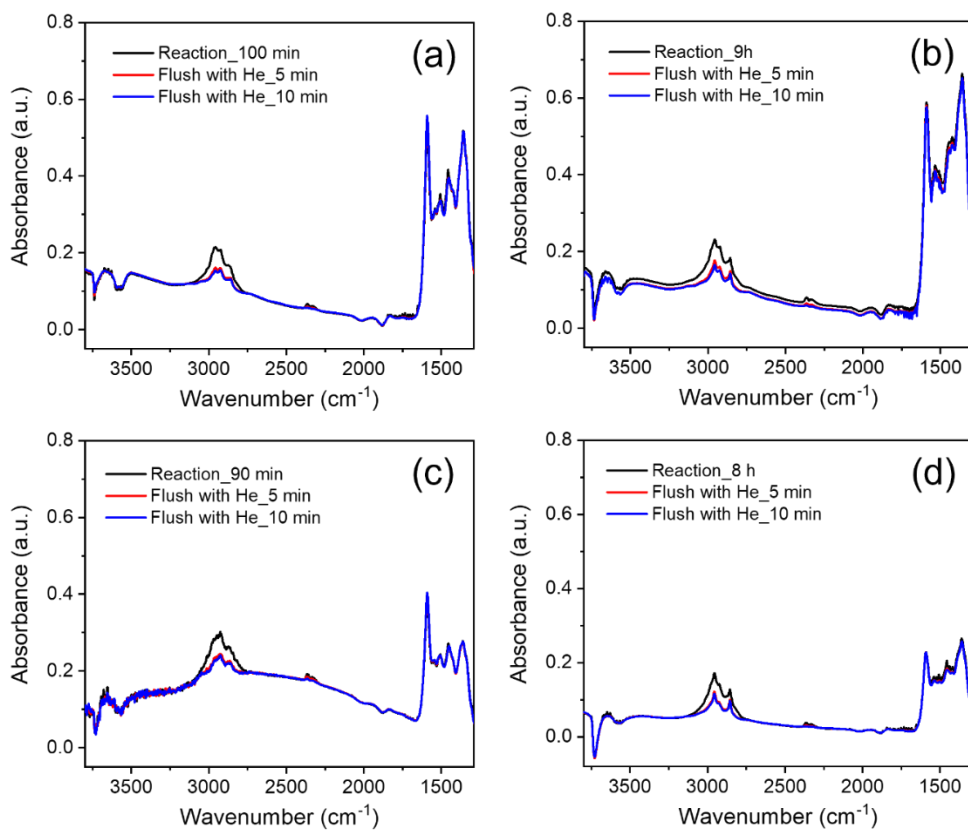
**Figure D16.** Distribution of cracked products at ca. 50% n-C<sub>16</sub> conversion.



**Figure D17.** Product yields (monobranched i-C<sub>16</sub>, multibranched i-C<sub>16</sub> and cracked products) as a function of n-C<sub>16</sub> conversion for: (a) Pt/MTW(20, SDA1), (b) Pt/MTW(50, SDA2), (c) Pt/MTW-Con and (d) Pt/MTW(100, SDA2).

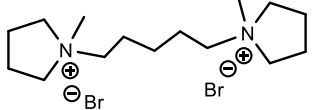
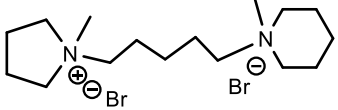
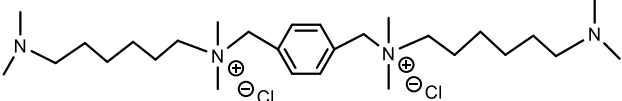
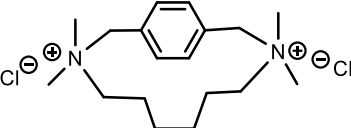
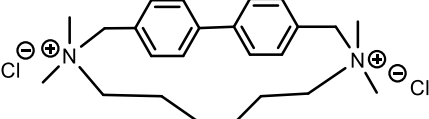
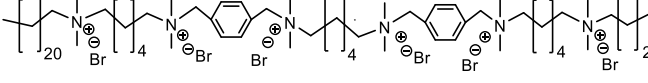
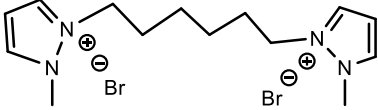
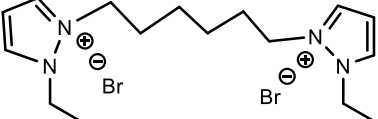
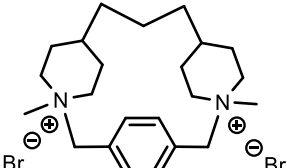


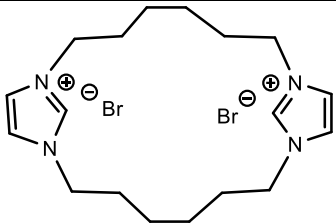
**Figure D18.** TG and DTG (inset) profiles of used catalysts after MTH reaction.



**Figure D19.** *In situ* IR spectra recorded during the MTH reaction and subsequent flushing with He: (a) MTW(20, SDA1), (b) MTW(50, SDA2), (c) MTW-Con and (d) MTW(100, SDA2). The spectra were normalized by the weight of the samples. The subsequent flushing with He after the MTH reaction has a negligible effect on the intensity of the spectra in the range of 1300-1700  $\text{cm}^{-1}$ , indicating the very limited contribution of signals in this range from organic species in the gas phase.

**Table D1.** Multi-quaternary ammoniums reported for the synthesis of hierarchical/nanocrystalline ZSM-12 zeolites.

Organic structure-directing agent	Si/Al (initial gel/ product)	Reference
	60/38	5
	60/47	27
	60/49	55
	50/55	29
	$\geq 40/\geq 40$	29
	50/50	28
	50/43	30
	50/40	30
	>75/--	56

	>75/--	56
---	--------	----

**Table D2.** Phases obtained in the as-synthesized samples as determined by XRD.

Initial gel	No OSDA	SDA 1	SDA 2	SDA 3
Si/Al=15 <sup>a</sup>	--	Amorphous	Amorphous	Amorphous
Si/Al=20 <sup>a</sup>	Amorphous	ZSM-12	ZSM-12+BEA	ZSM-12
Si/Al=50 <sup>b</sup>	Unknown	ZSM-12	ZSM-12	ZSM-12
Si/Al=100 <sup>b</sup>	Unknown	ZSM-12	ZSM-12	ZSM-12
Si/Al=+∞ <sup>c</sup>	Unknown	Unknown	Unknown	ZSM-12

<sup>a</sup> Crystallization at 160 °C for 8 days under rotation (50 rpm).

<sup>b</sup> Crystallization at 160 °C for 4 days under rotation (50 rpm).

<sup>c</sup> Crystallization at 160 °C for 6 days under rotation (50 rpm).

**Table D3.** Coke amount of used samples and average coke accumulation rate during the MTH reaction over ZSM-12 zeolites.

Sample	Reaction time (h)	Coke (wt%) <sup>a</sup>	R <sub>coke</sub> (mg mg <sup>-1</sup> h <sup>-1</sup> )
MTW(20, SDA1)	44	7.4	0.082
MTW(50, SDA2)	115	7.8	0.033
MTW-Con	13.2	4.8	0.172
MTW(100, SDA2)	105	6.6	0.030

<sup>a</sup> Determined by the weight loss between 300 °C and 750 °C of TG results.



**Table D4.** Product distribution during the MTH reaction after 0.5 h on stream over ZSM-12 catalysts.

Sample	Selectivity (%)							C <sub>3=</sub> /C <sub>2=</sub>
	CH <sub>4</sub>	C <sub>2=</sub>	C <sub>2</sub>	C <sub>3=</sub>	C <sub>3</sub>	C <sub>4+</sub>	Aromatics	
MTW (20, SDA1)	0.8	6.9	0.1	33.5	4.2	42.3	12.1	4.8
MTW (50, SDA2)	0.2	4.4	< 0.1	45.3	3.6	39.5	6.9	10.3
MTW-Con	1.1	6.6	0.3	47.3	3.0	36.5	5.1	7.2
MTW (100, SDA2)	0.2	2.2	< 0.1	51.6	2.9	40.4	2.7	23.4

# Chapter 6

## ***P*-phenylenedimethylene-bis(trimethylammonium) as a versatile diaquat template for synthesizing nanosized mordenite, EU-1 and ZSM-12 zeolites**

### **Abstract**

Nanocrystals of zeolites with substantially shortened diffusional pathways compared to bulk counterparts are attractive catalysts, but their synthesis often remains challenging and expensive. Here, we describe the utility of *p*-phenylenedimethylene-bis(trimethylammonium) dichloride, an organic diquatery ammonium compound, which can be easily prepared and is effective as an organic structure-directing agent (OSDA) in directing the synthesis of several nanosized zeolites. By modifying the gel composition (NaOH/Si and Si/Al ratios) and crystallization time, synthesis can be tuned to obtain nanosized mordenite, EU-1 and ZSM-12 zeolites. <sup>13</sup>C NMR spectra of the occluded OSDA reveal subtle differences in host-guest interactions between the OSDA and the respective zeolites, which derives from the flexibility of the OSDA. The relatively strong interaction between the OSDA and inorganic aluminosilica precursor species during the induction period explains how small zeolite nanocrystals are obtained. Nanosized EU-1 and ZSM-12 zeolites significantly outperform their corresponding bulk counterparts as acid catalysts in the methanol-to-hydrocarbons reaction and the alkylation of benzene with benzyl alcohol, respectively.

## 6.1 Introduction

Zeolites are microporous crystalline materials with well-defined channels and cavities in the molecular range.<sup>1</sup> They are technologically important materials with a main application as catalysts in chemical processes. Their utility in hydrocarbon conversion processes is related to tunable physicochemical properties, excellent shape selectivity and high (hydro)thermal stability.<sup>2</sup> In many applications, the performance of zeolite catalysts is hampered by diffusion limitations of reactants and products in micropores.<sup>3</sup> Decreasing the diffusion path length in the micropore space is an effective way to overcome such limitations.<sup>4</sup> Besides the fabrication of hierarchically porous zeolites with additional mesopores, it can also be effective to synthesize nanocrystalline zeolites with crystal domains less than 100 nm.<sup>5</sup> Nanosized zeolites are known to outperform bulk zeolites with, for instance, higher activity, better stability and improved selectivity to desired products, in particular for reactions involving bulky molecules and reactions involving consecutive reactions of the desired product to undesired ones.<sup>6,7</sup>

In the last two decades, several synthetic approaches have been developed to prepare nanocrystalline zeolites, among which one-step approaches based on conventional hydrothermal synthesis are the most attractive.<sup>8,9</sup> This typically involves the use of organic additives, *e.g.* cationic polymers as growth modifier, organosilanes as the mesoporegen or (poly)quaternary ammonium compounds template that can fulfil several roles.<sup>10-13</sup> For example, Ryoo and co-workers reported the synthesis of MFI nanosheets by use of a di-quaternary ammonium surfactant, where the hydrophilic di-quaternary ammonium group directs formation of MFI zeolite and the hydrophobic long-chain tail restricts crystal growth.<sup>14</sup> In follow-up work, they expanded this concept to prepare nanocrystalline forms of BEA, ZSM-12 and MRE zeolite by tuning the gel composition using a polyquaternary ammonium surfactant a similar synthesis route of MFI nanosheets. However, the use of these organic templates are costly, which limits their practical application.<sup>15</sup>

To solve this issue, a series of small and simple organic structure-directing agents (OSDAs), which are commercially available or can be prepared in a single step from available chemicals, have also been explored for synthesis of nanocrystalline zeolites.<sup>5,16</sup> For example, Corma and co-authors reported the direct synthesis of nanosized BEA and ZSM-5 zeolites by using simple alkyl-substituted mono-cationic cyclic ammonium compounds.<sup>17</sup> Tsapatsis and co-authors demonstrated the use of a tetrabutylphosphonium template for the synthesis of self-pillared pentasil zeolite nanosheets.<sup>18</sup> Recently, simple non-surfactant di-quaternary compounds have also been used for the nanocrystalline zeolite synthesis.<sup>19-23</sup> These diquaternary compounds are normally composed of an alkyl-chain linkage and nitrogen-

containing branches/cycles. The possibility to tune the flexibility of the linkage and the size and other properties of the head groups allows obtaining a variety of zeolites.<sup>20, 21, 24-26</sup> In view of the successful synthesis of nanocrystalline zeolites using non-surfactant diquatery ammonium compounds, we wondered about the structure-directing ability of low-cost *p*-phenylenedimethylene-bis(trimethylammonium) dichloride (Me<sub>3</sub>N-benzyl-NMe<sub>3</sub>), which has not been used yet for zeolite synthesis under alkaline condition via conventional hydrothermal synthesis. Different from the use of previous diquatery OSDAs is the rigidity of the benzyl linker.<sup>20, 21, 24, 26-29</sup> It is expected that Me<sub>3</sub>N-benzyl-NMe<sub>3</sub> can fit in 12-membered ring (12MR) and 10-membered ring (10MR) pores, which are common in zeolites used in industrial practice.<sup>30</sup>

In this work, we report the synthesis of nanosized MOR (2D pore network; 12/8MR; 0.67 × 0.70 nm, 0.26 × 0.57 nm, 0.34 × 0.48 nm), EU-1 (1D pore network; 10MR; 0.54 × 0.41 nm) and ZSM-12 (1D pore network; 12MR; 0.57 × 0.61 nm) zeolites by modifying the gel compositions in terms of NaOH/Si and Si/Al ratios and crystallization time with Me<sub>3</sub>N-benzyl-NMe<sub>3</sub> as the sole organic template. Me<sub>3</sub>N-benzyl-NMe<sub>3</sub> was synthesized from commercially available chemicals via a one-step procedure at ambient temperature. The crystallization behavior of nanocrystalline MOR, EU-1 and ZSM-12 was investigated by characterizing the intermediate solid products. As the benefit of nanosizing MOR zeolite has been well evidenced in Chapter 2 and Chapter 3, we focus on investigating the catalytic performance of nanosized EU-1 and ZSM-12 zeolites in the present work. The methanol-to-hydrocarbons (MTH) reaction was chosen as a model reaction to assess the catalytic performance of nanosized EU-1. In this reaction, conventional EU-1 zeolite suffers from a rapid catalyst deactivation caused by severe coke deposition.<sup>31, 32</sup> Nanosizing EU-1 may improve the desorption of coke precursors and thus result in a longer lifetime. Alkylation of benzene with benzyl alcohol was chosen to assess the improved accessibility of acid sites of nanosized ZSM-12.

## 6.2 Experimental section

### 6.2.1 Synthesis of OSDA

0.02 mol of 1,4-bis(chloromethyl)benzene (Sigma Aldrich, 98%) was dissolved in 150 ml acetonitrile (Biosolve, 99.8%). Then 15.3 g of trimethylamine solution (Sigma Aldrich, 31-35 wt% in ethanol) was added into the solution under stirring. The resulting solution was reacted for 3 days at ambient conditions. After the reaction, the white precipitate was collected by filtration, followed by washing with extra diethyl ether (Biosolve, 99.5%). The obtained solid product was dried at 50 °C overnight under evacuation. The product yield was

96%. The purity of the OSDA was confirmed by  $^1\text{H}$  NMR and  $^{13}\text{C}$  NMR spectra (Figures E1 and E2).

### 6.2.2 Synthesis of zeolites

In a typical synthesis, sodium hydroxide (Sigma Aldrich,  $\geq 98\%$ ) was dissolved in deionized water, followed by the addition of OSDA. After stirring for 5 min,  $\text{AlCl}_3 \cdot \text{H}_2\text{O}$  (Alfa Aesar, 99%) was added to the mixture. After further stirring for 5 min, Ludox AS-40 (Sigma Aldrich, 40 wt%) was added to the mixture. The molar composition of the final mixture was  $12 \text{ SiO}_2 : x \text{ Al}_2\text{O}_3 : y \text{ Na}_2\text{O} : 1.2 \text{ OSDA} : 480 \text{ H}_2\text{O}$  ( $x = 0.24\text{-}0.5$ ;  $y = 1.8\text{-}4.2$ ). After vigorous stirring for 24 h at room temperature, the mixture was transferred to a 45 ml Teflon-lined stainless-steel autoclave (Parr Instruments) and heated at  $160^\circ\text{C}$  in an oven under tumbling (50 rpm). After hydrothermal synthesis, the solid product was collected by centrifugation and washed with deionized water until  $\text{pH} < 8$ , followed by drying at  $30^\circ\text{C}$  overnight under evacuation. The OSDA was removed by calcination at  $550^\circ\text{C}$  for 8 h in air. The calcined samples were converted to ammonium form by triple ion-exchange with 1.0 M  $\text{NH}_4\text{NO}_3$  at  $70^\circ\text{C}$ . After drying at  $30^\circ\text{C}$  overnight under evacuation, the ammonium-form sample was calcined at  $550^\circ\text{C}$  for 4 h in a  $\text{O}_2/\text{N}_2$  (1/4 by volume) to obtain the final proton form.

Conventional ZSM-12 (denoted as ZSM-12-Con) was synthesized with methyltriethylammonium chloride (MTEACl, Alfa Aesar, 98%).<sup>15</sup> Conventional EU-1 (denoted as EU-1-Con) was synthesized with hexamethonium bromide (TCI,  $>98\%$ ).<sup>32</sup>

### 6.2.3 Characterization

X-ray diffraction (XRD) patterns were recorded on a Bruker D2 Phase diffractometer using  $\text{Cu K}\alpha$  radiation. Patterns were obtained in the  $2\theta$  range of  $5\text{-}50^\circ$ , with a step size of  $0.01^\circ$  and duration time of 0.25 s.

The chemical composition of the calcined zeolites was determined by inductively couple plasma optical emission spectrometry (ICP-OES). Prior to measurements, samples were dissolved in a 1 : 1 : 1 mixture of HF (40 wt%),  $\text{HNO}_3$  (60 wt%) and  $\text{H}_2\text{O}$  at ambient conditions.

The textural properties of the calcined zeolites were determined by Ar physisorption. The measurements were performed on a Micromeritics ASAP 2020 instrument. The samples were degassed at  $400^\circ\text{C}$  for 6 h prior to physisorption measurements. The BET surface area was calculated using the relative pressure range of 0.05-0.25. The micropore volume and external surface area were calculated using the  $t$ -plot method, while the mesopore volume was calculated using the Barrett-Joyner-Halenda (BJH) method.

Thermogravimetric analysis (TGA) was performed with a TGA/DSC 1 instrument (Mettler Toledo). The sample was heated from 40 °C to 800 °C at a rate of 5 °C/min in a flow of 20 ml/min O<sub>2</sub> and 40 ml/min He.

Scanning electron microscopy (SEM) images were obtained on a FEI Quanta 200F scanning electron microscopy at an accelerating voltage of 3 kV. Transmission electron microscopy (TEM) images were collected on a FEI Tecnai 20 operated at 200 kV.

The acidity of samples was determined by IR spectroscopy of adsorbed pyridine on a Bruker Vertex 70v spectrometer. The sample was prepared as a pressed wafer and pretreated *in situ* at 550 °C for 1 h in artificial air. After pretreatment, the cell was cooled to 150 °C and outgassed until the residual pressure was below  $1 \times 10^{-4}$  mbar. A background spectrum was collected. Pyridine was then introduced into the cell until the sample was fully saturated. Finally, spectra were recorded at 150 °C after outgassing for 1 h at 150 °C, 300 °C and 500 °C, respectively.

Solid-state nuclear magnetic resonance (NMR) measurements were performed on a 11.7 Tesla Bruker DMX500 NMR spectrometer, operating at 132 MHz for <sup>27</sup>Al and 125 MHz for <sup>13</sup>C. <sup>27</sup>Al magic angle spinning (MAS) NMR measurements were performed using a Bruker 2.5 mm MAS probe head and a 2.5 mm zirconia rotor, under a spinning speed of 25 kHz. <sup>1</sup>H-<sup>13</sup>C cross-polarization (CP) MAS NMR measurements were performed using a Bruker Triple Channel 4 mm MAS probe head and a 4 mm zirconia rotor, operated at a spinning speed of 10kHz. <sup>27</sup>Al and <sup>13</sup>C chemical shifts were referred to Al(NO<sub>3</sub>)<sub>3</sub> and solid adamantane, respectively.

Liquid-state NMR measurements were performed on a Bruker 400 MHz spectrometer. The obtained OSDA was first dissolved in deuterated water, followed by transfer of the solution into a 5 mm NMR tube. <sup>1</sup>H NMR spectra were collected with a total scan of 32 and a relaxation delay of 1 s. <sup>13</sup>C NMR spectra were collected with a total scan of 1024 and a relaxation delay of 2 s.

## 6.2.4 Catalytic activity measurements

### 6.2.4.1 Methanol to hydrocarbons (MTH)

The MTH reaction was performed in a fixed-bed downstream reactor. Samples were pressed, and then crushed and sieved to obtain particles in the range of 250-500 μm. This process has a negligible effect on the mesopore volume and external surface of zeolite samples. An amount of 100 mg of the catalyst (sieve fraction 250-500 μm) was loaded into a quartz reactor. First, the catalyst was pretreated *in situ* in artificial air at 550 °C for 1 h before cooling to the

reaction temperature of 350 °C. Methanol was fed to the reactor at a weight hourly velocity (WHSV) of 0.8 h<sup>-1</sup> by flowing He through a saturator containing methanol (VWR Chemicals, ≥ 99.8%). The products were analyzed by online gas chromatography (Interscience Compact GC). A thermal conductivity detector (TCD) coupled with an RT-Q-Bond pre-column (length 3 m; i.d. 0.32 mm; thickness 10 μm) and a Molsieve 5A column (length 10 m; i.d. 0.32 mm; thickness 30 μm) was used for the analysis of H<sub>2</sub> and CH<sub>4</sub>. A TCD coupled with an RT-Q-Bond pre-column (length 3 m; i.d. 0.32 mm; thickness 10 μm) and an RT-Q-Bond column (length 10 m; i.d. 0.32 mm; thickness 10 μm) was used for the analysis of C<sub>2</sub>-C<sub>3</sub> hydrocarbons, water and oxygenates. Hydrocarbons heavier than C<sub>3</sub> were separated on an Rtx-1 column (length 15 m; i.d. 0.32 mm; thickness 1 μm) and analyzed with a flame ionization detector (FID). Dimethyl ether was considered as a reactant.

#### **6.2.4.2 Alkylation of benzene with benzyl alcohol**

The liquid-phase alkylation of benzene with benzyl alcohol was performed in a round-bottom flask equipped with a reflux condenser and heated in a temperature-controlled oil bath. Typically, 0.15 g of catalyst was mixed with 26.7 ml (0.301 mol) of benzene in a glove box. After maintaining the reaction mixture at 80 °C for 30 min, 0.33 ml (0.003 mol) of BA was added. This moment was regarded as the start of the reaction. Liquid samples were taken periodically and separated from catalyst by filtration. Finally, the sample was analyzed by a gas chromatograph (Shimadzu GC-17 A) equipped with a flame ionization detector (FID) coupled with a Rxi-5ms column (length 30 m; i.d. 0.25 mm; thickness 0.5 μm).

## **6.3 Results and discussion**

### **6.3.1 Zeolite synthesis**

The zeolite syntheses undertaken in this study are listed in Table 6.1. XRD data of the obtained samples are collected in Figures 6.1 and E3. Phase-pure MOR zeolites were obtained in OSDA-free syntheses at a Si/Al gel ratio of 12 and NaOH/Si ratios of 0.6 and 0.7 in line with earlier studies showing that MOR zeolite can be obtained from low Si/Al gel ratio (Si/Al < 15) and high pH (NaOH/Si > 0.5).<sup>33, 34</sup> Based on the same gel composition in terms of inorganic compounds, the addition of Me<sub>3</sub>N-benzyl-NMe<sub>3</sub> led to the formation of a mixture of EU-1 and MOR zeolite for a NaOH/Si ratio of 0.6. However, when the NaOH/Si ratio was increased to 0.7, phase-pure MOR was obtained. This is likely due the fact that a high NaOH/Si ratio favors MOR formation.<sup>35</sup> In line with this, we found that, at a NaOH/Si ratio of 0.6, a decrease of the Si/Al gel ratio to 25 led to phase-pure EU-1 with OSDA, while MOR was formed without OSDA. At a Si/Al gel ratio of 25, decreasing the NaOH/Si ratio

to 0.5 and 0.4 with OSDA led to formation of a mixture of EU-1 and ZSM-12, while phase-pure ZSM-12 was formed at a NaOH/Si ratio of 0.3. EU-1 and ZSM-12 were not formed when the OSDA was omitted from the synthesis gel.

**Table 6.1.** Synthesis conditions and product phases.

Run	Template	Si/Al	NaOH/Si	Synthesis time (days)	Product
1	Na	12	0.6	1	MOR-Con
2	Na		0.7	1	MOR-Con(0.7)
3	OSDA		0.6	5	MOR+EU-1
4	OSDA		0.7	2	MOR-Nano
5	OSDA	25	0.6	4	EU-1-Nano
6	Na			5	MOR
7	OSDA		0.5	5	ZSM-12 + EU-1
8	OSDA		0.4	5	ZSM-12 + EU-1
9	OSDA		0.3	6	ZSM-12-Nano
10	Na		0.3	5	ZSM-5+Amorphous

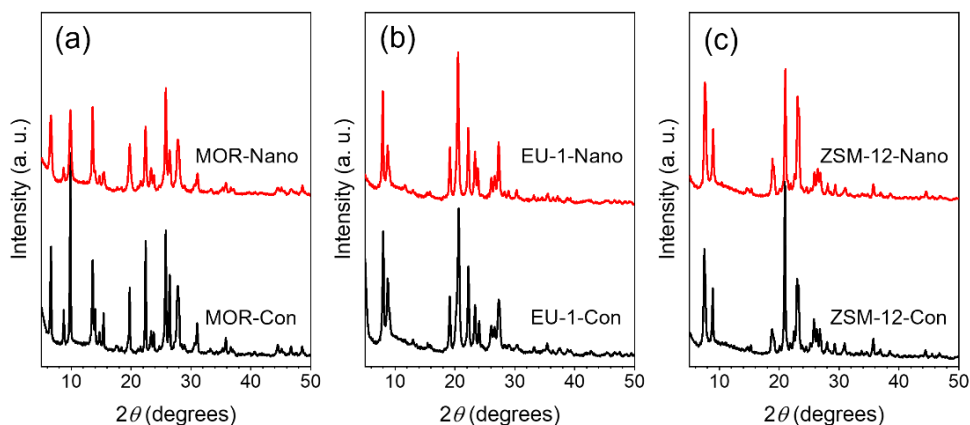


**Figure 6.1.** XRD patterns of as-synthesized zeolites.



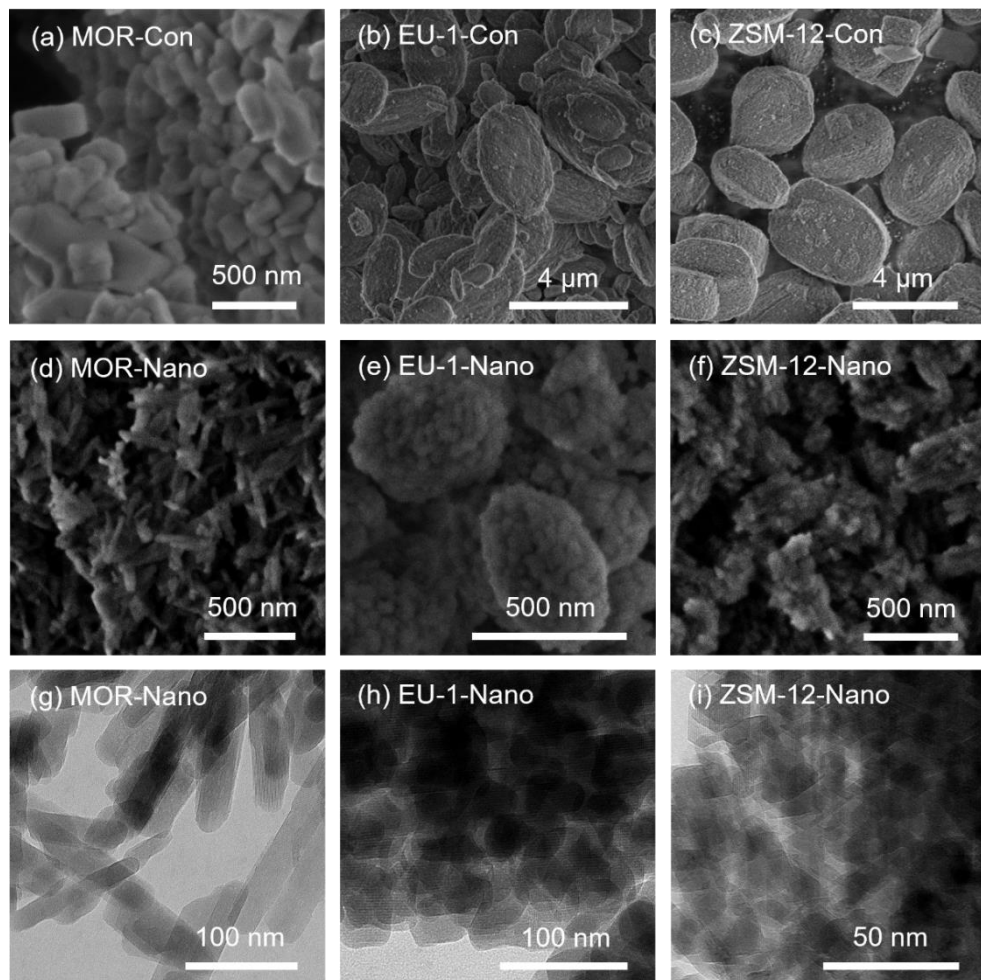


**Figure 6.2.** Representative SEM and TEM images of as-synthesized zeolites.

Representative SEM and TEM images are shown in Figure 6.2. Clearly, the use of  $\text{Me}_3\text{N-benzyl-NMe}_3$  led to formation of aggregated nanocrystals of zeolite. The lattice spacing obtained from Figure E4 is 1.35 nm, indicating that the nanorods of MOR-Nano are oriented parallel to the  $c$ -axis.<sup>36</sup> In conventional synthesis of MOR zeolite under highly alkaline conditions, crystals larger than 100 nm are obtained (Figures 6.2a and E5), consistent with previous studies.<sup>37, 38</sup> EU-1-Con and ZSM-12-Con synthesized from conventional recipes consist of bulky plate- and rugby-ball-like crystals, respectively (Figures 6.2b and 6.2c).

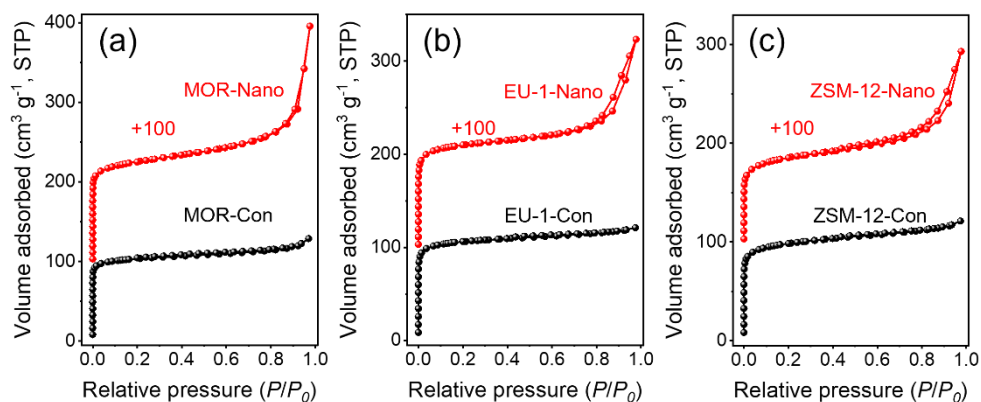


**Figure 6.3.** Ar physisorption isotherms of calcined zeolites.

**Table 6.2.** Textural properties of calcined zeolites determined by Ar physisorption.

Sample	$S_{\text{BET}}$ ( $\text{m}^2 \text{g}^{-1}$ )	$V_{\text{tot}}$ ( $\text{cm}^3 \text{g}^{-1}$ )	$V_{\text{micro}}$ ( $\text{cm}^3 \text{g}^{-1}$ ) ( <i>t</i> -plot)	$V_{\text{meso}}$ ( $\text{cm}^3 \text{g}^{-1}$ ) ( <i>BJH</i> )	$S_{\text{ext}}$ ( $\text{m}^2 \text{g}^{-1}$ ) ( <i>t</i> -plot)
MOR-Con	315	0.16	0.11	0.04	50
MOR-Nano	399	0.38	0.12	0.23	91
EU-1-Con	325	0.16	0.11	0.02	44
EU-1-Nano	353	0.30	0.11	0.16	86
ZSM-12-Con	301	0.16	0.10	0.03	47
ZSM-12-Nano	289	0.26	0.09	0.15	85

The textural properties of the calcined samples were determined by Ar physisorption (Figure 6.3). The steep Ar adsorption at  $P/P_0$  below 0.02 points to the presence of micropores.<sup>39</sup> The nanosized zeolites all display the type-IV isotherm with a hysteresis loop at  $P/P_0$  values between 0.6-0.97, which corresponds to interparticle condensation due to small crystals. The three conventional zeolites present type-I isotherms, consistent with their predominantly microporous nature.<sup>40</sup> The corresponding textural properties are listed in Table 6.2. All the nanocrystalline zeolites prepared with the OSDA present significantly larger mesopore volumes ( $> 0.14 \text{ cm}^3 \text{ g}^{-1}$ ) and external surface areas ( $> 80 \text{ m}^2 \text{ g}^{-1}$ ) than the corresponding

conventional samples. Thus, Me<sub>3</sub>N-benzyl-NMe<sub>3</sub> is an effective OSDA to direct the formation of nanosized MOR, EU-1 and ZSM-12 zeolite.

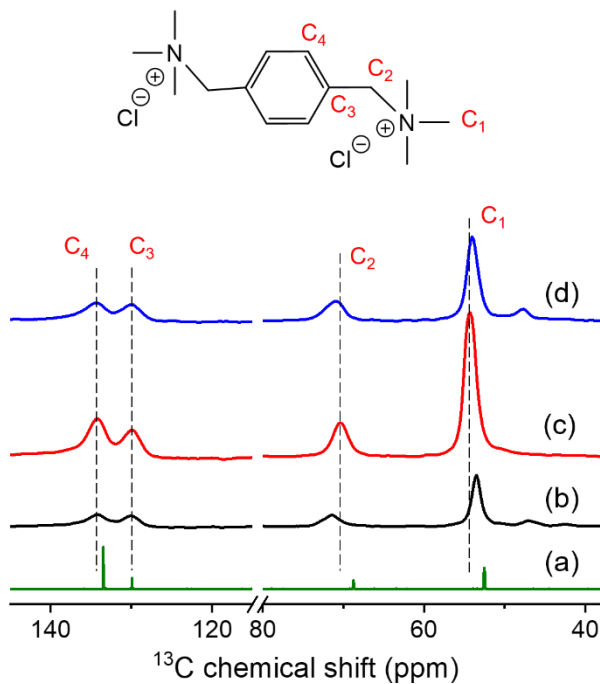


**Figure 6.4.** <sup>13</sup>C NMR spectra of Me<sub>3</sub>N-benzyl-NMe<sub>3</sub> in (a) dissolved in D<sub>2</sub>O and (b-d) in as-synthesized zeolites: (b) MOR-Nano, (c) EU-1-Nano and (d) ZSM-12-Nano.

As shown in Figure 6.4, the <sup>13</sup>C NMR spectra of as-synthesized zeolites match well with the one of the OSDA, indicating that the Me<sub>3</sub>N-benzyl-NMe<sub>3</sub> molecule is stable during the crystallization process. Some small differences are observed for the methyl and methylene carbon resonances of the OSDA occluded in different zeolites, which most likely derives from slightly different conformations of the OSDA in the particular micropores, which is closely related to the zeolite structure and topology.<sup>41, 42</sup>

### 6.3.2 Crystallization

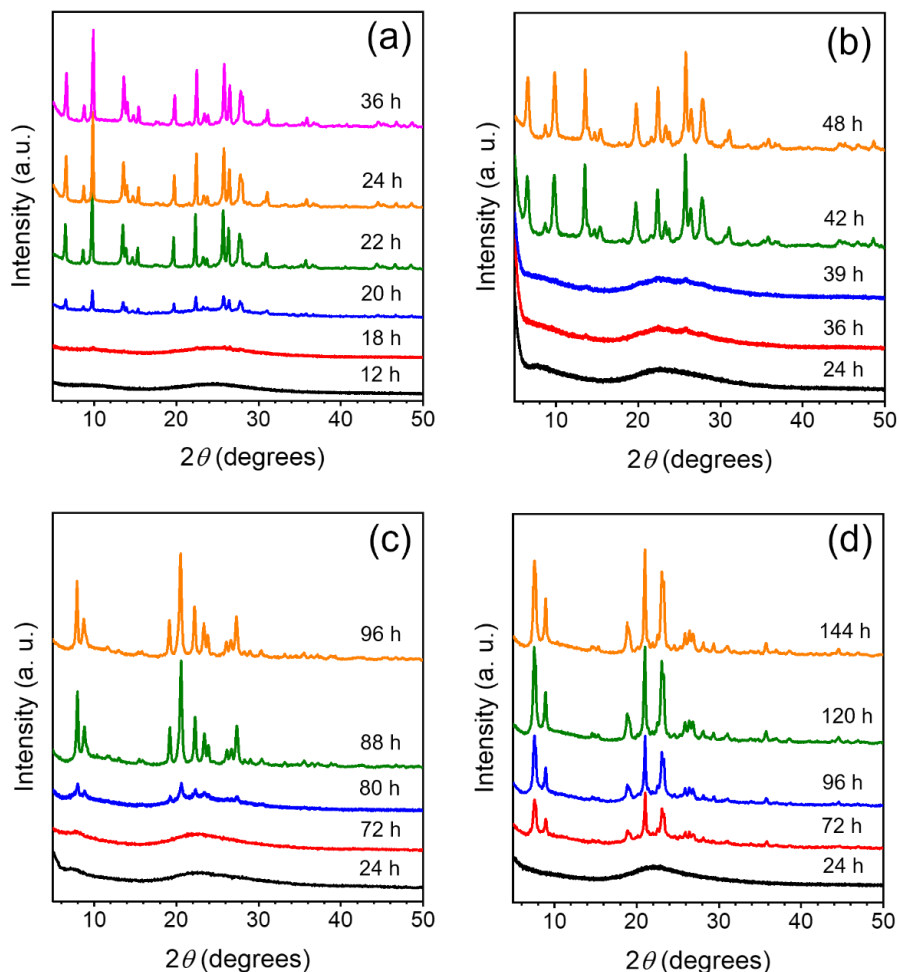


**Figure 6.5.** XRD patterns of solid samples obtained at different crystallization times: (a) MOR-Con, (b) MOR-Nano, (c) EU-1-Nano and (d) ZSM-12-Nano.

Next, to understand how the presence of the OSDA in the synthesis gel affects the evolution of the precursors into the final zeolites with different framework topologies, the solid products obtained at different crystallization times were characterized. For conventional MOR synthesized from the inorganic gel, the XRD results in Figure 6.5a show that fully crystalline samples can be obtained in 24 h via a rapid crystal growth process after an induction period of 18 h. On the other hand, adding the OSDA into the same gel significantly

prolongs the induction period to 36 h. Nevertheless, the crystal growth times for MOR-Con and MOR-Nano are comparable (~6 h). Highly crystalline EU-1-Nano was obtained after 96 h (Figure 6.5c), while full crystallization of ZSM-12-Nano took 144 h due to the much slower crystal growth rate.

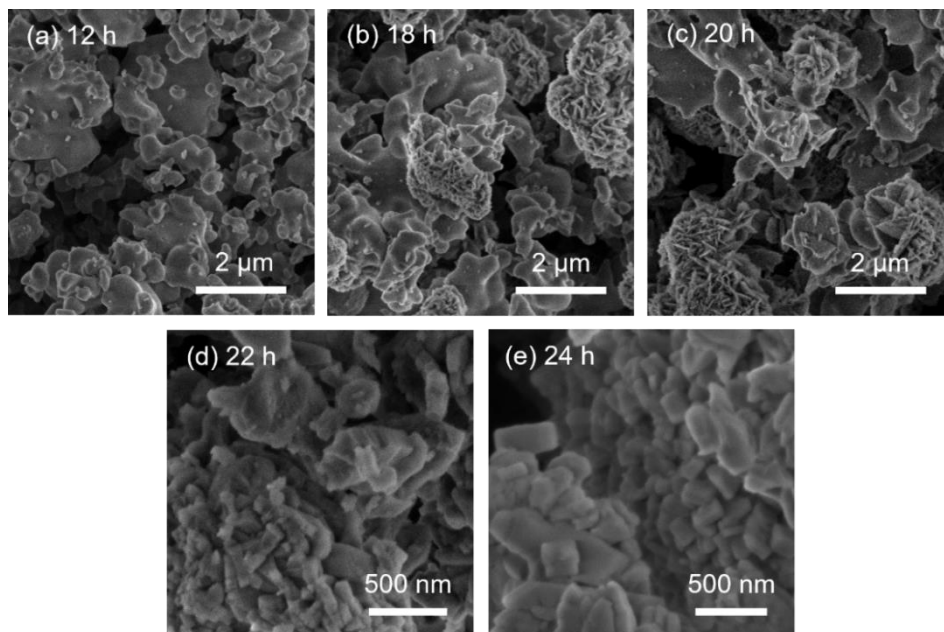


**Figure 6.6.** SEM images of solid products obtained at different crystallization times of MOR-Con.

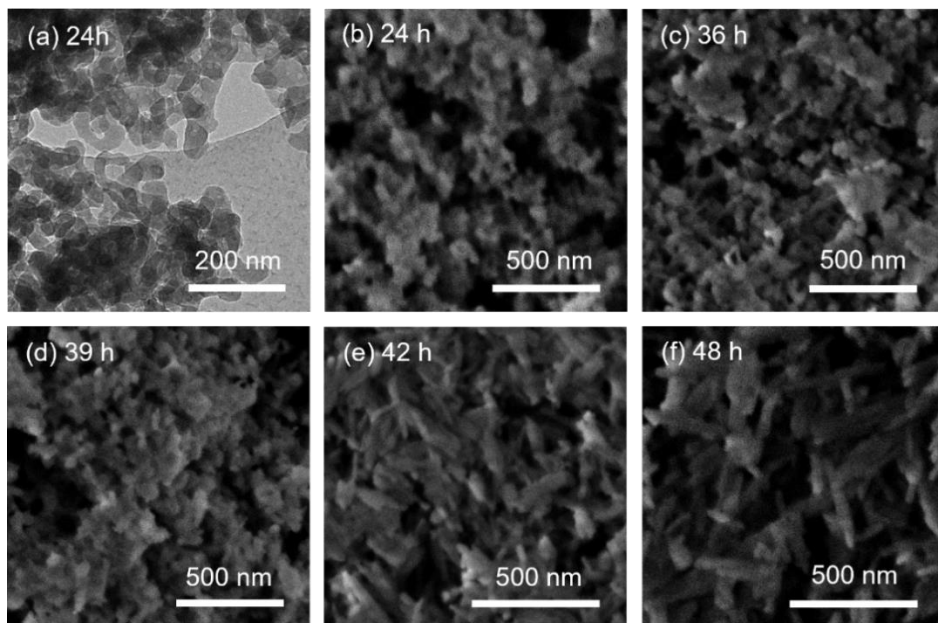


**Figure 6.7.** TEM (a) and SEM (b-f) images of solid products obtained at different crystallization times of MOR-Nano.

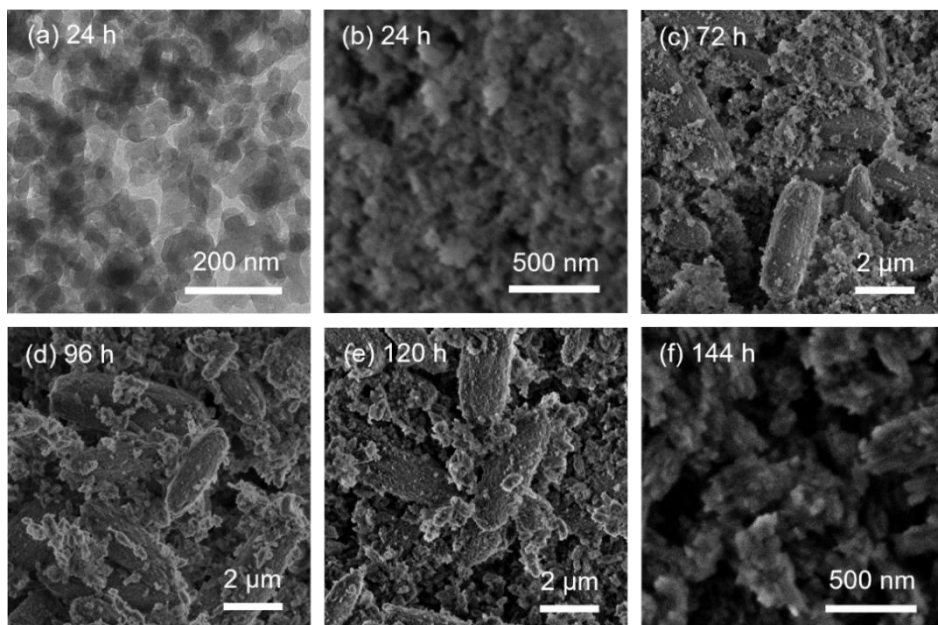


**Figure 6.8.** TEM (a) and SEM (b-f) images of solid products obtained at different crystallization times of ZSM-12-Nano.

The evolution of the morphology of the solid samples was analyzed by electron microscopy. For MOR-Con, irregular particles in the micrometer size were obtained throughout the whole crystallization process, resulting in the final bulk zeolite crystals with a size of 100-600 nm (Figure 6.6). In contrast, significantly smaller particles were already formed in the initial stages of hydrothermal synthesis of MOR-Nano (Figure 6.7). For EU-1-Nano, amorphous particles formed with sizes smaller than 50 nm, which were later still observed in aggregated form in the final crystalline EU-1-Nano (Figure E6). For ZSM-12-Nano, small particles (< 50 nm) were obtained after 24 h of hydrothermal synthesis. Prolonging the crystallization time to 72 h led to the formation of an additional phase consisting of rugby-ball-like particles. Only slight changes in the morphology were observed after further crystallization up to 120 h. Prolonging hydrothermal treatment from 120 h to 144 h resulted in the formation of loose nanoparticles with sizes smaller than 30 nm through the consumption of micron-sized particles with only a slight increase in the crystallinity (Figure 6.8).

TGA measurements were performed to investigate the interaction between the solid intermediates and the OSDA. The TG curves of all samples in Figure E7 show a major weight-loss feature between 250-700 °C due to the combustion of the OSDA. We assign the weight loss between 250-350 °C and 350-460 °C to respectively combustion of the OSDA balancing silanol defects and Si-O-Al sites. Notably, already during the induction period all the solid phases contain a substantial amount of OSDA (Tables E1-3), which is comparable to the amount contained in the final crystalline zeolites. This indicates the early strong interaction between the OSDA and the aluminosilicate precursor species, which can explain that the size of the solid precursors particles and the final zeolite are smaller than 50 nm. With ongoing crystallization, the weight-loss feature above 500 °C becomes stronger and shifts to higher temperature at the expense of the features at lower temperature, demonstrating the occlusion of the OSDA in the micropores.

### 6.3.3 Acidity

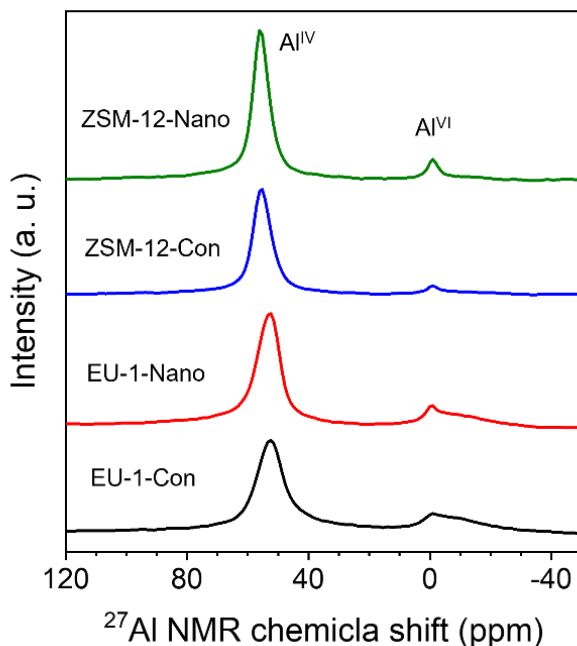


**Figure 6.9.**  $^{27}\text{Al}$  NMR spectra of calcined zeolites.

Next, ZSM-12-Nano and EU-1-Nano and their reference counterparts were chosen for further study. The Si/Al ratios of calcined zeolites determined by ICP elemental analysis are listed in Table 6.3. EU-1-Con and EU-1-Nano exhibit comparable Si/Al ratios (19.6 and 17.8, respectively). The Si/Al ratio of ZSM-12-Nano is 23.4, which is close to the initial gel ratio of 25. Compared to ZSM-12-Nano, ZSM-12-Con has a higher Si/Al ratio of 30.5. It should be noted that it is difficult to synthesize phase-pure ZSM-12 with a Si/Al ratio lower than 30 with MTEACl.<sup>43, 44</sup>  $^{27}\text{Al}$  NMR spectroscopy was used to investigate the chemical environment of the Al atoms in the zeolite samples. The corresponding spectra in Figure 6.9 are dominated by a main peak at 53 ppm and 56 ppm for EU-1 and ZSM-12 zeolites, respectively, corresponding to tetrahedrally coordinated framework Al ( $\text{Al}^{\text{IV}}$ ). The weak peak around 0 ppm is due to octahedrally coordinated non-framework Al ( $\text{Al}^{\text{VI}}$ ).<sup>45-47</sup> Deconvolution of these spectra shows that ~80 % of Al atoms are incorporated into the framework of EU-1-Con and EU-1-Nano, while more than 90% of Al is incorporated into the framework of ZSM-12-Con and ZSM-12-Nano. The acidity of the zeolites was characterized by IR spectroscopy after pyridine adsorption and subsequent evacuation at 150 °C, 300 °C and 500 °C. The bands at 1455  $\text{cm}^{-1}$  and 1545  $\text{cm}^{-1}$  are associated with



pyridine adsorbed on Lewis acid sites (LAS) and Brønsted acid sites (BAS), respectively (Figure E8).<sup>48</sup> The total density of BAS and LAS after evacuation of pyridine at 150 °C are given in Table 6.3. Both EU-1-Nano and ZSM-12-Nano display higher BAS densities than their bulk counterparts, in keeping with the differences in Al content.

**Table 6.3.** Si/Al ratios, fractions of framework Al, and acidity of the calcined zeolites.

Zeolite	Si/Al <sup>a</sup>	Al <sub>F</sub> (%) <sup>b</sup>	[BAS] <sup>c</sup> ( $\mu\text{mol g}^{-1}$ )	[LAS] <sup>d</sup> ( $\mu\text{mol g}^{-1}$ )
EU-1-Con	19.6	77.2	592	255
EU-1-Nano	17.8	82.5	759	207
ZSM-12-Con	30.5	91.0	488	113
ZSM-12-Nano	23.4	91.3	663	135

<sup>a</sup> Si/Al ratio determined by ICP.

<sup>b</sup> Fraction of framework Al determined by <sup>27</sup>Al NMR.

<sup>c</sup> Density of BAS determined by IR spectra of adsorbed pyridine after evacuation for 1 h at 150 °C.

<sup>d</sup> Density of LAS determined by IR spectra of adsorbed pyridine after evacuation for 1 h at 150 °C.

## 6.3.4 Catalytic activity

### 6.3.4.1 Methanol to hydrocarbons

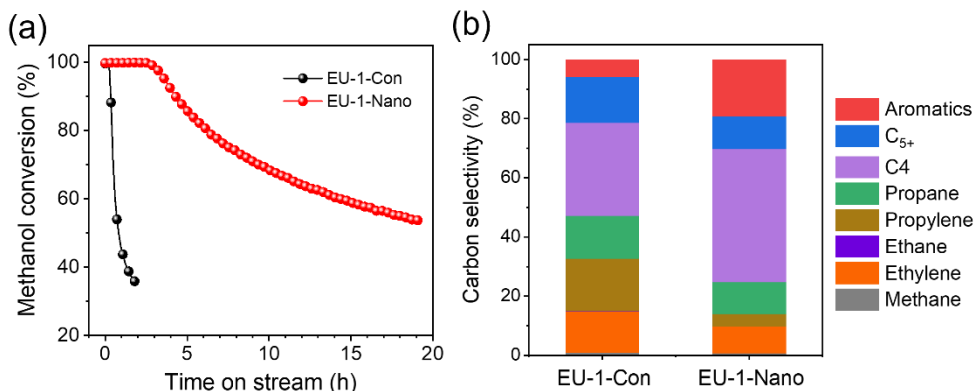


**Figure 6.10.** MTH performance of EU-1 zeolites: (a) methanol conversion as a function of reaction time and (b) product selectivity after 0.25 h time on stream.

The potential of nanocrystalline EU-1-Nano in acid catalysis was evaluated by determining its catalytic performance in the MTH reaction. The MTH process is a promising industrial chemical process for obtaining chemical building blocks and fuels from methanol, which can be obtained from conventional as well as renewable resources such as carbon dioxide (with green hydrogen) and biomass.<sup>49, 50</sup> Figure 6.10a shows the conversion of methanol as a function of time on stream at a temperature of 350 °C. At the start of the reaction, both catalysts can convert the methanol feed completely. The methanol conversion of EU-1-Con decreased rapidly with the methanol conversion decreasing to 50% in about 1 h. For EU-1-Nano, methanol conversion only started to decline after 3 h and it took 19 h to obtain a methanol conversion of 50%. As EU-1 zeolite possesses one-dimensional 10-membered ring (10-MR) channels (0.54 nm × 0.41 nm) along the *a*-axis with 12-membered ring (12-MR) side pockets (0.68 nm × 0.58 nm, 0.8 nm depth) along the *c*-axis, single-file diffusion can limit the performance of this zeolite.<sup>51</sup> This may not only result in rapid formation of coking of the zeolite micropore space, but also easily render the acid sites inaccessible.<sup>32</sup> The TG results in Figure E9 show that the coke content in used EU-1-Nano (8.1%) is substantially higher than in used EU-1-Con (4.9%), whereas the average coke formation rate of EU-1-Nano (4.7 mg g<sup>-1</sup> h<sup>-1</sup>) is much lower than that of EU-1-Con (29.2 mg g<sup>-1</sup> h<sup>-1</sup>). The coke content of EU-1-Nano is higher, because this sample converts more methanol. Considering the small difference in acidity between these two samples, the fact that EU-1-Nano containing more coke is still more active can be attributed to the improved accessibility of acid sites as a consequence of the reduced crystal size. Therefore, it can be concluded that the longer lifetime of EU-1-Nano is due to a higher accessibility of acid sites and a lower coke formation rate, thus resulting in a better utilization of micropores. The product distribution given in Figure 6.10b shows that EU-1 zeolite produces a wide range of hydrocarbons including light olefins and paraffins and gasoline-range products with a relatively small contribution of aromatics. As such, EU-1 can be compared with ZSM-22, in which the elliptical channels (0.57 nm × 0.46 nm) without side-pockets limit the amount of aromatics.<sup>52</sup> The presence of side-pockets in EU-1 provides less constraints to aromatics formation.<sup>31, 53</sup> As such, it is likely that the shortened diffusion pathways in nanosized EU-1 crystals leads to a higher rate of aromatics desorption, resulting in a larger contribution of aromatics to the product mixture. The shorter residence time of such coke precursors also lowers the rate of coking deactivation.

#### 6.3.4.2 Alkylation of benzene with benzyl alcohol

The alkylation of benzene with benzyl alcohol was chosen as a model reaction to evaluate the catalytic performance of ZSM-12 zeolites. The overall reaction pathway is displayed in Figure 6.11 left.<sup>54</sup> The products in this reaction are diphenylmethane (DPM) and dibenzyl ether (DBE). The conversion of BA as a function of the reaction time over nanosized and

conventional ZSM-12 zeolites are shown in Figure 6.11 right. ZSM-12-Con shows a low catalytic activity with a BA conversion of 13.5% at a DPM selectivity of 45% after 6 h. ZSM-12-Nano presents a much higher catalytic activity with a BA conversion of 55% and a DPM selectivity of 71% after the same reaction time. It has been well established that strong BAS are needed to polarize the benzylating agent.<sup>55, 56</sup> The one-dimensional channels ( $0.57 \times 0.61$  nm) of ZSM-12 zeolite can strongly impede the diffusion of the relatively large products DPM ( $0.49 \times 0.92$  nm) and DPE ( $0.49 \times 1.15$  nm).<sup>57</sup> Considering the relatively small differences in acidity between ZSM-12-Con and ZSM-12-Nano, the significantly improved activity of ZSM-12-Nano can be ascribed to the higher accessibility of the acid sites as a result of the much smaller zeolite crystal size.

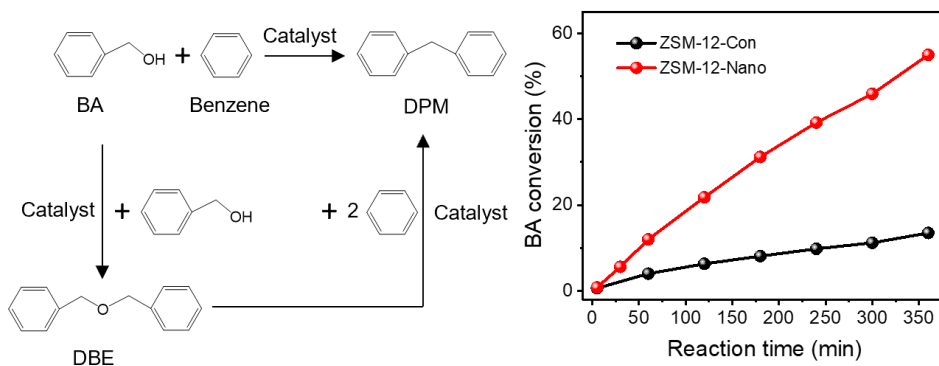


**Figure 6.11.** (Left) Reaction pathway for alkylation of benzene with benzyl alcohol (BA) and (right) catalytic conversion of BA over ZSM-12 zeolites.

## 6.4. Conclusions

In summary, this work describes the direct synthesis of nanosized MOR, EU-1 and ZSM-12 zeolites by simply modifying the synthesis, in terms of gel compositions (NaOH/Si and Si/Al ratios) and crystallization time, using  $\text{Me}_3\text{N-benzyl-NMe}_3$  as the sole OSDA.  $^{13}\text{C}$  NMR study reveals subtle differences in host-guest interactions between the OSDA and the respective zeolitic structures, which drives from the flexible and adaptable methyl and methylene groups of the OSDA. TGA in combination with electron microscopy reveals that the strong interaction between the OSDA and aluminosilicate precursors can effectively decreasing the particle size of solid products throughout the crystallization of MOR-Nano and EU-1-Nano, while ZSM-12-Nano exhibits a different crystallization behavior involving a slow transformation of bulk particles to nanocrystals through the longtime crystal growth stage. ZSM-12-Nano and EU-1-Nano display significantly improved deactivation resistance in

MTH reaction and highly improved catalytic activity in alkylation of benzene, respectively, as compared to their corresponding bulk counterparts. The improved catalytic performance of nanocrystalline zeolites is attributed to the enhanced mass transfer ability and better accessibility of acid sites. Overall, this work not only shows a facile route to synthesize nanosized MOR, EU-1 and ZSM-12 zeolites, but also highlights how to unlock the versatility of a simple OSDA in nanosized zeolite synthesis by means of its geometric flexibility and synergistic effect with the inorganic component.

## 6.5 References

1. J. Li, A. Corma and J. Yu, *Chem. Soc. Rev.*, 2015, **44**, 7112-7127.
2. M. Moliner, C. Martínez and A. Corma, *Angew. Chem. Int. Ed.*, 2015, **54**, 3560-3579.
3. J. Shi, Y. Wang, W. Yang, Y. Tang and Z. Xie, *Chem. Soc. Rev.*, 2015, **44**, 8877-8903.
4. H. Dai, Y. Shen, T. Yang, C. Lee, D. Fu, A. Agarwal, T. T. Le, M. Tsapatsis, J. C. Palmer, B. M. Weckhuysen, P. J. Dauenhauer, X. Zou and J. D. Rimer, *Nat. Mater.*, 2020, **19**, 1074-1080.
5. S. Mintova, J.-P. Gilson and V. Valtchev, *Nanoscale*, 2013, **5**, 6693-6703.
6. S. Mintova, M. Jaber and V. Valtchev, *Chem. Soc. Rev.*, 2015, **44**, 7207-7233.
7. E. Koohsaryan and M. Anbia, *Chin. J. Catal.*, 2016, **37**, 447-467.
8. H. Xu, W. Chen, G. Zhang, P. Wei, Q. Wu, L. Zhu, X. Meng, X. Li, J. Fei, S. Han, Q. Zhu, A. Zheng, Y. Ma and F.-S. Xiao, *J. Mater. Chem. A*, 2019, **7**, 16671-16676.
9. V. Valtchev and L. Tosheva, *Chem. Rev.*, 2013, **113**, 6734-6760.
10. Q. Zhang, S. Xiang, Q. Zhang, B. Wang, A. Mayoral, W. Liu, Y. Wang, Y. Liu, J. Shi, G. Yang, J. Luo, X. Chen, O. Terasaki, J.-P. Gilson and J. Yu, *Chem. Mater.*, 2020, **32**, 751-758.
11. A. Sakthivel, A. Iida, K. Komura, Y. Sugi and K. V. R. Chary, *Microporous Mesoporous Mater.*, 2009, **119**, 322-330.
12. X. Feng, N. Sheng, Y. Liu, X. Chen, D. Chen, C. Yang and X. Zhou, *ACS Catal.*, 2017, **7**, 2668-2675.
13. H. Chen, M. Wang, M. Yang, W. Shang, C. Yang, B. Liu, Q. Hao, J. Zhang and X. Ma, *J. Mater. Sci.*, 2019, **54**, 8202-8215.
14. M. Choi, K. Na, J. Kim, Y. Sakamoto, O. Terasaki and R. Ryoo, *Nature*, 2009, **461**, 246-249.
15. W. Kim, J.-C. Kim, J. Kim, Y. Seo and R. Ryoo, *ACS Catal.*, 2013, **3**, 192-195.

16. A. Molino, K. A. Łukaszuk, D. Rojo-Gama, K. P. Lillerud, U. Olsbye, S. Bordiga, S. Svelle and P. Beato, *Chem. Commun.*, 2017, **53**, 6816-6819.
17. E. M. Gallego, C. Paris, M. R. Díaz-Rey, M. E. Martínez-Armero, J. Martínez-Triguero, C. Martínez, M. Moliner and A. Corma, *Chem. Sci.*, 2017, **8**, 8138-8149.
18. X. Zhang, D. Liu, D. Xu, S. Asahina, K. A. Cychosz, K. V. Agrawal, Y. A. Wahedi, A. Bhan, S. A. Hashimi, O. Terasaki, M. Thommes and M. Tsapatsis, *Science*, 2012, **336**, 1684-1687.
19. K. Zhang, S. Luo, Z. Liu, C. Li, Z. Ke, X. Yan, Y. Wu and H. Xi, *Chem. Eur. J.*, 2018, **24**, 8133-8140.
20. X. Jia, Y. Zhang, Z. Gong, B. Wang, Z. Zhu, J. Jiang, H. Xu, H. Sun, L. Han, P. Wu and S. Che, *J. Phys. Chem. C*, 2018, **122**, 9117-9126.
21. R. Martínez-Franco, C. Paris, M. E. Martínez-Armero, C. Martínez, M. Moliner and A. Corma, *Chem. Sci.*, 2016, **7**, 102-108.
22. Y. Zhao, Z. Ye, L. Wang, H. Zhang, F. Xue, S. Xie, X.-M. Cao, Y. Zhang and Y. Tang, *Cryst. Growth Des.*, 2018, **18**, 1101-1108.
23. P. Lu, S. Ghosh, M. Dorneles de Mello, H. S. Kamaluddin, X. Li, G. Kumar, X. Duan, M. Abeykoon, J. A. Boscoboinik and L. Qi, *Angew. Chem. Int. Ed.*, 2021, **60**, 19214-19221.
24. A. Jackowski, S. I. Zones, S.-J. Hwang and A. W. Burton, *J. Am. Chem. Soc.*, 2009, **131**, 1092-1100.
25. Y. Kubota, M. M. Helmkamp, S. I. Zones and M. E. Davis, *Microporous Mater.*, 1996, **6**, 213-229.
26. S. B. Hong, *Catal. Surv. Asia*, 2008, **12**, 131-144.
27. P. Lu, S. Ghosh, M. Dorneles de Mello, H. S. Kamaluddin, X. Li, G. Kumar, X. Duan, M. Abeykoon, J. A. Boscoboinik and L. Qi, *Angew. Chem. Int. Ed.*, 2021, **133**, 19214-19221.
28. S. I. Zones and A. W. Burton, *J. Mater. Chem.*, 2005, **15**, 4215-4223.
29. P. Lu, L. Gómez-Hortigüela, L. Xu and M. A. Camblor, *J. Mater. Chem. A*, 2018, **6**, 1485-1495.
30. C. Martínez and A. Corma, *Coord. Chem. Rev.*, 2011, **255**, 1558-1580.
31. B. Jing, J. Li, Z. Li, S. Wang, Z. Qin, W. Fan and J. Wang, *J. Nanosci. Nanotechnol.*, 2017, **17**, 3680-3688.
32. M. H. M. Ahmed, O. Muraza, M. Yoshioka and T. Yokoi, *Microporous Mesoporous Mater.*, 2017, **241**, 79-88.
33. Y. Liu, N. Zhao, H. Xian, Q. Cheng, Y. Tan, N. Tsubaki and X. Li, *ACS Appl Mater Interfaces*, 2015, **7**, 8398-8403.

34. L. Zhang, S. Xie, W. Xin, X. Li, S. Liu and L. Xu, *Mater. Res. Bull.*, 2011, **46**, 894-900.
35. S.-H. Lee, C.-H. Shin, D.-K. Yang, S.-D. Ahn, I.-S. Nam and S. B. Hong, *Microporous Mesoporous Mater.*, 2004, **68**, 97-104.
36. C. Jo, J. Jung, H. S. Shin, J. Kim and R. Ryoo, *Angew. Chem. Int. Ed.*, 2013, **52**, 10014-10017.
37. L. Zhang, A. N. C. v. Laak, P. E. d. Jongh and K. P. d. Jong, *Microporous Mesoporous Mater.*, 2009, **126**, 115-124.
38. S. Li, H. Wu, R. C. J. van de Poll, R. R. M. Joosten, N. Kosinov and E. J. M. Hensen, *ChemCatChem*, 2022, **14**, e202101852.
39. J. Zhang, H. Shi, Y. Song, W. Xu, X. Meng and J. Li, *Inorganic Chemistry Frontiers*, 2021, **8**, 3077-3084.
40. S. Storck, H. Bretinger and W. F. Maier, *Appl. Catal., A*, 1998, **174**, 137-146.
41. S.-H. Lee, D.-K. Lee, C.-H. Shin, Y.-K. Park, P. A. Wright, W. M. Lee and S. B. Hong, *J. Catal.*, 2003, **215**, 151-170.
42. G. Giordano, J. Nagy and E. Derouane, *J. Mol. Catal. A: Chem.*, 2009, **305**, 34-39.
43. A. S. Araujo, A. O. Silva, M. J. Souza, A. C. Coutinho, J. M. Aquino, J. A. Moura and A. M. J. A. Pedrosa, *Adsorption*, 2005, **11**, 159-165.
44. G. Feng, Z.-H. Wen, J. Wang, Z.-H. Lu, J. Zhou and R. Zhang, *Microporous Mesoporous Mater.*, 2021, **312**, 110810.
45. K. T. G. Carvalho, D. S. Araújo Silva and E. A. Urquieta-Gonzalez, *Ind. Eng. Chem. Res.*, 2019, **58**, 7044-7051.
46. S. Pan, Q. Wu, X. Wang, F. Chen, X. Meng and F.-S. Xiao, *Microporous Mesoporous Mater.*, 2016, **235**, 246-252.
47. G. Dai, J. Ma, H. Xiao, W. Hao and R. Li, *Mater. Res. Bull.*, 2018, **100**, 76-82.
48. L.-E. Sandoval-Díaz, J.-A. González-Amaya and C.-A. Trujillo, *Microporous mesoporous materials*, 2015, **215**, 229-243.
49. U. Olsbye, S. Svelle, K. Lillerud, Z. Wei, Y. Chen, J. Li, J. Wang and W. Fan, *Chem. Soc. Rev.*, 2015, **44**, 7155-7176.
50. S. Dang, H. Yang, P. Gao, H. Wang, X. Li, W. Wei and Y. Sun, *Catal. Today*, 2019, **330**, 61-75.
51. P. C. Mihindou-Koumba, J. D. Comparot, S. Laforge and P. Magnoux, *J. Catal.*, 2008, **255**, 324-334.
52. S. Teketel, S. Svelle, K.-P. Lillerud and U. Olsbye, *ChemCatChem*, 2009, **1**, 78-81.
53. S. Teketel, W. Skistad, S. Benard, U. Olsbye, K. P. Lillerud, P. Beato and S. Svelle, *ACS Catal.*, 2012, **2**, 26-37.
54. H. Jin, M. B. Ansari, E.-Y. Jeong and S.-E. Park, *J. Catal.*, 2012, **291**, 55-62.

55. A. P. Singh, D. Bhattacharya and S. Sharma, *J. Mol. Catal. A: Chem.*, 1995, **102**, 139-145.
56. N. Candu, M. Florea, S. M. Coman and V. I. Parvulescu, *Appl. Catal., A*, 2011, **393**, 206-214.
57. X. Lu, Y. Guo, Y. Zhang, R. Ma, Y. Fu and W. Zhu, *Microporous Mesoporous Mater.*, 2020, **306**, 110459.

# Appendix E

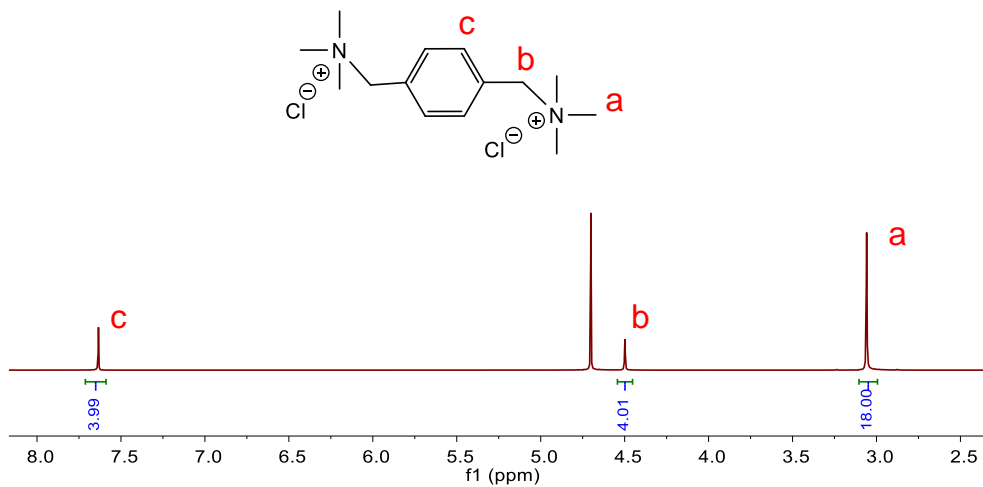


**Figure E1.** Liquid-state  $^1\text{H}$  NMR spectrum of  $\text{Me}_3\text{N}$ -benzyl- $\text{NMe}_3$  in  $\text{D}_2\text{O}$ .

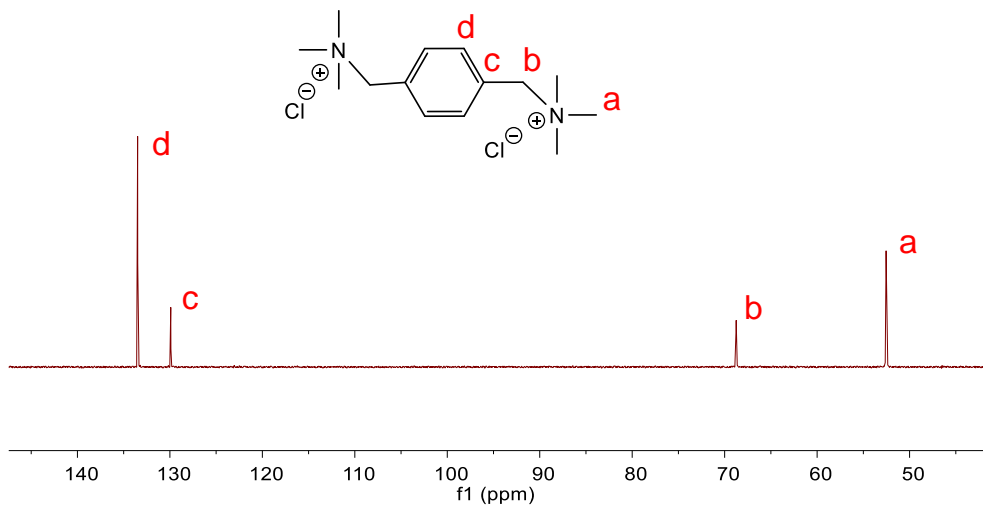


**Figure E2.** Liquid-state  $^{13}\text{C}$  NMR spectrum of  $\text{Me}_3\text{N}$ -benzyl- $\text{NMe}_3$  in  $\text{D}_2\text{O}$ .



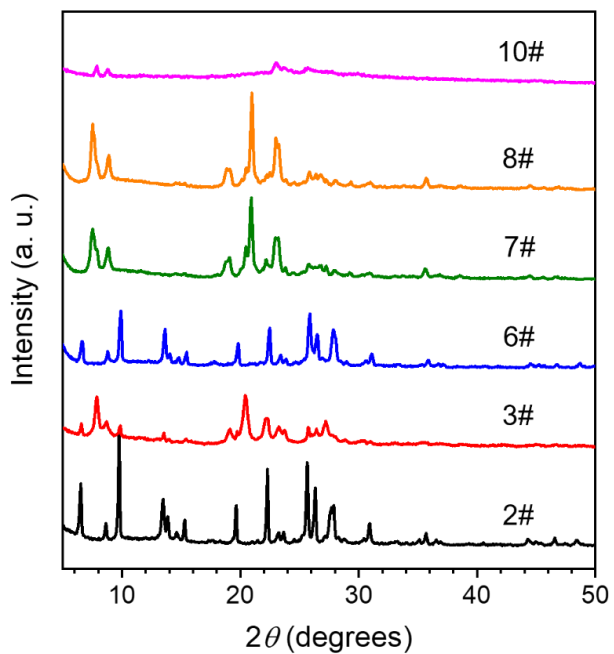


**Figure E3.** XRD patterns of solid products.

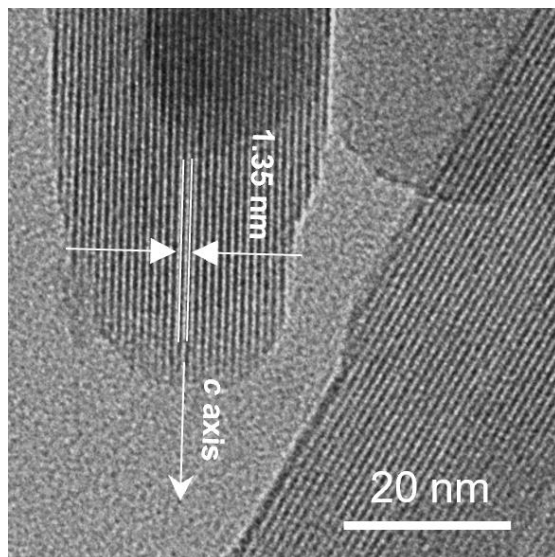


**Figure E4.** TEM image of as-synthesized MOR-Nano.

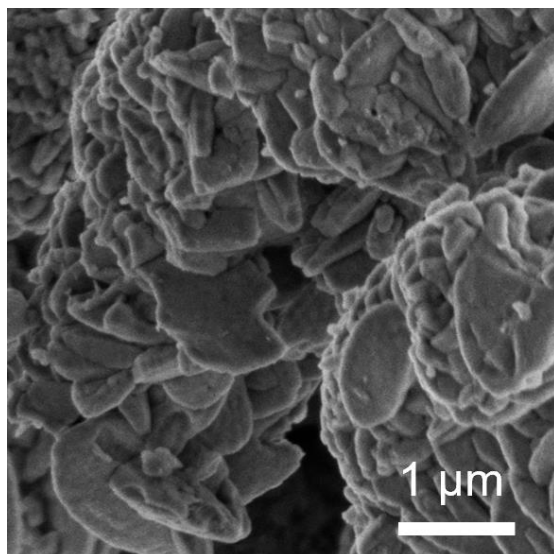


**Figure E5.** SEM image of as-synthesized MOR-Con(0.7).

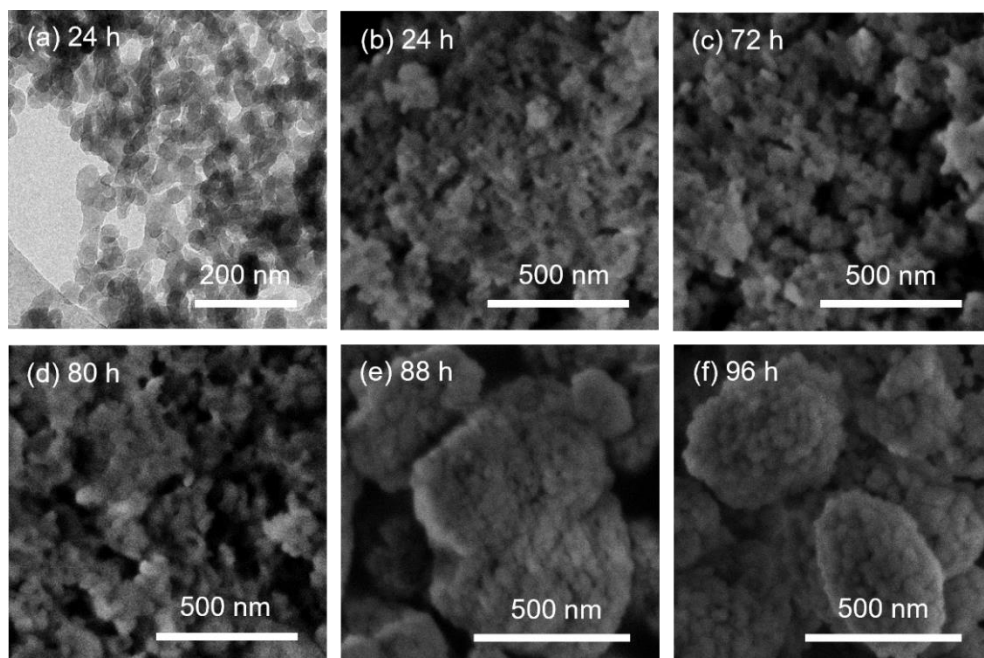


**Figure E6.** TEM (a) and SEM (b-f) images of solid products obtained at different crystallization times of EU-1-Nano.

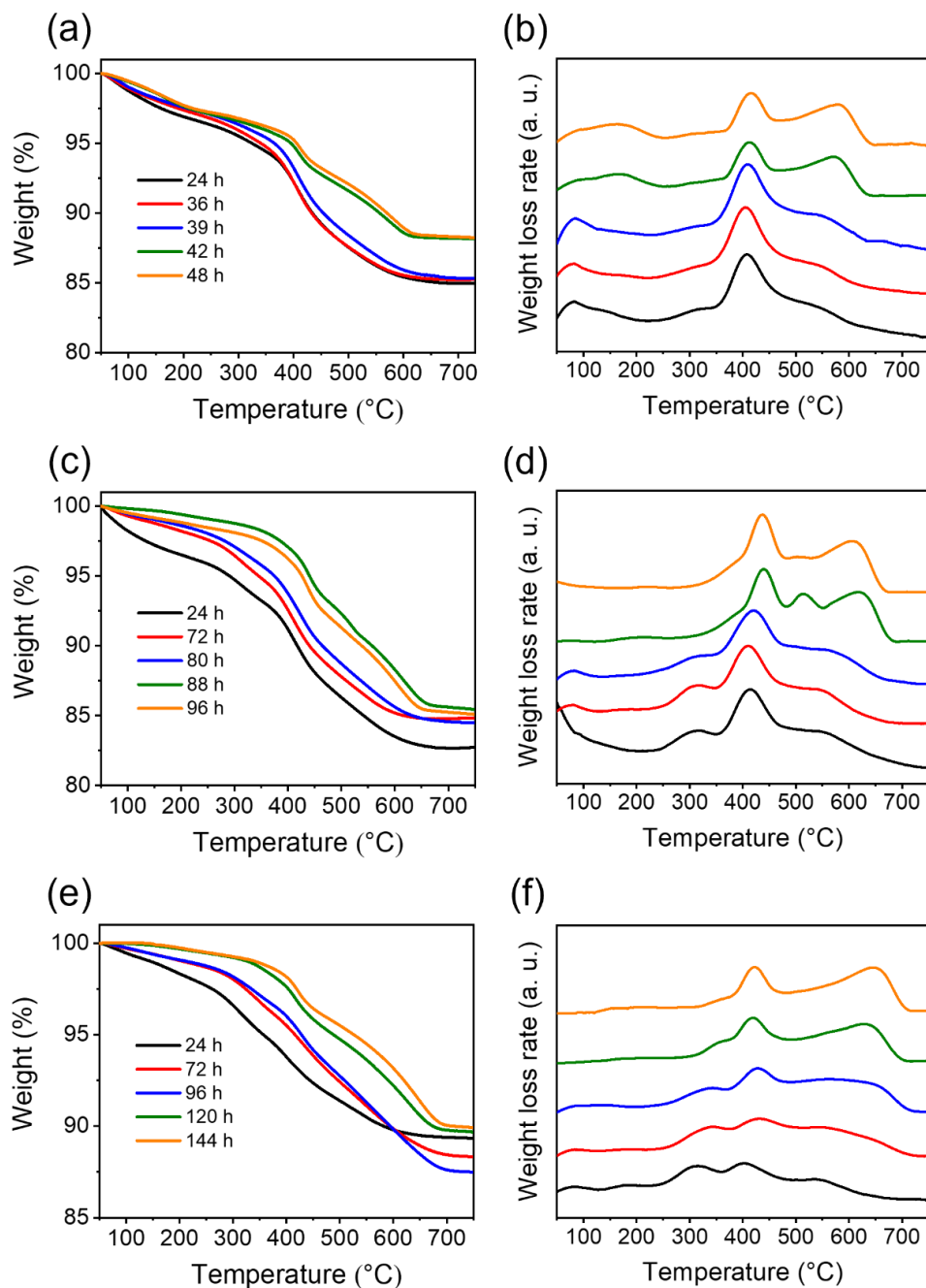


**Figure E7.** TG (left) and DTG (right) curves of samples obtained at different crystallization times: (a and b) MOR-Nano; (c-d) EU-1-Nano and (e and f) ZSM-12-Nano.

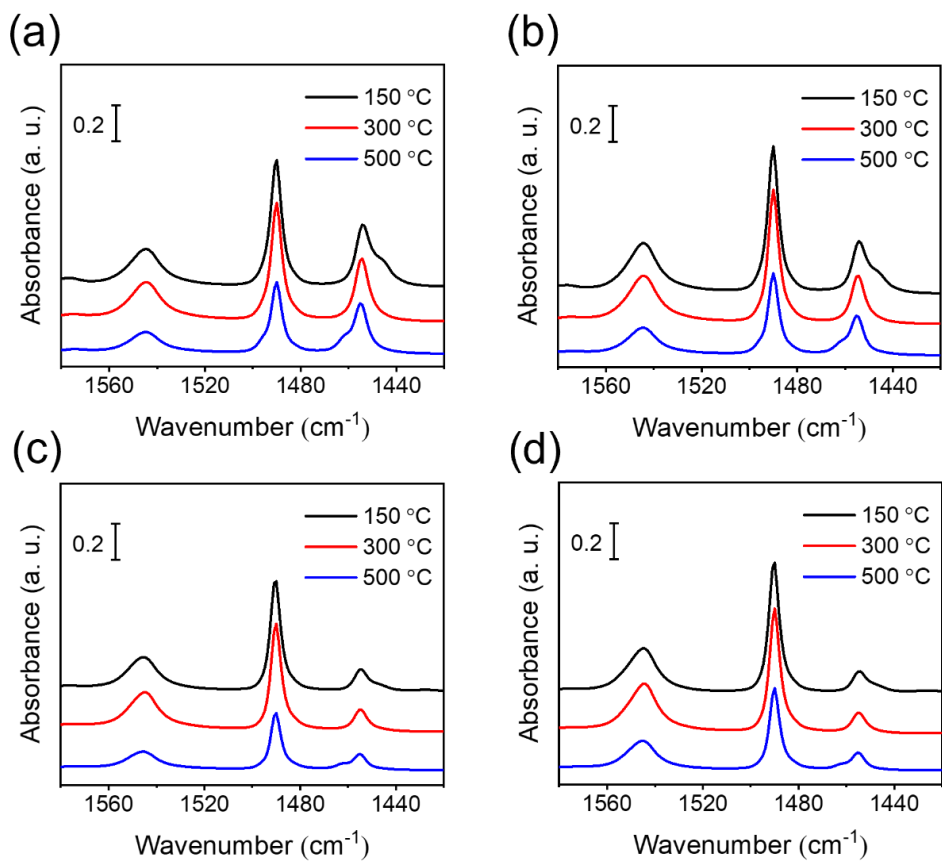


**Figure E8.** IR spectra of pyridine adsorbed on zeolites: (a) EU-1-Con, (b) EU-1-Nano, (c) ZSM-12-Con and (d) ZSM-12-Nano.

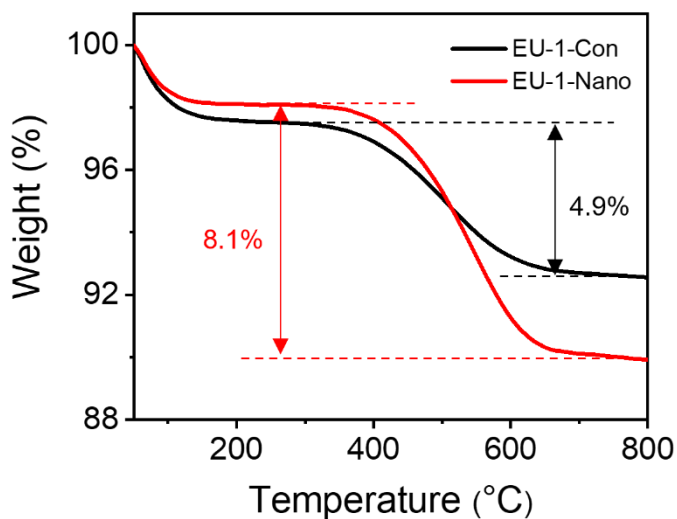


**Figure E9.** TG profiles of spent catalysts after MTH reaction.

**Table E1.** The contents of OSDA occluded in solid products obtained at different crystallization time for MOR-Nano.

Synthesis time (h)	24 h	36 h	39 h	42 h	48 h
Organic content (wt%)	11.3	11.5	11.7	8.9	8.9

**Table E2.** The contents of OSDA occluded in solid products obtained at different crystallization time for EU-1-Nano.

Synthesis time (h)	24 h	72 h	80 h	88 h	96 h
Organic content (wt%)	13.2	12.8	13.5	13.5	13.2

**Table E3.** The contents of OSDA occluded in solid products obtained at different crystallization time for ZSM-12-Nano.

Synthesis time (h)	24 h	72 h	96 h	120 h	144 h
Organic content (wt%)	8.3	10.2	11.1	9.7	9.5

**Table E4.** Product selectivity of MTH reaction after 15 min time on stream over EU-1 zeolites.

Sample	Selectivity (%)							
	CH <sub>4</sub>	C <sub>2</sub> H <sub>4</sub>	C <sub>2</sub> H <sub>6</sub>	C <sub>3</sub> H <sub>6</sub>	C <sub>3</sub> H <sub>8</sub>	C <sub>4</sub>	C <sub>5+</sub>	Aromatics
EU-1-Con	0.9	13.9	0.1	17.7	14.5	31.5	15.6	5.8
EU-1-Nano	0.7	9.0	< 0.1	4.3	10.6	45.2	11.0	19.2



# Chapter 7

## Summary and outlook

### **Nanosized zeolites directed by easily accessible non-surfactant diquats: synthesis, crystallization mechanism and catalytic applications**

Zeolites are an important class of inorganic crystalline materials possessing well-defined channels and cavities in the molecular range. They are widely used in industrial processes, in particular as heterogeneous catalysts to speed up chemical reaction rates, owing to their unique shape selectivity, tunable acidity and high (hydro)thermal stability. The shape selectivity introduced by zeolite micropores are of paramount importance, while diffusion limitations imposed by the micropores can limit the catalytic performance, particular when reactions involve bulky molecules and consecutive steps to undesired products. Decreasing the size of zeolite crystals below 100 nm (nanocrystals) is an effective way to overcome the problem of slow diffusion of guest molecules in zeolites. Acidity also plays a significant role in mediating the catalytic performance. Zeolite frameworks are constructed of corner-sharing  $TO_4$  atoms, where T refers to a tetrahedrally coordinated atom, most commonly Si and Al. The incorporation of Al atoms in the zeolite framework creates Brønsted acid sites (BAS), allowing the application of zeolites as acid catalysts. Among the many relevant physicochemical properties of zeolites, crystal size and acidity play important roles in the final performance of these catalysts. However, preparing zeolites with well-controlled properties is often challenging due to the complexity of zeolite crystallization. This work focused on the use of simple organic structure-directing agents (OSDAs) for the synthesis of nanosized zeolites of particular topologies and framework Si/Al ratios in order to optimize the catalytic performance.

In **Chapter 2**, nanosized mordenite (MOR) zeolites were hydrothermally synthesized with cetyltrimethylammonium (CTA) hydroxide as the sole organic template in comparison to a bulk reference MOR zeolite. Moreover, the aluminum source was modified by comparing  $Al(NO_3)_3$ ,  $AlCl_3$  and  $Al(OH)_3$ . All MOR zeolites prepared with CTA show a reduced crystal size compared to the reference. The crystal dimensions are predominantly reduced in the a- and b-direction, when  $AlCl_3$  and  $Al(OH)_3$  were used as the aluminum source. Besides a higher external surface area, the use of CTA also leads to a more defective zeolite structure



in which the BAS in the side-pockets are more accessible for pyridine. Nanocrystalline MOR zeolites showed a higher activity and improved product distribution in the alkylation of benzene with benzyl alcohol compared to their corresponding bulk counterparts. Although the  $n\text{-C}_{16}$  hydroconversion performance of nanosized MOR zeolite is also improved, the stronger confinement of reactants and intermediates in the more accessible side-pockets of MOR zeolite has a negative effect on the isomer yield during hydroconversion of  $n\text{-C}_{16}$ .

In **Chapter 3**, we developed the direct synthesis of nanosized MOR and BEA zeolites by use of non-surfactant diquatery ammonium compounds. We also considered the properties (size, shape and rigidity) of the organic molecules, because these aspects strongly impact the structure-directing ability of OSDAs. A total of 6 organic compounds, *i.e.* hexane- and *p*-xylene-bridged bis-methylpyrrolidinium, -methylpiperidinium and -DABCO diquats, were employed in this chapter. These organic molecules were synthesized from commercially available chemicals via a one-step procedure. The formation of either MOR or BEA zeolite depends strongly on the size, geometry and structural rigidity of the OSDA. Optimization of the recipes led to the successful synthesis of nanosized MOR (20-50 nm) and BEA (15-30 nm) zeolites. By investigating the solid products obtained during the crystallization process, the formation of nanocrystals could be linked to the strong interaction between diquat templates and aluminosilicate species during induction, which limits the amorphous precursor particles to a size below 50 nm. Specific strong framework stabilization by the pore-filling OSDA controls the formation of either zeolite topology. Nanosized MOR and BEA zeolites outperform their bulk counterparts in Friedel-Craft reactions. In hydroconversion of  $n\text{-C}_{16}$ , nanosized Pt/BEA shows a substantially higher isomer yield than bulk Pt/BEA limiting consecutive reactions due to the shorter residence time of reaction intermediates in the smaller zeolite domains. The  $n\text{-C}_{16}$  hydroconversion over three-dimensional BEA is not limited by mass transport under the given reaction conditions, while this is not the case for the one-dimensional MOR (**Chapter 2**) and ZSM-12 (**Chapter 5**) zeolites.

Considering that the highly acidic ( $\text{Si}/\text{Al} < 15$ ) ZSM-5 zeolites in nanocrystalline form can bring distinct advantages in their use as catalysts for obtaining useful chemicals from easily accessible C1 compounds such as methane and methanol, we developed the direct synthesis of Al-rich ZSM-5 nanocrystals by a conventional hydrothermal synthesis approach using *p*-phenylenedimethylene-bis(tripropylammonium) dichloride as the OSDA in **Chapter 4**. Nanosized ZSM-5 crystals (20-50 nm) with high acidity ( $\text{Si}/\text{Al} = 11$ ) and excellent yield (99%) were obtained (denoted as ZSM-5-11). A high NaOH/Si molar ratio of 0.6 is essential. The crystallization process of ZSM-5-11 shows a long induction period (~5 days) and a fast crystal growth step (~1 day) involving a solid-state transformation. An in-depth NMR study

combined with TGA measurements reveals that, after early electrostatic interaction between condensed aluminosilicate and the head groups of OSDA, ZSM-5 crystallizes around the OSDA. ZSM-5-11 was tested as such in methanol-to-hydrocarbons (MTH) and, following impregnation with 2 wt.% Mo, in methane dehydroaromatization (MDA). ZSM-5-11 displayed significantly improved aromatics productivity in both reactions in comparison to a commercial bulk ZSM-5 (Si/Al = 12.9), mainly due to the better utilization of the micropore space of the nanocrystalline zeolite.

**Chapter 5** was dedicated to the synthesis of nanosized ZSM-12 with a wider range of Si/Al ratios than the normal 35-100 range, especially at the acidic end (Si/Al < 30). As shown in Chapters 3 and 4, simple non-surfactant diquatery compounds can be effective for the synthesis of nanosized zeolites. Our starting point was to employ diquatery ammonium compounds that are more rigid than those used before in ZSM-12 synthesis, since a more rigid organic molecule can result in a higher selectivity for a particular structure. This led to the identification of three organic compounds (*p*-xylene-bridged bis-methylpyrrolidinium, -methylpiperidinium and -1,2-dimethylimidazolium). By use of these organic molecules as the OSDA, we investigated synthesis of ZSM-12 zeolites in a wide range of Si/Al ratios from 20 to  $+\infty$  by one-step hydrothermal synthesis. Nanosized ZSM-12 zeolites were obtained from aluminosilicate gels (Si/Al = 20, 50, 100), while bulk ZSM-12 could be obtained from an all-silica gel. NMR and TGA characterizations reveal the strong interaction between the OSDA and the zeolite framework. Due to the better acid site accessibility and shorter residence times of reaction intermediates in the smaller crystals, nanocrystalline ZSM-12 zeolites exhibit improved activity and enhanced isomer yields in the hydroconversion of *n*-C<sub>16</sub> in comparison to reference bulk ZSM-12 zeolite. In the MTH reaction, ZSM-12 nanocrystals display significantly improved lifetime over bulk ZSM-12 due to the lower coke formation rate and improved accessibility of acid sites. A high propylene selectivity (51.6%) and remarkably high C<sub>3</sub>=/C<sub>2</sub>= ratio (23.4) were obtained over nanosized ZSM-12 with Si/Al ratio of 70.

In **Chapter 6**, we explored the direct synthesis of nanosized zeolites using (*p*-phenylenedimethylene-bis(trimethylammonium) dichloride as the OSDA. By modifying the gel compositions (NaOH/Si and Si/Al ratios) and crystallization time, nanosized MOR, EU-1 and ZSM-12 were obtained. <sup>13</sup>C NMR characterization reveals the difference in host-guest interaction between the OSDA and the respective zeolite structures and emphasizes the flexibility endowed by the presence of methyl and methylene groups. TGA in combination with electron microscopy reveals that the strong interaction between the OSDA and aluminosilicate precursors can effectively limit the particle size of solid products throughout the crystallization of nanosized MOR and EU-1 zeolites. In contrast, nanosized ZSM-12 exhibits a different crystallization behavior involving a slow transformation of bulk particles

to nanocrystals during the longtime crystal growth stage. Nanosized EU-1 and ZSM-12 exhibit improved deactivation resistance in MTH reaction and improved catalytic activity in alkylation of benzene with benzyl alcohol reaction, respectively, as compared to their corresponding bulk counterparts. The improved catalytic performance for these two one-dimensional zeolites is due to the shortened diffusion pathways and better accessibility of acid sites as a result of much smaller zeolite crystal size.

The main findings in this thesis are direct synthesis of nanosized zeolites with improved catalytic performance in hydrocarbon conversion reactions. Using non-surfactant diquatery ammoniums as the sole organic template is an effective strategy for the direct synthesis of nanosized zeolites. We emphasized how to take advantage of several properties, *i.e.* rigidity, flexibility, size and shape, of the non-surfactant diquatery ammonium OSDAs and also its synergistic effect with the inorganic precursor species during hydrothermal zeolite synthesis with targeted physicochemical properties. In this context, we have synthesized highly acidic ZSM-5 (Si/Al = 11) and ZSM-12 (Si/Al = 18.3) zeolites in nanocrystalline form. Zeolite crystallization is a complex process involving numerous solid-liquid equilibria and silica condensation steps, some of which are kinetically and other thermodynamically controlled. The interplay of these aspects determines the final suitability of the organic molecule as an effective OSDA, while it remains challenging to predict the outcome in terms of zeolite topology and yield. We expect that the present work will contribute to inspiring more studies to tackle the ongoing challenges on the way to the rational design of zeolite synthesis. Further in-depth studies are necessary to reveal the host-guest interactions in detail during the nucleation and crystal growth processes. Molecular modelling methods, combined with X-ray diffraction techniques and other supplementary characterization techniques such as NMR will enable the identification of the specific locations of the OSDAs in zeolites, which will undoubtedly provide new guidance for the rational design of OSDAs towards the synthesis of a target zeolite material. To identify and decouple the different types of forces, *i.e.* H-bond, Van der Waals and electrostatic interactions, in the host-guest systems of the OSDA and the zeolite framework is also essential to interpret the role of OSDAs in zeolite synthesis and the location of the final acid sites.

# Acknowledgement

Being a PhD at the IMC group for almost 5 years is a really priceless experience for me. This long journey not only provided me the chance to learn a lot of scientific knowledge but also inspired me how to make a real scientific story. Obviously, this thesis would not be finished without the help from many people.

Firstly, I would like to thank my first promotor prof. Emiel Hensen. Emiel, thank you for providing me the opportunity to study in IMC group. I appreciate your great patience especially at the beginning of my PhD. You give me the freedom to choose my research directions. Your critical and constructive comments on my research are always strong motivating forces for me to move forward to finishing my PhD. Your enthusiasm about science impressed me a lot. Your help in writing not only made the paper publishable but also inspired me how to be a real scientist. This precious experience of working closely with you will be a good memory for me.

Secondly, I would like to thank my copromotor, dr. Nikolay Kosinov. You are always open to answer my questions whenever I came to your office. It was lucky to be your office neighbor, since I can always feel your passion in science. Thanks a lot for sharing the typical and latest publications relevant to zeolite synthesis which are indeed useful for my writing. Thanks a lot for your daily supervision in many ways. Your endless energy in work is always admired.

I would like to thank the committee members – prof. J. van der Schaaf, prof. J. Yu, prof. P.P. Pescarmona, prof. J.A.M. Kuipers and dr. M. Dusselier, who took time to read and evaluate my thesis. Your feedbacks helped me a lot to improve it.

The financial support from China Scholarship Council (CSC) is also highly appreciated.

Many thanks to our technical team in IMC group. Brahim, thanks a lot for your help, especially in NMR measurements and the data analysis. These NMR measurements are definitely helpful for my research. I appreciate that you responded to my questions even during your holiday. Tiny, thank you very much for helping to solve various issues in our lab. I admire your knowledge and high efficiency in solving these technical problems. Adelheid, thank you for the ICP measurements. Your kind remind about how to work properly in the lab is also appreciated. Thijs, thanks for your help during I was finalizing the experiment of my PhD research. Ingeborg and Rick from physical chemistry group, thanks for your help in electron microscopy.

Dear Emma, I am very grateful for your warm help to solve administrative and personal problems during the past years. Each time I asked you for help, you were always a good listener with much patience and then helped me efficiently. Best wish for your retirement. Sue, as a relay, you already do your job very well in my opinion. Thanks a lot for your help during my graduation phase.

Jiachun and Xianxuan, thank you very much for being my paranymphs. Jiachun, you joined IMC group only few days earlier than me. How time flies! I still remember the moment you took me to pick my own computer from ICT, which was almost five years ago. During my PhD, besides a good listener, you also helped me a lot in both my research and normal life. Although our research projects are totally different, we can always spend a long time to talk about some reactions in a general way (go to the periodic table). Best wishes to you! Xianxuan, I appreciate your willing to be involved in my Chapter 4. Your DFT calculations is indeed a necessary part to support my experimental results. During our discussion, I learned a lot from you about theoretical calculations. You are diligent and smart. Wish you the best luck with your research!

I would also like to thank the members who have been involved in my research. Lingqian, you taught me many skills about zeolite synthesis and characterization when I started my PhD. Your help is highly appreciated. Douglas, thank you for teaching me the bifunctional catalyst preparation and the hydroconversion test. I really appreciate your help and patience. Aleksei, thanks a lot for helping me in many ways. You were always willing to help me even when you were busy with your own things. Tan, you are a very friendly person. Thank you for the fruitful discussions we had. Hanglong from bio-organic chemistry group, thank you for ADF-STEM measurements and also for sharing knowledge of electron microscopy with me. Rim and Alexandra, thank you for the TEM measurements. Anna, thanks for your help in performing MTH reaction and the data processing. Yujie, thank you for performing the activity tests of my samples in MDA reaction. Pepe, we talked and shared a lot of our own insights about zeolite synthesis research in an open way.

I also would like to thank my other colleague and friends. Younes, my dear friend, you were always helping me throughout my PhD study. Yanan, we studied in the same group during both master and PhD study. Since you came to the Netherlands two years before me, you really helped me a lot in both research and life. Yue, my easygoing friend, I appreciate your patience to me. Best wishes for your thesis. Xiaofeng, we joined the IMC group at the same time and we helped each other a lot when we just started our PhD. Miao, thank you very much for your always kind help. Xianhong, your smile and humor always make our talks enjoyable. Hao, my bachelor classmate, wish you all the best for you PhD. Liang, thanks for

sharing your research with me, which broadened my knowledge in catalysis. Yu, you are young but seems already knowledgeable. Shiyue, thanks for your kind help in the lab. I also want to thank other current and former IMC members: Aleksei, Angelina, Arno, Bart, Bianca, Dimitra, Ferdy, Floriane, Freddy, Gabriela, Jan, Jan Philipp, Jason, Jérôme, Jiadong, Jinxun, Kaituo, Longfei, Long, Lu, Luke, Lulu, Marco, Marta, Mengyan, Michel, Panos, Qianqian, Robert, Sasha, Sidhanth, Tim, Tobias, Valentin, Valerii, Victor, Wilbert, Wei, Xiaoming, Yaqiong, Yvette, Zhaochun, Zhicheng...

Finally, my deepest appreciation goes to my family. 感谢父母一直对我求学生涯的理解和支持，你们的以身作则给予了我生活最大的动力，在过去几年对只能在家进行有限时间的陪伴深表惭愧。感谢哥哥少华一直对我在生活和学习方面无微不至的关心，莫大的幸运是我们能够在 TU/e 共同学习两年，你对生活的态度和理念一直是我学习的榜样。嫂子黄晗欢迎你将加入我们的大家庭，你对生活的积极态度深值我钦佩，对我生活上的照顾深表感谢。娜娜，感谢你一直以来对我的包容和鼓励，此刻你已从澳洲求学结束，我依然在荷兰，彼此漫长的等待终将收获属于我们的幸福。

李少杰

Shaojie Li

07/2022, Eindhoven

# List of publications

S. Li, H. Wu, R.C.J. van de Poll, R.R.M. Joosten, N. Kosinov and E.J.M. Hensen, Synthesis of nanocrystalline mordenite zeolite with improved performance in benzene alkylation and n-paraffins hydroconversion, *ChemCatChem*, 2022, 14, e202101852.

S. Li, R.C.J. van de Poll, N. Kosinov and E.J.M. Hensen, Facile synthesis of nanosized mordenite and beta zeolites with improved catalytic performance: non-surfactant diquaternary ammonium compounds as structure-directing agents, *Inorganic Chemistry Frontiers*, 2022, 9, 3200-3216.

S. Li, X. Ren, B. Mezari, Y. Liu, P. Pornsetmetakul, A. Liutkova, N. Kosinov and E.J.M. Hensen, Direct synthesis of Al-rich ZSM-5 nanocrystals with improved catalytic performance in aromatics formation from methane and methanol, submitted.

S. Li, B. Mezari, H. Wu, N. Kosinov and E.J.M. Hensen, Rigid diquat structure-directing agents for synthesis of ZSM-12 nanocrystals with improved performance in n-paraffins hydroconversion and methanol-to-hydrocarbons reactions, submitted.

S. Li, A. Liutkova, N. Kosinov and E.J.M. Hensen, *P*-phenylenedimethylene-bis(trimethylammonium) as a versatile diaquat template for synthesizing nanosized mordenite, EU-1 and ZSM-12 zeolites, submitted.

# Curriculum Vitae

Shaojie Li was born on the 6<sup>th</sup> of February 1990 in Baoding, Hebei, China. After finishing his high school degree in 2010 at Lixian High School in Lixian, he started his bachelor study in Chemical Engineering and Technology at China University of Petroleum (East China) in Qingdao. After obtaining his bachelor degree in 2014, he continued his master study at the same university under the supervision of prof. Chaohe Yang and prof. Xiaobo Chen. His study mainly focused on catalytic cracking of coker gas oil. In September 2017, he joined the group of Inorganic Materials and Catalysis at Eindhoven University of Technology as a PhD student with a scholarship from the China Scholarship Council. He worked on the synthesis of zeolite nanocrystals and their applications in heterogeneous catalysis under the supervision of prof.dr.ir Emiel Hensen. The main results are presented in this thesis.

